CONSTRAINING ALTERATION IN THE FOOTWALL OF THE SUDBURY IGNEOUS COMPLEX: A CASE STUDY OF THE ALTERATION FOOTPRINT TO THE PODOLSKY, CU(-NI)-PGE DEPOSIT, SUDBURY

by

Linette MacInnis

A thesis submitted in partial fulfillment
of the requirements for the degree of

Master of Science (MSc) in Geology

The Faculty of Graduate Studies
Laurentian University
Sudbury, Ontario, Canada

THESIS DEFENCE COMMITTEE/COMITÉ DE SOUTENANCE DE THÈSE
Laurentian Université/Université Laurentienne
Faculty of Graduate Studies/Faculté des études supérieures

Title of Thesis Titre de la thèse	CONSTRAINING ALTERATION IN THE FOOTWALL OF THE SUDBURY IGNEOUS COMPLEX: A CASE STUDY OF THE ALTERATION FOOTPRINT TO THE PODOLSKY, CU-(NI) PGE DEPOSIT, SUDBURY
Name of Candidate Nom du candidat	MacInnis, Linette
Degree Diplôme	Master of Science
Department/Program Département/Programme	Geology
Date of Defence Date de la soutenance	November 19, 2018

APPROVED/APPROUVÉ

Thesis Examiners/Examinateurs de thèse:

Dr. Daniel Kontak
(Supervisor/Directeur(trice) de thèse)

Dr. Doreen Ames
(Co-supervisor/Co-directeur(trice) de thèse)

Dr. Mike Lesher
(Committee member/Membre du comité)

Approved for the Faculty of Graduate Studies
Approuvé pour la Faculté des études supérieures
Dr. David Lesbarrères
Monsieur David Lesbarrères
Dean, Faculty of Graduate Studies
Doyen, Faculté des études supérieures

Dr. Attila Pantek
(External Examiner/Examinateur externe)

ACCESSIBILITY CLAUSE AND PERMISSION TO USE

Abstract

The footwall environment of the Sudbury Igneous Complex (SIC) host high-grade Cu-(Ni)-PGE deposits that have become a prime exploration target due to increases in metal prices and depletion of traditionally mined contact-style deposits that are high-grade Ni-Cu rich deposits. Understanding and constraining footwall deposits has been underway for some time, still, several aspects of these deposits that need to be constrained. With respect to alteration the nature, origin, relevance, and significance of these hydrothermal minerals have not yet been constrained.

A detailed study of the homogeneous grey gabbro unit that is hosted in the Podolsky 2000 deposit host's sharp-walled sulfide veins, rich in copper and PGEs was an ideal study area to look at alteration leading up to sharp-walled sulfide veins and its association to mineralization as the vein is approached. The initial step is to define and understand what the composition of the least altered grey gabbro with respect to its petrogenetic, spatial, and chronological relationship. Once the least altered grey gabbro is characterized alteration associated to these veins can be explored in detail. Alteration assemblages associated to these sharp-walled veins could potentially be implemented into an exploration tool for mining companies local to the area in search of such footwall deposits.

The least altered grey gabbro unit was not as homogenous as previously thought, after careful review of petrography, SEM-DES, geochemical bulk-rock data, isotope work, and U-Pb age dating; a suitable petrographic summary of the grey gabbro was achieved. Once a least altered summary was achieved, comparing this data to transects leading up to these sharp-walled sulfide veins and various samples of most altered grey gabbro were petrographically, geochemically, isotopically, compared to the least altered samples available.

Generally, understanding footwall deposits and unravelling the relevance and significance of these hydrothermal minerals was summarized in this thesis, unfortunately, these alteration trends are rather small and can only be observed <30 cm away from the vein, and are most obvious against the vein. This indicated that alteration signatures are not very strong outside of these sharp-walled sulfide veins, despite these veins ~1 m thick.

Table of Contents

List of Tables:

List of Figures:

List of Appendices:

Chapter 1: Thesis Introduction

Regional geological setting

The Sudbury Structure, which lies in the southern part of the Canadian Shield, is the product of an 1850 Ma bolide impact event (e.g., Dietz, 1960, 1964; Dressler, 1984; Krogh et al., 1984). This structure is located along the boundary of the ca. 2.7 Ga Superior Province, which lies to the northwest and forms the footwall rocks in the North Range, and the 2.5 Ga Southern Province, which lies to the southeast and forms the footwall rocks in the South Range. The Levack gneiss complex forms part of the Superior Province and is dominated by granitic rocks and a mixture of para- and ortho-gneisses rocks which record deformation and metamorphism at upper amphibolite to granulite facies (e.g., Card, 1994; Wodicka, 1997; Ames and Farrow, 2007). These rocks have been intruded by the 2640 Ma Cartier batholith and are cut by the 2450 Ma Matachewan mafic dyke swarm (Heaman, 1997). The North Range area also records the late Archean collisional event between the Superior and Southern provinces (e.g., Card, 1994; Wodicka, 1997). The Southern Province in the area includes part of the laterally extensive 2.5 to 2.2 Ga Huronian Supergroup that is comprised of metasedimentary and metavolcanic rocks (e.g., Ames and Farrow, 2007). The Southern Range rocks are intruded by layered anorthosite rocks from the East Bull Lake suite (2490-2470 Ma; Krogh et al., 1984) and gabbroic rocks from the Nippising diabase suite (2210-2217 Ma; Corfu and Andrews, 1986), and were metamorphosed to upper greenschist facies during the 1700 to 1900 Ma Penokean Orogeny event (Card, 1978). East of the Sudbury Structure (~15 km) is the Grenville Province, although splays of this structure extend further west into the study area (e.g., Card et al., 1984).

The Sudbury Structure is related to a bolide impact which produced a 200-250 km diameter transient crater that has since been reduced in size to an elliptical feature of 60 x 30 km

due to deformation and erosion (e.g., Grieves et al., 2010; Ames, 2008). The impact event produced a ca. 3 km thick melt sheet known as the Sudbury Igneous Complex (SIC) which generally consists of a lower gabbroic unit and upper granitic unit, with a granophyric texture (e.g. Dietz, 1960, 1964; Grieve et al., 1991). The SIC, as well as the overlying crater-fill rocks of the Whitewater Group and its surrounding area were strongly deformed during the 1700 to 1900 Ma Penokean Orogeny (eg. Milkereit and Green, 1992). In some cases, this has resulted in a strongly deformed and displaced mineralization which is related to the SIC.

The Sudbury Structure

The Sudbury Structure includes the 3-km thick SIC, the crystallized product of the impact-generated melt sheet. From the base to the top, the SIC consists of: (1) a sublayer noritic unit hosting mafic and ultramafic xenoliths, which is restricted to the North Range; (2) a mafic norite that grades upward to felsic norite; (3) a narrow (10s to locally 100s m) quartz gabbro; and (4) a monzogranitic unit referred to as the granophyre, based on its texture, that is dominated by quartz, plagioclase and K-feldspar with variable amphibole and biotite. Also related the SIC are offset dike rocks, which represent injections of the melt sheet into the underlying basement as both radial and concentric quartz diorite material.

Overlying the SIC is a crater fill sequence which is comprised of volcano-sedimentary strata from the Whitewater Group that is subdivided from base to top into four formations: the Onaping, Vermillion, Onwatin and Chelmsford formations. The lowermost unit, the Onaping Formation, is considered to represent a combination of fallback breccia and suevite combined with eruptive rocks related to phreatomagmatic explosions and volcanic eruptions. The overlying units consist of andesitic pyroclastics with a large vitric component (Onaping), carbonate

mounds (Vermillion), carbonaceous tuff (Onwatin), and feldspathic wacke (Chelmsford Formation; e.g., Ames and Farrow, 2007).

The Study Area and Thesis Objectives

This study focuses on defining the nature and origin of wall rock alteration marginal to Cu(-PGE)-rich footwall vein sulfide systems, which remains a poorly understood aspect of the ore environment in the Sudbury district. In order to do this, the actively mined, at the time of this study, Podolsky sulfide deposit, located in the North Range, was selected due to ease of access and appropriate geology, as discussed in the thesis. The deposit area lies in the Weisner Township approximately 32 km northeast of the city of Sudbury. The deposit area, referred to as the Whistle embayment, is a radial dike setting that underlies an embayment feature at the base of the SIC and crosscuts the Archean Levack gneiss complex. Thus, the Podolsky deposit area resides in the ~2 km long Whistle proportion of the radial offset that is proximal to the Whistle embayment (Giroux and Benn, 2005). More specifically, the Podolsky 2000 deposit, which is the area of study, resides ~200 m from the base of the Whistle embayment and ~650 m below the present surface. The deposit is a Cu-(Ni)-PGE hybrid deposit; in other words, it has features of both sharp-walled vein systems, which are essentially massive chalcopyrite (-pyrrhotite, -pentlandite) veins, and low-sulfide ore deposits, which contain <5 % disseminated sulfide material (e.g., Farrow et al., 2005).

The sharp-walled sulfide mineralisation selected for study resides dominantly in the grey gabbro unit (GG), which is a variably altered 234 m by 270 m gabbroic rock fragment of unknown provenance prior to this study. At the contact of the sulfide veins and the GG occur narrow, cm-scale alteration zones of epidote ± actinolite ± magnetite ± quartz; these alteration

halos grade over a cm to 1 m distance into the adjacent GG. The intent of this study is to focus on the nature and origin of this alteration. The use of mass balance and mineral chemical studies is used to chemically define the GG. The final phase of the project is to see if the geochemical signature is of sufficient scale to use as an application as a mineral deposit vector in the SIC area and perhaps in other environments.

In the context of the above, the objective is to use the study area to test if there is a large enough alteration zone around the sharp-walled veins that could be used to vector towards such mineralisation in this setting. In order to achieve this objective, the following was done: (1) map the distribution of units and alteration in the GG unit of the Podolsky 2000 deposit using archived drill core; (2) petrographically characterize the least altered GG unit; (3) use mineral and whole rock chemistry of the least-altered GG to assess its origin; (4) document the nature and extent of alteration marginal to the sharp-walled sulfide veins, with whole rock chemistry, use mass balance to assess mass change and element mobility in the alteration zone; and (5) assess the fluid reservoirs with the use of isotopes (S, O, Sr). Although not part of the original thesis goals, both the U-Pb and Ar-Ar geochronology were incorporated to address the potential source of the GG unit and the thermal evolution of the study area.

The results of this study have shown that the least altered parts of the GG unit are weakly and variably altered but can be characterized as a medium- to course-grained, homogeneous basic rock that is characterized by an ophitic texture typical of gabbroic rocks. Furthermore, the GG unit is shown to be intrusive with respect to Levack gneiss based on the chilled contacts observed which suggests it is itself a large fragment, an inclusion, in the offset dike rock setting. The latter is supported by U-Pb zircon geochronology and lithogeochemistry which indicate the GG unit is not sourced from the SIC, but instead was dislodged from a ca. >2714 Ma gabbroic

intrusion sourced in the basement rocks of the Superior Province referred to as the Joe Lake gabbro. A petrological study of the GG unit marginal to the footwall veins indicates the alteration zone is limited in scale and thus does not provide a significant vector to sulfide mineralisation.

Structure of Thesis

This thesis is presented in three chapters. Chapters 2 and 3 are written as manuscripts for publication in refereed scientific journals and as a result these chapters may contain duplication in order that they may exist as stand-alone contributions. The text, figures, and reference styles follow the format of Canadian Journal of Earth Sciences and Economic Geology, respectively.

Chapter 1 provides a brief non-technical introduction, an explanation of the structure of the thesis, and a statement of the responsibilities of the author and supervisory committee and other contributors to the thesis.

Chapter 2 is written as a manuscript entitled "**A Petrological and Geochronological Study of the Grey Gabbro Unit of the Podolsky Cu-Ni-PGE Deposit, Sudbury, Ontario: A 2714 Ma Gabbro Hosting 1850 Ma Impact-Related Mineralisation**" (to be submitted to *Canadian Journal of Earth Sciences*). The paper focuses on characterizing the geological setting and petrology of the GG unit that hosts part of the Podolsky Cu(-Ni)-PGE sharp-walled vein type deposit. The paper provides a detailed petrographic study of the GG, high precision TIMS and SHRIMP U-Pb zircon geochronology for the unit, and both mineral- and whole-rock geochemical data to allow complete characterization of the least-altered samples of the unit. The

data are used to infer the pre-impact history of the GG and reconstruct is paragenesis in the context of the impact event and subsequent mineralisation.

Chapter 3 is written as a manuscript entitled "**The chemical fingerprint of alteration marginal to a sharp-walled Cu(-Ni)-PGE vein setting in the Sudbury ore district revealed from the Podolsky deposit, Sudbury, Ontario**" (to be submitted to *Economic Geology*). This paper focuses on characterizing the mineralogy of the sharp-walled veins that cut the GG unit of the Podolsky deposit, the nature and the origin of the alteration marginal to these veins and assessing the source of the fluid reservoir. To do this a detailed petrological study was performed which included petrographic and SEM-EDS work of all rock types, whole-rock lithogeochemical traverses into the wall rock, LA ICP-MS analysis of chalcopyrite in vein and wall rock, and the integration of isotopic analysis of vein and wall rock materials (S, O, Sr). The results of this work are used to assess if such data could be used to provide criteria for targeting mineralisation in other footwall environments.

Statement of Responsibilities

The author was responsible for co-ordinating this study, collection of sample material used, and the characterization of the samples. However, several collaborators outside of Laurentian University were involved in the preparation of this thesis due to the need to acquiring relevant data to solve some of the problems posed, such as the age of the GG unit. The participation of Dr. Doreen Ames of the Geological Survey of Canada (GSC) who initiated the project and arranged for some of the analyses used in this study (see below). Several collaborators from mining companies such as Wallbridge Mining Company Limited and KGHM. The latter

managed the Podolsky deposit area during this study and provided insight and data in the context of the mining history and generously allowed important access to archived information (e.g., maps, photo library, Datamine Studio 3) used to produce the geology maps presented in Chapter 2. Several other people or institutions identified in the papers assisted with either providing background information and instruction regarding the use of the equipment used in the study (e.g., scanning electron microscope, electron microprobe) or by providing data such as the isotopic (O, S, Sr), geochronological (U-Pb, Ar-Ar), and whole-rock geochemical data.

This project was initiated as part of the Geological Survey of Canada Targeted Geoscience Initiative (TGI) - 4 Program and overseen in this context by Dr. Doreen Ames. At Laurentian, the study was supervised by Dr. Daniel Kontak. As the first author, I completed all the field related work, background research of the study area, prepared all the samples for analyses, performed all petrographic work, and generated the geological and alteration maps for the grey gabbro unit by using Datamine Studio 3 software provided by KGHM. The candidate wrote the first drafts of the two manuscripts which constitutes the main part of the thesis, which were edited by Dr. Kontak, and contain excerpts from Nicole Rayner (U-Pb geochronology) and Nancy Joyce (Ar-Ar geochronology). The final draft was read by Drs. D. Kontak, D. Ames, and M. Lesher.

Acknowledgements

This research was fully funded by the Geological Survey of Canada, with the under the Research Affiliate Program (RAP) TGI-4 Ni-Cu-PGE-Cr Project. I would like to thank Laurentian University for giving me the platform to step up to the academic challenge. I am grateful to my two supervisors, Dr. Daniel Kontak and Dr. Doreen Ames, without their patience this project would have never come to completion. Finally, I would like to thank my friends, family, colleagues, and of course, my significant other Steven, for the many discussions and unlimited morale support I have recieved.

References

Ames, D.E. and Farrow, C.E.G., 2007. Metallogeny of the Sudbury mining camp, Ontario.*in* Mineral Deposits of Canada: A Synthesis of Major Deposit Types, District Metallogeny, the Evolution of Geological Provinces, and Exploration Methods. *Edited by* W.D. Goodfellow. Geological Association of Canada, Mineral Deposits Division, Special Publication, 5, p. 329-350.

Ames, D.E., Davidson, A., and Wodicka, N., 2008. Geology of the giant Sudbury Polymetallic Mining Camp, Ontario, Canada. Society of Economic Geologists, v. 103, p. 1057-1077.

Card, K.D., 1978. Metamorphism of the Middle Precambrian (Aphebian) rocks of the eastern southern Province. *in* Metamorphism in the Canadian Shield. Geological Survey of Canada, paper, 78(10), p. 269-282.

Card, K.D., Gupta, V.K., McGrath, P.H., and Grant, F.S., 1984. The Sudbury structure: Its regional geological and geophysical setting. *in* Geology and Mineral Deposits of the Sudbury Structure. *Edited by* E.G. Pye, A.J., Naldrett, P.E. Giblin. Ontario Geological Survey, Special Volume, 1, p. 25-44.

Card, K.D., 1994. Geology of the Levack gneiss complex, the northern footwall of the Sudbury structure, Ontario. Geological Survey of Canada, Current Research, 1994, p. 269-278.

Corfu, F., and Andrews, A.J., 1986. A U-Pb age for mineralized Nipissing diabase, Gowganda. Canadian Journal of Earth Sciences, v.23, p. 107-109.

Dietz, R., 1960. Meteorite impact suggested by shatter cones in rock. Science, v. 73, p. 1781-1784.

Dietz, R.S., 1964. Sudbury structure as an astrobleme. Journal of Geology, v. 72, p. 412-434.

Dressler, B.O., 1984. General geology of the Sudbury area. *in* The Geology and Ore Deposits of the Sudbury Structure. *Edited by* E.G. Pye, A.J. Naldrett, and P. Giblin. Ontario Geological Survey, Special Publication, 1, p. 57-82.

Farrow, C.E.G., Everest, O.J., King, D.M., Jolette, C., 2005, Chapter 8: Sudbury Cu(-Ni)-PGE systems, Refining the classification using McCreedy West Mine and Podolsky project case studies, *in* Exploration for Platinum-Group Elements Deposits. *Edited by* J.M. Mungall. Mineralogical Association of Canada, Short Course, 35, p. 163-180.

Giroux, L.A., and Benn, K., 2005. Emplacement of the Whistle dike, the Whistle embayment and hosted sulfides, Sudbury impact structure, based on anisotropy of magnetic susceptibility and magnetic remanence. Economic Geology, v. 100, p. 1207-1227.

Grieve, R.A.F., Stoffler, D., and Deutsch, A., 1991. The Sudbury structure: Controversial or misunderstood. Journal of Geophysical Research, v. 96(5), p. 22753-22754.

Grieve, R.A., Ames, D.E., Morgan, J.V., and Artemieva, N., 2010. The evolution of the Onaping Formation at the Sudbury impact structure. The Meteoritics & Planetary Science, Nr. 5, p. 759-782.

Heaman, L.M., 1997. Global mafic magmatism at 2.45 Ga: Remnants of an ancient large igneous province?. Geology, v. 25, p. 299-302.

Krogh, T.E., Davis, D.W., and Corfu, F. 1984. Precise U-Pb zircon and baddeleyite ages for the Sudbury area.*in* The Geology and Ore Deposits of the Sudbury Structure. *Edited by* E.G. Pye, A.J. Naldrett, and P.E. Giblin. Ontario Geological Survey, Special Volume, 1, p. 431-447.

Milkereit, B., and Green, A., 1992. Deep geometry of the Sudbury structure from seismic reflection profiling. Geology, v.20, p. 807-811.

Wodicka, N., 1997. Sudbury Structure: Northern footwall rocks and Sudbury Igneous complex. *in* Timmins to Sudbury Transect: New Insights into the Regional Geology and Setting of Mineral Deposits. *Edited by* D.E. Ames. Geological Association of Canada-Mineralogical Association of Canada, Joint Annual Meeting, Ottawa '97, field trip B6, p. 73-93.

Chapter 2: A Petrological and Geochronological Study of the Grey Gabbro Unit of the Podolsky Cu-Ni-PGE Deposit, Sudbury, Ontario: A 2714 Ma Gabbro Hosting 1850 Ma Impact-Related Mineralisation

Linette MacInnis[1*], Daniel J. Kontak[1], Doreen Ames[2] and Nicole Rayner[2]

[1]Harquail School of Earth Sciences, Laurentian University, 935 Ramsey Lake Road, Sudbury, Ontario, P3E 2C6

[2]Geological Survey of Canada, 750-601 Booth Street, Ottawa, Ontario, K1A 0E8

Abstract

The Podolsky Cu(-Ni)-PGE sulphide deposit occurs in the Whistle Offset dyke in the North Range of the Sudbury Structure. It is comprised of Fe-Cu(-Ni) sulfide-rich veins (10s cm to meters) and Cu-Pt-Pd-Au veinlets and disseminations. The majority of the Cu(-Ni)-PGE ore is hosted in a large gabbroic rock, known as grey gabbro (GG), which herein is interpreted to be a fragment. A detailed petrographic, geochemical, istopic (Sr, O), and U-Pb zircon geochronological study reveals the GG crystallized at ca. 2714 ± 57 Ma.. It represents part of a larger gabbroic body intruded into rocks of the Levack Gneiss complex that was dislodged and injected into the Whistle Offset dyke during the 1.85 Ga Sudbury impact event. The parent intrusion is speculated to be equivalent to the Joe Lake gabbro, which is located about 14 km west of the Podolsky and which has a similar age, almost identical mineralogy and textures, and very similar whole rock geochemistry. Of relevance to this model is a textural record of the impact event and subsequent cooling of the superheated melt sheet that is recorded in the GG by

the highly modified primary, ophitic-textured pyroxene and plagioclase minerals in addition to the presence of clear, subhedral, neomorphic zircon which overgrows earlier, macroscopic (200-300 μm) zircon characterized by planar deformation features (PDFs). Whereas in situ U-Pb SHRIMP dating of the later zircon type yielded a 2714 ± 57 Ma date, U-Pb ID-TIMS dating of the former zircon type yielded 1849.9 ± 1 Ma which equates to the known age of the impact event. Thus, the GG unit records the generation of a large fragment during the 1.85 Ga Sudbury impact event which subsequently became an important host site of sharp-walled footwall sulfide ore in the Podolsky deposit.

Introduction

The footwall environment to the 1.85 Ga impact melt sheet which crystallized as the Sudbury Igneous Complex (SIC) hosts significant high-grade Cu(-Ni)-PGE vein-type deposits that have in recent years become major exploration targets in this mature (100+ year) mining camp (Lightfoot 2016). These footwall deposits are located in the basement rocks to the SIC and differ from the historically mined Ni-Cu contact deposits, which are found at the basal contact of the SIC in contact with high modified (i.e., thermally and mechanically) footwall rocks. Footwall deposits are defined by their sharp-walled vein geometry that often includes narrow alteration haloes and a metal endowment of Cu-PGEs (e.g., Farrow and Watkinson 1996, 1999; Farrow and Lightfoot 2002; Farrow et al. 2005). In addition to the contact and footwall ore deposits, significant Ni-Cu-PGE sulphide deposits are also present in radial offset dyke settings. The injection of melt prior to the crystallization of the melt sheet and the formation of the layered SIC are what relate these deposits to the SIC (Lightfoot et al. 2001; Ames et al. 2002).

Additionally, these rocks also host economic sulfide mineralisation (e.g., Lightfoot and Farrow 2002).

The Podolsky Cu(-Ni)-PGE deposit (2.1 M tonnes of ore grading 4.55 % Cu, 0.4 % Ni, 0.139 oz./ton Pt+Pd+Au; 2007-2011; courtesy of KGHM, 2013) is an unusual deposit in that it is hosted in a radial offset dyke setting and is classified as a "hybrid"-style deposit. The hybrid term reflects the nature of the mineralisation which contains characteristics of both sulfide-rich, most notably chalcopyrite-rich, sharp-walled veins and low-sulfide ore. The latter ore is characterized by the presence of sulfides as veinlets and or disseminations (Farrow et al. 2005). Within part of the Podolsky deposit, sharp-walled sulfide vein mineralisation occurs in a single unit that has been informally referred to as the grey gabbro (GG unit herein), which is both an unusual and rare host for footwall-style mineralisation in the Sudbury region. To understand the significance of this rock, the current study attempts to characterize and assess its origin and relevance to the footwall-style mineralisation.

To address the origin of the GG, this paper presents the results of an integrated mapping study of the unit using archived drill core which was combined with underground observations of the unit, a detailed petrographic and SEM-EDS study, combined mineral and whole rock geochemistry, isotopic (O, Sr) analysis to assess the source the GG unit, and combined U-Pb CA-TIMS and SHRIMP dating of zircon to constrain the age of the GG. Significantly the study shows that the GG originated as part of a composite fragment what was dislodged as part of the impact event and transported to its current location in the Whistle embayment structure of the SIC.

Regional Geology

The Paleoproterozoic (1850 Ma) Sudbury Structure (SS), a 60 x 30 km elliptical-shaped, northeast-oriented feature, is widely accepted to represent the erosional remnants of a much larger (200 km) transient impact crater (e.g., Dietz 1960, 1964; Card et al. 1984; Dressler 1984; Grieve et al. 1991). The SS is located at the boundary of the ca. 2.7 Ga Superior Province (North Range) and the 2.5 Ga Southern Province (South Range; Fig. 1); a late-stage Archean collisional event between the Superior and Southern provinces is recorded in the North Range (e.g., Card 1994; Wodicka 1997). The Levack gneiss complex, which underlies the area to the north of the SS, is comprised of gneissic and granitic units and records high-grade metamorphism and deformation as upper amphibolite to granulite facies (e.g., Card 1994; Wodicka 1997; Ames and Farrow 2007). The Southern Province, which underlies the area south of the SS, includes parts of the laterally extensive Huronian Supergroup that is comprised of metasedimentary and mafic to felsic metavolcanic rocks (e.g., Ames and Farrow 2007). These rocks have been intruded by the 2640 Ma Cartier batholith and are cut by the 2450 Ma Matachewan mafic dyke swarm (Heaman 1997). The East Bull Lake suite (2490-2470 Ma; Krogh et al. 1984), comprised of layered anorthosite rocks, and the Nippising diabase suite (2210-2217 Ma; Corfu and Andrews 1986) intrude the Southern range rocks. Several periods of deformation and metamorphism has occurred in this region, the most intense is likely the Penokean Orogeny (ca. 1850 Ma; Young et al. 2001; Lafrance and Kamber 2010; Mukwakwami et al. 2014).

The impact generated crater was filled with a melt sheet, now represented by its crystallized product the SIC, and overlying volcano-sedimentary strata of the Whitewater Group, which consists of four formations, from oldest to youngest: the Onaping, Vermilion, Onwatin, and Chemsford (Ames et al. 2002). The crater fill sequences consist of a basal fallback breccia

and overlying phreatomagmatic explosions and volcanic eruptions of the Onaping Formation (e.g., Ames 1999; Grieve et al. 2010; Lafrance et al. 2014), and the overlying sedimentary units of the Vermilion, Onwatin, and Chelmsford formation (Rousell 1984). Evidence in support of the 1850 Ma bolide impact event includes shatter cones distributed in a radial pattern around the SIC, high-pressure shock metamorphic mineral phases, and abundant pseudotachylite known as Sudbury breccia (Thompson et al. 1998; Rousell et al. 2003; Ames and Farrow 2007; Lafrance et al. 2008). All these features decrease in abundance away from the SS.

The SS has undergone a significant amount of regional compression in the NW-SE direction attributed to several pre- and post-impact orogenic events (e.g., Bailey et al. 2004; Ames and Farrow 2007; Lafrance and Kamber 2010). The North Range is realatively undeformed where the the South Range has endured a complex deformation event largely attributed to the South Range Shear zone (e.g., Ames and Farrow 2007; Lafrance and Kamber 2010; Mukwakwami et al. 2014). Much of the deformation along the South Range has been attributed to the Penokean Orogeny event which occurred between 1.9 Ga and 1.7 Ga (e.g., Milkereit and Green 1992; Young et al. 2001, Lafrance and Kamber 2010).

The dominant igneous units of the ca. 2.5 km thick Main Mass of the SIC include the following, which is listed from base to top (Dressler 1984; Ames and Farrow 2007; Ames et al. 2002): (1) a sublayer unit consisting of mafic- and ultramafic xenoliths in a matrix of norite; (2) mafic norite, in the North Range only, that grades upwards into felsic norite; (3) quartz gabbro, which represents a transitional rock; and (4) an amphibole- and biotite bearing monzogranitic unit (i.e., quartz and two feldspars) referred to as the granophyre based on its texture. The units are variably interpreted to represent the crystallization of an originally homogeneous melt sheet (Coats and Snajdr 1984; Lightfoot et al. 1997a; and Rousell et al. 1997), a product of density

segregation (Golightly 1994) or product of emultion segregation (Zieg and Marsh 2005). Also related to the SIC are two styles of offset dykes: (1) radial offset dikes, which can extend for up to 30 km from the SIC, and (2) concentric offset dykes, which can occur outwards for 14 km from the lower contact of the SIC (Wood and Spray 1998). The radial offset dykes vary compositionally between quartz monzodiorite-granodiorite-tonalite (Lightfoot et al. 2001) and are locally known as "quartz diorite" (QD); these dikes can be inclusion rich (IQD) and are locally mineralised in their cores. In contrast, the concentric offset dyke domains are dominated by pseudotachylitic breccia and are locally referred to as "Sudbury breccia" (e.g., Lafrance and Kamber 2010).

Geology of the Whistle embayment and offset dyke

The Whistle radial offset dyke has a strike length of ~12 km and is located approximately 32 km north-northeast of Sudbury (Fig. 1). This dyke radiates northeast and connects to the SIC at the base of the Whistle embayment, which contains Ni-rich massive sulfide contact-style mineralisation (Fig. 2). The embayment feature is funnel-shaped, ~350 m wide at the intersection with the SIC and is dominated by norite with sublayer at its base (Fig. 3a, b; Pattison 1979; Lightfoot et al. 1997b; Giroux and Benn 2005). This offset dyke cuts Archean Levack gneiss (Fig. 3c), which forms the basement rock to the SIC in this area, and this is composed of two units or rock types. The less dominant, but the first to form, is a medium-grained quartz diorite (i.e., the QD) that is in contact with the Levack gneiss. Subsequent to the the QD and coring the offset dyke is the inclusion-rich equivalent (i.e., IQD; Fig. 3d) which contains clasts variable in their size, shape and composition such as the Levack gneiss, metagabbro, Nippising diabase dykes, Matachewan diabase dyke and Sudbury breccia (Fig. 3e; e.g, Carter et al. 2009). The

matrix of the IQD often records a metamorphic texture and thus is termed the metabreccia (MTBX; Fig. 3f) unit of metamorphosed IQD and is located around the SS. Approximately 50 m away from the base of the Whistle embayment, the offset dyke discussed above cuts a discontinuous zone of Sudbury breccia (Bygnes, 2011; Lafrance et al. 2014), a unit of pseudotachylitc rock formed in the basement rocks to the SIC and related to the impact event (Rousell et al. 2003). The Podolsky deposit, located in the Whistle offset dyke (Fig. 2), occurs in both a large fragment of the GG unit (Fig. 3g-h), the subject of this study, and the metabreccia and inclusion quartz diorite units of the offset dyke.

Nature of the mineralisation in the Whistle embayment and Podolsky deposit

Mineralisation in the study area consists of both contact- and footwall low-sulfide -style ore. Within the Whistle embayment resides contact-style ore that is comprised of Ni-rich massive sulfide hosted by the sublayer norite (Fig. 2a) and which formed the Whistle open-pit mine that contained 5.7 M tonnes of ore grading 0.33 % Cu and 0.95 % Ni (Farrow et al. 2005). The Cu-PGE-rich Podolsky deposit, also referred to as the "2000 deposit", is a hybrid deposit with two ore types, which are a sharp-walled sulfide "footwall"- type ore and a low-sulfide ore characterized by veinlet and disseminated sulfide mineralisation. In addition, two rocks are host to the mineralisation: (1) breccia-hosted (MTBX-IQD) that typically consists of disseminated and blebby-type sulfide mineralisation; and (2) the GG unit (~230 m x 90 m x 275 m), the focus of this study, which hosts sharp-walled sulfide (i.e., chalcopyrite) veins with narrow (10s cm) alteration haloes with disseminatd sulfide ore. Between 2007 and 2011, the 2000 deposit produced 1.502 M tonnes of Cu-rich ore at 4.29 wt. % Cu, 0.38 wt. % Ni, and 0.139 oz./t TPMs

(Pt + Pd + Au; courtesy of KGHM; Fig. 2b). In March 2013, the deposit was placed on care and maintence.

Method of mapping the grey gabbro unit

The GG unit was mapped in select drill holes and this was supplemented by using a photo archive (courtesy of KGHM) of all the drill core at 1.5 m intervals (12 diamond drill holes). The drill holes were selected according to their spatial location and sampling availability. Of the drill holes used in the photo library, six were used to remap a plan-section targeting the mid-section of the deposit (1925 level) and a further six were used to remap a cross-section of the GG.

To define lithological variation in the GG, each 1.5 m interval was mapped for lithology, texture, fabric, percentage of sulfide mineralisation and alteration. Major and minor lithologies were distinguished by fabric (aligned plagioclase laths) and grain size (index of possible proximity to contacts). Mineralisation was separated into massive sulfide (100-85 % chalcopyrite over 10 cm) or semi-massive sulfide (85-55 % sulfide over 10 cm) to assess any patterns in the distribution of the mineralisation. Finally, the type and style of alteration was noted within each interval and its degree of intensity (Fig. 4).

Geological and petrographic features of the grey gabbro unit

Within the GG there occurs small intervals of other rock types that include metagabbro, matachewan diabase (Fig. 5a), QD (Fig. 5b), IQD (Fig. 5c), MTBX (Fig. 5d), and granite; these rock types conform to those used by mine geologists for mapping units in the SIC and area. The lack of continuity of the former suggest these units cross cut the GG. Remapping of the GG unit coincides with observations from examination of drill core that this unit is, at the macroscopic

scale, texturally uniform with an overall medium- to coarse-grained, equigranular texture and consisting of 55 % mafic clots and 45 % plagioclase (Fig. 5e-f; see Figs. 3e and 4). The unit locally changes into small domains of pegmatite (<20 cm) characterized by a coarser grain size and pinkish-orange colour (Fig. 5g-h). No overall trends for pegmatite distribution were noted in the GG unit was noted.

Historically, small domains of felsic-rich rock in the GG unit were logged as Levack gneiss. It has been debated among the mine geologists (pers. commun. 2011) whether these sections represent inclusions of Levack gneiss or sections of granite resulting from fractionation of the GG where the unit coarsens and trends toward a pegmatite (Fig. 3h). The GG is observed in one locality to become finer-grained proximal to the Levack gneiss contact, a feature which was also noted elsewhere in the mine based on discussions with mine geologists, unfortunately the exact locations of these observations were not recorded. Thus, observations by the researchers and the mine geologists are consistent with an aparent intrusive relationship between the GG unit and the Levack gneiss with the reduction in grain size attributed to chilling. This aspect, which appears to be a contradiction based on its fragmental nature, is addressed later.

Based on the maps produced from plan- and cross-sections (Fig. 6), the following points are noted regarding the general features of the grey gabbro and its relationship to mineralisation and alteration:

1. The upper proportion of the GG unit (i.e., above the 1850 level) records a slight to moderate foliation with either a weak or no foliation noted below this point;
2. Epidote alteration is present in the lower quarter of the cross-section (Fig. 6a) and is abundant in the southeast part of the plan section (Fig. 6b);
3. A moderate correlation is noted between non-foliated GG and mineralisation; and

4. A strong correlation is noted between the increased abundance of epidote-rich alteration halos along fractures and bordering veins and the overall amount of mineralisation.

Representative scanned thin section (Figs. 4b-d, 4f-h, and 7a, b) reveal the GG is medium- to fine-grained and homogeneous with a "salt-and-pepper" texture. The original primary mineral phases, interpreted to have been plagioclase and clinopyroxene, were variably modified due to post crystallization metamorphic and hydrothermal processes, as discussed below. In thin section, a relict ophitic texture is commonly observed, now defined by mafic clots and subhedral domains of calcic plagioclase. Less abundant minerals, present as subhedral to anhedral grains, include: orthopyroxene, hornblende, biotite, ilmenite, zircon, apatite and quartz.

The plagioclase domains (1.5 mm) consist of fine-grained (0.2 mm), sub-equant laths of labradorite (An_{50}) with a granoblastic "mosaic" texture (Fig. 7c, d); they resemble textures seen in gabbroic rocks in contact aureoles (e.g., Hobson et al. 1998). In these plagioclase domains, finer-grained assemblages of quartz, epidote, sericite, and oligoclase (An_{20}) are present (Fig. 7e, f); trace amounts of disseminated chalcopyrite also occur. Rarely present are domains of granophyric quartz and alkali feldspar (0.5 mm) with variable apatite.

The mafic clots consist of mixed assemblages with rare residual pyroxene; no areas of only primary pyroxene were observed. These mixed assemblages consist of: 1) sub- to anhedral augite (10 %, 1-2 mm, pink-green pleochroism; Fig. 7g-j); 2) relict sub- to anhedral enstatic pyroxene (<1 %, 0.5-1 mm, pale red to green-brown pleochroism); 3) relict sub- to anhedral amphibole (<1 %, 0.5-1 mm, pale green to green-brown pleochroism; Fig. 8a, b); 4) complete or partial pseudomorphism of the pyroxene by fibrous actinolitic amphibole (20 %, 1-2 mm, tan-green pleochroism; Fig. 8c-h); 5) relict and secondary, sub- to euhedral biotite (15%; brilliant red-brown to a dark-brown pleochroism) that replaced primary amphibole (Fig. 8i-l); 6) relict

subhedral ilmenite typically resides within or beside biotite (1 %, 0.5 mm; Fig. 9a); 7) secondary oxide phases (hematite, magnetite, rutile) as accessory phases in the mafic clots (Fig. 8l).

Oxide phases are not abundant but are consistently present throughout the unit. Ilmenite is the primary oxide phase (<1 %, <0.5 mm) and is present as subhedra in red-brown biotite. Exsolution lamellae of magnetite define a trellis texture, as observed in both reflected light and in SEM BSE images (Fig. 9b-g). Rutile is only observed using the SEM and is present as small grains in biotite (Fig. 8l). Trace magnetite occurs in ilmenite as an exsolution texture, but proximal sulphide veins, ilmenite is altered and completely replaced by magnetite (Fig. 9b-g).

Locally coarse (2 mm) apatite euhedra are present in late-stage granophyic domains of the GG. In addition, apatite is commonly observed in granitic pegmatite segregations (Fig. 9h). A common accessory phase is zircon, which is present in two habits. The most common type is as coarse (<300 μm; 10a-i) subhedral to anhedral grains with a diffuse, red-brown colour (Fig. 10a-c). These grains are often decorated by abundant (80-90 %) inclusion trails (Fig. 10a-f) and are like planar deformation features (PDFs) reported in shocked zircons from impact sites (e.g., Corfu and Andrews 1986). These zircons are rimmed by a second zircon, which is a scalloped textured variety characterized by their clarity, lack of colour, euhedral terminations, and inclusion-free nature (Fig. 10g-h). This zircon variety may also occur along fractures in the earlier zircon PDFs (Fig. 10l). Further details of zircon are noted below in regards to sampling for U-Pb geochronology.

Lastly, alteration or development of secondary phases of variable origin (see discussion below) is present in the GG unit and includes quartz, epidote, sericite, chlorite, alkali feldspar, calcite, and actinolite. These assemblages are observed as alteration selvages (Fig. 11a-b) and micro-veins (Fig. 11c-d).

Analytical Methods

Whole-rock chemistry

The whole-rock chemistry was determined on 23 samples from the Podolsky deposit which included nineteen least altered samples of GG, three diabases, and one pegmatite (Table 1; Appendix 1). Of these, seventeen samples were analysed for a complete suite of elements (major, traces, rare earth elements, volatiles (loss on ignition (LOI), H_2O^+, H_2O^-, CO_2, S, F) at Acme Laboratories, Vancouver, British Columbia. The analytical methods used included: 1) whole rock fusion by X-ray fluorescence (XRF) for major and some trace elements; 2) ICP-MS after aqua regia digestion for precious- and base metals; 3) ICP-MS after a lithium metaborate / tetraborate fusion and a nitric acid digestion for rare earth and refractory elements; 4) LECO inductive combustion and infrared absorption for C and S; and 5) titration analysis for FeO. A further six samples were analysed by the GeoLabs, Sudbury, Ontario using the following procedures: 1) XRF on pressed pellets for select trace elements (Cr, Mn, Ti, Zr); 2) closed beaker multi-acid digestion followed by ICP-MS for minor-, trace-, and rare earth elements; 3) hydride-generation ICP-MS for Se and Te elements; and 4) LECO inductive combustion and infrared absorption for CO_2 and S. Inclusion of standards and duplicates were done to assess analytical precision and accuracy. The complete list of data is provided in Table 1 and Appendix 1.

Mineral chemistry

The major and accessory mineral phases in the GG were characterized using a JEOL 6400 scanning electron microscope (SEM) with an INCA energy dispersive spectrometer (EDS) and dectector system housed in the Mineral Analytical Centre (MAC) at Laurentian University, Sudbury, Ontario. Operating conditions were: accelerating voltage 20 keV, 1.005 ηA beam current, acquisition count times of 5-10 seconds but 30 seconds for rasters where reported, and a

working distance of 15 mm. Well characterized standards (jadeite, diopside, orthoclase, corundum, quartz, chalcopyrite, pyrophanite) were used to calibrate the instrument. The detection limits are about 0.15 wt. %.

The chemistry of clinopyroxene, amphibole, biotite, and chlorite were further determined using wave length dispersive spectrometry (WDS) with a Cameca SX-100 electron microprobe (EMP analysis) housed in the Ontario Geological Survey Geoscience Laboratories (GeoLabs), Sudbury, Ontario. The instrument was calibrated using a variety of in-house mineral standards and operating parameters were 20 keV accelerating voltage and a beam current of 20 ηA. A focused beam (1 μm) was used on all the phases with the exception of biotite for which a defocused beam (5 μm) was used. The detection limits for most elements was 0.025 wt. %. The complete list of data is provided in Table 2.

Strontium and oxygen isotopic analyses

Strontium isotopes were analyzed on two GG samples (Table 3) at the Carleton Isotope Geochemistry & Geochronology Research Centre (IGGRC), Ottawa, Ontario. Samples were dissolved in 2.5 N HCL and pipetted into a 14-ml Bio-Rad borosilicate glass chromatography column containing 3.0 mL of Dowex AG50-X8 cation resin, dried down and the residue dissolved in 0.26 N HCl. The strontium was then loaded onto a single Ta filament with H_3PO_4 and is run at filament temperatures of 1350-1500°C. Isotope ratios were normalized to $^{86}Sr/^{87}Sr$ = 0.11940 to correct for fractionation. Two standards were run with the analysis - NIST SRM987 and the Eimer and Amend (E&A) $SrCO_3$. Separated Rb is loaded with H_3PO_4 onto one side of a double Re filament assembly and run at temperatures of 1250-1300°C on a ThermoFinnigan Triton Tl thermal ionization mass spectrometer.

Oxygen isotopic analyses for five least altered GG samples were determined at the Queen's University Facility for Isotopic Analysis in Kingston, Ontario. The standard BrF_5 procedures of Clayton and Mayeda (1963) were used to liberate oxygen the isotopic ratios were determined using a Thermo-Finnigan MAC 253 and a DELTA^{PLUS}XP stable isotope ratio mass spectrometer. Results (Table 3) are reported using the standard format of $\delta^{18}O$ (VSMOW) in values of per mil (‰); repeated analyses of standards indicate data are reproducible to ± 0.1‰.

U-Pb zircon geochronology and nature of zircon types

A sample of least alterted the medium-grained GG from the 1700 level of the Podolsky mine was submitted for U-Pb geochronology at the Geological Survey of Canada (11AV-74, lab number z10633). Electric-pulse disaggregation (EPD; Rudashevsky et al. 1995) using a Spark-2 instrument was employed to comminute 1 kg of sample. Heavy minerals were separated from the sieved rock powder (<250 μm) using heavy liquids (methylene iodide) followed by sorting using a Frantz isodynamic separator. Prior to analysis the internal features of the zircons (zoning, structures, alteration, etc.) were characterized using a Zeiss Evo® SEM in backscattered electron (BSE) and cathodoluminescence (CL) images. The extracted zircon separate was analysed by both the isotope dilution–thermal ionization mass spectrometry (ID-TIMS) and the sensitive high-resolution ion microprobe (SHRIMP) techniques. Zircon grains analysed by ID-TIMS were treated with the chemical abrasion method (Mattinson 2005) before being submitted for U-Pb chemistry. Dissolution of zircon in concentrated hydrofluoric (HF) acid, extraction of U and Pb, and mass spectrometry followed the methods described by Parrish et al. (1987). Data reduction and numerical propagation of analytical uncertainties follow Roddick (1987). Analytical blanks

for Pb were 1 pg (lower limit of detection). Results are presented in Table 4 with uncertainties reported at the 2σ level.

SHRIMP analytical procedures and U-Pb calibration details are given in Stern (1997) and Stern and Amelin (2003). Selected zircons were cast in 2.5 cm diameter epoxy mounts along with fragments of the GSC laboratory standard zircon (z6266, with $^{206}Pb/^{238}U$ age = 559 Ma). The midsections of the zircons were exposed using 9, 6, and 1 μm diamond compound, and the internal features of the zircons (such as zoning, structures, alteration, etc.) were assessed. Footnotes supplied on accompanying data tables highlight ion probe analytical details regarding spot size, beam current, number of scans and error in calibrating the external errors of the $^{206}Pb/^{238}U$ ratios of the samples (see Stern and Amelin 2003). Measurement of the $^{207}Pb/^{206}Pb$ ratio in a secondary zircon standard (z1242; accepted age 2679 Ma, B. Davis personal communication 2014) was carried out to assess if an intra-element fractionation correction was required. No Pb-isotope fractionation correction was needed; the common Pb correction used the Pb composition of the surface blank (Stern 1997). Isoplot v. 3.00 (Ludwig 2003) was used to generate concordia plots and calculate weighted means. SHRIMP isotopic data are presented in Table 5, with errors on isotopic ratios and spot ages given at 1σ uncertainty. All ages quoted in the text, and error ellipses on all concordia diagrams are given at the 2σ uncertainty level.

Although the zircons have been described above, aspects relevant to selection of material for dating is further provided. Two morphological types in roughly equal proportion are present with one sub-population consisting of clear, colourless, euhedral, prismatic (elongate to stubby), well-faceted and terminated crystals with few fractures and rare clear inclusions (Fig. 12a). The latter features, in addition to CL images showing the zircons are strongly luminescent with sharp oscillatory and sector zoning, suggest growth from a magma (Fig. 12b; Corfu et al. 2003).

The second zircon sub-population consists of highly fractured, anhedral, pale brown, cloudy fragments; in rare instances these zircons are overgrown by a clear, colourless zircon similar to the morphology described above (Fig. 13a). The fractured zircon has relatively poor CL response (Fig. 13b), whereas the clear overgrowths luminesce strongly (Fig. 13b). Corresponding BSE images faintly mimic the CL zoning and more clearly illustrate fractures and inclusions (Fig. 13b). These BSE images also clearly show the presence of crystallographically oriented features, which include short fractures or small pits, which resemble PDF features due to shock impact (Krogh et al. 1984; Bohor et al. 1993; Krogh et al. 1993a, b; Krogh et al. 1996; Pidgeon et al. 2011).

Analytical results

Whole-rock geochemistry

Nineteen samples of least altered GG were used to assess its chemistry. The data reveal only minor geochemical differences throughout the GG unit and overall the major- and trace-element abundances are relatively homogeneous (Table 1). On a volatile-free basis, the rocks have about 50 wt. % SiO_2, 15.8–16.8 wt. % Al_2O_3, 5-10 wt. % CaO, and 5.0-8.5 wt. % MgO. On a volatile-free basis, the average normative mineralogy of the unit is 59 % An, 12 % Or, 8 % Cpx, 4 % Opx, 12 % Fo, 1 % Ilm, 1 % Mt, and 2 % Apt. Harker-type variation diagrams (Fig. 14) shows a strong positive correlation between MgO and SiO_2, whereas FeO_T, CaO, P_2O_5, and Al_2O_3 have a strong negative correlation. These trends suggest there has been minor accumulation of clinopyroxene in the unit. For other elements (e.g., TiO_2, Fe_2O_3, MnO, Na_2O, and K_2O) the Harker diagrams reflect minor amounts of fractionation in the grey gabbro unit (Cox et al. 1979). Magenesium numbers range from 40.9 to 64.0 with an average value of 49.5

(n=19; Table 1). Samples plot in the field for subalkaline rocks based on total alkalies (TAS; Fig. 15a) and Zr/TiO_2 versus SiO_2 (Fig. 15b) and correspond to fields for gabbro/basalt.

In terms of trace element geochemistry, the primitive mantle normalized plots were used as a reference to assess elemental enrichment or depletion (Fig. 16a). The GG unit shows an overall restricted range in its trace element chemistry with both the largest enrichment and the greatest variation seen for the large ion lithophile elements (LILE), in particular Pb and Ba, whereas the most depletion is seen for the high field strength elements (HFSE) relative to LILEs, as denoted by negative spikes in Th, Nb, Ta, Zr, and Hf. The chondrite-normalized rare-earth element (REE) plot (Fig. 16b), which also shows a very restricted range for the data, indicates relative enrichment in the LREE, a strongly fractionated pattern, and the absence of an Eu anomaly, either positive or negative. In the same diagram, reference plots are shown for OIBs CFBs and MORBs, which indicate that the data for the GG unit is most like the profile for OIBs.

Mineral Chemistry

Plagioclase

Plagioclase compositions (Fig. 17, Appendix 2a) for both the laths and coarser-grained domains (i.e., raster mode) are uniformly An_{50}. In contrast, smaller plagioclase grains intergranular to the laths or found along fractures aligned with quartz-chalcopyrite-epidote assemblages (Fig. 7e) range in compositions from An_{20} to An_0 (Fig. 17).

Pyroxene

The chemistry for pyroxene, both EMP and SEM-EDS analyses, indicates uniform compositions (Fig. 18a; Table 2a). The dominant pyroxene type is a low-Ti, Mg-rich augite with

an average composition of $Ca_{45}En_{42}Fs_{14}$, which overlaps the diopside-augite field. Lesser enstatitic pyroxene with a uniform composition of $Ca_1En_{72}Fs_{26}$ is noted. Raster analyses of the mineral clots after clinopyroxene grains or glomeroclasts reveal a chemistry and stoichiometry that equates to the pyroxene noted above (Fig. 18a; Appendix 2b).

Amphibole

Amphibole chemistry was obtained using EMP and SEM-EDS analyses. The data are plotted in Figure 18 and representative analyses are given in Table 2b with the complete data provided in Appendix 2b. All the amphibole, after relict pyroxene, show a large range in chemistry is the Ca-Mg-Fe ternary (Fig. 18a). In the amphibole classification diagrams, the data correspond to the fields for magnesiohornblende and actinolite, and also fall in the field for low-pressure amphibole (Fig. 18b, c).

Biotite and Chlorite

Results of EMP analyses for biotite (Table 2c) indicate a uniform chemistry regardless of type of occurrence (i.e., replacing amphibole, or as singular grains in the mafic clots). Biotites are enriched in both Mg (15 wt. % MgO; *mg* values averaging 0.67) and Ti (5-6 wt. % TiO_2) and contains F, but in low abundance with values between 0.3 to 0.6 wt. %, and Cl is lower at <0.06 wt. %.

The EMP analysis of chlorite (Table 2d), which occurs after biotite, indicates uniform chemistry with *mg* values of 0.55, thus like the biotite it replaces.

Oxides

The chemistry for Fe-Ti oxides, as determined with the SEM-EDS, indicates a variation in composition between magnetite and ilmenite (Appendix 2c, 2d). Ilmenite is enriched in titanium and contains a trace amount of manganese. Magnetite is enriched in iron and contains a trace amount of titanium.

Geochronology of the grey gabbro

TIMS results

Six single-grain fractions of euhedral zircon were analysed by ID-TIMS (Table 4). The weighted mean $^{207}Pb/^{206}Pb$ ages of the five most concordant (0.1-0.3 % discordance) analyses are 1849.9 ± 1.0 Ma (Fig. 19a; MSWD = 0.25, probability of fit = 0.91). A sixth fraction that is slightly older (1854 Ma) and slightly more discordant (0.7 %) is interpreted to reflect the incorporation of a minor amount of inherited zircon.

SHRIMP results

Twenty-one analyses were carried on fifteen anhedral zircon grains, with a small number of analyses targeting euhedral overgrowths on those same grains (Table 5). The anhedral zircon is characterized by U concentrations between 40-230 ppm and Th/U ratios greater than 1. The zircon grains yield $^{207}Pb/^{206}Pb$ ages between 2606 Ma and 2133 Ma and are typically between 3-10 % discordant. Examination of the data on a concordia diagram (Fig. 19b) indicates the results from the anhedral zircon form a linear array with an upper intercept of ca. 2.68 Ga and a lower intercept of ca. 1.83 Ga. However, if the lower intercept is anchored at 1850 Ma, the known time of the impact event and cause of the discordia array seen in Figure 19b, then an upper intercept

age of 2714 ± 52 Ma is calculated and is considered to define the best approximation of the minimum age for the GG unit. The SHRIMP results from the four euhedral overgrowths are consistent with this lower intercept (i.e., 1850 Ma) but are relatively imprecise due to their low U content (Table 5). The zircon overgrowths also have Th/U ratios greater than 1. The consistency of the SHRIMP age, U concentration, and Th/U values of the overgrowths with the TIMS results for the euhedral zircon support the interpretation that the overgrowths and euhedral zircon are a single generation with an age similar tothat from the TIMS analysis of 1849.9 ± 1.0 Ma.

Oxygen and Strontium Isotopes

Results for $\delta^{18}O$ analyses for five whole-rock GG samples (Table 3) indicate values from +6.6 to +8.1‰. Inspection of the data indicate no strong correlation of the data with either the degree of alteration in the samples based on petrography or chemical parameters (e.g., abundance of LOI or CO_2).

Strontium isotopic data were analysed on two GG samples and are given in Table 3. The whole rock samples have low $^{87}Rb/^{86}Sr$ ratios due to the mafic nature of the rock; thus, an initial Sr_i ($^{87}Sr/^{86}Sr$) could be measured with a high degree of certainty. The results indicated that $^{87}Sr/^{86}Sr$ is uniform with Sr_i values of 0.70199 to 0.70092 at an age corrected value of 2714 Ma, which is the inferred age of crystallization of the grey gabbro unit noted above, and Sr_i values of 0.70342 and 0.70305 at 1850 Ma, which is the time of the impact event.

Discussion

The nature and origin of the GG unit of the Podolsky deposit is very complicated and its origin has been unravelled by integrating mapping its distribution with detailed petrographic and

SEM-EDS studies, whole-rock and mineral chemistry, isotope geochemistry, and finally, geochronology. Each of these aspects is discussed below in the context of how it contributes to understanding the nature and evolution of the grey gabbro unit.

Origin of the grey gabbro based on field relationships

The geological model the Podolsky deposit (i.e., KGHM geology; January 2013) shows the GG as a fragment residings in the Whistle offset. This model was strongly supported by infill definition drilling and complemented by underground mapping. Observations in this study, in addition to those of the mine geologists, suggest a chilled margin occurs along the contact between the GG and Levack gneiss. The latter suggests therefore an intrusive relationship between the GG and Levack gneiss. Thus, the fragment located in the throat of the Whistle offset is comprised of both the GG unit and part of its original wall rock, the Levack gneiss. Therefore, the outline of the grey gabbro unit only provides a minimum estimate of the size of what is herein interpreted to be a composite fragment (see Fig. 6).

Interpretation of the petrographic features and mineral chemistry of the grey gabbro

Petrographic observations of the GG indicate multiple processes are recorded which are grouped into two distinct events: (1) an initial intrusive event, and (2) a subsequent impact event. The timing of these events, as constrained from the U-Pb dating, are dicussed below and a mineral paragenesis for the observed features is summarized in Figure 20. Whereas the first event resulted in the residual primary textures due to the crystallization of the GG and its late-stage deuteric alteration, the subsequent event resulted in a far more complex development of textures which includes: 1) shocked induced features imposed by high pressures and high

temperatures; 2) subsequent contact metamorphism related to cooling of the melt sheet; and 3) hydrothermal alteration associated with emplacement of the sulfide veins. Furthermore, subsequent deformation and metamorphism events (e.g., Penokean orogeny) may also have affected the GG, but are not considered here. Given the complexity of this paragenesis, the following is merely considered a preliminary interpretation with more work likely to result in a modification of this.

The unravelling of the aforementioned events is related to specific petrographic features, each of which is discussed below: (1) ophitic texture; (2) mosaic texture of the plagioclase; (3) nature of the mafic clots; and (4) hydrothermal equilibration of primary magmatic phases.

Relict ophitic texture and implications for a gabbroic protolith

The ophitic texture observed in the GG in plane polarized light gives way to a different and more complicated texture in cross nicols. The former image is importantly comparable to those of fresh gabbroic samples, such as the Skaergaard intrusion, thus it is apparent the primary protolith of this unit was a gabbro. The general ophitic texture of the GG has thus been preserved which indicates a primary magmatic origin despite multiple overprinting events that greatly modified the primary mineral phases. In addition, the presence of coarse pegmatite pods is further evidence of the primary gabbroic affinity of the GG.

Texture and chemistry of the mosaic plagioclase domains

The plagioclase domains seen in plane polarized light are composite in nature with the subhedral outlines enclosing areas of mosaic-textured granoblastic polygonal grains of small (20-30 μm), equant, unzoned laths of An_{50} composition (Fig. 7c, d). The interior parts of these

domains may be partly altered (e.g., carbonate, epidote and sericite) and relate to infiltration of fluids associated with the sulfide veins (Fig. 7e, f). The mosaic texture is somewhat similar to that observed in the leucocratic footwall breccia unit beneath the SIC and whose origin is attributed to anatexis and or recrystallization of feldspar due to radiant heat (i.e., conductive) from the cooling melt sheet (e.g., Lesher, 2017). Equigranular plagioclase crystals due to recrystallization often occurs under conditions of low pressure, and high temperature, such as contact metamorphic aureoles (e.g., Hobson et al., 1998). Here the source of heat is considered to have been the SIC, as discussed in more detail below. Given the geological setting, it is important to consider that due to its similar textural appearance, mosaic textures are often mistaken for maskelynite texture, which is the result of impact events. Considering the similarities between these two textures, we defer to the work of Chen and Gorsey (2000) who specify that maskelynite texture is characterized by the following: (1) component of isotropic glass; (2) presence of planar deformation features; and (3) a texture consisting of smooth radiating grains. Careful petrographic observations of these plagioclase domains in many samples under high magnification, complemented with SEM-EDS observations, indicate that the aforementioned features are lacking. Thus, whereas these plagioclase domains may have originally been maskelynite in nature, their current texture is attributed to subsequent thermal annealing related to static thermal metamorphism (Fig. 21).

With regards to the chemistry of these plagioclase domains, their bulk composition (An_{50}) provides an average of what may originally have been zoned grains of higher and lower calcic compositions (e.g., An_{70} to An_{40}), as is typical of plagioclase in basic rocks of both intrusive and extrusive origin (e.g., Le Bas et al. 1986; Le Bas and Streckeisen 1991). In contrast, the more albitic compositions (An_{0-20}) for grains found along the boundaries of the laths relate to

the later infiltration of fluids, which produced epidote with Fe-Cu sulfides (Fig. 21; see Figs. 7e, f, and 11).

Texture and chemistry of the mafic clots

The primary mineral assemblage of the mafic clots is dominated by augite with minor amounts of enstatite, magnesiohornblende, biotite, ilmenite and zircon, as discussed previously. These clots preserved their original subhedral outlines, but the varied presence of minerals produces different textures. Relict pyroxene, mainly a titaniferous augite (Figs. 8, 21), suggests a magmatic precursor. Such an origin is further supported by the raster analyses of several clots (Fig. 18a) which conform to a stoichiometric augite chemistry ($Ca_{35}En_{48}Fs_{17}$). The petrographic observations and chemistry suggest therefore the post-crystallization modification of the clots was essentially isochemical and that the primary augitic composition was retained.

In addition to the primary mineral assemblages of the mafic clots, locally intense but variable alteration occurred such that the primary mafic phases were altered to actinolite and chlorite. In addition, biotite shows some alteration to Fe-Ti–rich phase (e.g. magnetite, ilmenite, titanite, and rutile; Fig. 8j-l) and ilmenite shows both exsolution textures and variable replacement to magnetite (Fig. 9).

The present textural and mineralogical features of the clots are considered, as with plagioclase, to reflect a multi-stage process. Initially, some deuteric modification likely occurred during cooling of the GG along with subsequent regional deformation of the area (Fig. 20). The latter conclusion is suggested based on our examination of a representative sample of the Joe Lake gabbro, the petrologically and age equivalent rock to the GG, which showed good preservation of primary mineralogical and textural features (Fig. 4). Accordingly, it is concluded

that most of the textural and mineralogical modification of the mafic clots are attributed to pressure-temperature conditions related to the impact event. In this case, the formation of amphibole and a secondary biotite phase may reflect high temperature equilibration of the clots during contact metamorphic conditions, as noted for plagioclase. Subsequent equilibration with hydrothermal fluids related to the sharp-walled sulfide veins is responsible for formation of actinolite and chlorite.

Alteration mineralogy

As summarized in the mineral paragenesis diagram in Figure 21, several minerals formed due to infiltration of hydrothermal fluids. Phases present in the plagioclase domains, either together or alone, include secondary plagioclase (An_{20-0}), K-feldspar (Or_{10-0}), sericite and epidote. The preferential localization of K-feldspar proximal the mafic clots suggest at least some of this potassium may originate in the mafic clots, such as due to chloritization of biotite. The formation of epidote along intra-grain boundaries of the plagioclase laths coexisting with quartz, An_{20}, and chalcopyrite, indicates this alteration is related to fluids coincident with the sharp-walled sulfide vein emplacement. In contrast, epidote forming as part of saussuritization may be due to earlier deuteric alteration of plagioclase. An increase of sericite replacing plagioclase is observed near late-stage quartz ± epidote ± carbonate ± sulfide veins, which is also due to fluids related to the later sulfide event.

Within the mafic clots, evidence of hydrothermal fluids is provided by the presence of actinolite replacing relict pyroxene and by chlorite occurring along the rim of the pyroxene. Despite the two types of biotite (i.e., one is euhedral, and the other is anhedral and decrepitated) both have similar compositions (Fig. 8).

Finally, the presence of alteration selvages and micro-veins lined by varying amounts of quartz, epidote, chlorite, alkali-feldspar, magnetite, and rarely, actinolite, biotite, calcite and sulfides, occurs throughout the grey gabbro (Fig. 11). These cavities represent a dissolution event and can be seen to locally form a net-texture. They are also considered to be late when compared to the formation of the grey gabbro and are believed to be related to contact metamorphism that occurred immediately following the 1850 Ma bolide impact and before the emplacement of sulfide rich veins. These alteration selvages and micro-veins are further discussed in a companion paper (Chapter 3).

Chemical affinity of the grey gabbro unit

The whole-rock geochemical data for the GG unit clusters in the field for alkali gabbro in discriminant plots (Fig. 15a, b), which also indicates importantly that there has been limited element mobility despite its complex post-crystallization history. Other discrimination diagrams, which are not shown, also confirm that this unit is of alkali-gabbroic affinity (e.g., Irvine and Baragar 1971; Winchester and Floyd 1977; Le Bas et al. 1986). The K_2O value 1.79 wt. % for the unit is also consistent with the alkaline nature of this unit (e.g., Dickenson 1967; Green and Ringwood 1968). Harker variation diagrams plots show that some chemical variation occurs, as is expected for fractionation (Fig. 14b-f). The sole exception to these fractionated trends is MgO (Fig. 14a), which has a positive correlation with SiO_2, suggesting that in part, the physical and chemical nature of the unit is partly a function of cumulus pyroxene.

Extended spider (multi-element) diagrams of the GG normalized to primitive mantle (Sun and McDonough 1995) show relative enrichment of the LILE (K, Rb, Ba, Sr, Th, U) and Pb with less variation and negative anomalies for the HFSE (Zr, Nb, Hf, Ta), which is attributed to

metasomatic enrichment in its source area. The variable enrichment in K, Rb, Ba, Sr and Pb is attributed at least in part to alteration of the felsic domains, which is the plagioclase, where saussuritization and sericitization are observed. The REE plot as a tight group with limited spread and a strongly fractionated pattern with $(La/Lu)_N = 36$ (Fig. 16b). Notably, there is a lack of any Eu anomaly, either positive or negative, which can be interpreted to indicate either limited fractionation or accumulation of plagioclase, or alternatively, a relatively oxidized melt which preferentially stabilized Eu^{3+}.

Comparison of the REE data of the GG to representative patterns for common basic rocks (Fig. 16b) shows it overlaps with the field for OIBs. The alkali nature of this unit, as noted above, and its enrichment in LILE are also consistent with the comparison to OIB suites but is an unlikely source due to a well understood regional geological history, instead, it is more suitable to consider that the magma source that has been intensely metasomatised prior to crystallization, see below.

Sourcing the Grey Gabbro unit

Of particular relevance to the nature of the GG is its source in the region. Given that the unit is a fragment in the Whistle offset, sourcing this unit has implications for the physical dynamics associated with the impact event and transport of material, hence, we address the potential source rocks (Appendix 1). The age of the GG unit, further discussed below, is inferred to be ca. 2714 ± 54 Ma; the latter age thus provides constraints on possible equivalent rocks in the area. For purpose of completeness however, other units in the region are included in the compilation shown in Figure 22.

A compilation of literature data provides the basis for Figure 22 in which to compare the GG to rocks of the Sudbury region. As seen in Figure 22a, there are no units in the SIC that are similar to the GG. In addition, examination of the geochemical data for the regional basic intrusive rocks indicates that only the Joe Lake gabbro, and similar age rocks, is comparable (Fig. 22a). This unit, which is located ~14 kilometres west of the Podolsky deposit (see Fig. 1), is one of several gabbroic bodies in the Sudbury area that are texturally comparable to the GG. Samples of this unit are petrographically similar to the grey gabbro (see Fig. 4) and a recent U-Pb TIMS zircon analysis for it yielded an age of 2657 ± 9 Ma (Bleeker et al. 2013; Ames et al. 2013). This age has been interpreted by the authors as indicating the time of crystallization of the zircon and, hence, emplacement of the Joe Lake intrusion. Thus, the presently available geological, geochemical and geochronological data constrain the Joe Lake gabbro as the nearest equivalent rock unit to the GG unit at Podolsky. We also note that this unit, like the GG, is in contact with Levack gneiss, which satisfies the contact relationship that has been observed in drill core (see above).

The average $\delta^{18}O$ value of 7.2‰ for the GG fall above similar data for fresh basalts and mafic lavas of mantle origin, which range between 5 to 7‰ (Kyser 1986). These data suggest that either the extraction in the mantle was enriched in $\delta^{18}O$ or the melt was contaminated. Strontium isotope values of 0.70199 to 0.70092 are similar for all samples of the GG are also consistent with a mantle source.

The enriched values of LREEs and LILEs in the GG have signatures similar to those observed within OIB settings (Fig. 16). Due to a well-understood regional geological history, it is more suitable to consider that the magma source was intensely metasomatised prior to crystallization. Supporting this, Percival (2007) stated that the presence of calc-alkaline basalts

within the Superior Province is generated by metasomatism from fluids or melts in a suprasubduction zone environment. Reservoirs underneath continents have been influenced by subducted material that has been isolated from other proportions of the mantle for long periods of time and is typically associated to alteration of crustal contamination due to an increase of CO_2 and H_2O-rich metasomatic fluids (Kyser 1986). Rousell et al. (1997) established that during the Paleoproterozoic, several layered mafic intrusions, including the geochemically similar Joe Lake gabbro, were emplaced due to an episode of continental rifting, which occurred along the Murray fault zone. Other studies have also documented alkaline olivine diabase dikes that have a chemistry suggesting derivation form a previously metasomatism mantle source which has been suggested to relate to subduction along the southern edge of the Superior Province (e.g. Shellnut and MacRae 2012).

Interpretation of U-Pb zircon ages

The U-Pb zircon dating using two independent methods - TIMS and SHRIMP – provided ages of ca. 2714 and 1850 Ma for two different textural grops of zircon in the GG. These results can be interpreted in three different ways: 1) the GG is 1850 Ma and the older zircons are due to inheritance from the Levack gneiss; 2) the GG is post 1850 Ma, that is it post-dates the SIC event, and contains inherited 2714 Ma zircons and 1850 Ma zircons; or 3) the GG is 2714 Ma (i.e., part of the basement units) and the younger zircons grew at 1850 Ma. These three scenarios have to be interpreted in terms of the following feature of the GG: 1) forms part of a composite fragment in the Whistle offset environment; 2) it is cut by sharp-walled footwall Cu-rich veins which relate to the 1850 Ma Sudbury event; 3) characterized by unusal petrographic textures such as domains of granoblastic plagioclase; 4) its similarity of age, petrography and chemistry

to the nearby Joe Lake gabbro or its lateral equivalents; 5) lack of similar to other units in the SIC; and 6) the ages for the two distinct textural types of dated zircons.

Given the aforementioned constraints and what has been discussed in regards to the geological setting of the GG - relationship to the footwall sulphide veins, chilled margin with Levack gneiss, textural evolution and geochemistry - the first two scenarios are not considered to be tenable. Instead we suggest that the most likely interpretation of the older U-Pb zircon data is that the GG originated as a ca. 2714 ± 54 Ma intrusion, which is strongly supported by similar petrological features and age, that is 2657 ± 9 Ma (Bleeker et al. 2013; Ames et al. 2013), to the Joe Lake gabbro located 14 km to the west. Thus, the GG is most likely part of a suite of gabbroic bodies emplaced in the North Range area at ca. 2700 Ma. The occurrence of one such body in the Whistle embayment area, the GG, is likely due to the dislodegment of part of one such body due to the 1850 Ma Sudbuy impact event. This study as therefore documented perhaps the largest fragment contained within the SIC melt sheet environment. The impact event is also considered responsible for the planar features (i.e., PDF textures) observed in the anhedral, cloudy, red-brown anhedral zircons dated at 2714 Ma.

In contrast to the older zircons, the second population dated at 1849.9 ± 1 Ma, which is characterized by subhedral to euhedral habits, clarity and zoning, reflects their neomorphic growth. That the age is identical to that for the impact event (Krogh et al. 1984; Davis 2008) and strongly suggests a temporal connection, whereas its morphology and internal features (e.g., CL zoning) indicate its growth from a melt. Similar interpretations for zircons sharing these same features have been made in both terrestrial and lunar settings. In the first case, Kenny et al. (2017) dated neoblastic zircon, texturally identical to those in the GG, from a sampled collected from the top of the Sudbury impact melt sheet, hence in some respects to nature of the zircon

morphotypes in the GG. In the second analogous example, Grange et al. (2013) interpret the origin of similarly complex, multi-stage textures observed in lunar zircons to reflect an impact related event.

Conclusions

The grey gabbro (GG) unit is an important host rock to high-grade Cu(-Ni)-PGE sulphide ore in the Podolsky deposit of the North Range of the Sudbury area. It occurs as a large fragment in the Whistle embayment of the SIC and was studied to elucidate its petrology, age and origin given its importance as a host rock to ore. Observations based logging of drill core and underground mapping, which constrain its size (275 m x 230 m x 90 m), indicate an original intrusive origin for the unit based on a chilled contact with the Levack gneiss. Thus, results of this study suggest therefore that it is part of a much larger composite fragment that was dislodged during the 1850 Ma bolide impact event that formed the SIC.

Petrological study of the GG has shown that it records a complex textural evolution that reflects multiple processes. The presence of relic features, such as a medium- to coarse-grained, homogeneous, ophitic-texture, in concert with whole-rock geochemistry, indicates the GG shares features similar to those typical of gabbroic rocks and hence indicates it is a mafic intrusion. However, a later, post-crystallization history is also suggested by: 1) the presence of granoblastic polygonal laths that replace original plagioclase crystals; 2) mafic clots composed mainly of biotite and amphiboles that replace original augite; and 3) presence of two zircon morpho-types, one anhedral, red-brown and full of PDF features and a second neomorphic type that overgrows the former. The age of these zircons was constrained by U-Pb ziron dating to 2714 ± 54 Ma and 1849.9 ± 1 Ma by SHRIMP and TIMS methods, respectively. These textural features and ages

are interpreted to indicate the GG was intruded into the Archean basement rocks at ca. 2700 Ma and was subsequently dislodged during the impact event at 1850 Ma with later thermal equilibration related to cooling of the impact-generated melt sheet.

A comparative study of the GG to the nearby Joe Lake gabbro indicates they share similar ages, petrographic features and whole rock geochemistry. Thus, the GG represents part of a series of similar gabbroic intrusions that were present in the North Range prior to the Sudbury impact event. It is expected that other such fragments should be found in embayments of the SIC.

Acknowledgements

The Geological Survey of Canada (GSC) under the Research Affiliate Program (RAP) – TGI-4 Ni-Cu-PGE-Cr Project, supported this research. We thank our colleagues from the GSC who provided insight and expertise that greatly assisted in the research, although they may not agree with all the interpretations/conclusions of this paper.

We thank Queen's University Facility for Isotopic Analysis Centre for providing us with oxygen isotope results, Carleton Isotope Geochemistry & Geochronology Research Centre for providing us with strontium isotope results, and the GSC's geochronology division for providing us with results and comments to improve the manuscript.

References

Ames, D.E. 1999. Geology and regional hydrothermal alteration of the crater-fill Onaping Formation: association with Zn-Pb-Cu mineralisation, Sudbury Structure, Canada. Ph.D. thesis, Department of Earth Sciences, Carleton University, Ottawa, ON.

Ames, D.E., Buckle, J., Davidson, A., and Card, K. 2005. Sudbury bedrock compilation: Geology. Geological Survey of Canada, Open File, **4570**.

Ames, D.E. and Farrow, C.E.G. 2007. Metallogeny of the Sudbury mining camp, Ontario. *In* Mineral Deposits of Canada: A synthesis of major deposit types, district metallogeny, the evolution of geological provinces, and exploration methods. *Edited by* W.D. Goodfellow. Geological Association of Canada, Mineral Deposits Division, Special Publication, **5**: 329-350.

Ames, D.E., Golightly, J.P., Lightfoot, P.C., and Gibson, H.L. 2002. Vitric compositions in the Onaping Formation and their relationship to the Sudbury Igneous Complex, Sudbury Structure. Economic Geology, **97**: 1541-1562.

Ames, D.E., Hanley, J.J., Tuba, G., Bleeker, W., and Kamo, S. 2013. Primitive Source Revealed in the Sudbury impact structure: Implications for cratering and metal sources. [Extended Abstract] Lunar and Planetary Institute Conference, Sudbury, Ontario.

Ames, D.E., Farrow, C.E.G., Jonasson, I.R., Pattison, E.F., and Golightly, J.P. 2014. Geochemistry of 44 Ni-Cu-platinum group element deposits in the contact, footwall, offset, and breccia belt envrionments, Sudbury mining district, Canada. Geological Survey of Canada, Open File, **6578**.

Bailey, J., Lafrance, B., McDonald, A.M., Fedorowich, J.S., Kamo, S., and Archibald, D.A., 2004, Mazatzal-Labradorian-age (1.7-1.6 Ga) ductile deformation of the South Range

Sudbury impact structure at the Thayer Lindsley mine, Ontaro. Canadian Journal of Earth Sciences, **41**: 1491-1505.

Bleeker, W., Kamo, S., and Ames, D., 2013. New field observations and U-Pb age data for footwall (target) rocks at Sudbury: Towards a detailed cross-section through the Sudbury Structure. [Extended Abstract] Lunar and Planetary Institute Conference, Sudbury, Ontario.

Bohor, B.F., Betterton, W.J., and Krogh, T.E. 1993. Impact-shocked zircons: discovery of shock-induced textures reflecting increasing degrees of shock metamorphism. Earth and Planetary Science Letters, **119** (3): 419–424.

Bygnes, L.C. 2011. Emplacement of metabreccia and Cu-PGE-rich sufide veins along the Whistle offset of the Sudbury impact structure. M.Sc. thesis, Department of Earth Sciences, Laurentian University, Sudbury, ON.

Card, K.D. 1994. Geology of the Levack gneiss complex, the northern footwall of the Sudbury Structure, Ontario. Geological Survey of Canada, Current Research, **1994**: 269-278.

Card, K.D., Gupta, V.K., McGrath, P.H., and Grant, F.S. 1984. The Sudbury Structure: Its regional geological and geophysical setting. *In* The Geology and Ore Deposits of the Sudbury Structure. *Edited by* E. G. Pye, A. J. Naldrett, and P. Giblin. Ontario Geological Survey, Special Publication, **1**: 25-44.

Carter, W. M., Watkinson, D. H., Ames, D. E., and Jones, P. C. 2009. Quartz diorite magmas and Cu-(Ni)-PGE mineralisation, Podolsky deposit, Whistle Offset structures, Sudbury, Ontario.Geological Survey of Canada, Open File, **6134**.

Chen, M., and Gorsey, A. 2000. The nature of maskelynite in shocked meteorites: Not diaplectic glass but a glass quenched from shock-induced dense melt at high pressure. Earth and Planetary Science Letters, **179**: 489-502.

Clayton, R.N., and Mayeda, T.K. 1963. The use of bromine pentafluoride in the extraction of oxygen from oxides and silcates for isotropic analysis. Geochimica et Cosmochimica Acta, **27:** 43-52.

Coats, C.J.A., and Snajdr, P. 1984. Ore deposits of the North Range, Onaping-Levack area, Sudbury. Ontario. Geological Survey, Special Volume, **1**: 327–346.

Corfu, F., and Andrews, A.J. 1986. A U-Pb age for mineralized Nipissing diabase, Gowganda. Canadian Journal of Earth Sciences, **23**: 107-109.

Corfu, F., Hanchar, J.M., Hoskin, P.O.W., and Kinny, P. 2003. Atlas of zircon textures. Reviews in Mineralogy and Geochemistry, **23**: 469-500.

Cox, K.G., Bell, J.D., and Plankhurst, R.J. 1979.The interpretation of igneous rocks. Chapman and Hall, London, UK.

Davis, D. 2008. Sub-million-year age resolution of Precambrian igneous events by thermal extraction-thermal ionization mass spectrometer Pb dating of zircons: Application to crystallization of the Sudbury impact melt sheet. Geology, **36**: 383-386.

Dickenson, W.R. 1967. Circum-Pacific andesite types. [Abstract] Trans America Geophysics Union, **48**: 263.

Dietz, R. 1960. Meteorite impact suggested by shatter cones in rock. Science, **73**: 1781-1784.

Dietz, R.S. 1964. Sudbury structure as an astrobleme. Journal of Geology, **72**: 412-434.

Dressler, B.O. 1984. General geology of the Sudbury area. *In* The Geology and Ore Deposits of the Sudbury Structure.*Edited by* E. G. Pye, A. J. Naldrett, and P. Giblin. Ontario Geological Survey, Special Publication, **1**: 57-82.

Farrow, C.E.G., and Watkinson, D.H. 1996. Geochemical characteristics of the epidote zone: its development and associated Ni-Cu-PGE remobilization by saline fluids, Fraser mine, Sudbury, Ontario. Exploration Mining Geology, **5**: 17-31.

Farrow, C.E.G., and Watkinson, D.H. 1999. An evaluation of the role of fluids in Ni-Cu-PGE-bearing, mafic-ultramafic systems. *In* Dynamic processes in magmatic ore deposits and their application in mineral exploration. *Edited by* R.R., Keays, C.M. Lesher, P.C.

Farrow, C.E.G., and Lightfoot, P.C. 2002. Sudbury PGE revisited: Towards and integrated model. *In* Geology, Geochemistry, Mineralogy and Mineral Beneficiation of Platinum-Group Elements. *Edited by* L.J. Cabri. Canadian Institute of Mining, Special Volume, **54**: 273-297.

Farrow, C.E.G., Everest, J.O., King, D.M., and Jolette, C. 2005. Sudbury Cu(-Ni)-PGE Systems: Refining the classification using McCreedy West mine and Podolsky project case studies. *In* Exploration for Platinum Group Element Deposits. *Edited by* J. E. Mungall. Mineralogical Association of Canada, Short Course Series, **35**: 163-180.

Fleet, M.E., and Barnett, R.L. 1978. Al^{iv}/Al^{vi} Partitioning in Calciferous Amphiboles from the Frood Mine, Sudbury, Ontario. Canadian Mineralogist, **16**: 527-532.

Golightly, J.P. 1994. The Sudbury Igneous Complex as an impact melt: evolution and ore genesis. *In* Proceedings Sudbury-Noril'sk Symposium. *Edited by* P.C. Lightfoot, A.J. Naldrett. Ontario Geol Survey Special, **5**: 105-118.

Grange, M.L., Pidgeon, R.T., Nemchin, A.A., Timms, N.E., and Meyer, C. 2013. Interpreting U-Pb data from primary and secondary features in lunar zircon. Geochimica et Cosmochimica Acta, **101**: 112-132.

Green, T.H., and Ringwood, A.E. 1968. Genesis of the Calc-alkaline igneous rock suite.

Contributions to Mineralogy and Petrology, **18 (2)**: 105-162.

Grieve, R.A.F., Stoffler, D., and Deutsch, A. 1991. The Sudbury Structure: Controversial or misunderstood?. Journal of Geophysical Research, **96**(E5): 22753-22754.

Grieve, R.A.F., Ames, D.E., Morgan, J.V., and Artemieva, N. 2010. The evolution of the Onaping Formation at the Sudbury impact structure. Meteoritics and Planetary Science, **45**(5): 759-782.

Giroux, L.A., and Benn, K. 2005. Emplacement of the Whistle dyke, the Whistle embayment and hosted sulfides, Sudbury impact structure, based on anisotropies of magnetic susceptibility and magnetic remanence. Economic Geology, **100**: 1207-1227.

Hawthorne, F.C., and Oberti, R. 2007. Classification of the amphiboles. Reviews in Mineralogy and Geochemistry, **67**: 55-88.

Heaman, L.M. 1997. Global mafic magmatism at 2.45 Ga: Remnants of an ancient large igneous province?. Geology, **25**: 299-302.

Hobson, A., Bussy, F., and Hernandez, J. 1998. Shallow-level migmatization of gabbros in a metamorphic contact aureole, Fuerteventura basal complex, Canary Islands. Journal of Petrography, **39**: 1025-1037.

Irvine, T.N., and Baragar, W.R.A. 1971. A guide to the chemical classification of the common volcanic rocks. Canadian Journal of Earth Sciences, 8(5): 523-548.

Kenny, G.G., Morales, L.F., Whitehouse, M.J., Petrus, J.A., Kamber, B.S. 2017. The formation of large neoblasts in shocked zircon and their utility in dating impacts. Geology, **45**(11): 1003-1006.

Krogh, T.E., Davis, D.W., and Corfu, F. 1984. Precise U-Pb zircon and baddeleyite ages for the Sudbury area. *In* The Geology and Ore Deposits of the Sudbury Structure. *Edited by* E.G.

Pye, A.J. Naldrett, and P.E. Giblin. Ontario Geological Survey, Special Volume, **1**: 431-447.

Krogh, T.E., Kamo, S.L., and Bohor, B.F. 1993a. Fingerprinting the K/T impact site and determining the time of impact by U–Pb dating of single shocked zircons from distal ejecta. Earth and Planetary Science Letters, **119**(3): 425–429.

Krogh, T.E., Kamo, S.L., Sharpton, V.L., Marin, L.E., and Hildebrand, A.R. 1993b. U–Pb ages of single shocked zircons linking distal K/T ejecta to the Chicxulub crater. Nature, **366**: 731–734.

Krogh, T.E., Kamo, S.L., and Bohor, B.F. 1996. Shock metamorphosed zircons with correlated U–Pb discordance and melt rocks with concordant protolith ages indicate an impact origin for the Sudbury Structure. *In* Earth Processes: Reading the Isotopic Code. *Edited by* A. Basu, and S. Hart. American Geophysical Union, Washington, D.C.

Kyser, T.K. 1986. Stable isotope variations in the mantle. *In* Review in Mineralogy: Stable isotopes in high temperatures geological processes. *Edited by* J.W. Valley, H.P. Taylor, Jr., and J.R. O'Neil. Mineralogical Society of America, **16**: 141-164.

Lafrance, B., Legault, D., Ames, D.E. 2008. The Formation of the Sudbury breccia in the North Range of the Sudbury impact structure. Precambrian Research, **165**: 107-119.

Lafrance, B., and Kamber, B.S. 2010. Geochemical and microstructural evidence for *in situ* formation of pseudotachylitic Sudbury breccia by shock-induced compression and cataclasis. Precambrian Research, **180**: 237-250.

Lafrance, B., Bygnes, L., and McDonald, A.M. 2014. Emplacement of metabreccia along the Whistle offset dyke, Sudbury: implications for post-impact modification of the Sudbury impact structure. Canadian Journal of Earth Sciences, **51**: 466-484.

Le Bas, M.J., Le Maitre, R.W., Streckeisen, A., and Zanettin, B. 1986. A chemical classification of volcanic rocks based on the total alkali-silica diagram. Journal of Petrology, **27**(3): 745-750.

Le Bas, M.J., and Streckeisen, A.L. 1991. The IUGS systematics of igneous rocks. Journal of the Geological Socitey, **148**: 825-833.

Leake, B.E., Woolley, A.R., Arbs, C.E.S., Birch, W.D., Gilbert, M.C., Grice, J.D., Hawthorne, F.C., Kato, A., Kisch, H.J., Krivovichev, V.G., Linthout, K., Laird, J., Mandarino, J.A., Maresch, W.V., Nickel, E.H., Rock, N.M.S., Schumacher, J.C., Smith, D.C., Stephenson, N.C.N., Ungaretti, L., Whittaker, E.J.W., and Guo, Y. 1997. Nomenclature of amphiboles: Report of the subcommittee on amphiboles of the International Mineralogical Association, commission on new minerals and mineral names. The Canadian Mineralogist, **35**: 219-246.

Leake, B.E., Woolley, A.R., Birch, W.D., Burke, E.A.J., Ferraris, G., Grice, J.D., Hawthorne, F.C., Kisch, H.J., Krivovichevm V.G., Schumacher, J.C., Stephenson, N.C.N., and Whittaker, E.J.W. 2003. Nomenclature of amphiboles: Additions and revisions to the International Mineralogical Associations amphibole nomenclature. The Canadian Mineralogist, 41: 1355-1370.

Lesher, C.M. 2017. Roles of Xenomelts, Xenoliths, Xenocrysts, Xenovolatiles, Residues, and Skarns in the Genesis, Transport, and Localization of Magmatic Fe-Ni-Cu-PGE Sulfides and Chromite. Ore Geology Reviews. **90**: 465-484.

Lightfoot, P.C., Naldrett, A.J., Gorbachev, N.S., Doherty, W., and Fedorenko, V.A. 1990. Geochemistry of the Serberian Trap of the Noril'sk area, USSR, with implications for the relative contributions of crust and mantle to flood basalt magmatism. Mineralolgy and

Petrology, **104**: 631-644.

Lightfoot, P.C., Keays, R.R., Morrison, G.C., Bite, A., and Farrell, K.P. 1997a. Geologic and geochemical relationships between the contact sublayer, inclusions, and the main mass of the Sudbury Igneous Complex; A case study of the Whistle Mine Embayment. Economic Geology, **92**(6): 647-673.

Lightfoot, P.C., Keays, R.R., Morrison, G.C., Bite, A., and Farrell, K.P., 1997b. Geochemical relationships in the Sudbury Igneous Complex: Origin of the main mass and offset dikes. Economic Geology, **92**(3): 289-307.

Lightfoot, P.C., Keays, R.R., and Doherty, W. 2001. Chemical evolution and origin of nickel sulfide mineralization in the Sudbury Igneous Complex, Ontario, Canada. Economic Geology, **96**(8): 1855-1875.

Lightfoot, P.C., and Farrow, C.E. 2002. Geology, geochemistry, and mineralogy of the Worthington Offset Dike: A genetic model for offset dike mineralization in the Sudbury Igneous Complex. Economic Geology, **97**(7): 1419-1446.

Lightfoot, P.C. 2016. Nickel Sulfide Ores and Impact Melts: Origin of the Sudbury Igneous Complex, 1st Edition. Elsevier, Cambridge, MA.

Ludwig, K.R. 2003. User's manual for Isoplot/Ex rev. 3.00: A geochronological toolkit for Microsoft Excel. Berkeley Geochronology Center, Special Publication **4**: 70.

Mattinson, J.M. 2005. Zircon U-Pb chemical abrasion ("CA-TIMS") method: Combined annealing and multi-step partial dissolution analysis for improved precision and accuracy of zircon ages. Chemical Geology, **220**(1-2): 47-66.

McDonough, W.F., and Sun, S.-s. 1995. Composition of the Earth. Chemical Geology, **120**: 223-253.

Milkereit, B., and Green, A., 1992. Deep geometry of the Sudbury structure from seismic reflection profiling. Geology, **20**: 807-811.

Morimoto, N., Fabries, J., Ferguson, A.K., Ginzburg, I.V., Ross, M., Seifert, F.A., Zussman, J., Aoki, K., and Gottardi, G. 1988. Nomenclature of Pyroxenes. American Mineralogist, **73**: 1123-1133.

Mukwakwami, J., Lesher, M., and Lafrance, B. 2014. Geochemistry of Deformed and Hydrothermally Mobilized Magmatic Ni-Cu-PGE Ores at the Garson Mine, Sudbury. Society of Economic Geology, **100**: 367-386.

Parrish, R.R., Roddick, J.C., Loverridge, W.D., and Sullivan, R.W. 1987. Uranium – lead analytical techniques at the Geochronology Laboratory, Geological Survey of Canada. *In* Radiogenic Age and Isotropic Studies: Report 1. *Edited by* Geological Survey of Canada. Geological Survey of Canada, **87-2**: 3-7.

Pattison, E.F. 1979. The Sublayer: its characteristics and relationship to the Main Mass of the Sudbury irruptive. Canadian Mineralogist, **17**: 257-274.

Percival, J.A., 2007. Geology and Metallogeny of the Superior Province, Canada, *In* Mineral Deposits of Canada: A Synthesis of Major Deposit-Types, District Metallogeny, the Evolution of Geological Province, and Exploration Methods. *Edited by* W.D. Goodfellow. Geological Association of Canada, Mineral Deposits Division, Special Publication, No. **5**: 903-928.

Pidgeon, R.T., Nemchin, A.A., and Kamo, S.L. 2011. Comparison of structures in zircons from lunar and terrestrial impactites. Canadian Journal of Earth Sciences, **48**: 107–116.

Roddick, J.C. 1987. Generalized numerical error analysis with applications to geochronology and thermodynamics. Geochimica et Cosmochimica Acta, **51**(8): 2129-2135.

Rousell, D.H. 1984. Onwatin and Chelmsford Formations. *In* The Geology and Mineral Deposits of the Sudbury Structure. *Edited by* E. G. Pye, A. J. Naldrett, and P. Giblin. Ontario Geological Survey, Special Publication, **1**: 235-251.

Rousell, D.H., Fedorowich, J.S., Dressler, B.O. 2003. Sudbury Breccia (Canada): a product of the 1850 Ma Sudbury Event and host to footwall Cu-Ni-PGE deposits. Science Direct, **60** (3-4): 147-174.

Rousell, D.H., Gibson, H.L., and Jonasson, I.R., 1997. The tectonic, magmatic and mineralization history of the Sudbury Structure. Exploration and Mining Geology, **6**: 1-22.

Rudashevsky, N.S., Burakov, B.E., Lupal, S.D., Thalhammer, O.A.R., and Saini-Eidukat, B. 1995.Liberation of accessory minerals from various rock types by electric-pulse disintegration—method and application. Transactions of the Institute of Mining and Metallurgy, **104**: 25–29.

Shellnut, J.G., and MacRae, N.D. 2012. Petrogenesis of the Mesoproterozoic (1.23 Ga) Sudbury dyke swarm and its questionable relationship to plate separation. International Journal of Earth Sciences, **101**: 3-23.

Stern, R.A. 1997. The GSC Sensitive High Resoultion Ion microprobe (SHRIMP): analytical techniques of ziron U-Th-Pb age determinations and performance evaluation. *In* Radiogenic Age and Isotopic Studies: Report 10. Geological Survey of Canada, Current Research, **1997-F**: 1-31.

Stern, R.A., and Amelin, Y. 2003. Assessment of errors in SIMS zircon U-Pb geochronology using a natural zircon standard and NIST SRM 610 glass. Chemical Geology, **197**(1-4): 111–142.

Thompson, L.M., Spray, J.G., and Kelly, S.P. 1998. Laser probe argon-40/argon-39 dating of pseudotachylyte from the Sudbury Structure: Evidence for postimpact thermal overprinting in the North Range. Meteoritics and Planetary Science, **33**(6): 1259-1269.

Winchester, J.A., and Floyd, P.A. 1977. Geochemical discrimination of different magma series and their differentiation products using immobile elements. Chemical Geology, **20**: 325–343.

Wood, C.R., and Spray, J.G. 1998. Origin and emplacement of offset dykes in the Sudbury impact structure: Constraints from Hess. Meteoritics and Planetary Science, **33**(2): 337-347.

Wodicka, N. 1997. Sudbury Structure: Northern footwall rocks and Sudbury Igneous complex. *in* Timmins to Sudbury Transect: New Insights into the Regional Geology and Setting of Mineral Deposits. *Edited by* D.E. Ames. Geological Association of Canada-Mineralogical Association of Canada, Joint Annual Meeting, Ottawa '97, field trip **B6**: 73-93.

Young, G. M., Long, D.G.F., Fedo, C.M., Nesbitt, H.W. 2001. Paleoproterozoic Huronian basin: product of a Wilson cycle punctuated by glaciations and a meteorite impact. Sedimentary Geology, **141-142**: 233-254.

Zieg, M.J., and Marsh, B.D. 2005. The Sudbury Igneous Complex: Viscous emulsion differentiation of a superheated impact melt sheet. Geological Society of America Bulletin, **117**(11-12): 1427-1450.

Tables:

wt. %	LLD	LM-P-019	LM-P-021	LM-P-025	LM-P-028	LM-P-030	LM-P-032A	LM-P-033	LM-P-036	LM-P-037
	ACME Labs	ACME Labs	ACME Labs	ACME Labs	ACME Labs	ACME Labs	ACME Labs	ACME Labs	ACME Labs	ACME Labs
SiO_2	0.10	50.00	51.30	51.10	50.90	50.20	49.70	49.80	51.60	50.10
TiO_2	0.01	1.36	1.07	1.00	1.10	1.39	1.30	1.25	1.06	1.39
Al_2O_3	0.01	16.50	16.83	16.15	16.58	15.50	16.23	15.89	15.25	16.04
FeO_T		10.16	9.33	9.34	9.30	10.36	10.45	10.20	10.51	10.67
FeO		9.82	9.02	9.03	8.99	10.02	10.10	9.86	10.16	10.31
Fe_2O_3		1.09	1.00	1.00	1.00	1.11	1.12	1.10	1.13	1.15
Fe_2O_{3T}	0.01	10.91	10.02	10.03	9.99	11.13	11.22	10.96	11.29	11.46
MgO	0.01	5.28	5.91	6.61	6.13	6.05	5.84	5.97	6.94	5.04
MnO	0.01	0.14	0.13	0.15	0.14	0.14	0.15	0.15	0.14	0.16
CaO	0.01	7.82	8.40	8.30	7.95	5.91	8.02	7.49	5.18	6.89
Na_2O	0.01	3.91	3.94	3.50	3.64	4.68	3.62	3.58	4.25	3.17
K_2O	0.01	1.75	1.31	1.74	2.00	1.98	1.75	1.94	1.15	2.90
P_2O_5	0.01	0.73	0.66	0.52	0.57	0.82	0.73	0.69	0.66	0.74
LOI		1.44	0.84	1.03	1.24	2.49	1.09	1.57	2.80	1.82
Total		98.38	99.57	99.09	98.99	97.77	98.54	97.69	97.49	97.86
C	0.02	0.06	0.02	0.03	0.03	0.10	0.03	0.06	b.d.	0.06
FeO	0.01	6.48	5.70	6.14	6.13	6.23	6.93	7.00	7.85	7.06
S	0.02	0.21	0.21	0.21	0.17	0.22	0.25	0.19	0.14	0.30
ppm										
B	1.00	1	b.d.	b.d.	3	2	1	2	b.d.	b.d.
Li	0.10	20.3	18.2	20.7	20.4	34.2	17.5	26.3	17.2	20.4
ppb										
Se	100.00	b.d.	b.d.	100.00	b.d.	200.00	200.00	300.00	600.00	200.00
Au	0.50	b.d.	b.d.	b.d.	0.60	b.d.	b.d.	b.d.	1.60	3.20
Pd	10.00	b.d.	b.d.	b.d.	b.d.	b.d.	b.d.	b.d.	b.d.	b.d.
Pt	2.00	b.d.	b.d.	b.d.	b.d.	b.d.	b.d.	b.d.	b.d.	b.d.
Ag	2.00	143	209	297	494	113	305	1275	542	247
ppm										
Cu	0.01	38.30	49.00	47.20	245.20	56.90	48.90	1613.10	1088.40	2887.60
Ni	0.10	43.90	63.20	70.00	63.90	42.10	58.30	55.30	716.70	62.40
Co	0.20	33.70	34.00	37.10	35.00	32.10	36.50	35.60	41.10	32.30
Cr	0.50	45.10	80.80	84.60	82.40	39.70	59.40	75.70	63.80	49.90
Mn	1.00	280	178	236	265	240	243	315	680	454
Zn	1.00	94.00	65.00	86.00	86.00	71.00	94.00	88.00	127.00	107.00
Sn	1.00	1	1	1	1	1	n.a.	1	2	4
Ga	0.50	20.1	19.4	18.8	19.5	18.8	19.6	20	16.5	22.3
Ge	0.10	0.1	0.1	b.d.	b.d.	b.d.	0.1	b.d.	0.1	0.1
In	0.02	b.d.	b.d.	b.d.	b.d.	b.d.	b.d.	b.d.	b.d.	b.d.
Cd	0.01	0.18	0.56	1.03	2.07	0.02	0.62	0.36	0.12	0.08
Zr	0.10	284.90	215.60	224.80	239.10	241.40	251.60	246.10	115.80	311.90
Ba	0.10	1222.00	960.00	1003.00	1097.00	1111.00	1173.00	1233.00	295.00	1308.00
Pb	0.02	13.30	23.90	55.10	37.50	3.00	20.10	17.50	3.50	3.60
Th	0.30	4.50	1.80	1.90	2.00	3.60	2.30	2.60	5.50	4.80
U	0.05	0.10	0.20	0.10	0.10	0.40	0.10	0.20	0.20	0.30
Bi	0.02	0.05	n.a.	0.09	0.13	b.d.	b.d.	0.15	b.d.	0.1
Ti	0.05	0.21	0.17	0.3	0.28	0.15	0.3	0.21	0.18	0.69
Rb	0.01	42.40	29.50	41.60	47.90	72.70	43.00	48.60	30.70	121.00
Sr	0.05	987.00	1030.80	957.20	956.70	685.20	946.20	939.50	437.10	872.80
Nb	0.02	9.40	8.10	7.30	7.40	8.30	8.40	8.50	7.40	18.10
Cs	0.03	0.50	0.20	0.50	1.00	0.70	0.50	0.70	0.70	2.90
Be	0.01	0.30	0.20	0.10	0.20	0.40	0.30	0.30	0.50	0.70
Hf	0.05	5.80	5.10	5.20	5.10	5.00	5.00	5.30	2.60	7.30
Y	0.01	23.50	19.90	19.40	20.00	23.60	23.10	21.30	22.00	30.60
Ta	0.10	0.30	0.30	0.30	0.30	0.30	0.30	0.20	0.30	0.90
Sc	1.00	1.80	1.80	1.90	1.50	2.20	2.20	2.10	2.30	2.60
V	0.10	174.00	169.00	158.00	156.00	183.00	201.00	191.00	147.00	189.00
Mo	0.20	0.21	0.19	0.16	0.21	0.36	0.23	0.22	0.21	0.34
As	0.10	0.6	0.1	0.7	0.9	0.7	0.4	0.1	0.6	0.4
Sb	0.02	b.d.	b.d.	b.d.	b.d.	b.d.	b.d.	b.d.	0.02	0.04
W	0.02	n.a.	n.a.	n.a.	n.a.	n.a.	n.a.	n.a.	n.a.	n.a.
Hg	0.10	n.a.	n.a.	n.a.	n.a.	n.a.	n.a.	n.a.	n.a.	n.a.
Te	0.50	b.d.	b.d.	b.d.	b.d.	b.d.	b.d.	b.d.	b.d.	b.d.
La	0.10	96.00	76.40	68.00	74.40	82.90	82.80	81.60	90.50	91.20
Ce	0.10	186.20	154.00	134.90	149.80	169.30	165.50	162.20	180.80	181.90
Pr	0.10	21.67	17.77	16.38	17.92	20.64	19.86	19.44	21.08	21.56
Nd	0.10	76.60	67.10	65.60	67.30	78.20	73.20	72.30	75.70	79.10
Sm	0.10	11.90	10.48	9.77	9.84	11.97	11.48	11.07	11.64	13.13
Eu	0.10	3.01	2.47	2.47	2.53	2.83	2.92	2.77	2.51	2.77
Gd	0.10	8.26	7.30	6.83	7.10	8.32	8.16	7.76	8.14	9.91
Tb	8.00	0.91	0.80	0.76	0.81	0.95	0.90	0.87	0.89	1.11
Dy	0.01	4.63	3.82	3.99	4.10	4.93	4.59	4.65	4.42	5.56
Ho	0.1	0.73	0.68	0.70	0.70	0.76	0.72	0.73	0.70	0.97
Er	0.02	1.98	1.75	1.91	1.77	1.91	1.98	1.97	1.71	2.82
Tm	0.1	0.28	0.25	0.23	0.24	0.27	0.27	0.25	0.26	0.37
Yb	0.01	1.79	1.48	1.54	1.47	1.79	1.60	1.56	1.70	2.40
Lu	0.02	0.24	0.21	0.21	0.21	0.25	0.24	0.23	0.23	0.32
Mg#		46.3	48.6	54.0	49.2	48.1	49.3	52.3	54.6	43.9

Table 1: Major and trace element analyses (XRF and ICP-MS) characterizing the grey gabbro unit. LLD: lower limit of detection; n.a. = not analysed; b.d. = below detection; Mg# = MgO/(Mgo+FeO); ppm = parts per million; ppb = parts per billion; wt. % = weight percent.

wt. %	LLD	LM-P-038	LM-P-042	LM-P-039A	LM-P-039B	LLD	LM-P-007
	ACME Labs	ACME Labs	ACME Labs	ACME Labs	ACME Labs	ActLabs	ActLabs
SiO_2	0.10	49.80	52.10	49.50	47.50	0.01	51.4
TiO_2	0.01	1.30	1.46	1.51	0.87	0.001	0.883
$Al2O_3$	0.01	16.25	15.61	16.38	16.24	0.01	14.79
FeO_T		10.07	8.44	9.92	10.75		7.1
FeO		9.74	8.15	9.59	10.40		6.7
Fe_2O_3		1.08	0.91	1.07	1.16		1.29
Fe_2O_{3T}	0.01	10.82	9.06	10.66	11.55	0.01	7.59
MgO	0.01	5.32	7.05	5.93	5.13	0.01	7.57
MnO	0.01	0.14	0.14	0.16	0.13	0.001	0.145
CaO	0.01	7.31	7.84	7.57	10.10	0.01	8.51
Na_2O	0.01	3.23	3.47	4.23	3.56	0.01	3.22
K_2O	0.01	2.94	1.68	0.76	0.28	0.01	1.41
P_2O_5	0.01	0.67	0.47	0.81	0.84	0.01	0.48
LOI		1.63	1.79	2.41	2.53		0.98
Total		97.75	98.28	97.42	96.79		98.91
C	0.02	0.06	0.06	0.03	b.d.	0.01	0.06
FeO	0.01	6.81	6.68	7.00	5.96	0.1	7.4
S	0.02	0.19	0.15	0.20	0.54	0.01	0.23
ppm							
B	1.00	b.d.	2	1	1	1	n.a.
Li	0.10	17.1	18.5	14.3	13.4	1	22
ppb							
Se	100.00	200.00	200.00	200.00	300.00	2	n.a.
Au	0.50	0.80	3.10	2.00	6.20	1	b.d.
Pd	10.00	b.d.	b.d.	b.d.	b.d.	1	1
Pt	2.00	b.d.	b.d.	b.d.	b.d.		b.d.
Ag	2.00	522	358	1090	383	500	2300
ppm							
Cu	0.01	2149.00	361.40	1572.80	5616.60	10	50
Ni	0.10	49.80	72.40	54.80	49.30	20	120
Co	0.20	32.70	34.40	36.80	29.70	0.5	68
Cr	0.50	56.60	103.60	59.30	47.10	20	220
Mn	1.00	414	355	528	412	2	1130
Zn	1.00	96.00	77.00	112.00	90.00	0.5	125
Sn	1.00	1	b.d.	b.d.	2	1	b.d.
Ga	0.50	20.5	17.1	18.6	21.5	1	18
Ge	0.10	b.d.	0.1	0.1	0.1	0.5	1.7
In	0.02	b.d.	b.d.	b.d.	b.d.	0.2	b.d.
Cd	0.01	0.08	0.21	0.12	0.09	0.2	b.d.
Zr	0.10	303.40	189.10	310.40	329.30	0.05	208
Ba	0.10	1758.00	900.00	842.00	154.00	0.05	940
Pb	0.02	9.00	15.10	6.40	16.40	0.01	15
Th	0.30	6.40	1.80	4.00	3.50	0.05	2.23
U	0.05	0.50	0.20	0.20	0.20	0.01	0.21
Bi	0.02	b.d.	0.08	b.d.	b.d.	0.005	b.d.
Ti	0.05	0.59	0.24	0.07	0.05	0.01	0.38
Rb	0.01	110.40	45.10	19.10	8.10	0.01	39
Sr	0.05	862.60	846.90	829.50	1341.80	0.01	882
Nb	0.02	10.00	6.00	8.30	10.20	0.01	7.1
Cs	0.03	2.70	0.90	0.40	0.30	0.01	0.5
Be	0.01	0.50	0.10	0.20	0.30	0.005	2
Hf	0.05	6.30	4.30	6.90	7.10	0.01	4.6
Y	0.01	23.40	17.30	24.70	26.10	0.002	18.5
Ta	0.10	0.50	0.20	0.30	0.30	1	1.71
Sc	1.00	1.90	1.40	1.60	2.50	3	23
V	0.10	172.00	119.00	197.00	217.00	5	147
Mo	0.20	0.37	0.15	0.2	0.41	0.05	b.d.
As	0.10	0.6	2.1	0.6	1	0.01	b.d.
Sb	0.02	0.03	b.d.	0.02	0.09	0.1	b.d.
W	0.02	n.a.	n.a.	n.a.	n.a.	0.05	327
Hg	0.10	n.a.	n.a.	n.a.	n.a.	1	b.d.
Te	0.50	b.d.	b.d.	b.d.	0.04	2	b.d.
La	0.10	93.80	64.10	95.80	98.30	0.2	65
Ce	0.10	181.50	126.30	189.60	198.20	0.1	137
Pr	0.10	21.60	14.90	22.66	23.39	1	15.6
Nd	0.10	78.30	54.20	83.50	88.90	0.1	59.6
Sm	0.10	11.91	9.00	13.15	13.62	0.5	9.85
Eu	0.10	2.91	2.21	2.72	3.56	0.01	2.27
Gd	0.10	8.45	6.28	9.05	9.70	1	6.5
Tb	8.00	0.95	0.67	1.00	1.04	5	0.8
Dy	0.01	4.67	3.52	5.09	5.12	5	3.84
Ho	0.1	0.78	0.58	0.78	0.86	1	0.68
Er	0.02	2.16	1.56	2.21	2.42	0.2	1.82
Tm	0.1	0.30	0.22	0.28	0.33		0.261
Yb	0.01	1.88	1.35	1.86	2.00		1.63
Lu	0.02	0.26	0.19	0.25	0.27		0.242
Mg#		46.7	58.1	49.8	44.2		64.0

Table 1 (cont.): Major and trace element analyses (XRF and ICP-MS) characterizing the grey gabbro unit. LLD: lower limit of detection; n.a. = not analysed; b.d. = below detection; Mg# = MgO/(Mgo+FeO); ppm = parts per million; ppb = parts per billion; wt. % = weight percent.

wt. %	LLD	11AV-72	11AV-73	11AV-74	11AV-53	11AV-56
	GeoLabs	GeoLabs	GeoLabs	GeoLabs	GeoLabs	GeoLabs
SiO_2	0.04	47.72	48.10	51.23	49.90	50.77
TiO_2	0.01	1.55	1.54	0.89	1.43	1.14
Al_2O_3	0.02	16.05	16.33	15.76	16.29	16.43
FeO_T		12.09	11.91	8.80	10.31	9.11
FeO		11.69	11.51	8.51	9.96	8.80
Fe_2O_3		1.30	1.28	0.95	1.11	0.98
Fe_2O_{3T}	0.01	12.99	12.79	9.45	11.07	9.78
MgO	0.01	5.04	5.12	6.83	4.86	5.71
MnO	0.002	0.15	0.15	0.14	0.16	0.13
CaO	0.01	8.36	8.42	7.94	7.15	7.73
Na_2O	0.02	3.31	3.33	3.00	3.38	3.55
K_2O	0.01	2.04	2.05	2.11	2.34	1.90
P_2O_5	0.002	1.17	1.16	0.65	0.76	0.61
LOI		1.15	1.15	1.56	1.78	0.99
Total		98.35	98.97	97.97	97.29	97.72
C	0.03	0.16	0.12	0.08	0.28	0.14
FeO		n.a.	n.a.	n.a.	n.a.	n.a.
S	0.01	0.27	0.26	0.19	0.16	0.19
ppm						
B		n.a.	n.a.	n.a.	n.a.	n.a.
Li	0.40	16.7	17.1	18.9	19.3	14.3
ppb						
Se	3.50	73.30	71.10	95.00	229.50	136.40
Au	2.00	2.00	2.00	2.00	4.00	2.30
Pd		n.a.	n.a.	n.a.	n.a.	n.a.
Pt		n.a.	n.a.	n.a.	n.a.	n.a.
Ag	0.01	120	130	250	710	590
ppm						
Cu	1.00	43.00	47.00	67.00	1389.00	105.00
Ni	1.00	46.00	45.00	100.00	66.00	69.00
Co	0.13	39.61	39.92	40.94	33.57	35.48
Cr	3.00	56.00	57.00	166.00	58.00	121.00
Mn	6.00	1037	1027	1022	1065	901
Zn	3.00	183.00	167.00	140.00	219.00	125.00
Sn	0.16	1.56	1.55	1.17	1.72	1.48
Ga	0.04	20.9	21.29	17.79	20.23	19.83
Ge		n.a.	n.a.	n.a.	n.a.	n.a.
In	0.02	0.004	0.003	0.003	0.006	0.013
Cd	0.01	0.252	0.152	0.358	0.151	0.923
Zr	0.04	218.00	193.00	157.00	105.00	220.00
Ba	0.12	1172.70	1117.80	1000.30	2460.73	1257.20
Pb	0.01	12.40	12.40	26.60	18.50	69.40
Th	0.06	2.00	2.21	2.44	2.47	3.73
U	0.01	0.31	0.32	0.25	0.14	0.13
Bi	0.00	0.01	0.01	0.08	0.09	1.26
Ti	0.01	0.37	0.367	0.408	0.369	0.304
Rb	0.00	59.99	59.92	61.84	62.79	47.40
Sr	0.01	956.40	980.60	839.00	901.10	988.00
Nb	0.00	9.78	9.54	7.52	10.25	8.72
Cs	0.01	1.27	1.36	1.31	0.73	0.44
Be	0.00	1.37	1.37	1.19	1.49	1.47
Hf	0.01	4.67	4.18	3.66	2.51	4.74
Y	0.00	25.11	24.95	19.06	24.51	21.87
Ta	6.00	0.37	0.37	0.24	0.33	0.26
Sc	0.80	21.30	21.10	20.10	19.90	20.30
V	0.60	238.30	235.60	131.00	183.90	154.80
Mo	0.02	0.65	0.73	0.33	0.48	0.32
As	0.01	0.9	1	2.5	b.d.	b.d.
Sb	0.01	b.d.	b.d.	0.08	0.11	b.d.
W	0.01	0.42	0.92	0.05	b.d.	b.d.
Hg	0.23	0.01	0.01	b.d.	b.d.	0.01
Te	0.60	0.01	0.01	0.01	b.d.	b.d.
La	0.03	93.83	94.46	73.21	92.12	85.96
Ce	0.01	197.29	195.09	148.35	188.58	170.73
Pr	0.04	23.49	23.13	17.59	22.31	19.86
Nd	0.14	87.94	88.08	65.69	84.88	74.22
Sm	0.05	13.87	13.98	10.29	13.57	11.59
Eu	0.02	3.22	3.32	2.45	3.32	2.87
Gd	1.10	9.13	9.26	6.80	9.04	7.65
Tb	0.80	1.06	1.07	0.81	1.07	0.93
Dy	0.08	5.32	5.43	4.16	5.34	4.61
Ho	0.80	0.93	0.93	0.72	0.94	0.81
Er	0.04	2.39	2.34	1.94	2.43	2.13
Tm	0.05	0.30	0.30	0.25	0.31	0.28
Yb	0.01	1.87	1.83	1.57	1.87	1.72
Lu	1.00	0.26	0.26	0.23	0.26	0.24
Mg#		40.9	41.6	56.3	43.9	51.0

Table 1 (cont.): Major and trace element analyses (XRF and ICP-MS) characterizing the grey gabbro unit. LLD: lower limit of detection; n.a. = not analysed; b.d. = below detection; Mg# = MgO/(Mgo+FeO); ppm = parts per million; ppb = parts per billion; wt. % = weight percent.

Sample	LMC1	LMC2	LMC3	LMC4	LMC5	LMC6	LMC7	LMC8	LMC9
SiO_2	51.766	52.180	52.034	52.215	52.366	51.611	51.688	51.560	51.960
TiO_2	0.320	0.350	0.303	0.265	0.465	0.318	0.327	0.338	0.317
Al_2O_3	2.562	1.781	2.353	1.586	1.764	2.259	2.462	2.472	2.269
Cr_2O_3	0.081	0.100	0.109	0.097	0.029	0.057	0.070	0.048	0.074
FeO_T	8.800	7.988	8.112	8.289	7.591	8.635	8.639	8.681	7.977
MnO	0.233	0.271	0.229	0.26	0.253	0.248	0.215	0.255	0.235
MgO	13.753	15.108	14.413	14.761	15.064	14.062	14.262	13.893	14.793
CaO	21.736	21.506	21.912	21.655	22.053	21.682	21.701	21.541	21.895
Na_2O	0.527	0.343	0.45	0.363	0.413	0.426	0.443	0.492	0.418
K_2O	0.003	0.000	0.000	0.000	0.008	0.002	0.011	0.000	0.007
Total	99.78	99.63	99.92	99.49	100.01	99.30	99.82	99.28	99.95
Cations calculated on that basis of 6 Oxygen p.f.u.									
Si p.f.u.	1.93	1.94	1.93	1.94	1.93	1.93	1.92	1.92	1.92
Al	0.07	0.06	0.07	0.06	0.07	0.07	0.08	0.08	0.08
T site	2.00	2.00	2.00	2.00	2.00	2.00	2.00	2.00	2.00
Ti	0.01	0.01	0.01	0.01	0.01	0.01	0.01	0.01	0.01
Al	0.04	0.01	0.03	0.01	0.01	0.03	0.03	0.03	0.02
Cr	0.00	0.00	0.00	0.00	0.00	0.00	0.00	0.00	0.00
Fe^{3+}	0.05	0.05	0.05	0.05	0.06	0.05	0.06	0.05	0.07
Fe^{2+}	0.20	0.18	0.18	0.19	0.16	0.20	0.19	0.20	0.16
Mg	0.70	0.75	0.72	0.74	0.76	0.71	0.71	0.70	0.74
M1 site	1.00	1.00	1.00	1.00	1.00	1.00	1.00	0.99	1.00
Fe^{2+}	0.02	0.02	0.02	0.02	0.02	0.02	0.02	0.02	0.02
Mn	0.01	0.01	0.01	0.01	0.01	0.01	0.01	0.01	0.01
Mg	0.07	0.09	0.07	0.08	0.07	0.07	0.08	0.07	0.08
Ca	0.87	0.86	0.87	0.86	0.87	0.87	0.86	0.86	0.87
Na	0.04	0.02	0.03	0.03	0.03	0.03	0.03	0.04	0.03
M2 site	1.00	1.00	1.00	1.00	1.00	1.00	1.00	1.00	1.00
cations	4.00	4.00	4.00	4.00	4.00	4.00	4.00	4.00	4.00
oxygen	6.00	6.00	6.00	6.00	6.00	6.00	6.00	6.00	6.00
$Fe_T/(Fe_T+Mg)$	0.26	0.23	0.24	0.24	0.22	0.26	0.25	0.26	0.23
$Fe^{2+}/(Fe^{2+}+Mg)$	0.23	0.19	0.20	0.20	0.18	0.22	0.21	0.22	0.18

Table 2a: Major and trace element analyses (EMP) of pyroxene minerals from least altered grey gabbro samples, LM-P-007 and LM-P-043i.

Sample	LMC10	LMC11	LMC12	LMC13	LMC14	LMC15	LMC16	LMC17	LMC18
SiO_2	52.044	51.280	52.402	51.298	51.704	51.907	52.021	51.696	51.546
TiO_2	0.227	0.297	0.549	0.240	0.223	0.250	0.246	0.257	0.246
Al_2O_3	2.071	2.565	1.717	2.369	2.378	2.144	2.028	2.258	2.439
Cr_2O_3	0.075	0.088	0.040	0.060	0.091	0.052	0.079	0.067	0.063
FeO_T	8.118	8.478	8.158	8.361	8.705	8.03	8.189	8.406	9.321
MnO	0.224	0.228	0.293	0.238	0.227	0.258	0.249	0.248	0.3
MgO	14.414	14.034	14.857	14.253	13.638	14.316	14.721	13.855	13.34
CaO	22.101	21.439	21.519	21.763	22.189	22.089	21.746	22.139	21.595
Na_2O	0.395	0.509	0.402	0.441	0.473	0.397	0.366	0.412	0.533
K_2O	0.000	0.010	0.000	0.000	0.000	0.000	0.005	0.000	0.001
Total	99.67	98.93	99.94	99.02	99.63	99.44	99.65	99.34	99.38
Si p.f.u.	1.93	1.92	1.94	1.92	1.93	1.93	1.93	1.93	1.93
Al	0.07	0.08	0.06	0.08	0.07	0.07	0.07	0.07	0.07
T site	2.00	2.00	2.00	2.00	2.00	2.00	2.00	2.00	2.00
Ti	0.01	0.01	0.02	0.01	0.01	0.01	0.01	0.01	0.01
Al	0.02	0.03	0.02	0.02	0.03	0.03	0.02	0.03	0.04
Cr	0.00	0.00	0.00	0.00	0.00	0.00	0.00	0.00	0.00
Fe^{3+}	0.05	0.06	0.04	0.07	0.06	0.05	0.06	0.05	0.05
Fe^{2+}	0.18	0.18	0.19	0.17	0.20	0.18	0.18	0.20	0.22
Mg	0.73	0.71	0.74	0.72	0.70	0.73	0.73	0.71	0.68
M1 site	1.00	1.00	1.00	1.00	1.00	1.00	1.00	1.00	1.00
Fe^{2+}	0.02	0.02	0.02	0.02	0.02	0.02	0.02	0.02	0.02
Mn	0.01	0.01	0.01	0.01	0.01	0.01	0.01	0.01	0.01
Mg	0.07	0.08	0.09	0.07	0.06	0.07	0.08	0.06	0.06
Ca	0.88	0.86	0.85	0.87	0.89	0.88	0.87	0.89	0.87
Na	0.03	0.04	0.03	0.03	0.03	0.03	0.03	0.03	0.04
M2 site	1.00	1.00	1.00	1.00	1.00	1.00	1.00	1.00	1.00
cations	4.00	4.00	4.00	4.00	4.00	4.00	4.00	4.00	4.00
oxygen	6.00	6.00	6.00	6.00	6.00	6.00	6.00	6.00	6.00
$Fe_T/(Fe_T+Mg)$	0.24	0.25	0.24	0.25	0.26	0.24	0.24	0.25	0.28
$Fe^{2+}/(Fe^{2+}+Mg)$	0.20	0.21	0.21	0.19	0.22	0.20	0.20	0.22	0.24

Table 2a (cont.): Major and trace element analyses (EMP) of pyroxene minerals from least altered grey gabbro samples, LM-P-007 and LM-P-043i.

Sample	LMC19	LMC20	LMC21	LMC22	LMC23	LMC24	LMC25	LMC26
SiO_2	51.487	51.476	51.254	51.311	51.408	51.245	51.324	51.788
TiO_2	0.319	0.301	0.269	0.327	0.303	0.333	0.278	0.268
Al_2O_3	2.441	2.462	2.486	2.428	2.487	2.481	2.454	2.203
Cr_2O_3	0.043	0.041	0.030	0.020	0.016	0.029	0.047	0.048
FeO_T	9.207	9.757	9.495	8.67	9.772	9.565	8.855	8.113
MnO	0.296	0.277	0.284	0.278	0.281	0.247	0.265	0.251
MgO	13.571	13.211	13.115	13.87	13.254	13.213	13.817	14.226
CaO	21.337	21.618	21.871	21.731	21.768	21.577	21.709	21.748
Na_2O	0.462	0.56	0.564	0.449	0.582	0.562	0.48	0.397
K_2O	0.002	0.000	0.002	0.000	0.005	0.000	0.000	0.001
Total	99.17	99.70	99.37	99.08	99.88	99.25	99.23	99.04
Si p.f.u.	1.93	1.92	1.92	1.92	1.92	1.92	1.92	1.94
Al	0.07	0.08	0.08	0.08	0.08	0.08	0.08	0.06
T site	2.00	2.00	2.00	2.00	2.00	2.00	2.00	2.00
Ti	0.01	0.01	0.01	0.01	0.01	0.01	0.01	0.01
Al	0.04	0.03	0.03	0.03	0.03	0.03	0.03	0.03
Cr	0.00	0.00	0.00	0.00	0.00	0.00	0.00	0.00
Fe^{3+}	0.04	0.06	0.07	0.06	0.08	0.06	0.07	0.04
Fe^{2+}	0.22	0.22	0.21	0.19	0.21	0.22	0.19	0.19
Mg	0.68	0.67	0.68	0.71	0.68	0.68	0.70	0.72
M1 site	1.00	1.00	1.00	1.00	1.00	1.00	1.00	1.00
Fe^{2+}	0.02	0.02	0.02	0.02	0.02	0.02	0.02	0.02
Mn	0.01	0.01	0.01	0.01	0.01	0.01	0.01	0.01
Mg	0.07	0.06	0.05	0.07	0.06	0.06	0.07	0.07
Ca	0.86	0.87	0.88	0.87	0.87	0.87	0.87	0.87
Na	0.03	0.04	0.04	0.03	0.04	0.04	0.03	0.03
M2 site	1.00	1.00	1.00	1.00	1.00	1.00	1.00	1.00
cations	4.00	4.00	4.00	4.00	4.00	4.00	4.00	4.00
oxygen	6.00	6.00	6.00	6.00	6.00	6.00	6.00	6.00
$Fe_T/(Fe_T+Mg)$	0.28	0.29	0.29	0.26	0.29	0.29	0.26	0.24
$Fe^{2+}/(Fe^{2+}+Mg)$	0.25	0.25	0.24	0.21	0.23	0.24	0.21	0.21

Table 2a (cont.): Major and trace element analyses (EMP) of pyroxene minerals from least altered grey gabbro samples, LM-P-007 and LM-P-043i.

Sample	LMC27	LMC28	LMC29	LMC30	LMC31
SiO_2	53.613	53.566	53.553	53.463	53.848
TiO_2	0.138	0.089	0.113	0.074	0.107
Al_2O_3	0.887	1.085	0.989	1.275	1.042
Cr_2O_3	0.007	0.041	0.029	0.022	0.031
FeO_T	19.059	19.340	19.371	18.750	18.539
MnO	0.511	0.528	0.535	0.500	0.474
MgO	24.370	24.735	24.635	25.081	24.644
CaO	1.369	0.828	0.875	0.668	1.212
Na_2O	0.000	0.000	0.000	0.000	0.000
K_2O	0.000	0.002	0.000	0.000	0.004
Total	99.961	100.217	100.125	99.838	99.903
Si p.f.u.	1.97	1.96	1.96	1.96	1.95
Al	0.03	0.04	0.04	0.04	0.04
T site	2.00	2.00	2.00	2.00	1.99
Ti	0.00	0.00	0.00	0.00	0.00
Al	0.01	0.01	0.01	0.01	0.00
Cr	0.00	0.00	0.00	0.00	0.00
Fe^{3+}	0.02	0.03	0.03	0.03	0.50
Fe^{2+}	0.29	0.28	0.29	0.28	0.28
Mg	0.68	0.68	0.68	0.69	0.67
M1 site	1.00	1.00	1.00	1.00	1.46
Fe^{2+}	0.28	0.28	0.28	0.27	0.28
Mn	0.02	0.02	0.02	0.02	0.02
Mg	0.65	0.67	0.67	0.68	0.66
Ca	0.05	0.03	0.03	0.03	0.05
Na	0.00	0.00	0.00	0.00	0.00
M2 site	1.00	1.00	1.00	1.00	1.00
cations	4.00	4.00	4.00	4.00	4.00
oxygen	6.00	6.00	6.00	6.00	6.00
$Fe_T/(Fe_T+Mg)$	0.30	0.30	0.31	0.30	0.32
$Fe^{2+}/(Fe^{2+}+Mg)$	0.30	0.29	0.30	0.29	0.30

Table 2a (cont.): Major and trace element analyses (EMP) of pyroxene minerals from least altered grey gabbro samples, LM-P-007 and LM-P-043i.

Sample	LMA1	LMA2	LMA3	LMA4	LMA5	LMA6
SiO_2	46.857	54.178	54.771	53.189	48.127	55.116
TiO_2	1.371	0.023	0.111	0.034	1.431	0.000
Al_2O_3	8.340	2.214	1.991	1.589	7.006	1.150
Cr_2O_3	0.098	0.055	0.085	0.010	0.129	0.056
Fe_2O_3	1.210	1.114	0.988	1.747	1.198	1.067
FeO	10.830	10.001	8.876	15.689	10.760	9.586
MnO	0.136	0.210	0.272	0.428	0.159	0.286
MgO	14.545	16.691	17.416	12.781	14.728	16.985
NiO	0.000	0.000	0.000	0.000	0.000	0.000
ZnO	0.000	0.000	0.000	0.000	0.000	0.000
CaO	11.691	13.139	12.949	11.593	11.583	13.138
Na_2O	1.597	0.119	0.143	0.076	1.195	0.029
K_2O	0.357	0.270	0.061	0.090	0.698	0.019
F	0.551	0.170	0.147	0.010	0.183	0.132
Cl	0.030	0.230	0.030	0.020	0.066	0.005
H_2O*	1.799	1.965	2.038	2.050	1.964	2.035
Subtotal	99.41	100.38	99.89	99.30	99.23	99.60
O=F,Cl	0.24	0.12	0.07	0.01	0.09	0.06
Total	99.17	100.26	99.82	99.29	99.14	99.55
	Cations calculated on the basis of 23 (O,F,Cl) p.f.u.					
Si p.f.u.	6.8	7.72	7.76	7.76	6.98	7.87
Al^{IV}	1.2	0.28	0.24	0.24	1.02	0.13
T site	8.00	8.00	8.00	8.00	8.00	8.00
Al^{VI}	0.22	0.09	0.10	0.03	0.18	0.07
Ti	0.15	0.00	0.01	0.00	0.16	0.00
Cr	0.01	0.01	0.01	0.00	0.01	0.01
Fe^{3+}	0.53	0.08	0.12	0.53	0.45	0.02
Fe^{2+}	0.93	1.25	1.05	1.59	1.00	1.26
Mn	0.02	0.03	0.03	0.05	0.02	0.03
Mg	3.14	3.55	3.68	2.78	3.18	3.62
C site	5.00	5.00	5.00	5.00	5.00	5.00
Ca	1.82	2.01	1.97	1.81	1.80	2.01
B site	1.82	2.01	1.97	1.81	1.80	2.01
Na	0.45	0.03	0.04	0.02	0.34	0.01
K	0.07	0.05	0.01	0.02	0.13	0.00
A site	0.51	0.08	0.05	0.04	0.47	0.01
F	0.25	0.08	0.07	0.00	0.08	0.06
Cl	0.01	0.06	0.01	0.01	0.02	0.00
OH*	1.74	1.87	1.93	1.99	1.90	1.94
W site	2.00	2.00	2.00	2.00	2.00	2.00
Cations	13.00	13.00	13.00	13.00	13.00	13.00
Oxygen	23.00	23.00	23.00	23.00	23.00	23.00
$Mg/(Mg+Fe^{2+})$	0.772	0.740	0.779	0.635	0.762	0.74
$Fe^{3+}/(Fe^{3+}+Al^{VI})$	0.707	0.449	0.561	0.939	0.721	0.20

Table 2b: Major and trace element analyses (EMP) of amphibole minerals from least altered grey gabbro samples, LM-P-007 and LM-P-043i.

Sample	LMA7	LMA8	LMA9	LMA10	LMA11	LMA12
SiO_2	45.788	54.570	49.507	53.642	55.224	54.595
TiO_2	2.240	0.190	1.596	0.163	0.076	0.040
Al_2O_3	9.102	2.760	5.792	2.417	1.583	1.877
Cr_2O_3	0.068	0.020	0.036	0.049	0.021	0.005
Fe_2O_3	1.063	0.810	1.059	1.214	0.986	1.050
FeO	9.541	7.273	9.509	10.903	8.859	9.428
MnO	0.128	0.190	0.153	0.341	0.297	0.300
MgO	14.877	19.370	16.294	15.938	17.791	17.315
NiO	0.000	0.000	0.000	0.000	0.000	0.000
ZnO	0.000	0.000	0.000	0.000	0.000	0.000
CaO	11.471	11.840	11.676	11.856	12.214	12.495
Na_2O	1.670	0.340	1.033	0.355	0.233	0.233
K_2O	1.134	0.110	0.616	0.146	0.032	0.017
F	0.459	0.550	0.461	0.028	0.209	0.171
Cl	0.075	0.010	0.041	0.029	0.015	0.015
H_2O*	1.826	1.900	1.866	2.074	2.023	2.029
Subtotal	99.44	99.93	99.64	99.16	99.56	99.57
O=F,Cl	0.21	0.23	0.20	0.02	0.09	0.08
Total	99.23	99.70	99.44	99.14	99.47	99.50
Cations calculated on the basis of 23 (O,F,Cl) p.f.u.						
Si p.f.u.	6.66	7.56	7.09	7.68	7.79	7.74
Al^{IV}	1.34	0.44	0.91	0.32	0.21	0.26
T site	8.00	8.00	8.00	8.00	8.00	8.00
Al^{VI}	0.22	0.02	0.06	0.08	0.05	0.06
Ti	0.24	0.02	0.17	0.02	0.01	0.00
Cr	0.01	0.00	0.00	0.01	0.00	0.00
Fe^{3+}	0.37	0.75	0.52	0.44	0.38	0.33
Fe^{2+}	0.92	0.19	0.74	1.01	0.78	0.91
Mn	0.02	0.02	0.02	0.04	0.04	0.04
Mg	3.22	4.00	3.48	3.40	3.74	3.66
C site	5.00	5.00	5.00	5.00	5.00	5.00
Ca	1.79	1.76	1.79	1.82	1.85	1.90
B site	1.79	1.76	1.79	1.82	1.85	1.90
Na	0.47	0.09	0.29	0.10	0.06	0.06
K	0.21	0.02	0.11	0.03	0.01	0.00
A site	0.68	0.11	0.40	0.13	0.07	0.07
F	0.21	0.24	0.21	0.01	0.09	0.08
Cl	0.02	0.00	0.01	0.01	0.00	0.00
OH*	1.77	1.76	1.78	1.98	1.90	1.92
W site	2.00	2.00	2.00	2.00	2.00	2.00
Cations	13.00	13.00	13.00	13.00	13.00	13.00
Oxygen	23.00	23.00	23.00	23.00	23.00	23.00
$Mg/(Mg+Fe^{2+})$	0.78	0.96	0.82	0.77	0.83	0.80
$Fe^{3+}/(Fe^{3+}+Al^{VI})$	0.63	0.98	0.89	0.84	0.88	0.85

Table 2b (cont.): Major and trace element analyses (EMP) of amphibole minerals from least altered grey gabbro samples, LM-P-007 and LM-P-043i.

Sample	LMA13	LMA14	LMA15	LMA16	LMA17	LMA18
SiO_2	54.696	54.817	56.320	55.199	55.40	54.75
TiO_2	0.100	0.042	0.000	0.062	0.06	0.04
Al_2O_3	1.524	1.813	0.584	1.260	1.66	1.60
Cr_2O_3	0.028	0.041	0.010	0.013	0.02	0.01
Fe_2O_3	1.167	1.036	0.852	1.146	0.98	1.14
FeO	10.480	9.304	7.651	10.294	8.83	10.21
MnO	0.392	0.323	0.214	0.437	0.28	0.39
MgO	16.663	17.418	18.722	17.074	17.66	16.95
NiO	0.000	0.000	0.000	0.000	0.00	0.00
ZnO	0.000	0.000	0.000	0.000	0.00	0.00
CaO	12.223	12.263	13.235	12.016	12.49	12.38
Na_2O	0.170	0.235	0.041	0.162	0.22	0.20
K_2O	0.081	0.028	0.035	0.019	0.02	0.02
F	0.121	0.129	0.000	0.120	0.12	0.15
Cl	0.006	0.015	0.003	0.015	0.01	0.01
H_2O*	2.052	2.055	2.126	2.064	2.07	2.04
Subtotal	99.70	99.52	99.79	99.88	99.83	99.89
O=F,Cl	0.05	0.06	0.00	0.05	0.05	0.06
Total	99.65	99.46	99.79	99.83	99.77	99.83
Cations calculated on the basis of 23 (O,F,Cl) p.f.u.						
Si p.f.u.	7.77	7.75	7.94	7.79	7.81	7.76
Al^{IV}	0.23	0.25	0.06	0.21	0.19	0.24
T site	8.00	8.00	8.00	8.00	8.00	8.00
Al^{VI}	0.03	0.06	0.04	0.00	0.09	0.02
Ti	0.01	0.00	0.00	0.01	0.01	0.00
Cr	0.00	0.00	0.00	0.00	0.00	0.00
Fe^{3+}	0.40	0.39	0.01	0.52	0.25	0.39
Fe^{2+}	0.99	0.83	0.99	0.83	0.91	0.95
Mn	0.05	0.04	0.03	0.05	0.03	0.05
Mg	3.53	3.67	3.93	3.59	3.71	3.58
C site	5.00	5.00	5.00	5.00	5.00	5.00
Ca	1.86	1.86	2.00	1.82	1.89	1.88
B site	1.86	1.86	2.00	1.82	1.89	1.88
Na	0.05	0.06	0.01	0.04	0.06	0.05
K	0.01	0.01	0.01	0.00	0.00	0.00
A site	0.06	0.07	0.02	0.05	0.06	0.06
F	0.05	0.06	0.00	0.05	0.05	0.07
Cl	0.00	0.00	0.00	0.00	0.00	0.00
OH*	1.94	1.94	2.00	1.94	1.94	1.93
W site	2.00	2.00	2.00	2.00	2.00	2.00
Cations	13.00	13.00	13.00	13.00	13.00	13.00
Oxygen	23.00	23.00	23.00	23.00	23.00	23.00
$Mg/(Mg+Fe^{2+})$	0.78	0.82	0.80	0.81	0.80	0.79
$Fe^{3+}/(Fe^{3+}+Al^{VI})$	0.94	0.87	0.17	1.00	0.74	0.94

Table 2b (cont.): Major and trace element analyses (EMP) of amphibole minerals from least altered grey gabbro samples, LM-P-007 and LM-P-043i.

Sample	LMA19	LMA20	LMA21	LMA22	LMA23
SiO_2	54.01	53.88	48.60	46.49	53.69
TiO_2	0.08	0.05	1.13	1.23	0.09
Al_2O_3	2.16	2.43	6.77	8.19	2.48
Cr_2O_3	0.00	0.02	0.08	0.08	0.01
Fe_2O_3	1.19	1.24	1.08	1.15	1.26
FeO	10.68	11.13	9.67	10.33	11.34
MnO	0.37	0.38	0.16	0.21	0.36
MgO	16.22	15.62	16.15	15.29	15.81
NiO	0.00	0.00	0.00	0.00	0.00
ZnO	0.00	0.00	0.00	0.00	0.00
CaO	12.13	12.14	11.58	11.60	12.04
Na_2O	0.24	0.26	1.37	1.48	0.29
K_2O	0.20	0.07	0.64	0.91	0.16
F	0.00	0.06	0.45	0.50	0.09
Cl	0.03	0.03	0.05	0.07	0.04
H_2O*	2.09	2.06	1.87	1.81	2.05
Subtotal	99.39	99.35	99.58	99.33	99.70
O=F,Cl	0.01	0.03	0.20	0.23	0.05
Total	99.38	99.32	99.38	99.10	99.65
Cations calculated on the basis of 23 (O,F,Cl) p.f.u.					
Si p.f.u.	7.71	7.72	6.97	6.74	7.66
Al^{IV}	0.29	0.28	1.03	1.26	0.34
T site	8.00	8.00	8.00	8.00	8.00
Al^{VI}	0.08	0.13	0.11	0.14	0.08
Ti	0.01	0.00	0.12	0.13	0.01
Cr	0.00	0.00	0.01	0.01	0.00
Fe^{3+}	0.38	0.33	0.61	0.66	0.45
Fe^{2+}	1.04	1.15	0.67	0.73	1.05
Mn	0.04	0.05	0.02	0.03	0.04
Mg	3.45	3.34	3.45	3.30	3.36
C site	5.00	5.00	5.00	5.00	5.00
Ca	1.86	1.86	1.78	1.80	1.84
B site	1.86	1.86	1.78	1.80	1.84
Na	0.07	0.07	0.38	0.41	0.08
K	0.04	0.01	0.12	0.17	0.03
A site	0.10	0.08	0.50	0.58	0.11
F	0.00	0.03	0.20	0.23	0.04
Cl	0.01	0.01	0.01	0.02	0.01
OH*	1.99	1.97	1.79	1.75	1.95
W site	2.00	2.00	2.00	2.00	2.00
Cations	13.00	13.00	13.00	13.00	13.00
Oxygen	23.00	23.00	23.00	23.00	23.00
$Mg/(Mg+Fe^{2+})$	0.77	0.74	0.84	0.82	0.76
$Fe^{3+}/(Fe^{3+}+Al^{VI})$	0.83	0.72	0.85	0.83	0.85

Table 2b (cont.): Major and trace element analyses (EMP) of amphibole minerals from least altered grey gabbro samples, LM-P-007 and LM-P-043i.

Sample	LMB1	LMB2	LMB3	LMB4	LMB5	LMB6	LMB7	LMB8	LMB9	LMB10
SiO_2	37.196	37.403	37.370	37.062	37.482	37.597	37.953	37.193	37.173	37.675
TiO_2	5.912	5.815	5.552	5.883	5.365	5.282	5.165	4.744	5.160	5.596
Al_2O_3	13.823	14.045	13.823	13.860	13.665	13.667	13.583	13.970	13.473	13.626
FeO	12.942	13.423	13.536	13.327	13.146	13.396	13.656	12.497	15.269	13.094
MnO	0.077	0.063	0.056	0.055	0.138	0.136	0.105	0.090	0.152	0.130
MgO	15.329	15.163	15.049	14.998	15.711	15.625	15.466	15.755	14.272	15.400
CaO	0.000	0.003	0.030	0.008	0.000	0.001	0.011	0.064	0.011	0.008
Na_2O	0.154	0.145	0.054	0.160	0.123	0.131	0.107	0.057	0.069	0.111
K_2O	9.211	9.299	9.454	9.342	9.459	9.285	9.562	9.298	9.410	9.388
F	0.604	0.583	0.570	0.692	0.391	0.409	0.486	0.546	0.290	0.435
Cl	0.058	0.065	0.055	0.047	0.074	0.085	0.089	0.101	0.106	0.075
Cr_2O_3	0.094	0.076	0.084	0.107	0.025	0.032	0.014	0.033	0.065	0.030
H2O*	3.722	3.753	3.737	3.674	3.827	3.818	3.794	3.704	3.822	3.809
Subtotal	99.12	99.84	99.37	99.22	99.41	99.46	99.99	98.05	99.27	99.38
O=F,Cl	0.27	0.26	0.25	0.30	0.18	0.19	0.22	0.25	0.15	0.20
Total	98.85	99.58	99.12	98.91	99.22	99.27	99.77	97.80	99.13	99.18
Cations calculated on the basis of 24 (O,OH,F,Cl)										
Si p.f.u.	5.54	5.54	5.57	5.54	5.58	5.59	5.62	5.59	5.59	5.60
Al^{IV}	2.43	2.45	2.43	2.44	2.40	2.39	2.37	2.41	2.39	2.39
Z site	7.97	8.00	8.00	7.98	7.97	7.98	8.00	8.00	7.98	7.99
Al^{VI}	0.00	0.00	0.00	0.00	0.00	0.00	0.00	0.07	0.00	0.00
Ti	0.66	0.65	0.62	0.66	0.60	0.59	0.58	0.54	0.58	0.63
Fe	1.61	1.66	1.69	1.66	1.64	1.67	1.69	1.57	1.92	1.63
Mn	0.01	0.01	0.01	0.01	0.02	0.02	0.01	0.01	0.02	0.02
Mg	3.41	3.35	3.34	3.34	3.48	3.46	3.42	3.53	3.20	3.41
Y site	5.69	5.67	5.66	5.67	5.74	5.74	5.70	5.72	5.72	5.68
Na	0.04	0.04	0.02	0.05	0.04	0.04	0.03	0.02	0.02	0.03
K	1.75	1.76	1.80	1.78	1.79	1.76	1.81	1.78	1.81	1.78
X site	1.80	1.80	1.81	1.83	1.83	1.80	1.84	1.80	1.83	1.81
OH*	3.70	3.71	3.72	3.66	3.80	3.79	3.75	3.71	3.84	3.78
F	0.28	0.27	0.27	0.33	0.18	0.19	0.23	0.26	0.14	0.20
Cl	0.01	0.02	0.01	0.01	0.02	0.02	0.02	0.03	0.03	0.02
Cations	15.46	15.47	15.48	15.48	15.54	15.52	15.53	15.52	15.53	15.48
Al total	2.43	2.45	2.43	2.44	2.40	2.39	2.37	2.48	2.39	2.39
$Fe^{2+}/(Fe^{2+}+Mg)$	0.32	0.33	0.34	0.33	0.32	0.32	0.33	0.31	0.38	0.32

Table 2c: Major and trace element analyses (EMP) of biotite minerals from least altered grey gabbro samples, LM-P-007 and LM-P-043i.

Sample	LMB11	LMB12	LMB13	LMB14	LMB15	LMB16	LMB17	LMB18	LMB19	LMB20
SiO_2	36.122	37.741	36.021	36.274	35.673	36.433	36.417	35.897	36.052	35.840
TiO_2	6.180	5.689	4.660	5.330	2.861	3.254	2.711	4.791	4.559	5.258
Al_2O_3	13.650	13.647	13.699	13.380	15.374	14.637	14.892	14.259	14.268	13.943
FeO	12.925	12.477	20.191	19.687	20.023	19.299	19.261	20.044	19.461	19.866
MnO	0.110	0.086	0.146	0.177	0.187	0.156	0.141	0.181	0.156	0.168
MgO	14.761	16.071	10.948	10.990	10.846	11.462	11.613	11.035	11.419	10.831
CaO	0.013	0.013	0.044	0.010	0.088	0.000	0.017	0.021	0.014	0.027
Na_2O	0.201	0.136	0.037	0.061	0.000	0.000	0.006	0.010	0.000	0.034
K_2O	8.618	9.348	9.078	9.289	9.295	9.516	9.400	9.130	9.297	9.044
F	0.557	0.528	0.261	0.361	0.289	0.416	0.498	0.324	0.483	0.366
Cl	0.055	0.065	0.138	0.094	0.091	0.082	0.127	0.111	0.123	0.112
Cr_2O_3	0.027	0.026	0.073	0.050	0.074	0.080	0.052	0.059	0.041	0.039
H2O*	3.655	3.788	3.727	3.710	3.711	3.684	3.625	3.729	3.654	3.696
Subtotal	96.87	99.62	99.02	99.41	98.51	99.02	98.76	99.59	99.53	99.22
O=F,Cl	0.25	0.24	0.14	0.17	0.14	0.19	0.24	0.16	0.23	0.18
Total	96.63	99.38	98.88	99.24	98.37	98.83	98.52	99.43	99.30	99.04
Si p.f.u.	5.51	5.58	5.56	5.57	5.53	5.60	5.61	5.50	5.52	5.51
Al^{IV}	2.45	2.38	2.44	2.42	2.47	2.40	2.39	2.50	2.48	2.49
Z site	7.96	7.96	8.00	7.99	8.00	8.00	8.00	8.00	8.00	8.00
Al^{VI}	0.00	0.00	0.05	0.00	0.33	0.25	0.31	0.08	0.10	0.04
Ti	0.71	0.63	0.54	0.62	0.33	0.38	0.31	0.55	0.53	0.61
Fe	1.65	1.54	2.61	2.53	2.59	2.48	2.48	2.57	2.49	2.56
Mn	0.01	0.01	0.02	0.02	0.02	0.02	0.02	0.02	0.02	0.02
Mg	3.35	3.54	2.52	2.52	2.50	2.63	2.67	2.52	2.61	2.48
Y site	5.72	5.73	5.73	5.68	5.79	5.75	5.79	5.75	5.75	5.71
Na	0.06	0.04	0.01	0.02	0.00	0.00	0.00	0.00	0.00	0.01
K	1.68	1.76	1.79	1.82	1.84	1.87	1.85	1.79	1.82	1.77
X site	1.74	1.80	1.80	1.84	1.84	1.87	1.85	1.79	1.82	1.78
OH*	3.72	3.74	3.84	3.80	3.83	3.78	3.72	3.81	3.73	3.79
F	0.27	0.25	0.13	0.18	0.14	0.20	0.24	0.16	0.23	0.18
Cl	0.01	0.02	0.04	0.02	0.02	0.02	0.03	0.03	0.03	0.03
Cations	15.42	15.49	15.53	15.51	15.63	15.62	15.64	15.54	15.56	15.50
Al total	2.45	2.38	2.49	2.42	2.81	2.65	2.70	2.58	2.58	2.53
$Fe^{2+}/(Fe^{2+}+Mg)$	0.33	0.30	0.51	0.50	0.51	0.49	0.48	0.50	0.49	0.51

Table 2c (cont.): Major and trace element analyses (EMP) of biotite minerals from least altered grey gabbro samples, LM-P-007 and LM-P-043i.

Sample	LMCHL1	LMCHL2	LMCHL3
SiO2	26.806	26.882	26.907
TiO2	0.020	0.055	0.051
Al2O3	20.678	20.461	20.961
FeO	23.874	22.110	22.326
MnO	0.272	0.301	0.320
MgO	16.478	18.022	17.596
CaO	0.044	0.000	0.000
Na2O	0.000	0.000	0.000
K2O	0.098	0.005	0.015
H2O*	11.606	11.996	11.769
Subtotal	99.88	99.83	99.95
O=F,Cl	0.00	0.00	0.00
Total	99.88	99.83	99.95
Based on 28 oxygens and with Fe2+/Fe3+ and OH calculated assuming full site occupancy			
Si p.f.u.	4.37	4.36	4.35
Al iv	3.63	3.64	3.65
T site	8.00	8.00	8.00
Al vi	0.34	0.27	0.34
Fe	3.25	3.00	3.02
Mn	0.04	0.04	0.04
Mg	4.00	4.36	4.24
M1 Site	7.63	7.67	7.64
OH*	4.00	4.00	4.00
F	0.00	0.00	0.00
Cl	0.00	0.00	0.00
Cations	15.63	15.67	15.64
Al total	3.97	3.91	3.99
$Fe^{2+}/(Fe^{2+}+Mg)$	0.45	0.41	0.42

Table 2d: Major and trace element analyses (EMP) of chlorite minerals from least altered grey gabbro samples, LM-P-007 and LM-P-043i.

Sample Number	$\delta^{18}O$	$^{87}Sr/^{86}Sr$
LM-P-019	8.1	
LM-P-021		
LM-P-025	7.7	
LM-P-028		
LM-P-030		
LM-P-032A		
LM-P-033		
LM-P-036		
LM-P-037		
LM-P-038		
LM-P-042	6.7	
LM-P-039A		
LM-P-039B		
LM-P-007	6.9	0.703422
LM-P-043G	6.6	0.70305
LM-P-060 (actinolite separate sample)	5	0.703054

Table 3: Isotopic results for Oxygen and Strontium analyses. $\delta^{18}O$ = oxygen isotope values; $^{87}Sr/^{86}Sr$ = strontium isotope values. Oxygen dataset (whole rock samples - WR): LM-P-007, LM-P-019, LM-P-025, LM-P-042, LM-P-043G, LM-P-043K, and LM-P-043P; Strontium dataset: LM-P-007 (WR), LM-P-043G (WR), and LM-P-060 (separated actinolite crystals).

Fract.[1]	Description[2]	Wt. ug	U ppm	Pb[3] ppm	206Pb[4] 204Pb	Pb[5] pg	Isotopic Ratios[6] 208Pb 206Pb	207Pb 235U	±1SE Abs	206Pb 238U	±1SE Abs	Corr.[7] Coeff.	207Pb 206Pb	±1SE Abs	Ages (Ma)[8] 206Pb 238U	±2SE	207Pb 235U	±2SE	207Pb 206Pb	±2SE	% Disc
11AV-74 (Z10633)																					
A16-1	Clr, Co, El, Pr, NM0	4	51	29	1781	2	0.87	5.1789	0.0075	0.33207	0.00037	0.8571	0.11311	0.00009	1848.4	3.6	1849.1	2.5	1850.0	2.7	0.1
A16-2	Clr, Co, El, Pr, NM0	5	78	45	3977	2	0.90	5.1652	0.0061	0.33128	0.00030	0.9084	0.11308	0.00006	1844.6	2.9	1846.9	2.0	1849.5	1.9	0.3
A16-3	Clr, Co, St, Pr, nIn,NM0	12	21	12	1190	4	0.84	5.1745	0.0080	0.33104	0.00034	0.8009	0.11337	0.00011	1843.4	3.3	1848.4	2.6	1854.1	3.4	0.7
C16-1	Clr, Co, El, Pr, M1	6	59	35	7873	1	0.98	5.1758	0.0061	0.33186	0.00031	0.9269	0.11311	0.00005	1847.4	3.0	1848.6	2.0	1850.0	1.7	0.2
C16-2	Clr, Co, El, Pr, M1	6	33	19	3776	0	0.92	5.1821	0.0069	0.33216	0.00037	0.9083	0.11315	0.00006	1848.8	3.5	1849.7	2.3	1850.6	2.1	0.1
C16-3	Clr, Co, El, Pr, M1	4	42	24	975	4	0.93	5.1826	0.0086	0.33252	0.00034	0.8006	0.11304	0.00012	1850.6	3.3	1849.8	2.8	1848.8	3.7	-0.1

Notes:

[1] All zircon fractions are composed of single grains and were chemically abraded using a modified procedure from Mattinson (2005). All fractions composed of single grains.

[2]Zircon descriptions: Co=Colorless, Clr=Clear, nIn=Numerous Inclusions, Eu=Euhedral, Pr=Prismatic, El=Elongate, St=Stubby Prism, NM0=NonMag @1.8A 0oSS, M1=Magnetic @ 1.8A 1oSS.

[3]Radiogenic Pb

[4]Measured ratio, corrected for spike and fractionation

[5]Total common Pb in analysis corrected for fractionation and spike

[6]Corrected for blank Pb and U and common Pb, errors quoted are 1 sigma absolute; procedural blank values for this study are 0.1 pg U and 1 pg Pb;
Pb blank isotopic composition is based on the analysis of procedural blanks; corrections for common Pb were made using Stacey-Kramers (1975) compositions.

[7]Correlation Coefficient

[8]Corrected for blank and common Pb, errors quoted are 2 sigma in Ma

The error on the calibration of the GSC ^{205}Pb-^{233}U-^{235}U spike utilized in this study is 0.22% (2σ).

Table 4: U-Pb Thermal ionization mass spectrometry (TIMS) LA-ICP-MS analytical data.

Spot name	U (ppm)	Th (ppm)	Th U	Yb (ppm)	Hf (ppm)	$^{204}Pb/^{206}Pb$	% ±	$^{206}Pb^*$ (ppm)	f(206)^{204} %	$^{208}Pb/^{207}Pb$	% ±	$^{207}Pb/^{235}U$	% ±	$^{206}Pb/^{238}U$	% ±	Corr Coeff	Age (Ma) $^{207}Pb/^{206}Pb$	% ±	$^{206}Pb/^{238}U$	±	$^{207}Pb/^{206}Pb$	±	Disc. %
10633-8.2	11	20	1.94	61	7870	3.2E-3	20	3	5.587	0.547	4.2	4.60	9.3	0.319	1.75	0.188	0.1046	9.2	1784	27	1707	169	-5.2
10633-36.2	29	51	1.85	79	9640	7.9E-5	46	8	0.137	0.575	2.9	5.03	2.1	0.325	1.74	0.845	0.1121	1.1	1816	28	1834	20	1.1
10633-1.2	12	20	1.74	64	7091	3.4E-3	20	3	5.621	0.476	3.8	5.25	11.6	0.338	3.67	0.315	0.1128	11.0	1876	60	1845	200	-1.9
10633-2.2	19	34	1.86	73	7716	2.4E-3	20	5	4.154	0.552	3.0	5.29	6.1	0.331	1.56	0.254	0.1160	5.9	1843	25	1896	107	3.2
10633-2.1	89	122	1.42	121	9867	8.9E-4	20	30	1.536	0.416	2.4	7.31	2.4	0.399	1.23	0.518	0.1326	2.0	2167	23	2133	36	-1.8
10633-7.1	126	242	1.98	182	9100	3.0E-5	65	44	0.052	0.574	1.1	8.39	1.1	0.408	1.03	0.927	0.1491	0.4	2206	19	2335	7	6.6
10633-15.1	81	87	1.10	67	9579	-2.7E-5	37	27	-0.047	0.330	1.8	8.03	1.1	0.390	1.04	0.915	0.1491	0.5	2125	19	2336	8	10.6
10633-36.1	38	55	1.52	81	7516	3.1E-4	64	13	0.531	0.429	2.3	8.34	2.4	0.402	1.50	0.632	0.1504	1.8	2179	28	2351	32	8.6
10633-19.1	111	226	2.10	204	6823	3.6E-5	41	38	0.063	0.623	1.1	8.61	1.2	0.404	1.14	0.930	0.1545	0.4	2187	21	2396	8	10.3
10633-6.1	108	197	1.90	181	10083	2.8E-4	62	39	0.490	0.546	2.2	9.15	2.3	0.425	1.51	0.668	0.1562	1.7	2281	29	2415	28	6.6
10633-10.1	161	404	2.58	306	7629	5.4E-5	234	61	0.094	0.746	1.4	9.63	1.7	0.443	1.24	0.718	0.1576	1.2	2364	25	2430	20	3.2
10633-1.1	69	146	2.19	153	6941	1.7E-4	33	26	0.298	0.643	1.3	9.40	1.2	0.432	1.07	0.857	0.1579	0.6	2313	21	2434	11	5.9
10633-23.2	90	189	2.16	191	7685	1.8E-4	34	34	0.310	0.601	1.9	9.49	1.6	0.432	1.27	0.803	0.1594	0.9	2313	25	2449	16	6.6
10633-9.1	173	202	1.21	185	10034	2.6E-4	28	63	0.448	0.336	2.1	9.37	1.4	0.423	1.14	0.789	0.1605	0.9	2275	22	2461	15	8.9
10633-21.1	139	257	1.91	211	8744	6.8E-5	65	51	0.117	0.548	1.0	9.49	1.1	0.428	1.03	0.897	0.1608	0.5	2296	20	2464	9	8.0
10633-11.1	105	207	2.04	205	8034	8.7E-5	21	40	0.150	0.572	1.9	9.92	1.4	0.447	1.17	0.842	0.1610	0.7	2381	23	2466	13	4.1
10633-9.2	232	212	0.95	149	11253	2.2E-5	41	90	0.038	0.275	1.1	10.19	1.2	0.452	1.14	0.971	0.1635	0.3	2405	23	2492	5	4.2
10633-23.1	132	249	1.95	221	8729	5.3E-5	50	50	0.092	0.521	1.9	10.00	1.5	0.440	1.31	0.865	0.1650	0.8	2350	26	2507	13	7.5
10633-4.1	64	106	1.71	108	8233	4.8E-5	71	25	0.083	0.474	2.6	10.44	1.6	0.458	1.28	0.793	0.1653	1.0	2432	26	2511	17	3.8
10633-5.1	85	167	2.02	184	8385	-1.1E-5	38	34	-0.019	0.577	1.9	10.67	1.4	0.460	1.24	0.861	0.1683	0.7	2439	25	2541	12	4.8
10633-8.1	221	571	2.67	376	7531	7.7E-5	39	92	0.133	0.757	1.1	11.70	1.2	0.485	1.08	0.903	0.1750	0.5	2548	23	2606	9	2.7

Notes:

Spot name follows the convention x-y.z; where x = sample number, y = grain number and z = spot number.

f206^{204} refers to mole percent of total 206Pb that is due to common Pb, calculated using the 204Pb-method; common Pb composition used is the surface blank (4/6: 0.05770; 7/6: 0.89500; 8/6: 2.13840)

* refers to radiogenic Pb (corrected for common Pb)

Errors are reported at 1σ uncertainty level unless otherwise noted

Analytical details

IP66S: 25 µm spot; 5 or 6 scans; ~9nA O- primary beam intensity, U-Pb calibration error 1.0% (included).

No mass fractionation correction applied.

Table 5: U-Pb Sensitive high-resolution ion microprobe (SHRIMP) LA-ICP-MS analytical data

Figures:

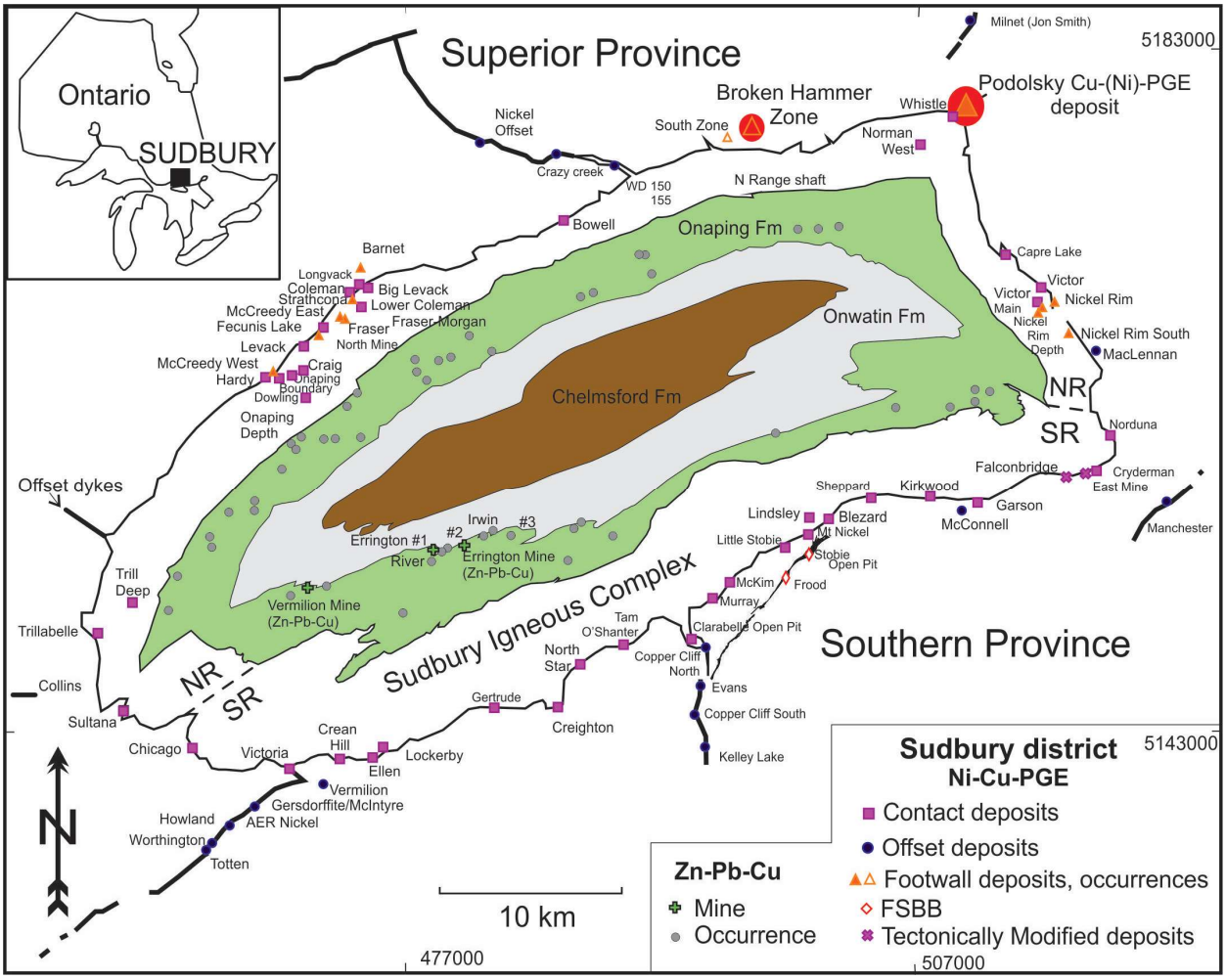

Fig. 1: A simplified geological map of the Sudbury mining district showing the main geological features: Superior and Southern provinces, Sudbury Igneous Complex (SIC), the crater fill sequence of the Whitewater Group (Onaping, Onwatin and Chelmsford formations) and the locations of the different ore deposit types (i.e., contact, offset, footwall). Note that the SIC is broken into the North and South ranges (NR, SR), respectively. Two areas of relevance to this study are highlighted in red, namely the Podolsky mine, a Cu-(Ni)-PGE hybrid deposit, located on the Whistle offset, the Broken hammer deposit (Joe Lake intrusion), a footwall Cu-PGE deposit. The figure has been modified from Ames and Farrow (2007).

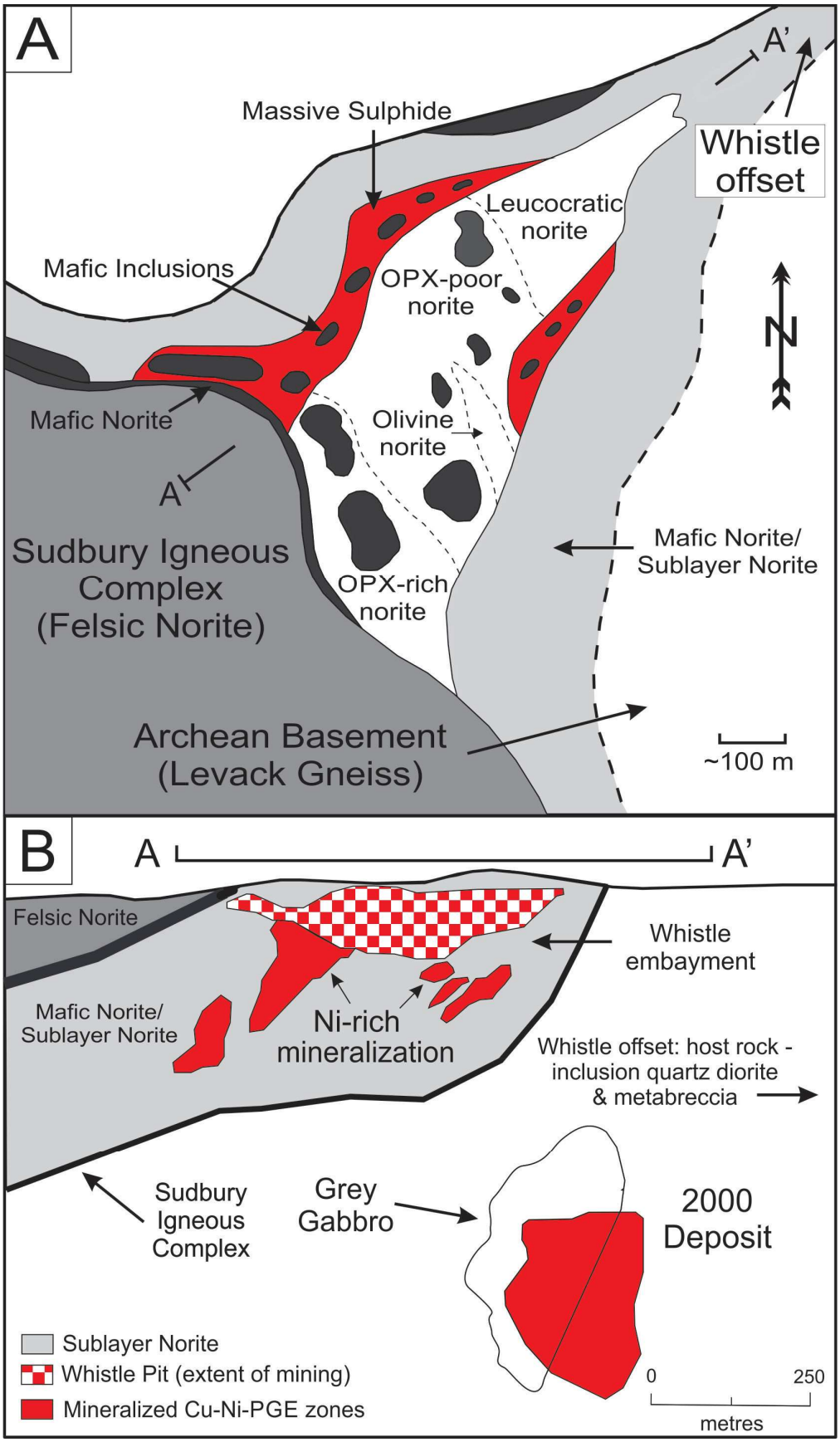
A
A'
Massive Sulphide
Whistle offset
Leucocratic norite
Mafic Inclusions
OPX-poor norite
N
Mafic Norite
Olivine norite
A
Sudbury Igneous Complex (Felsic Norite)
Mafic Norite/ Sublayer Norite
OPX-rich norite
Archean Basement (Levack Gneiss)
~100 m
B
A
A'
Felsic Norite
Whistle embayment
Mafic Norite/ Sublayer Norite
Ni-rich mineralization
Whistle offset: host rock - inclusion quartz diorite & metabreccia
Sudbury Igneous Complex
Grey Gabbro
2000 Deposit
Sublayer Norite
Whistle Pit (extent of mining)
Mineralized Cu-Ni-PGE zones
0
250
metres

Fig. 2: Maps showing the geology of the Whistle embayment area of the SIC (see Fig. 1): a) A schematic map in plan-view of the Whistle embayment showing the relationship between the main rock types of the SIC and those of the offset structure. Also note the presence of the Levack gneiss, which is the basement rock in this area and the contact ore in the Whistle embayment, which had been mined by INCO for nickel ('Whistle Pit"). Map has been modified from Lightfoot et al. (1997b); b) Cross section of Whistle embayment along line A-A' in Figure 2a, which shows the base of the SIC and its contained Ni-rich contact ore, the Whistle embayment structure, and the outline of the grey gabbro fragment that hosts a proportion of the Podolsky deposit. The figure has been modified from Farrow et al. (2005).

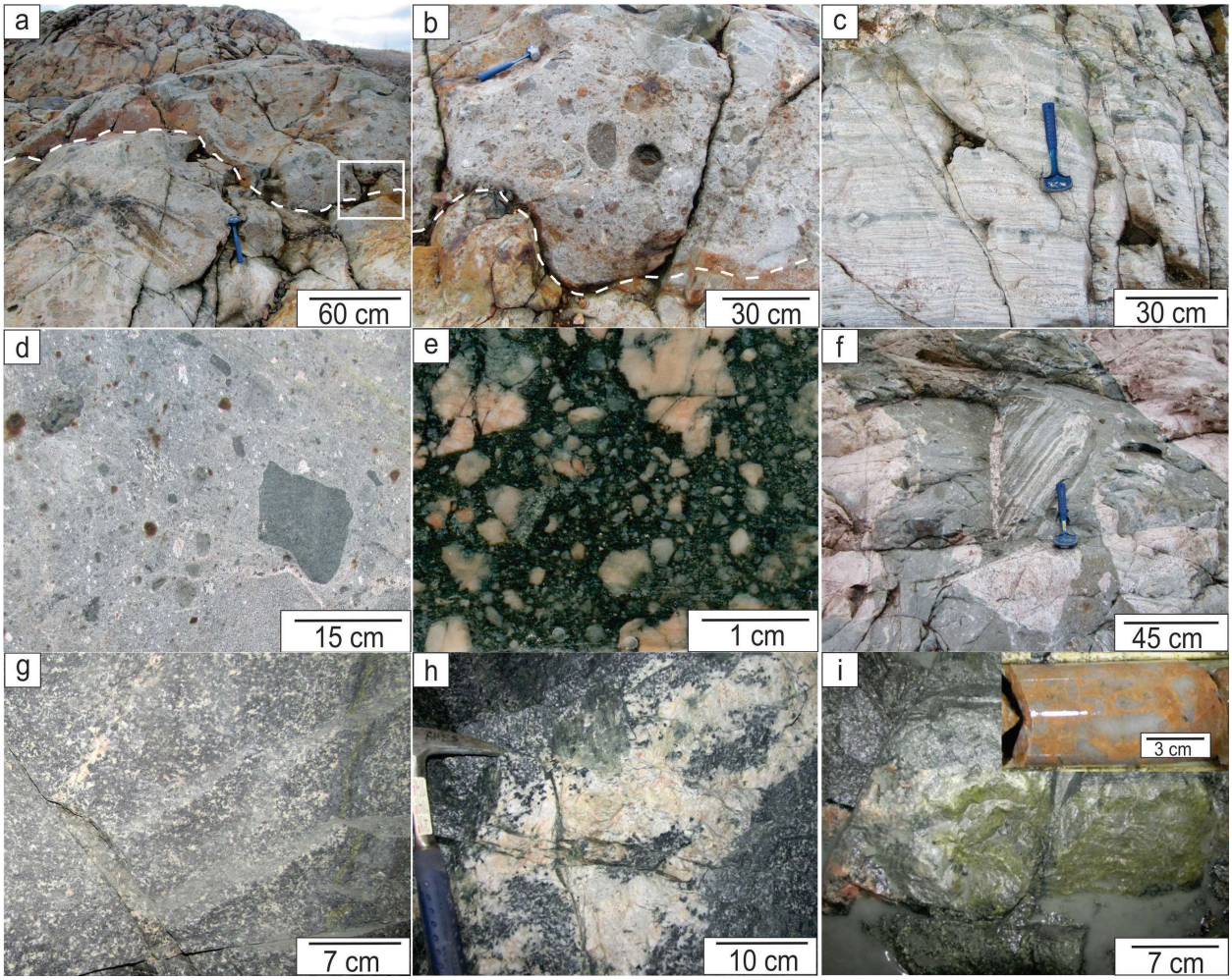

Fig. 3: Outcrop photos showing the regional rock types located around the Podolsky deposit area: a) Contact between the the sublayer norite (upper proportion of dashed line) and the Whistle offset, metabreccia and inclusion quartz diorite (lower proportion of dashed line) in the Whistle embayment area; b) Close up of the contact seen in the previous photo (outlined by the white box); c) Outcrop of Levack gneiss, which is the host rock for the Whistle offset; d) Inclusion quartz diorite (IQD) located in the Whistle offset with fragments of mafic and felsic clasts; e) Typical Sudbury breccia (i.e., pseudotachylite) showing rock fragments (Levack gneiss) in a black aphanitic matrix; f) Metabreccia unit located in the Whistle offset which contains fragments of the Levack gneiss and other granitoid rocks; g) The grey gabbro unit at the 1700 level of the Podolsky mine showing its typical coarse texture and plagioclase and clinopyroxene mineralogy; h) Clot of felsic material (quartz, K-feldspar and plagioclase) hosted by the grey gabbro unit as seen on the 1700 level of the Podolsky deposit; i) A pod of quartz-K-feldspar pegmatite hosted by the grey gabbro unit as seen on the 1700 level of the Podolsky deposit. Note that the fracture surface is coated in epidote. Inset image shows a similar rock intersected in drill core.

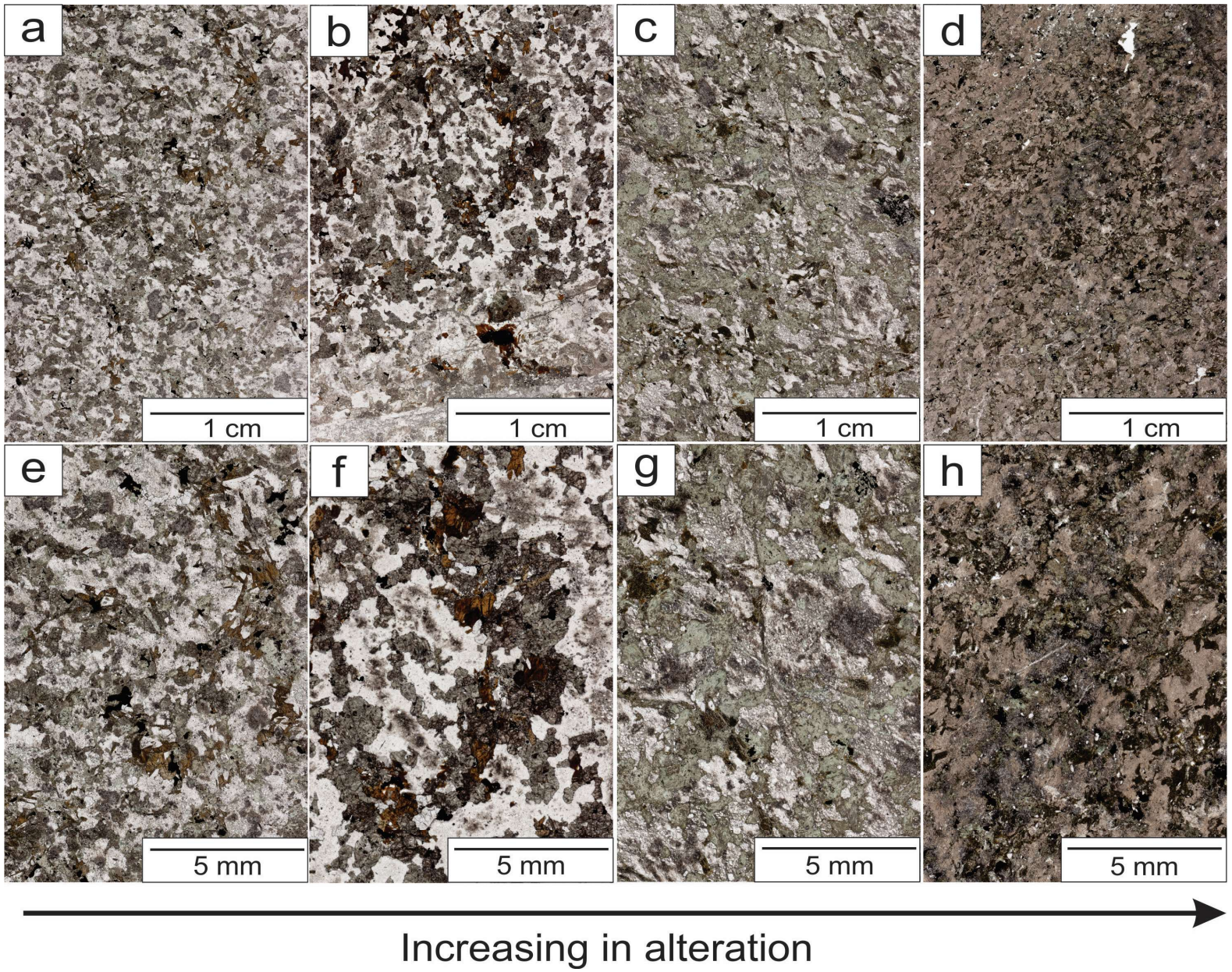
a
1 cm
b
1 cm
c
1 cm
d
1 cm
e
5 mm
f
5 mm
g
5 mm
h
5 mm
Increasing in alteration

Fig. 4: A series of scanned, polished thin, sections of the grey gabbro unit that show the alteration present in this unit in addition to a sample of the Joe Lake gabbroic intrusion. Note all images taken in plane light. a and e) Sample of the Joe Lake intrusion located at the Broken Hammer deposit ~14 km west of the Podolsky deposit. This sample shows well preserved textural intergrowth of plagioclase and clinopyroxene; b and f) Least altered grey gabbro that shows typical plagioclase and clinopyroxene textures; c and g) Sample showing increased alteration; note the lack definition between the mafic and felsic minerals and the increase in the amount of saussertization and sericitation of plagioclase; d and h) Sample of most intense alteration which is located close to a hydrothermal/chalcopyrite vein; note that the sample contains strongly altered felsic and mafic mineral phases.

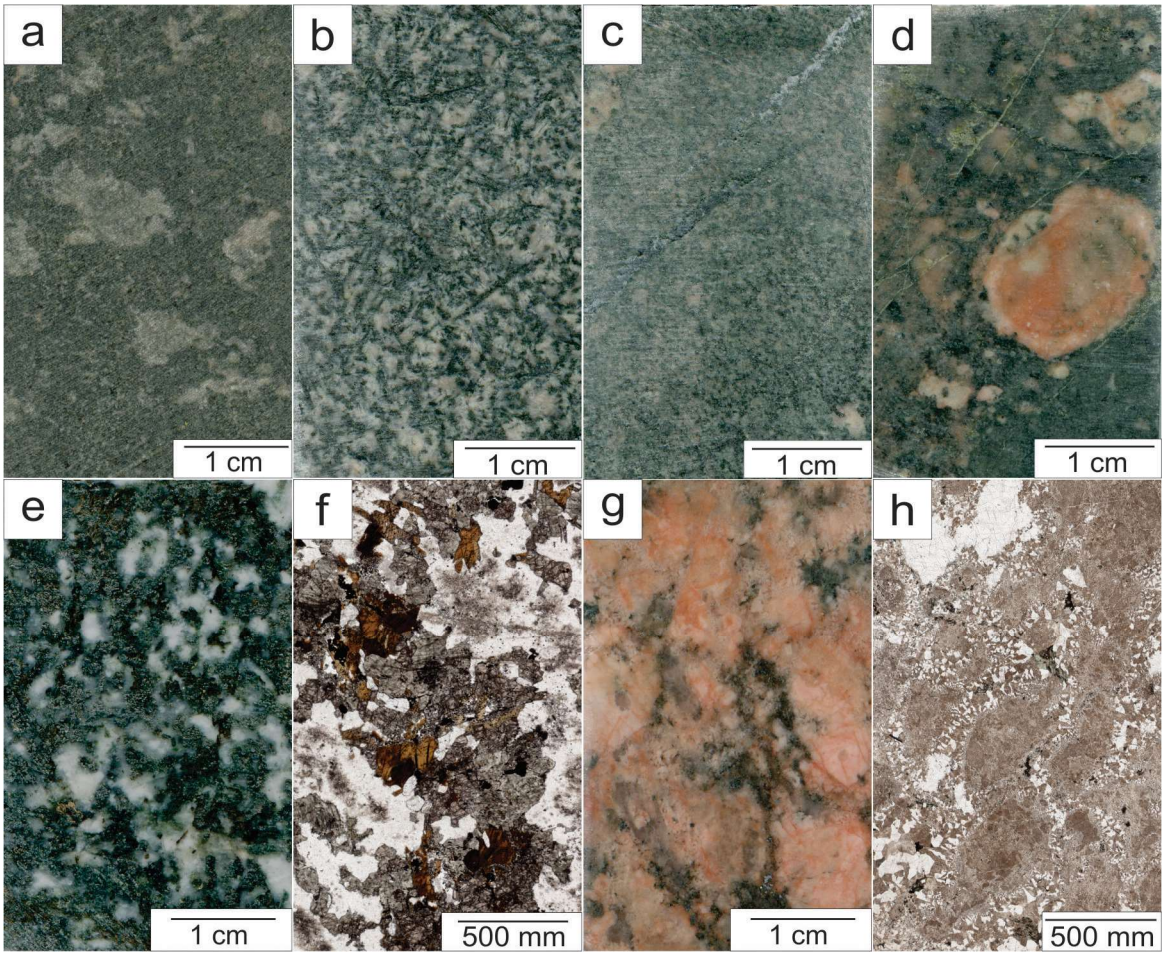

Fig. 5: Examples of the main rock types located at the Podolsky deposit area as seen in cut slabs and thin section: a) Matachewan diabase dyke showing its distinctive glomoroporphyritic texture with plagioclase clots in a very fine-grained matrix; b) Quartz diorite comprised of coarse radial/acicular amphibole grains and plagioclase; c) Inclusion quartz diorite rock with subrounded clasts comprised of granititc, gneissic, and feldspathic fragments; d) Metabreccia rock comprised of fragments of monzogranite and mafic gneiss in an altered and recrystallized matrix; e) Metabreccia unit seen in thin section (plane polarized light), which shows large phenocrysts of subrounded localized granitoid rock fragments hosted by an altered fine-grained matrix; f) Grey gabbro dominated by clinopyroxene and plagioclase; g) Thin section of grey gabbro (plane polarized light) showing the subhedral outlines of the plagioclase and pyroxene and complexity within the mafic clots of original pyroxene; h) Pegmatite rock cutting grey gabbro that is dominated by potassium feldspar; i) Thin section of previous sample of pegmatite showing an abundance of granophyric texture.

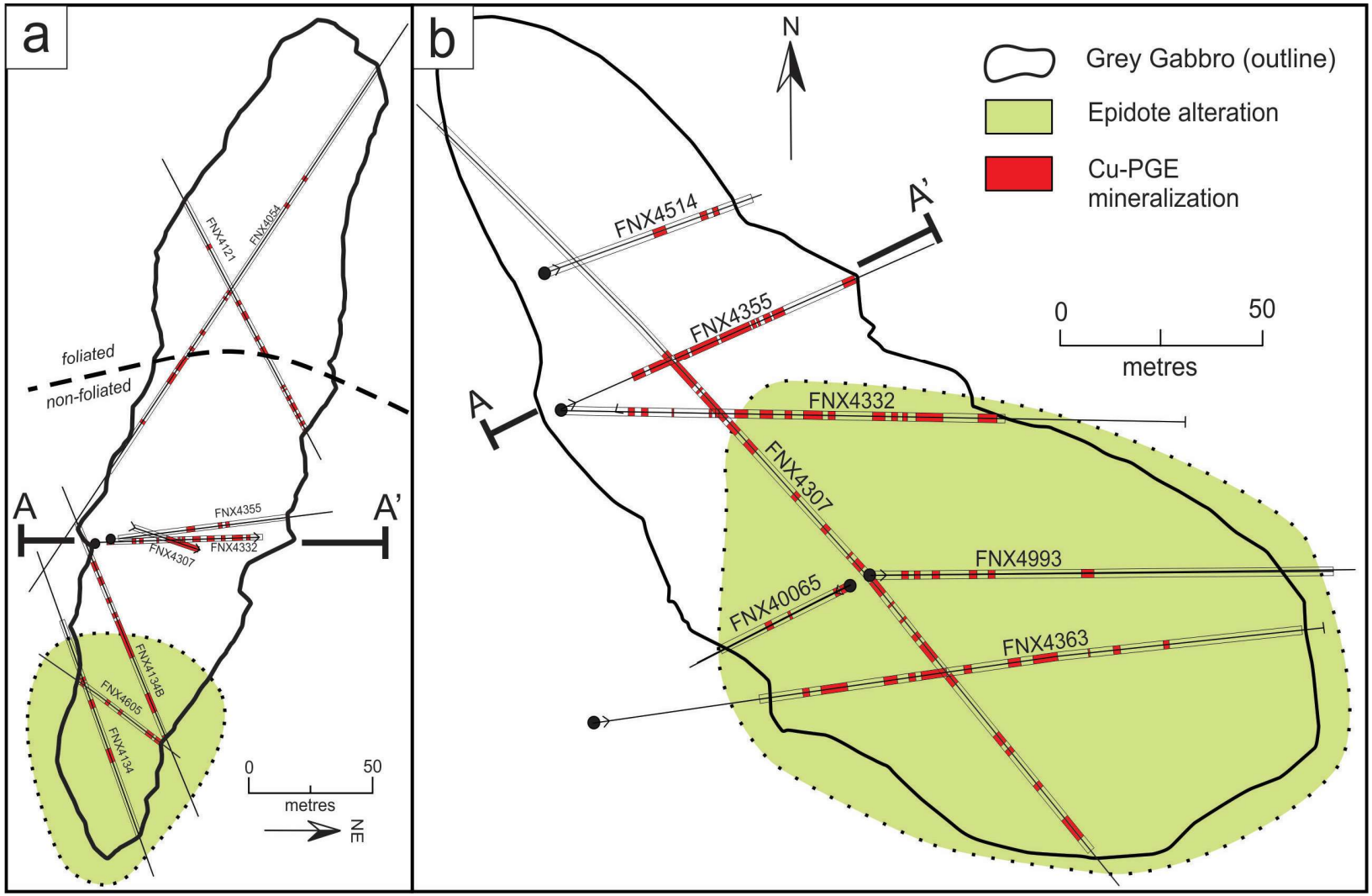

Fig. 6: A summary of information derived from relogging of drill core from the Podolsky deposit which intersected the grey gabbro fragment shown in vertical (a) and plan (b) sections. The maps show the relationship of epidote alteration and foliation in relation to the sharp-walled Cu-(Ni)-PGE mineralisation trend. Note that A and A' are in relation to the vertical and plan view maps on the ~1925 level.

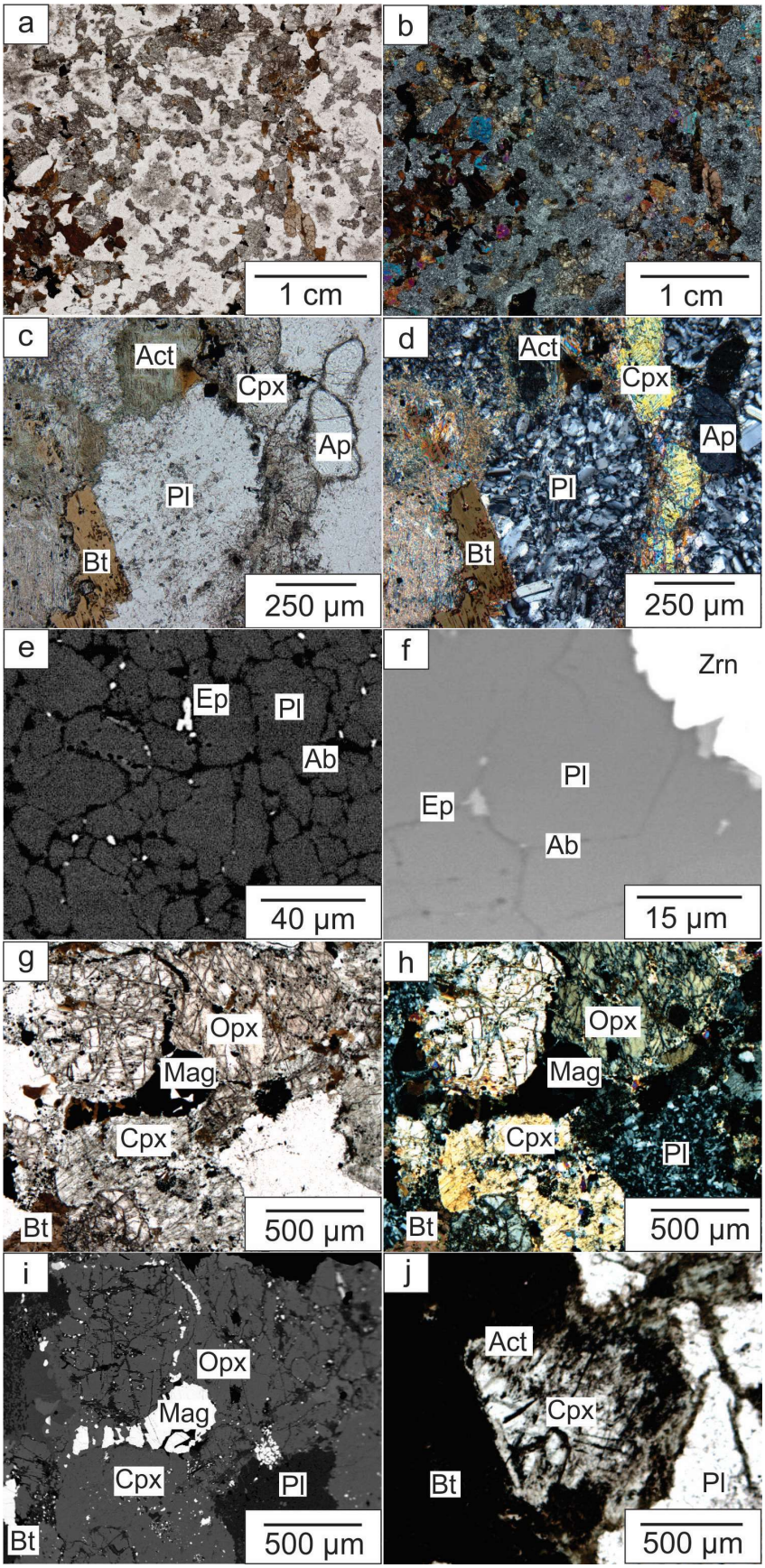
a
1 cm
b
1 cm
c
Act
Cpx
Ap
Pl
Bt
250 µm
d
Act
Cpx
Ap
Pl
Bt
250 µm
e
Ep
Pl
Ab
40 µm
f
Zrn
Pl
Ep
Ab
15 µm
g
Opx
Mag
Cpx
Bt
500 µm
h
Opx
Mag
Cpx
Pl
Bt
500 µm
i
Opx
Mag
Cpx
Pl
Bt
500 µm
j
Act
Cpx
Bt
Pl
500 µm

Fig. 7: Representative images of the grey gabbro unit seen in polished thin sections (PTS) and backscattered electron (BSE) images showing some of the petrographic features: a, b) PTS showing salt- and pepper texture seen in plane polarized light (PPL; a) and in cross polarized light (CPL; b); c) PTS of fresh, unaltered plagioclase in PPL; d) PTS of fresh plagioclase showing a granoblastic "mosaic" texture as seen in CPL; e) BSE image of plagioclase showing a granoblastic "mosaic" texture. Note that epidote, quartz, sericite, and albite become more abundant as plagioclase is altered as seen by the change in the grey scale (i.e., more albitic); f) Closeup BSE of previous image showing plagioclase altering to epidote, quartz, sericite, and albite; g) PTS of fresh unaltered pyroxene in PPL; h) Same as previous image but in CPL; i) BSE image of same area as in images g and h showing the development of fractures in the phases; j) PTS showing the relationship between a remnant clinopyroxene and actinolite. Abbreviations used are as follows: Act: actinolite; Cpx: clinopyroxene; Ap: apatite; Pl: plagioclase; Bt: biotite; Ep: epidote; Ab: albite; Zrn: zircon; Opx: orthopyroxene; Mag: magnetite.

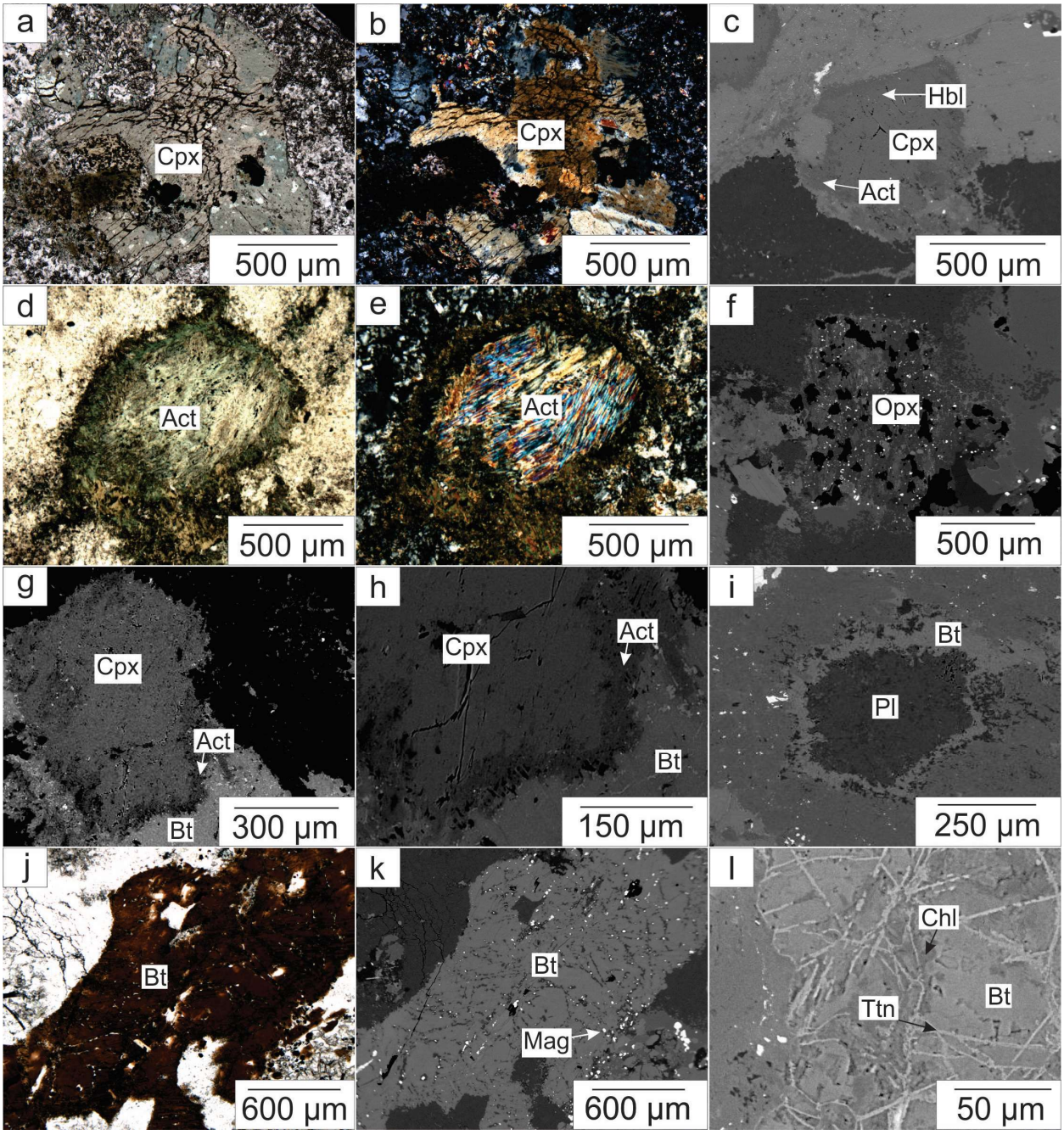
a
Cpx
500 µm
b
Cpx
500 µm
c
Hbl
Cpx
Act
500 µm
d
Act
500 µm
e
Act
500 µm
f
Opx
500 µm
g
Cpx
Act
Bt
300 µm
h
Cpx
Act
Bt
150 µm
i
Bt
Pl
250 µm
j
Bt
600 µm
k
Bt
Mag
600 µm
l
Chl
Ttn
Bt
50 µm

Fig. 8: Examples of mafic mineral clots in the grey gabbro observed in polished thin sections (PTS) and backscattered electron (BSE) images: a) PTS of grey gabbro showing alteration of clinopyroxene to amphibole (plane-polarized light; PPL); b) PTS of grey gabbro showing alteration of clinopyroxene to amphibole (crossed-polarized light; CPL); c) BSE image of clinopyroxene altering to hornblende and then to actinolite; d) PTS of a pseudomorphic actinolite which has completely replaced clinopyroxene (PPL); e) PTS of a pseudomorphic actinolite that has completely replaced clinopyroxene (CPL); f) BSE image of orthopyroxene containing, oxides, hornblende, and actinolite; g) BSE image of clinopyroxene rimmed by actinolite; note contact between biotite and clinopyroxene; h) BSE of previous image showing the relationship of actinolite between clinopyroxene and biotite; i) BSE image of plagioclase rimmed by biotite; j) PTS of primary biotite hosting magnetite, ilmenite and zircon; k) BSE image of biotite hosting, magnetite, ilmenite, and zircon; l) BSE image of a very altered primary biotite that has been partially replaced by titanite, and chlorite. Abbreviations used are as follows: CPX: clinopyroxene; Act: actinolite; Hbl: Hornblende; Opx: orthopyroxene; Bt: biotite; Pl: plagioclase; Mag: magnetite; Chl: chlorite; Ttn: titanite.

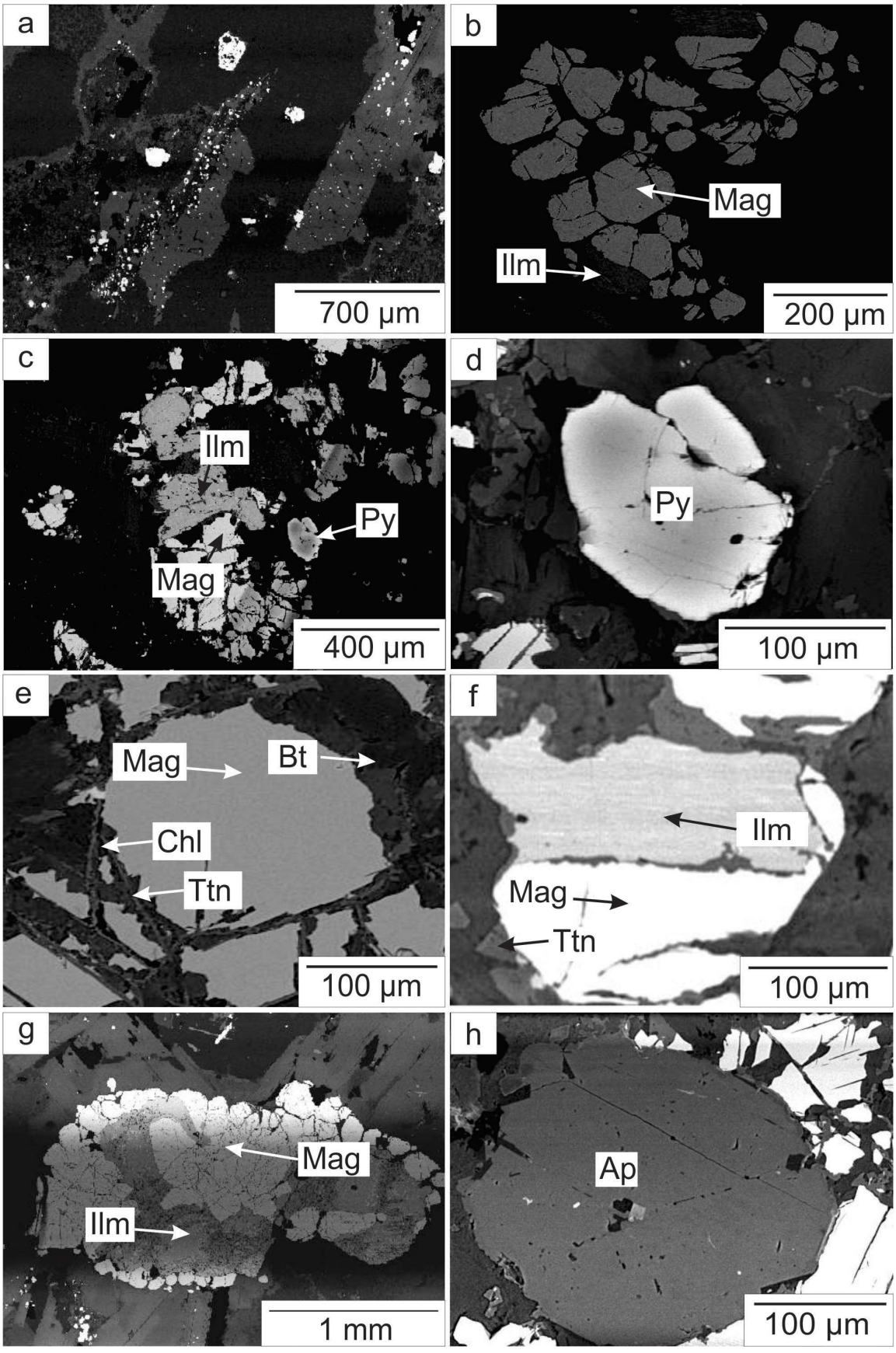
a
700 µm
b
Mag
Ilm
200 µm
c
Ilm
Py
Mag
400 µm
d
Py
100 µm
e
Mag
Bt
Chl
Ttn
100 µm
f
Ilm
Mag
Ttn
100 µm
g
Mag
Ilm
1 mm
h
Ap
100 µm

Fig. 9: Backscattered electron (BSE) images showing features of the grey gabbro. a) BSE image showing concentration of oxide and sulfide phases in the mafic minerals, in particular biotite; b) BSE image of a euhedral cluster of magnetite and a few grains of ilmentite; c) BSE image of magnetite, ilmenite, and a trace pyrite in biotite; d) Close up previous image of subhedral pyrite; e) BSE image showing the complexity of alteration within the biotite; Ilmenite is being replaced by magnetite while biotite is reacting to chlorite and titanite; f) BSE image of ilmenite with magnetite that is rimmed by titanite. The phases are hosted in biotite, which is being replaced by chlorite; g) BSE image showing primary ilmenite (dark grey) being replaced by magnetite (light grey); h) BSE image of euhedral apatite in biotite that is surrounded by magnetite. Abbreviations used are as follows: Ap: apatite; Ilm: ilmenite; Py: pyrite; Mag: magnetite, Ttn: titanite; Chl: Chlorite.

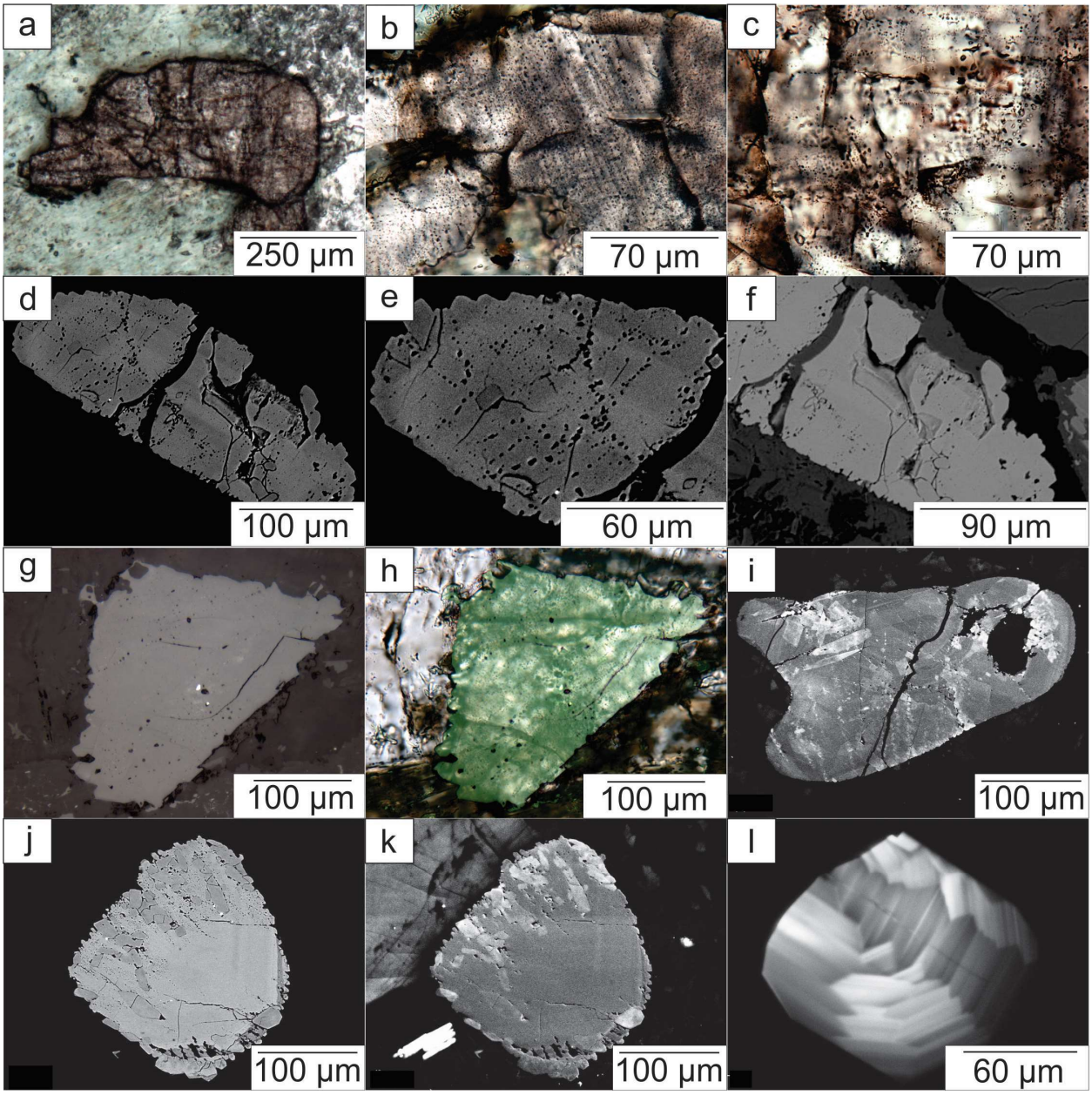
a
250 µm
b
70 µm
c
70 µm
d
100 µm
e
60 µm
f
90 µm
g
100 µm
h
100 µm
i
100 µm
j
100 µm
k
100 µm
l
60 µm

Fig. 10: A series of images of zircons located in the grey gabbro: a) Red-brown anhedral zircon hosted in actinolite; b) A closer image of the previous anhdreal zircon showing linear features which represent PDFs; c) A closer image of the zircon in image (k) showing the PDFs; d) Backscatter image of an anhedral zircon showing PDFs and zoning; e) Close up backscatter image of upper proportion of zircon in previous figure showing zoning and PDFs. Note the edge of the zircon grain is scalloped textured; f) Close up backscatter image of lower half of zircon grain shown in image (d) showing continuance of scalloped texture and zoning; g) Reflected light image of anhedral zircon; note that the rim of zircon appears to be scalloped; h) Combined reflected and plane-polarized light image highlighting zircon rim while allowing interior of mineral to be defined. Note the presence of PDFs and holes in the zircon grain; i) Cathodoluminescence (CL) image of an anhedral zircon that is very altered, as noted by the varied grey to white reflection of the grain and the large hole in the center of the mineral; j) Backscatter image of an anhedral zircon showing zoning and growth of neomorphic zircon along the margin. Note that in the center of grain there is no change of colour indicating uniform zircon; k) CL image of the previous anhedral zircon showing the same pattern at a different grey scale; l) A CL image of a neomorphic type zircon used for age dating. Note the well-developed prismatic growth zones present are classic textures found in zircons from igneous settings.

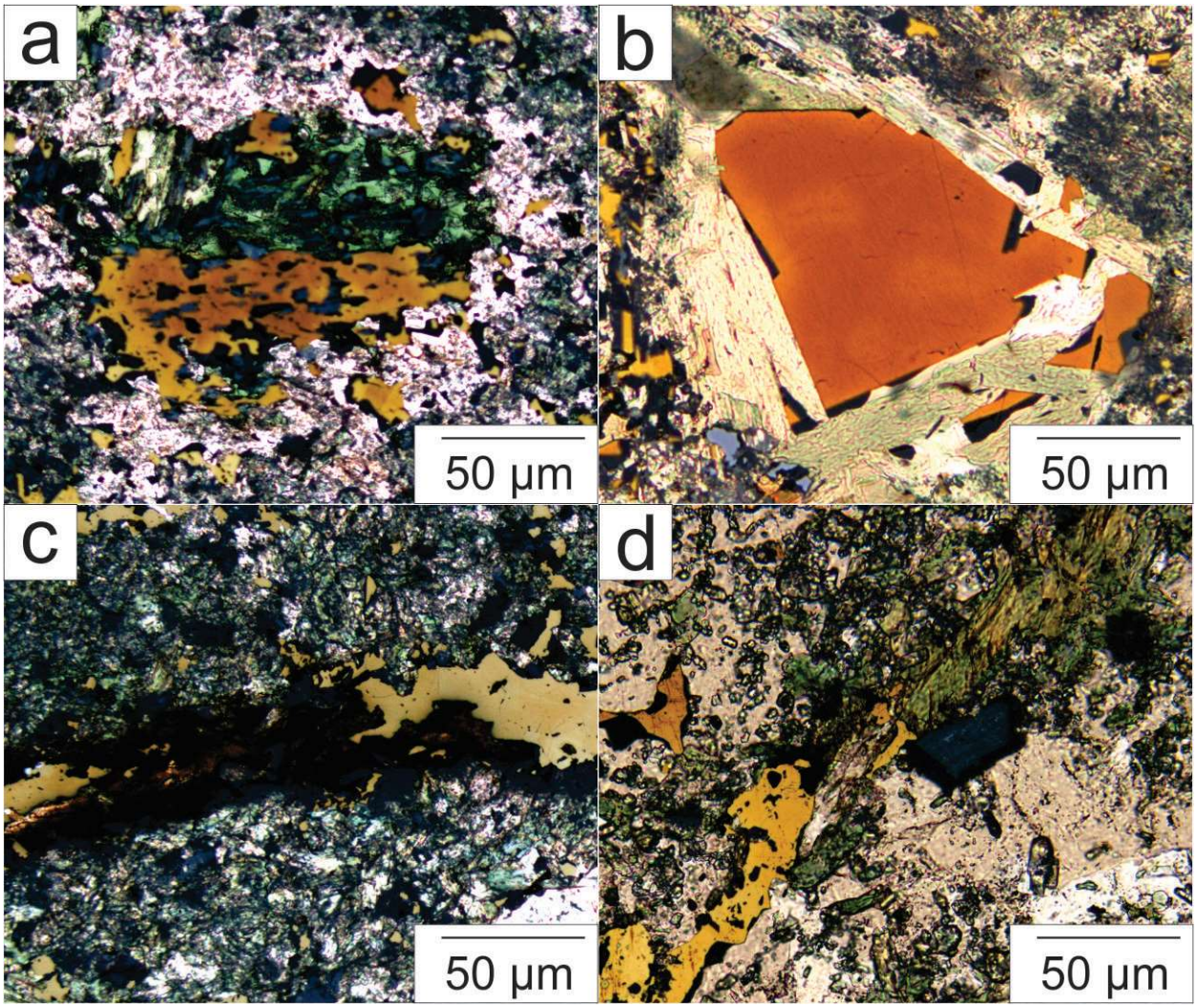

Fig. 11: a) Combined plane polarized and reflected light image of an alteration selvage comprised of chlorite (green) and chalcopyrite (yellow); b) Combined plane polarized and reflected light image of an alteration selvage comprised of actiolite (green) and chalcopyrite (yellow); c) Combined cross polarized and reflected light image of a chlorite-rich micro-vein (brown) hosting chalcopyrite (yellow); d) Combined plane polarized and reflected light image of a chlorite-rich micro-vein (green) hosting chalcopyrite (yellow).

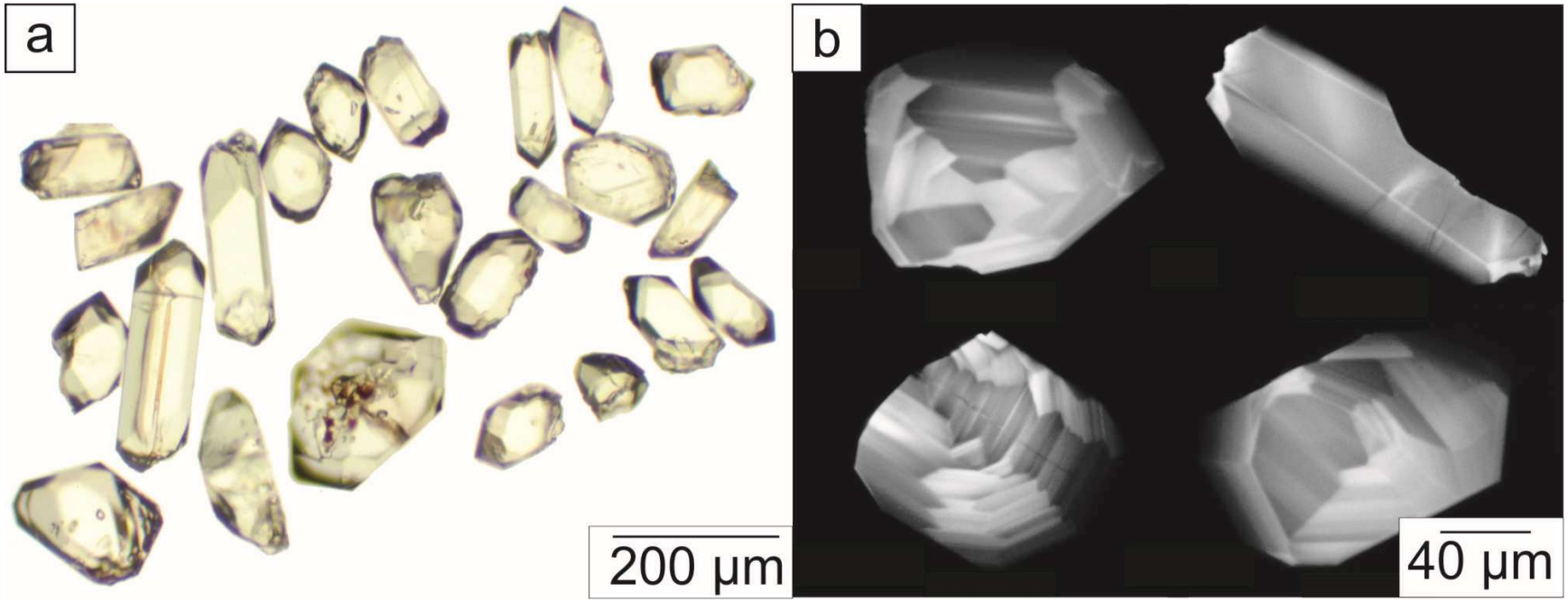

Figure 12: a) Transmitted light photomicrograph of euhedral, prismatic zircon including those analysed by TIMS. Zircons have been annealed for 48h at 1000°C. b) Cathodoluminescence images of euhedral, prismatic zircon.

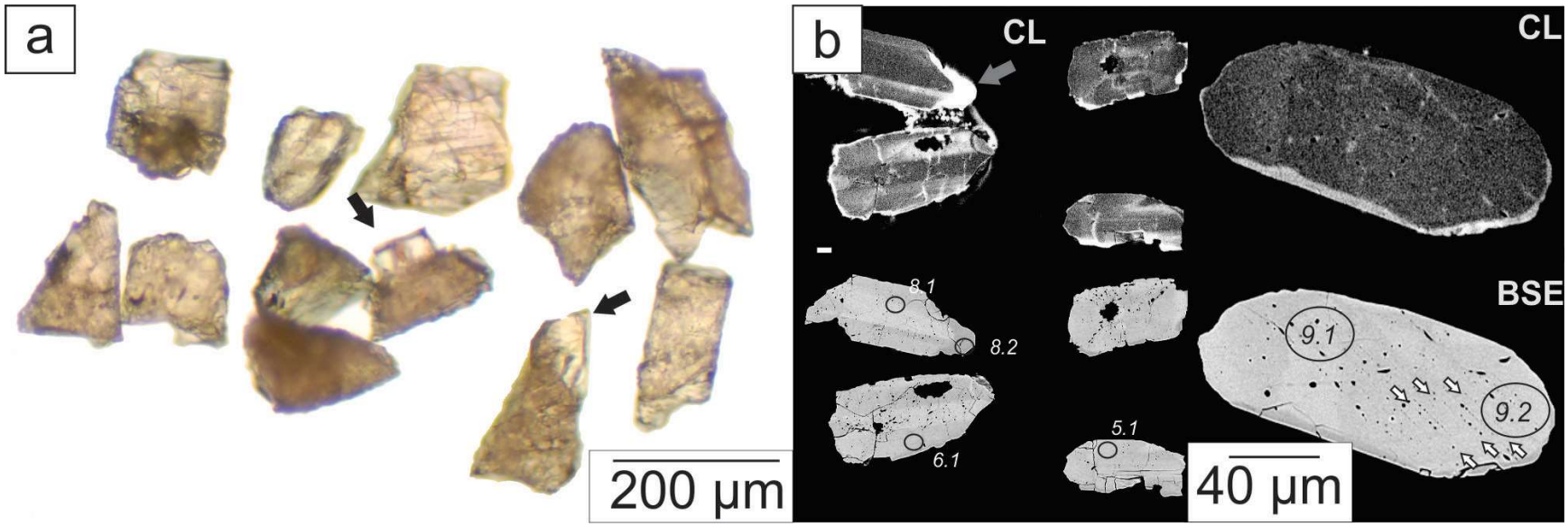

Figure 13: a) Transmitted light photomicrograph of anhedral, shocked zircon selected for SHRIMP analysis. Arrows indicate overgrowths of euhedral zircon. b) Complementary cathodoluminescence/Backscattered electron images of shocked zircon. Grey arrow indicates overgrowth of euhedral zircon. Note enhanced brightness of euhedral zircon relative to anhedral-shocked zircon. b) Contrast is maximized to enhance zoning in shocked zircon; intensity difference obscures zoning in euhdral zircon. Crystallographically oriented features, interpreted as pairs of small, grey arrows indicate impact-related planar deformation features. SHRIMP analysis site shown by black ellipses labelled with corresponding spot name from Table 5.

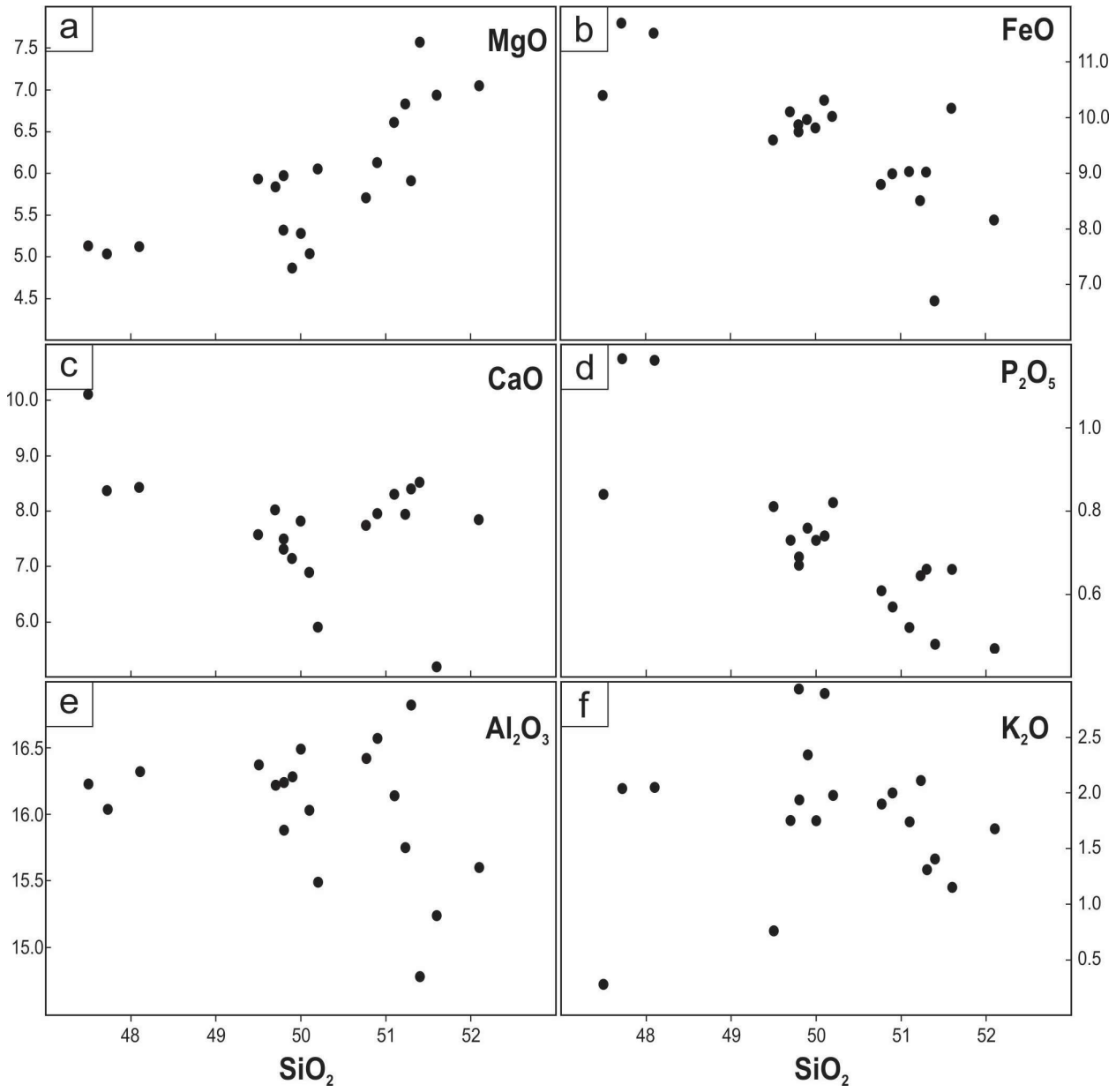

Fig. 14: A series of Harker-type variation diagrams for the whole-rock geochemistry of the grey gabbro. Note that the increase in the data for MgO shows a positive correlation whereas all the other plots show expended trends for the fractionation of a basic melt.

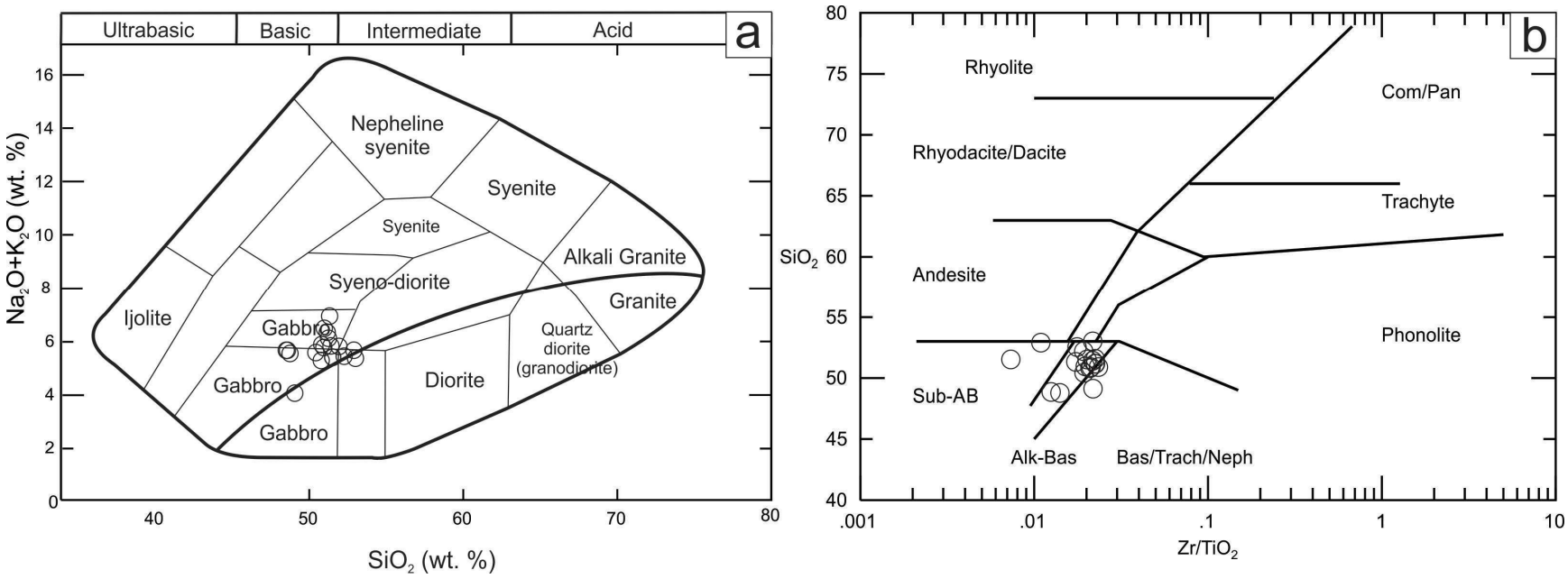

Fig. 15: Classification of the grey gabbro using discrimination diagrams a) Total alkalis versus silica (TAS) discrimination diagram from Cox et al. (1979). Note that the data for the grey gabbro fall into a tight cluster in the alkaline gabbroic section; b) Silica versus Zr/TiO2 diagram of Winchester and Floyd (1977) which show the data plot as a tight cluster in the alkali-basalt field.

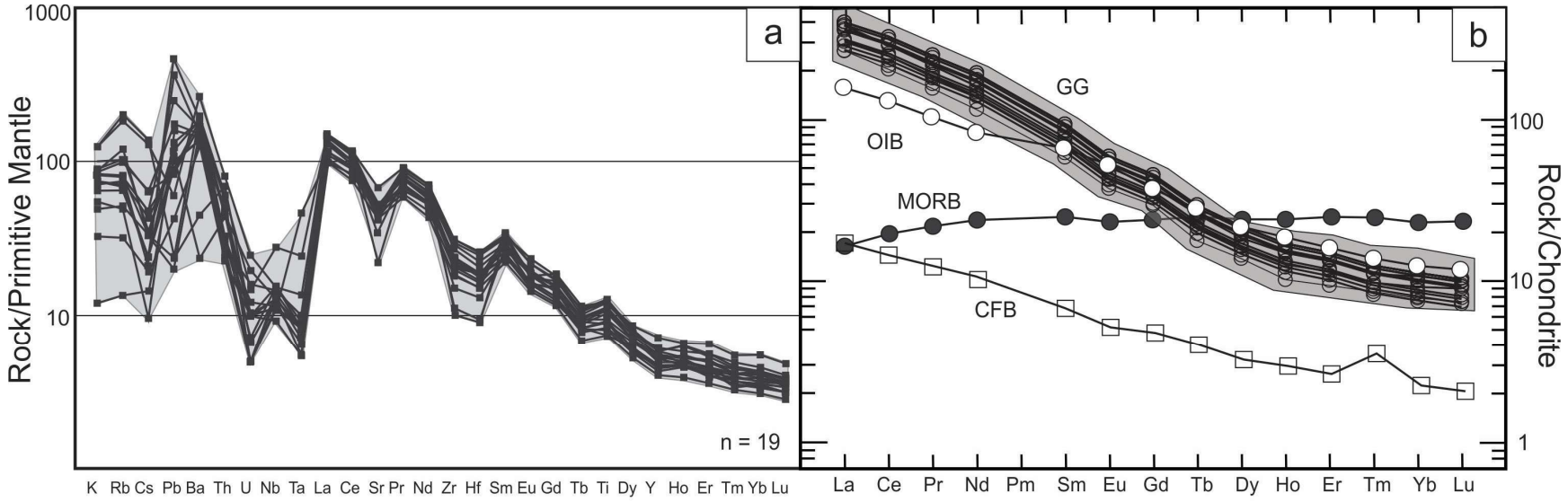

Fig. 16: a) Extended multi-element plot of the grey gabbro normalized to primitive mantle (from McDonough and Sun 1995); b) Primitive mantle normalized REE diagram of the grey gabbro compared to the average geochemistry for ocean island basalt (OIB), mid-ocean ridge basalt (MORB) from Sun and McDonough (1995), and continental flood basalt (CFB) from Lightfoot et al. (1990).

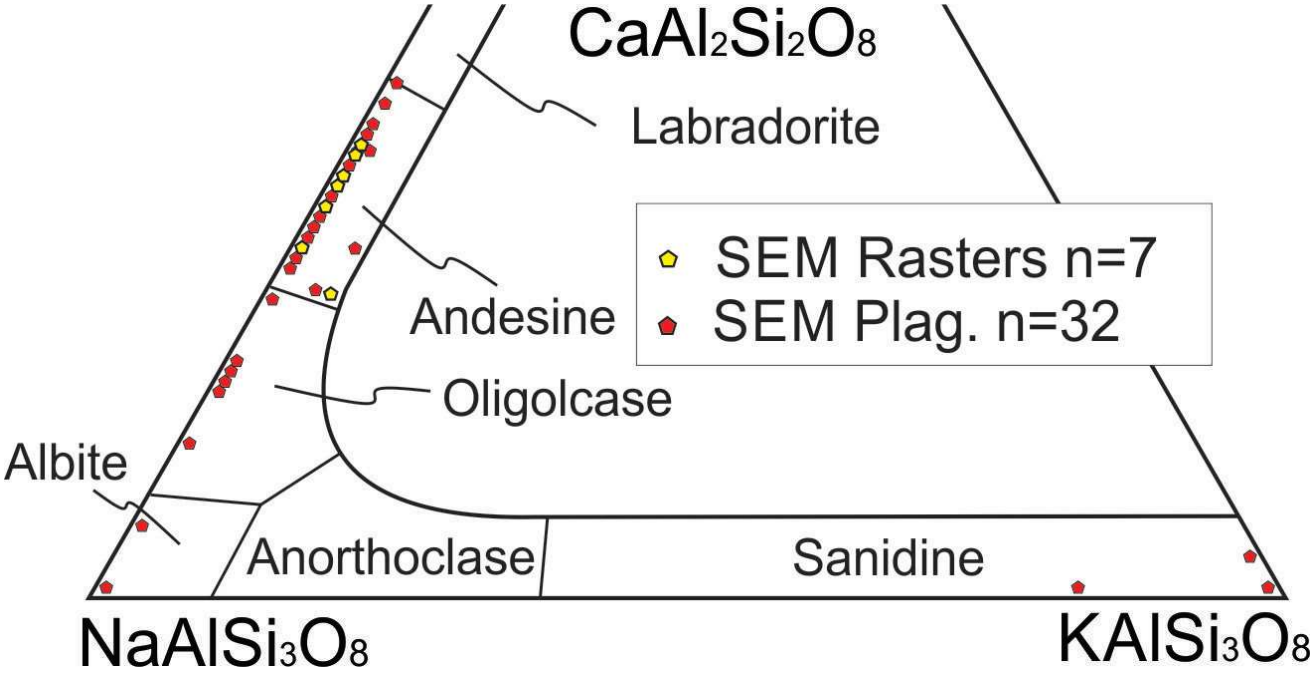

Fig. 17: Plot of the composition of feldspar laths and some alkali feldspar from the grey gabbro; note the dominant plagioclase composition is labradorite (An50). A minor amount of the data, which are for texturally later feldspar grains, plot at An20 and An0, which is discussed in the text. Note the the yellow dots are for raster analysis and red dots are for point analysis.

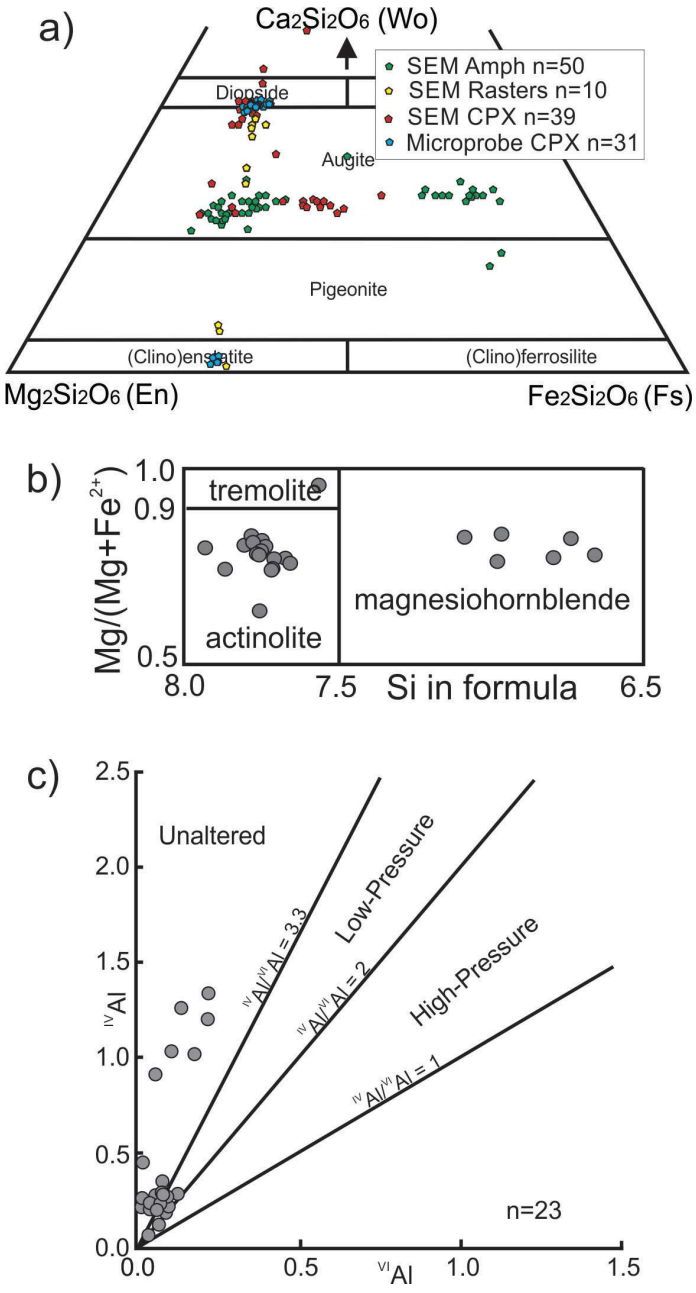

Fig. 18: Plots of chemical data for pyroxene and amphibole in the grey gabbro unit collected using both the SEM-EDS and EMP analytical methods. a) Wo-En-Fs pyroxene ternary diagram with data for mphibole, clinopyroxene, and orthopyroxene plots after Morimoto et al. (1988). Note the raster data for the pyroxene, which is discussed in the text. b) Amphibole data plotted in the amphibole classification diagra of Leake et al. (1997, 2003) and Hawthorne and Oberti (2007); c) Plot of Al^{IV} versus Al^{VI} for amphiboles after Fleet and Barnett (1978) which is used to discriminate pressure of formation.

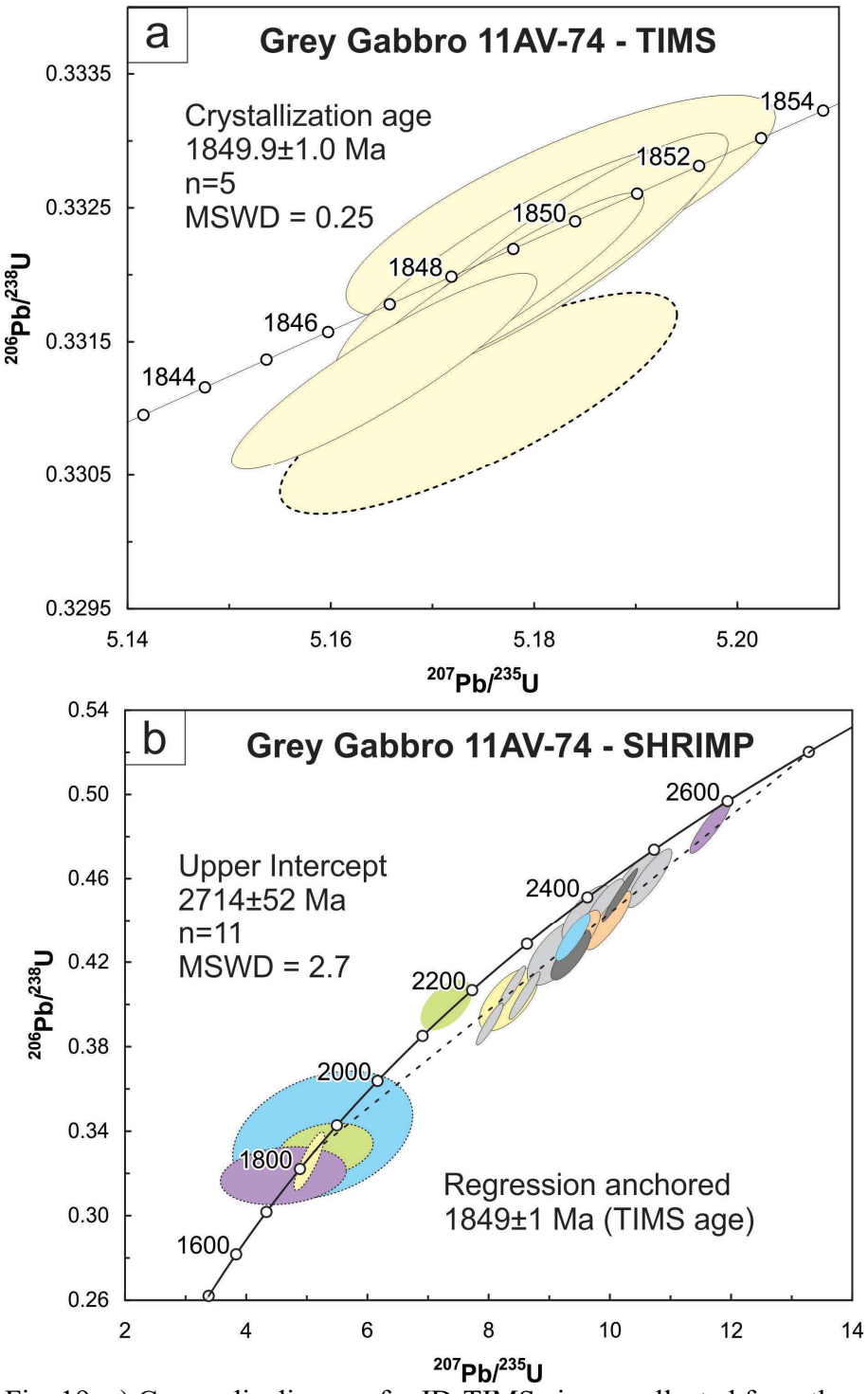

Fig. 19: a) Concordia diagram for ID-TIMS zircon collected from the grey gabbro; the error ellipses are plotted at 2σ. See text for discussion of the data. The analysis excluded from the calculation of the weighted mean is shown by the dashed ellipse; b) Concordia diagram for SHRIMP analysis of zircon from the grey gabbro; note the error ellipses plotted at 2σ. Colours other than light grey show pairs of analyses on a single grain. Analyses of shocked zircon are shown by the solid outline; euhedral overgrowths are shown by dashed outline; and analyses excluded from regression are shown with no outline.

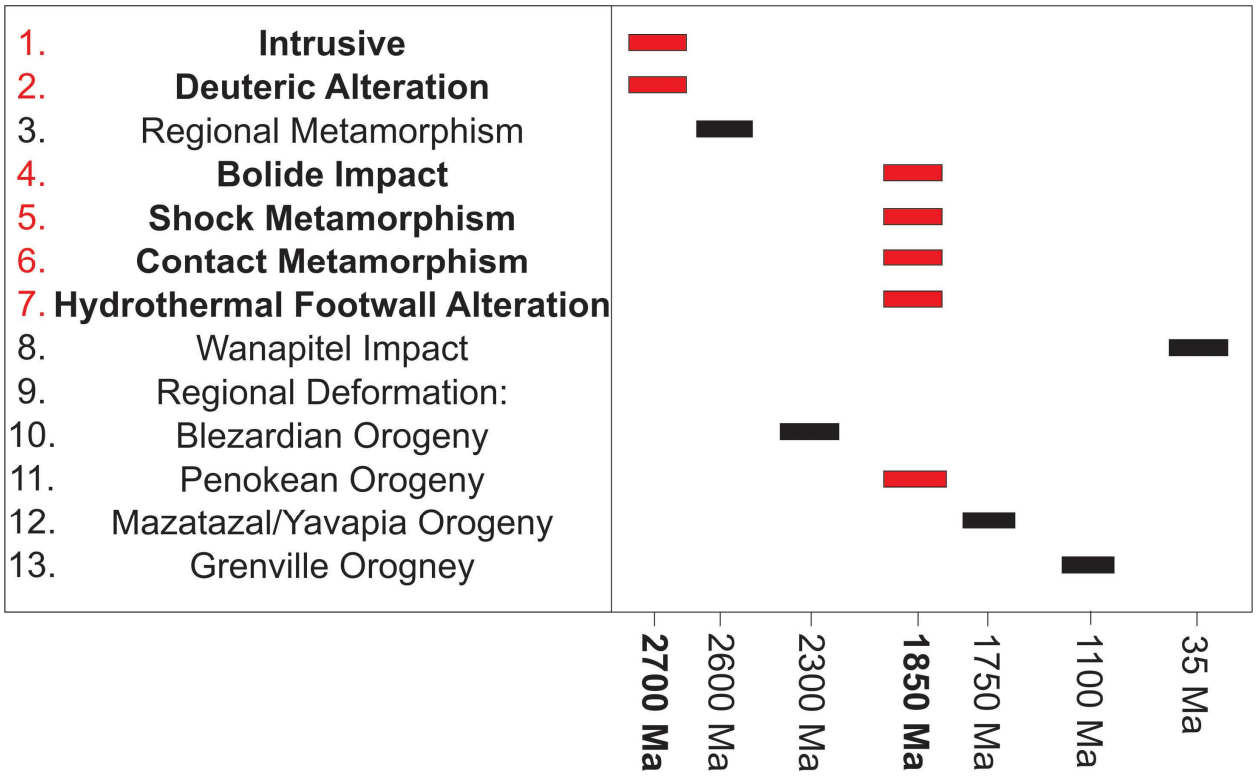

Fig. 20: A summary of the various geological events local to the Sudbury district (modified from Ames et al. 2005). The events highlighted in red are considered to have been responsible for the most significant alteration observed within the grey gabbro unit at the Podolsky deposit.

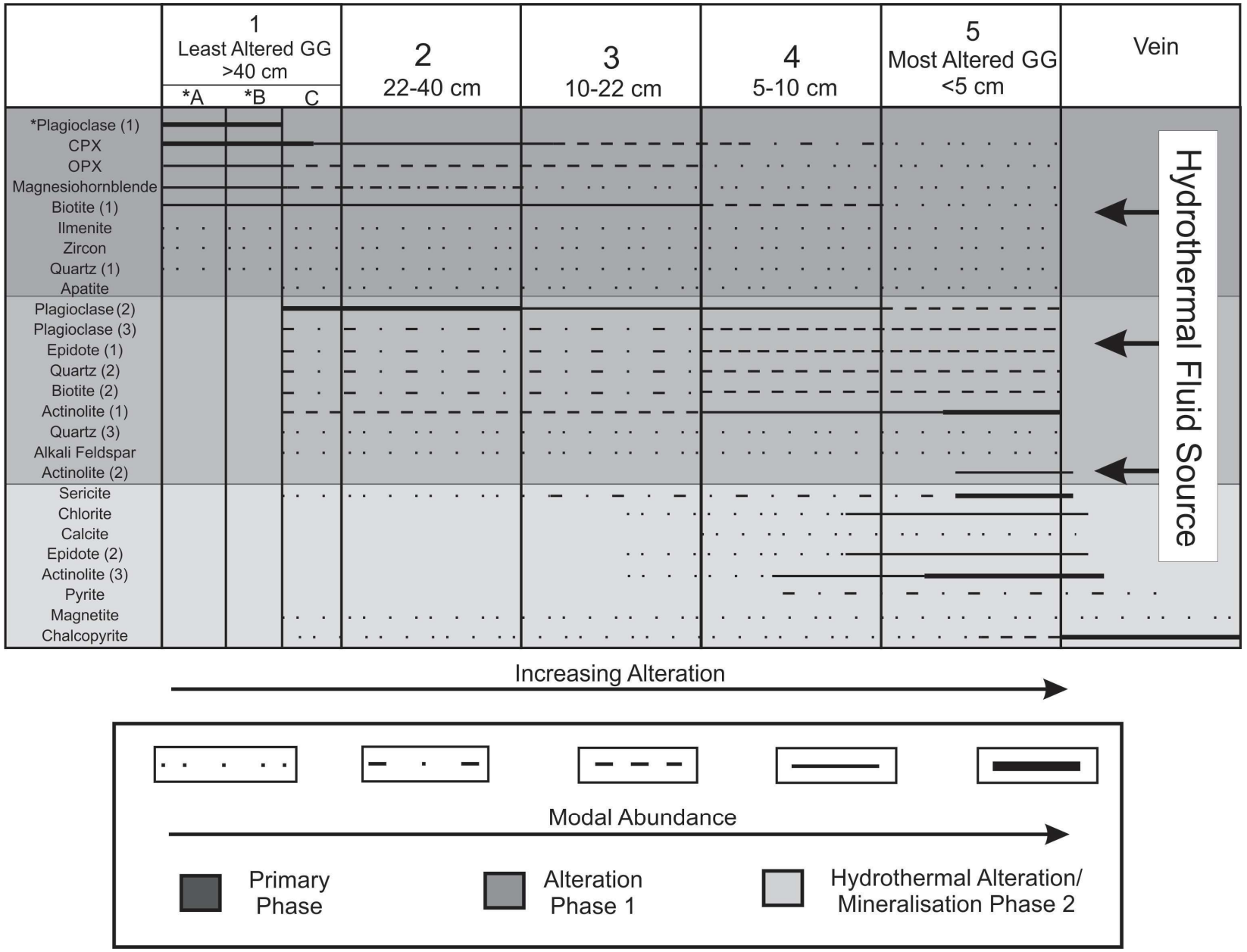
1
Least Altered GG
>40 cm
*A
*B
C
2
22-40 cm
3
10-22 cm
4
5-10 cm
5
Most Altered GG
<5 cm
Vein
*Plagioclase (1)
CPX
OPX
Magnesiohornblende
Biotite (1)
Ilmenite
Zircon
Quartz (1)
Apatite
Plagioclase (2)
Plagioclase (3)
Epidote (1)
Quartz (2)
Biotite (2)
Actinolite (1)
Quartz (3)
Alkali Feldspar
Actinolite (2)
Sericite
Chlorite
Calcite
Epidote (2)
Actinolite (3)
Pyrite
Magnetite
Chalcopyrite
Hydrothermal Fluid Source
Increasing Alteration
Modal Abundance
Primary Phase
Alteration Phase 1
Hydrothermal Alteration/ Mineralisation Phase 2

Fig. 21: A mineral paragenesis which summarizes the history of the grey gabbro along these transects toward the sharp-walled sulphide vein. Along the x-axis is the distance away from the sharp-walled sulphide vein is broken into centimeters, where changes become evident (i.e., point 1: >40 cm; point 2: 40-22 cm; point 3: 22-10 cm; point 4: 10-5 cm; point 5: <5 cm). The y-axis represents the minerals present, broken into three different phases: 1. primary phase; 2. alteration phase; 3. Hydrothermal alteration/mineralisation phase 2 immediately following the cooling of the SIC. Note that the hydrothermal alteration increases towards the sharp-walled sulfide vein. Point 1: is broken into three sections; 1A: Original composition of grey gabbro, not observed; 1B: Grey Gabbro prior to the bolide impact event at ca. 1850, not observed; 1C: Least altered grey gabbro, observed today.

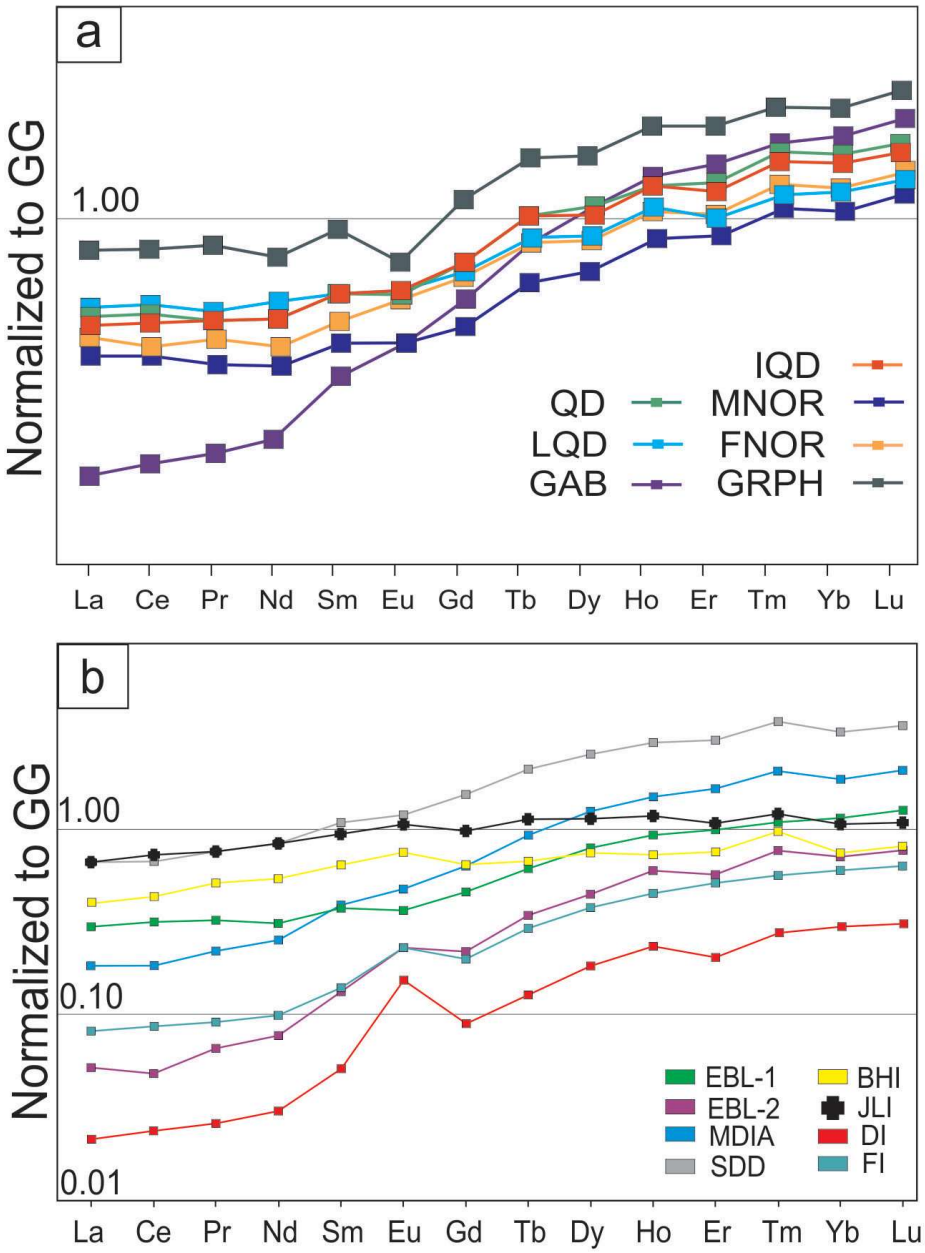

Fig. 22: a) Comparison of the rare earth element ratios for the units of the SIC normalized to grey gabbro. QD: quartz diorite, n = 22; LQD: leucocratic quartz diorite, n = 15; GAB: gabbro, n = 1; IQD: inclusion quartz diorite, n = 17; MNOR: mafic norite, n = 7; FNOR: felsic norite, n = 18; GRPH: granophyre, n = 25; b) Comparison of rare earth element ratios for other rock types around the SIC normalized to grey gabbro. EBL-1: East Bow Lake gabbro, n=1; EBL-2: East Bow Lake gabbronorite, n=1; MDIA: Matachewan diabase dyke, n=1; SDD: Sudbury Diabase Dyke, n=1; BHI: Broken Hammer (Joe Lake) intrusion, n = 1; JLI: Joe Lake intrusion, n=1; DI: Drury intrusion, n=1; FI: Falconbridge intrusion, n=1. Note data is from the following authors: Carter et al. 2009; Lightfoot and Farrow 2002; Lightfoot et al. 1997a; Ames et al. 2014; for more detail see Appendix 1.

Appendices:

wt. %	Method	LLD	LM-P-020 ACME Labs	LM-P-029 ACME Labs	LM-P-041 ACME Labs	11AV-55 GeoLabs	12AV-44 GeoLabs	*03AV-16	*03AV-44	*03AV-50	*03AV-56	*03AV-57	*03AV-60
			Diabase	Diabase	Diabase	Pegmatite	JL Intrusion	QD	QD>IQD	QD-IQD	QD	QD	QD>LQD
SiO_2	WR-XRF	0.10	48.60	49.30	48.30	73.15	51.43	49.3	61.5	61.9	55	61.3	60.9
TiO_2	WR-XRF	0.01	2.09	1.99	2.05	0.21	0.684	1.66	0.66	0.74	1.12	0.71	0.73
Al_2O_3	WR-XRF	0.01	12.42	12.68	12.38	14.10	15.71	15.1	14.2	13.7	14.3	14.4	14.1
Fe_2O_{3T}	WR-XRF	0.01	18.40	18.12	17.79	1.33	2.85	11.7	8.8	8.1	11	8.1	8.2
MgO	WR-XRF	0.01	5.05	5.23	5.07	0.50	6.49	6.25	3.47	3.41	4.33	3.3	3.33
MnO	WR-XRF	0.01	0.26	0.25	0.24	0.02	0.133	0.2	0.12	0.11	0.14	0.12	0.12
CaO	WR-XRF	0.01	8.88	9.36	9.44	0.78	8.67	9.3	4.38	3.32	5.46	3.74	4.19
Na_2O	WR-XRF	0.01	2.31	2.23	2.28	4.00	3.03	2.9	3.3	4.2	3	3.5	3.4
K_2O	WR-XRF	0.01	0.84	0.86	0.64	5.02	1.12	2.35	2.46	1.87	1.98	2.91	2.28
P_2O_5	WR-XRF	0.01	0.28	0.26	0.26	0.02	0.29	0.34	0.15	0.13	0.25	0.15	0.14
LOI			0.93	0.42	1.13	0.74	1.95	0.04	0.1	0.1	0.13	0.11	0.11
Total			99.08	100.24	98.40	99.13	98.81	100.3	100.7	99.8	99	99.9	99
TOT/C	LECO	0.02	0.80	0.60	1.20	0.03	0.04	n.a.	n.a.	n.a.	n.a.	n.a.	n.a.
FeO	S.E.-Assay	0.01	0.19	0.19	0.32	b.d.	5.8	n.a.	n.a.	n.a.	n.a.	n.a.	n.a.
TOT/S	LECO	0.02	0.08	b.d.	b.d.	0.01	0.25	n.a.	n.a.	n.a.	n.a.	n.a.	n.a.
ppb													
Se	ICP-MS	100.00	500.00	200.00	140.00	64.70	b.d.	n.a.	n.a.	n.a.	n.a.	n.a.	n.a.
Au	ICP-MS	0.50	1.20	1.00	32.70	2.00	1	n.a.	n.a.	n.a.	n.a.	n.a.	n.a.
Pd	ICP-MS	10.00	b.d.	b.d.	94.00	b.d.	b.d.	n.a.	n.a.	n.a.	n.a.	n.a.	n.a.
Pt	ICP-MS	2.00	b.d.	b.d.	14.00	b.d.	3.8	n.a.	n.a.	n.a.	n.a.	n.a.	n.a.
Ag	ICP-MS	2.00	1133	588	1741	0.06	0.8	0.2	0.2	0.1	2.8	0.6	0.2
Re	ICP-MS	1	b.d.	b.d.	2	b.d.	b.d.	n.a.	n.a.	n.a.	n.a.	n.a.	n.a.
ppm													
Cu	ICP-MS	0.01	305.20	145.60	3029.00	69.00	30	43	66	44	2720	636	105
Ni	ICP-MS	0.10	34.20	34.50	108.20	218.00	60	146	203	195	350	316	221
Co	ICP-MS	0.20	1.00	1.00	0.60	3.39	41	47	27	25	35	21	30
Cr	ICP-MS	0.50	25.60	35.30	28.20	25.00	70	232	158	153	155	153	147
Zn	ICP-MS	1.00	129.00	66.00	59.00	26.00	b.d.	137	99	88	126	83	83
Sn	ICP-MS	1.00	1	1	2	2.40	b.d.	1.1	1.6	1.9	2.6	4.2	2.3
Ga	ICP-MS	0.50	20.4	18.3	18.1	13.54	19	18	17	15	19	18	18
In	ICP-MS	0.02	b.d.	b.d.	b.d.	0.02	b.d.	0.06	0.17	0.07	0.16	0.09	0.33
Cd	ICP-MS	0.01	1.34	0.5	0.08	0.872	b.d.	b.d.	0.3	b.d.	0.4	0.2	0.3
La	ICP-MS	0.10	19.90	18.40	17.90	61.06	32.5	20	33	29	40	36	35
Ce	ICP-MS	0.10	42.50	40.20	39.30	114.23	71.8	48	68	60	82	73	69
Pr	ICP-MS	0.02	5.54	5.17	5.18	11.83	8.67	6.4	7.5	6.9	10	8.5	8
Nd	ICP-MS	0.30	23.70	22.10	23.30	38.55	36.3	28	27	25	38	31	29
Sm	ICP-MS	0.05	5.76	5.61	5.73	4.99	7.03	6.1	5	4.5	6.8	5.3	5
Eu	ICP-MS	0.02	1.85	1.79	1.79	1.12	1.92	1.7	1.3	1.1	1.7	1.3	1.2
Gd	ICP-MS	0.05	7.40	6.94	7.21	2.39	4.72	5.5	4.2	3.6	5.6	4.1	4
Tb	ICP-MS	0.01	1.20	1.13	1.13	0.22	0.62	0.79	0.6	0.54	0.8	0.59	0.59
Dy	ICP-MS	0.05	7.74	7.02	7.38	0.86	3.06	4.6	3.4	3	4.6	3.4	3.4
Ho	ICP-MS	0.02	1.65	1.58	1.51	0.13	0.52	0.93	0.69	0.62	0.89	0.65	0.66
Er	ICP-MS	0.03	4.97	4.57	4.69	0.29	1.37	2.5	1.8	1.6	2.3	1.7	1.7
Tm	ICP-MS	0.01	0.72	0.66	0.68	0.04	0.188	0.34	0.28	0.25	0.35	0.27	0.27
Yb	ICP-MS	0.05	4.55	4.10	4.30	0.23	1.21	2.2	1.8	1.6	2.2	1.7	1.7
Lu	ICP-MS	0.01	0.68	0.67	0.68	0.04	0.199	0.34	0.28	0.25	0.34	0.27	0.26
Zr	ICP-MS	0.10	163.70	154.10	153.50	228.00	80	165	157	147	185	167	167
Ba	ICP-MS	1.00	311.00	247.00	192.00	1691.50	559	378	697	780	660	993	766
Pb	ICP-MS	0.10	25.00	6.60	3.80	72.60	6	7	7	6	58	40	7
Th	ICP-MS	0.20	3.80	3.30	3.60	26.72	1.07	0.95	8.2	7.5	6.1	8.2	7.9
U	ICP-MS	0.10	0.80	0.80	0.80	1.02	0.21	0.3	1.7	1.4	1.2	1.8	1.6
Bi	ICP-MS	0.02	0.15	0.05	0.96	0.03	b.d.	b.d.	b.d.	b.d.	2.2	0.7	0.3
Rb	ICP-MS	0.10	28.50	27.50	17.90	92.57	24	85	61	33	35	62	44
Sr	ICP-MS	0.50	266.70	153.10	279.10	315.80	792	411	445	383	469	441	455
Nb	ICP-MS	0.10	8.20	7.40	7.80	3.11	3.2	9.4	8.5	8.2	8.8	8.4	8.4
Cs	ICP-MS	0.10	1.00	1.00	0.60	0.13	0.5	3.1	0.72	0.23	0.3	0.31	0.36
Be	ICP-MS	0.10	0.10	0.10	b.d.	0.89	1	0.8	1.5	1.5	1.4	1.4	1.5
Hf	ICP-MS	0.10	4.30	4.00	3.90	5.76	1.9	3.7	4.3	3.5	4.4	4.1	3.8
Y	ICP-MS	0.10	48.10	44.50	43.50	3.32	13.6	26	20	18	26	20	20
Ta	ICP-MS	0.10	0.60	0.50	0.50	0.10	0.14	0.51	0.58	0.53	0.53	0.53	0.55
Sc	ICP-MS	0.10	3.20	2.90	4.30	2.70	21	23	16	15	23	15	15
V	ICP-MS	8.00	452.00	435.00	442.00	16.80	155	225	125	114	188	118	120
Mo	ICP-MS	0.01	0.54	0.47	0.5	0.85	b.d.	1.2	26	32	27	21	25
As	ICP-MS	0.1	4.5	1.3	0.2	b.d.	b.d.	3.7	4.3	3.5	4.4	4.1	3.8
Sb	ICP-MS	0.02	0.06	0.04	0.03	b.d.	b.d.	b.d.	0.3	0.4	0.6	0.5	0.4
Te	ICP-MS	0.02	b.d.	b.d.	0.38	0.01	b.d.	b.d.	b.d.	b.d.	0.7	0.3	b.d.

Appendix 1: Goechemiscal dataset of rock types located within the Podolksy deposit and geochemical data collected from literature located within and around the Sudbury Structure. Major and trace element analyses (XRF and ICP-MS) characterizing the grey gabbro unit. Apprviations used are as follows: n.a. = not analysed; b.d. = below detection; Mg# = MgO/(MgO+FeO); ppm = parts per million; ppb = parts per billion; wt% = weight percent; * Carter et al. 2009; ** = Lightfoot and Farrow 2002; [3] = Lightfoot et al. 1997a; [φ] = Ames et al. 2014; WR-XRF = whole rock x-ray flouresence; ICP-MS = Inductively coupled plasma mass spectrometry; LLD = lower limits of detection; QD = Quartz diorite; LQD = Leucocratic quartz diorite; IQD = Inclusion quartz diorite;; FWBX = Footwall breccia; JL Intrusion = Joe Lake Intrusion.

wt. %	Method	LLD	*03AV-61	*03AV-62	*03AV-80	*03AV-28	*03AV-24	*03AV-17	*03AV-13	*03AV-45	*03AV-46	*03AV-72	*03AV-73
			QD	QD	*QD>IQD	LQD	LQD	LQD	LQD	LQD	LQD	LQD	LQD
SiO_2	WR-XRF	0.10	61.9	60.2	61.4	61	60	57.8	59	61.9	60.5	59.5	60.5
TiO_2	WR-XRF	0.01	0.76	0.88	0.77	0.8	0.74	0.98	0.8	0.73	0.7	0.65	0.95
Al_2O_3	WR-XRF	0.01	14.4	14.8	14.2	14	13.8	14	13.9	13.9	15	14.1	14.7
Fe_2O_{3T}	WR-XRF	0.01	7.5	8.3	7	7.4	8.3	8.8	7.3	9.4	7.2	9.6	7.9
MgO	WR-XRF	0.01	3.58	3.3	3.34	3.94	4.59	4.47	4.15	3.37	3.39	3.49	2.75
MnO	WR-XRF	0.01	0.07	0.1	0.1	0.11	0.15	0.15	0.13	0.06	0.1	0.08	0.1
CaO	WR-XRF	0.01	1.69	4.16	4.5	4.62	5.13	5.83	7.06	1.31	4.22	2.78	4.44
Na_2O	WR-XRF	0.01	3.6	5	4.1	3.7	3.3	3.4	5.7	2.9	4.4	3	4.4
K_2O	WR-XRF	0.01	2.34	0.5	2.02	1.67	2.13	1.7	0.6	2.78	1.88	3.14	1.14
P_2O_5	WR-XRF	0.01	0.16	0.22	0.14	0.15	0.2	0.27	0.19	0.14	0.15	0.13	0.21
LOI			0.3	0.28	0.11	0.16	0.16	0.15	0.06	0.23	0.12	0.25	0.1
Total			100.2	100.7	99.1	99.4	100.2	99.3	99.8	100.6	99.9	100.7	98.7
TOT/C	LECO	0.02	n.a.	n.a.	n.a.	n.a.	n.a.	n.a.	n.a.	n.a.	n.a.	n.a.	n.a.
FeO	S.E.-Assay	0.01	n.a.	n.a.	n.a.	n.a.	n.a.	n.a.	n.a.	n.a.	n.a.	n.a.	n.a.
TOT/S	LECO	0.02	n.a.	n.a.	n.a.	n.a.	n.a.	n.a.	n.a.	n.a.	n.a.	n.a.	n.a.
ppb													
Se	ICP-MS	100.00	n.a.	n.a.	n.a.	n.a.	n.a.	n.a.	n.a.	n.a.	n.a.	n.a.	n.a.
Au	ICP-MS	0.50	n.a.	n.a.	n.a.	n.a.	n.a.	n.a.	n.a.	n.a.	n.a.	n.a.	n.a.
Pd	ICP-MS	10.00	n.a.	n.a.	n.a.	n.a.	n.a.	n.a.	n.a.	n.a.	n.a.	n.a.	n.a.
Pt	ICP-MS	2.00	n.a.	n.a.	n.a.	n.a.	n.a.	n.a.	n.a.	n.a.	n.a.	n.a.	n.a.
Ag	ICP-MS	2.00	0.2	0.1	0.2	b.d.	0.2	0.2	0.2	0.2	b.d.	0.1	b.d.
Re	ICP-MS	1	n.a.	n.a.	n.a.	n.a.	n.a.	n.a.	n.a.	n.a.	n.a.	n.a.	n.a.
ppm													
Cu	ICP-MS	0.01	365	75	50	67	446	190	43	61	60	741	82
Ni	ICP-MS	0.10	143	1340	104	54	81	222	103	228	124	287	129
Co	ICP-MS	0.20	22	21	21	29	30	27	24	25	23	23	20
Cr	ICP-MS	0.50	147	138	150	176	191	155	187	177	144	185	64
Zn	ICP-MS	1.00	80	110	92	123	108	118	76	102	95	85	70
Sn	ICP-MS	1.00	1.6	2.5	1.6	1.7	1.6	1.7	2.5	1.8	1.8	1.9	1.5
Ga	ICP-MS	0.50	18	19	18	18	18	18	18	17	18	18	19
In	ICP-MS	0.02	0.06	0.09	0.08	b.d.	0.07	0.05	0.09	0.08	b.d.	0.06	0.07
Cd	ICP-MS	0.01	b.d.	0.4	0.4	b.d.	b.d.	0.3	b.d.	b.d.	b.d.	0.2	b.d.
La	ICP-MS	0.10	34	35	35	36	41	41	49	29	23	39	39
Ce	ICP-MS	0.10	68	72	70	74	83	86	92	58	50	77	77
Pr	ICP-MS	0.02	7.8	8.7	7.9	8.2	9.3	10	10	6.6	5.8	8.8	8.9
Nd	ICP-MS	0.30	28	33	29	30	35	39	37	25	21	32	32
Sm	ICP-MS	0.05	4.5	5.6	5.2	5.6	6.3	7.6	6.5	4.4	3.6	5.7	5.1
Eu	ICP-MS	0.02	0.98	1.6	1.3	1.2	1.2	1.5	1.7	1.1	1.2	1.6	1.5
Gd	ICP-MS	0.05	3.6	4.6	4.1	4.4	5	6	5	3.6	3	4.6	3.6
Tb	ICP-MS	0.01	0.5	0.64	0.59	0.64	0.74	0.82	0.72	0.52	0.43	0.63	0.48
Dy	ICP-MS	0.05	2.9	3.6	3.3	3.7	4.2	4.4	4.2	3	2.5	3.6	2.5
Ho	ICP-MS	0.02	0.54	0.69	0.69	0.74	0.83	0.88	0.82	0.61	0.49	0.67	0.49
Er	ICP-MS	0.03	1.4	1.8	1.8	2.1	2.3	2.4	2.3	1.5	1.3	1.7	1.2
Tm	ICP-MS	0.01	0.22	0.27	0.28	0.3	0.32	0.35	0.33	0.24	0.2	0.27	0.17
Yb	ICP-MS	0.05	1.5	1.7	1.8	2	2.2	2.2	2.1	1.6	1.3	1.7	1
Lu	ICP-MS	0.01	0.22	0.25	0.28	0.33	0.35	0.35	0.33	0.24	0.19	0.26	0.17
Zr	ICP-MS	0.10	165	158	161	222	234	247	223	157	77	173	170
Ba	ICP-MS	1.00	749	137	701	700	722	641	169	813	619	937	567
Pb	ICP-MS	0.10	6	23	8	11	7	16	7	6	7	7	6
Th	ICP-MS	0.20	8.5	6	8.5	10	11	7.6	10	7.7	2.1	9.2	3.4
U	ICP-MS	0.10	1.7	0.9	1.7	2	2.3	1.4	1.9	1.9	0.62	2.1	0.34
Bi	ICP-MS	0.02	b.d.	0.3	-0.2	-0.2	-0.2	0.2	-0.2	-0.2	0.3	-0.2	-0.2
Rb	ICP-MS	0.10	53	11	38	23	40	20	8.3	62	38	91	32
Sr	ICP-MS	0.50	310	448	412	298	4141	372	568	224	414	358	611
Nb	ICP-MS	0.10	8.2	7.4	8.4	9.9	9.7	8.9	9.6	8.3	8.9	8.6	5.3
Cs	ICP-MS	0.10	0.44	0.19	0.16	0.25	0.2	0.21	0.07	0.56	0.25	1	0.22
Be	ICP-MS	0.10	1.9	0.8	1.2	1.4	1.3	1.3	1.1	1.4	1.5	1.6	1.4
Hf	ICP-MS	0.10	4.1	3.7	3.9	5.5	5.9	6.5	5.4	4.3	1.9	4.1	3.1
Y	ICP-MS	0.10	17	21	20	23	25	26	24	17	15	20	14
Ta	ICP-MS	0.10	0.52	0.42	0.53	0.6	0.62	0.5	0.61	0.58	0.76	0.55	0.23
Sc	ICP-MS	0.10	16	17	16	18	19	21	17	16	14	17	14
V	ICP-MS	8.00	121	140	123	140	149	167	142	125	116	133	136
Mo	ICP-MS	0.01	16	14	18	1.3	0.8	1.3	0.4	48	22	51	24
As	ICP-MS	0.1	4.1	3.7	3.9	5.5	5.9	6.5	5.4	4.3	1.9	4.1	3.1
Sb	ICP-MS	0.02	0.4	0.6	0.3	0.3	b.d.	b.d.	b.d.	0.5	b.d.	0.4	0.3
Te	ICP-MS	0.02	b.d.	b.d.	b.d.	b.d.	b.d.	b.d.	b.d.	b.d.	b.d.	b.d.	b.d.

Appendix 1 (cont.): Goechemiscal dataset of rock types located within the Podolksy deposit and geochemical data collected from literature located within and around the Sudbury Structure. Major and trace element analyses (XRF and ICP-MS) characterizing the grey gabbro unit. Apprviations used are as follows: n.a. = not analysed; b.d. = below detection; Mg# = MgO/(MgO+FeO); ppm = parts per million; ppb = parts per billion; wt% = weight percent; * Carter et al. 2009; ** = Lightfoot and Farrow 2002; [3] = Lightfoot et al. 1997a; [φ] = Ames et al. 2014; WR-XRF = whole rock x-ray flouresence; ICP-MS = Inductively coupled plasma mass spectrometry; LLD = lower limits of detection; QD = Quartz diorite; LQD = Leucocratic quartz diorite; IQD = Inclusion quartz diorite;; FWBX = Footwall breccia; JL Intrusion = Joe Lake Intrusion.

wt. %	Method	LLD	*03AV-74	*03AV-75	*03AV-76	*03AV-77	*03AV-78	*03AV-79	*03AV-47	*03AV-55	*03AV-81	*03AV-82	*03AV-83
			LQD	LQD	LQD/QD	LIQD	LIQD	LIQD>LQD	IQD	IQD	IQD-QD	IQD-(FWBX)	IQD
SiO_2	WR-XRF	0.10	58.9	60.7	60.3	58.6	60.7	59.9	58.9	55.2	56.8	54.8	50.5
TiO_2	WR-XRF	0.01	0.86	0.73	0.74	0.78	0.73	0.77	0.93	1.13	0.88	1.05	1.07
Al_2O_3	WR-XRF	0.01	17.2	14.5	14.2	13.9	14.3	14.4	13.7	14.4	15.1	16.9	13.4
Fe_2O_{3T}	WR-XRF	0.01	6.1	8.2	9	9.9	8	8.6	9	10.2	10.6	8.6	14.5
MgO	WR-XRF	0.01	1.9	3.63	3.16	4.32	3.45	3.71	3.42	4.08	4.18	4.2	5.64
MnO	WR-XRF	0.01	0.06	0.11	0.11	0.11	0.1	0.11	0.1	0.14	0.15	0.11	0.18
CaO	WR-XRF	0.01	3.93	4.48	3.88	3.33	4.05	4.75	6.74	6.18	6.19	3.08	7.23
Na_2O	WR-XRF	0.01	5.5	3.3	3.4	3.1	4.2	3.5	4.1	2.8	3.2	6	2.4
K_2O	WR-XRF	0.01	1.97	2.73	1.99	2.31	2.22	2.17	1.14	2.96	2.13	2.24	2.23
P_2O_5	WR-XRF	0.01	0.31	0.16	0.12	0.16	0.14	0.13	0.2	0.28	0.2	0.35	0.22
LOI			0.09	0.13	0.16	0.18	0.09	0.1	0.06	0.1	0.07	0.18	0.12
Total			98.7	100.3	99.8	99	100.2	99.8	99.6	99.1	101.8	99.7	99.9
TOT/C	LECO	0.02	n.a.	n.a.	n.a.	n.a.	n.a.	n.a.	n.a.	n.a.	n.a.	n.a.	n.a.
FeO	S.E.-Assay	0.01	n.a.	n.a.	n.a.	n.a.	n.a.	n.a.	n.a.	n.a.	n.a.	n.a.	n.a.
TOT/S	LECO	0.02	n.a.	n.a.	n.a.	n.a.	n.a.	n.a.	n.a.	n.a.	n.a.	n.a.	n.a.
ppb													
Se	ICP-MS	100.00	n.a.	n.a.	n.a.	n.a.	n.a.	n.a.	n.a.	n.a.	n.a.	n.a.	n.a.
Au	ICP-MS	0.50	n.a.	n.a.	n.a.	n.a.	n.a.	n.a.	n.a.	n.a.	n.a.	n.a.	n.a.
Pd	ICP-MS	10.00	n.a.	n.a.	n.a.	n.a.	n.a.	n.a.	n.a.	n.a.	n.a.	n.a.	n.a.
Pt	ICP-MS	2.00	n.a.	n.a.	n.a.	n.a.	n.a.	n.a.	n.a.	n.a.	n.a.	n.a.	n.a.
Ag	ICP-MS	2.00	0.3	0.2	0.2	b.d.	b.d.	0.1	0.2	0.4	0.2	0.2	0.3
Re	ICP-MS	1	n.a.	n.a.	n.a.	n.a.	n.a.	n.a.	n.a.	n.a.	n.a.	n.a.	n.a.
ppm													
Cu	ICP-MS	0.01	1420	38	550	89	86	132	30	551	145	89	342
Ni	ICP-MS	0.10	234	129	937	295	183	204	238	227	208	294	777
Co	ICP-MS	0.20	19	25	85	26	20	31	24	31	30	38	79
Cr	ICP-MS	0.50	46	143	147	221	166	157	203	150	172	144	177
Zn	ICP-MS	1.00	53	70	75	95	74	105	90	110	107	75	131
Sn	ICP-MS	1.00	1.7	1.5	1.9	1.5	1.9	1.6	2.1	2.1	1.7	1.5	1.9
Ga	ICP-MS	0.50	21	18	17	20	18	19	19	19	20	19	18
In	ICP-MS	0.02	0.09	0.38	0.08	0.06	0.08	0.09	0.12	0.11	0.29	0.05	0.13
Cd	ICP-MS	0.01	b.d.	0.4	b.d.	b.d.	b.d.	b.d.	b.d.	0.4	0.3	b.d.	0.2
La	ICP-MS	0.10	42	34	34	30	33	34	33	43	39	40	27
Ce	ICP-MS	0.10	83	69	68	58	68	70	72	89	79	82	57
Pr	ICP-MS	0.02	9.3	8.2	7.6	6.8	7.9	8.3	8.9	11	9.5	9.6	7.3
Nd	ICP-MS	0.30	34	31	28	25	29	321	34	41	35	36	29
Sm	ICP-MS	0.05	5.4	5.3	4.9	4.5	4.9	6.1	6.2	7.4	6.4	6.6	5.8
Eu	ICP-MS	0.02	1.5	1.4	1.2	1.1	1.2	1.4	1.4	1.8	1.7	1.7	1.7
Gd	ICP-MS	0.05	3.7	4.3	3.9	3.6	3.9	4.8	5	5.8	5.1	5	5.1
Tb	ICP-MS	0.01	0.44	0.61	0.57	0.51	0.55	0.68	0.7	0.8	0.71	0.64	0.77
Dy	ICP-MS	0.05	2.1	3.5	3.3	3	3.3	3.8	3.9	4.5	4	3.5	4.4
Ho	ICP-MS	0.02	0.37	0.7	0.66	0.59	0.63	0.75	0.74	0.86	0.77	0.63	0.86
Er	ICP-MS	0.03	0.85	1.8	1.7	1.5	1.6	1.9	1.9	2.2	2	1.5	2.2
Tm	ICP-MS	0.01	0.12	0.28	0.27	0.25	0.25	0.29	0.3	0.32	0.29	0.22	0.35
Yb	ICP-MS	0.05	0.69	1.8	1.8	1.6	1.6	1.8	1.9	2.1	1.9	1.3	2.1
Lu	ICP-MS	0.01	0.11	0.28	0.27	0.24	0.25	0.28	0.29	0.31	0.31	0.2	0.35
Zr	ICP-MS	0.10	120	163	157	144	177	139	204	189	172	180	123
Ba	ICP-MS	1.00	952	922	764	712	776	873	247	1150	733	802	783
Pb	ICP-MS	0.10	10	9	8	5	27	10	4	41	13	4	9
Th	ICP-MS	0.20	4.1	7.1	8	6.7	7.1	6.5	5.1	5.5	6	4.6	3
U	ICP-MS	0.10	0.43	1.6	2	1.3	1.4	1.5	1.1	0.97	1	0.38	0.62
Bi	ICP-MS	0.02	-0.2	0.3	0.7	-0.2	-0.2	-0.2	-0.2	0.3	0.3	-0.2	0.2
Rb	ICP-MS	0.10	37	62	48	48	40	45	16	52	51	45	56
Sr	ICP-MS	0.50	612	414	543	365	432	454	899	521	557	320	513
Nb	ICP-MS	0.10	4.7	8.4	8.5	7.6	8.3	8.3	8.3	8.7	8	6.4	5.6
Cs	ICP-MS	0.10	0.21	0.29	0.26	0.38	0.24	0.33	0.08	0.28	0.8	0.12	0.57
Be	ICP-MS	0.10	1.4	1.4	1.6	1.5	1.5	1.6	1.4	1.4	1.3	0.7	1.1
Hf	ICP-MS	0.10	2.8	4.1	3.8	4.2	3.8	3.6	3.8	4.5	4.1	4	3.2
Y	ICP-MS	0.10	11	21	19	17	19	21	22	25	23	18	26
Ta	ICP-MS	0.10	0.2	0.51	0.56	0.47	0.49	0.53	0.45	0.47	0.44	0.25	0.3
Sc	ICP-MS	0.10	6.9	17	14	17	15	19	22	22	19	17	31
V	ICP-MS	8.00	103	137	117	134	124	129	144	189	159	167	253
Mo	ICP-MS	0.01	25	16	26	32	37	30	33	29	34	18	45
As	ICP-MS	0.1	2.8	3.7	4.1	3.8	4.2	3.6	3.8	4.5	4.1	4	3.2
Sb	ICP-MS	0.02	0.6	0.3	0.4	0.4	0.4	0.4	0.3	0.7	0.3	b.d.	1
Te	ICP-MS	0.02	b.d.	b.d.	b.d.	b.d.	b.d.	b.d.	b.d.	b.d.	b.d.	b.d.	b.d.

Appendix 1 (cont.): Goechemiscal dataset of rock types located within the Podolksy deposit and geochemical data collected from literature located within and around the Sudbury Structure. Major and trace element analyses (XRF and ICP-MS) characterizing the grey gabbro unit. Apprviations used are as follows: n.a. = not analysed; b.d. = below detection; Mg# = MgO/(MgO+FeO); ppm = parts per million; ppb = parts per billion; wt% = weight percent; * Carter et al. 2009; ** = Lightfoot and Farrow 2002; [3] = Lightfoot et al. 1997a; [9] = Ames et al. 2014; WR-XRF = whole rock x-ray flouresence; ICP-MS = Inductively coupled plasma mass spectrometry; LLD = lower limits of detection; QD = Quartz diorite; LQD = Leucocratic quartz diorite; IQD = Inclusion quartz diorite;; FWBX = Footwall breccia; JL Intrusion = Joe Lake Intrusion.

wt. %	Method	LLD	*03AV-84	*03AV-68	*03AV-40	** 93PCL-426	** 94DEP-012	** 94PCL-236	** 94PCL-255	** 94PCL-3080	** 94PCL-3031
			IQD	IQD-FWBX	GABBRO	QD	QD	QD	QD	QD	QD
SiO_2	WR-XRF	0.10	54	57	47	59.3	61	56.5	58.1	56.4	58.2
TiO_2	WR-XRF	0.01	1.01	0.82	0.99	0.83	0.84	0.89	0.89	0.76	0.86
Al_2O_3	WR-XRF	0.01	14.4	15.8	12.5	14.6	16.6	14.5	14.7	15.4	14.9
Fe_2O_{3T}	WR-XRF	0.01	13.3	9	17.4	8.4	7.81	10.02	8.69	9.38	8.86
MgO	WR-XRF	0.01	4.29	3.51	5.74	4.22	3.29	4.45	3.88	4.65	4.08
MnO	WR-XRF	0.01	0.16	0.12	0.23	0.12	0.07	0.14	0.13	0.14	0.12
CaO	WR-XRF	0.01	5.86	5.18	9.4	4.99	2.58	5.83	6.03	6.04	6.13
Na_2O	WR-XRF	0.01	3	3.8	2.8	2.29	4.1	3.08	2.77	2.04	2.98
K_2O	WR-XRF	0.01	2.16	2.07	3.88	1.94	0.35	1.72	1.94	1.91	1.66
P_2O_5	WR-XRF	0.01	0.28	0.38	0.07	0.15	0.16	0.13	0.13	0.1	0.13
LOI			0.05	0.09	0.15	1.74	1.83	1.5	1.22	1.93	1.03
Total			100.3	99.6	99.2	98.6	98.7	98.7	98.5	98.8	99
TOT/C	LECO	0.02	n.a.	n.a.	n.a.	b.d.	0.25	b.d.	b.d.	0.19	b.d.
FeO	S.E.-Assay	0.01	n.a.	n.a.	n.a.	n.a.	n.a.	n.a.	n.a.	n.a.	n.a.
TOT/S	LECO	0.02	n.a.	n.a.	n.a.	0.02	0.04	0.28	0.05	0.01	0.02
ppb											
Se	ICP-MS	100.00	n.a.	n.a.	n.a.	n.a.	n.a.	n.a.	n.a.	n.a.	n.a.
Au	ICP-MS	0.50	n.a.	n.a.	n.a.	b.d.	b.d.	25	b.d.	b.d.	b.d.
Pd	ICP-MS	10.00	n.a.	n.a.	n.a.	5	b.d.	116	b.d.	b.d.	b.d.
Pt	ICP-MS	2.00	n.a.	n.a.	n.a.	b.d.	b.d.	117	b.d.	b.d.	b.d.
Ag	ICP-MS	2.00	0.2	0.3	0.1	n.a.	n.a.	n.a.	n.a.	n.a.	n.a.
Re	ICP-MS	1	n.a.	n.a.	n.a.	n.a.	n.a.	n.a.	n.a.	n.a.	n.a.
ppm											
Cu	ICP-MS	0.01	266	131	949	50	153	151	83	57	63
Ni	ICP-MS	0.10	643	305	258	71	65	111	66	105	83
Co	ICP-MS	0.20	53	30	128	27	22	48	31	30	31
Cr	ICP-MS	0.50	192	163	153	185	167	189	160	243	167
Zn	ICP-MS	1.00	104	88	125	103	103	106	82	126	89
Sn	ICP-MS	1.00	2.1	1.7	1.9	n.a.	n.a.	n.a.	n.a.	n.a.	n.a.
Ga	ICP-MS	0.50	20	20	17	n.a.	n.a.	n.a.	n.a.	n.a.	n.a.
In	ICP-MS	0.02	0.1	0.4	0.11	n.a.	n.a.	n.a.	n.a.	n.a.	n.a.
Cd	ICP-MS	0.01	b.d.	0.4	b.d.	n.a.	n.a.	n.a.	n.a.	n.a.	n.a.
La	ICP-MS	0.10	39	43	12	33.3	43.3	33.4	34.9	30.8	35
Ce	ICP-MS	0.10	82	85	26	70.5	85.6	67.8	72.7	62.3	69.8
Pr	ICP-MS	0.02	10	9.8	3.3	8.6	9.5	8	8.7	7.7	8.7
Nd	ICP-MS	0.30	39	37	14	30.6	35.2	30.9	32.6	28.6	32.8
Sm	ICP-MS	0.05	7.3	6.2	3.3	6.5	6.19	5.71	6.22	5.54	6.09
Eu	ICP-MS	0.02	1.8	1.9	1	1.61	2.04	1.46	1.55	1.31	1.4
Gd	ICP-MS	0.05	5.7	4.6	3.8	5.96	5.36	5.55	6.06	5.02	5.6
Tb	ICP-MS	0.01	0.73	0.61	0.63	0.96	0.8	0.84	0.93	0.76	0.82
Dy	ICP-MS	0.05	4	3.1	4.2	5.62	4.6	4.6	5.03	4.47	4.89
Ho	ICP-MS	0.02	0.75	0.57	0.89	1.2	1	0.95	1.04	0.87	0.93
Er	ICP-MS	0.03	1.9	1.4	2.6	3.2	2.83	2.74	2.95	2.48	2.85
Tm	ICP-MS	0.01	0.28	0.2	0.38	0.48	0.47	0.4	0.43	0.35	0.39
Yb	ICP-MS	0.05	1.7	1.3	2.6	3.02	2.97	2.59	2.85	2.41	2.69
Lu	ICP-MS	0.01	0.27	0.19	0.41	0.45	0.47	0.4	0.41	0.37	0.4
Zr	ICP-MS	0.10	143	216	76	166	184	167	219	157	179
Ba	ICP-MS	1.00	906	930	172	510	127	481	479	477	642
Pb	ICP-MS	0.10	11	11	6	n.a.	n.a.	n.a.	n.a.	n.a.	n.a.
Th	ICP-MS	0.20	5.1	4.9	1	12.5	9.8	8.3	8.6	8.6	9.2
U	ICP-MS	0.10	0.71	0.77	0.23	3.36	2.96	2	1.94	2.02	1.96
Bi	ICP-MS	0.02	-0.2	0.5	0.9	n.a.	n.a.	n.a.	n.a.	n.a.	n.a.
Rb	ICP-MS	0.10	54	45	12	90	25	78	79	112	59
Sr	ICP-MS	0.50	534	596	411	305	398	307	316	316	430
Nb	ICP-MS	0.10	8	6.9	4.1	13.1	10.7	10.1	11.4	9.8	10.8
Cs	ICP-MS	0.10	1.1	0.47	0.1	8	0.9	3.2	3.5	18.1	5.8
Be	ICP-MS	0.10	1.4	1.4	1.1	n.a.	n.a.	n.a.	n.a.	n.a.	n.a.
Hf	ICP-MS	0.10	3.4	4.9	2	4.46	4.61	4.34	b.d.	3.87	4.44
Y	ICP-MS	0.10	22	17	27	n.a.	n.a.	n.a.	n.a.	n.a.	n.a.
Ta	ICP-MS	0.10	0.37	0.32	0.25	0.95	0.75	0.66	0.7	0.62	0.68
Sc	ICP-MS	0.10	21	15	37	19.5	20	29	19	17	17
V	ICP-MS	8.00	181	126	251	149	144	299	171	153	154
Mo	ICP-MS	0.01	62	39	48	n.a.	n.a.	n.a.	n.a.	n.a.	n.a.
As	ICP-MS	0.1	3.4	4.9	2	n.a.	n.a.	n.a.	n.a.	n.a.	n.a.
Sb	ICP-MS	0.02	0.6	0.5	0.6	n.a.	n.a.	n.a.	n.a.	n.a.	n.a.
Te	ICP-MS	0.02	b.d.	b.d.	0.3	n.a.	n.a.	n.a.	n.a.	n.a.	n.a.

Appendix 1 (cont.): Goechemiscal dataset of rock types located within the Podolksy deposit and geochemical data collected from literature located within and around the Sudbury Structure. Major and trace element analyses (XRF and ICP-MS) characterizing the grey gabbro unit. Apprviations used are as follows: n.a. = not analysed; b.d. = below detection; Mg# = MgO/(MgO+FeO); ppm = parts per million; ppb = parts per billion; wt% = weight percent; * Carter et al. 2009; ** = Lightfoot and Farrow 2002; [3] = Lightfoot et al. 1997a; [9] = Ames et al. 2014; WR-XRF = whole rock x-ray flouresence; ICP-MS = Inductively coupled plasma mass spectrometry; LLD = lower limits of detection; QD = Quartz diorite; LQD = Leucocratic quartz diorite; IQD = Inclusion quartz diorite;; FWBX = Footwall breccia; JL Intrusion = Joe Lake Intrusion.

wt. %	Method	LLD	** 93PCL-425	** 93PCL-428	** 94PCL-239	** 94PCL-225	** 94PCL-3063	** 94DEP-056	** 94DEP-057	** 94PCL-252	** 94DEP-034	** 94PCL-261
			QD	QD	QD	QD	QD	QD	QD	QD	QD	QD
SiO_2	WR-XRF	0.10	57.1	59	51.4	55.4	49.9	56	56.8	56	59.9	57.3
TiO_2	WR-XRF	0.01	0.75	0.89	0.8	0.81	0.73	0.88	0.96	0.69	0.94	1.02
Al_2O_3	WR-XRF	0.01	15.3	14.8	12.8	15	12.6	14.6	14	15.5	14.1	14
Fe_2O_{3T}	WR-XRF	0.01	8.71	8.18	15.06	9.41	17.99	9.53	10.73	9.5	9.22	10.5
MgO	WR-XRF	0.01	4.51	4.07	5.39	5.54	4.38	4.64	3.66	4.34	3.19	3.75
MnO	WR-XRF	0.01	0.13	0.13	0.15	0.13	0.14	0.14	0.11	0.11	0.11	0.14
CaO	WR-XRF	0.01	5.89	5.99	5.99	6.52	5.33	6.24	5.35	5.1	5.37	5.88
Na_2O	WR-XRF	0.01	2.44	2.78	2.08	2.8	2.08	2.73	2.65	2.76	2.87	2.64
K_2O	WR-XRF	0.01	1.84	1.66	1.57	1.69	1.67	1.76	1.65	2.78	1.42	1.89
P_2O_5	WR-XRF	0.01	0.14	0.16	0.11	0.13	0.1	0.16	0.14	0.1	0.15	0.13
LOI			1.74	1.18	0.74	1.65	1.23	0.68	0.63	1.73	0.5	0.61
Total			98.6	98.9	96	99.1	96.2	97.4	96.7	98.6	97.8	97.8
TOT/C	LECO	0.02	b.d.	b.d.	0.31	b.d.	b.d.	0.06	0.21	0.14	0.11	b.d.
FeO	S.E.-Assay	0.01	n.a.	n.a.	n.a.	n.a.	n.a.	n.a.	n.a.	n.a.	n.a.	n.a.
TOT/S	LECO	0.02	0.02	0.02	2.41	0.17	3.45	0.05	1.58	0.09	0.8	0.6
ppb												
Se	ICP-MS	100.00	n.a.	n.a.	n.a.	n.a.	n.a.	n.a.	n.a.	n.a.	n.a.	n.a.
Au	ICP-MS	0.50	b.d.	b.d.	b.d.	b.d.	b.d.	b.d.	b.d.	b.d.	b.d.	b.d.
Pd	ICP-MS	10.00	b.d.	b.d.	b.d.	b.d.	b.d.	b.d.	b.d.	b.d.	b.d.	b.d.
Pt	ICP-MS	2.00	b.d.	b.d.	b.d.	b.d.	b.d.	b.d.	b.d.	b.d.	b.d.	b.d.
Ag	ICP-MS	2.00	n.a.	n.a.	n.a.	n.a.	n.a.	n.a.	n.a.	n.a.	n.a.	n.a.
Re	ICP-MS	1	n.a.	n.a.	n.a.	n.a.	n.a.	n.a.	n.a.	n.a.	n.a.	n.a.
ppm												
Cu	ICP-MS	0.01	177	243	3343	216	3707	292	1811	93	1607	899
Ni	ICP-MS	0.10	135	154	3384	313	7331	176	2952	231	1246	793
Co	ICP-MS	0.20	30	28	130	38	223	35	92	30	46	52
Cr	ICP-MS	0.50	164	173	396	226	194	190	153	238	131	140
Zn	ICP-MS	1.00	119	76	91	92	48	114	154	78	112	98
Sn	ICP-MS	1.00	n.a.	n.a.	n.a.	n.a.	n.a.	n.a.	n.a.	n.a.	n.a.	n.a.
Ga	ICP-MS	0.50	n.a.	n.a.	n.a.	n.a.	n.a.	n.a.	n.a.	n.a.	n.a.	n.a.
In	ICP-MS	0.02	n.a.	n.a.	n.a.	n.a.	n.a.	n.a.	n.a.	n.a.	n.a.	n.a.
Cd	ICP-MS	0.01	n.a.	n.a.	n.a.	n.a.	n.a.	n.a.	n.a.	n.a.	n.a.	n.a.
La	ICP-MS	0.10	29.7	34.8	29.5	29.8	20.5	33	31.4	29.7	38.3	35.3
Ce	ICP-MS	0.10	61.7	71.1	60	61.7	43.6	66.7	66.5	60	78.7	72.5
Pr	ICP-MS	0.02	7.3	8.5	7.1	7.4	5.5	7.8	7.7	7.1	9	8.8
Nd	ICP-MS	0.30	26.4	31.2	27.4	28.5	21.3	29.5	29.1	26.3	33.9	33
Sm	ICP-MS	0.05	5.17	6.11	5.22	5.29	4.34	5.85	5.64	4.77	6.24	6.49
Eu	ICP-MS	0.02	1.27	1.4	1.27	1.31	0.99	1.37	1.42	1.15	1.51	1.52
Gd	ICP-MS	0.05	4.56	5.67	5.06	4.93	4.16	5.1	5.25	4.45	5.81	6.39
Tb	ICP-MS	0.01	0.67	0.85	0.75	0.72	0.67	0.78	0.83	0.65	0.88	0.97
Dy	ICP-MS	0.05	3.82	4.7	4.2	4.04	4.03	4.61	4.95	3.58	5.23	5.54
Ho	ICP-MS	0.02	0.85	1.05	0.87	0.83	0.8	0.97	1.05	0.71	1.1	1.15
Er	ICP-MS	0.03	2.27	2.8	2.43	2.27	2.39	2.64	2.84	2.05	2.99	3.25
Tm	ICP-MS	0.01	0.33	0.42	0.35	0.33	0.34	0.42	0.46	0.3	0.48	0.49
Yb	ICP-MS	0.05	2.11	2.68	2.37	2.21	2.31	2.47	2.71	1.97	2.8	3.15
Lu	ICP-MS	0.01	0.33	0.41	0.35	0.32	0.34	0.38	0.41	0.29	0.42	0.46
Zr	ICP-MS	0.10	161	184	153	154	143	177	174	156	187	186
Ba	ICP-MS	1.00	575	454	467	527	556	511	451	548	360	526
Pb	ICP-MS	0.10	n.a.	n.a.	n.a.	n.a.	n.a.	n.a.	n.a.	n.a.	n.a.	n.a.
Th	ICP-MS	0.20	7.8	9.8	6.9	6.5	7.8	8	9.8	8.1	10.9	10
U	ICP-MS	0.10	1.85	2.26	1.64	1.42	1.85	1.7	2.57	1.72	2.97	2.55
Bi	ICP-MS	0.02	n.a.	n.a.	n.a.	n.a.	n.a.	n.a.	n.a.	n.a.	n.a.	n.a.
Rb	ICP-MS	0.10	90	70	67	62	77	78	78	22	65	82
Sr	ICP-MS	0.50	316	333	242	331	238	294	291	298	271	273
Nb	ICP-MS	0.10	9.3	11.4	8.9	8.7	9	9.4	10.9	8.5	11.1	12.1
Cs	ICP-MS	0.10	7.3	3.6	2.9	2	3.7	3.8	4.2	6	3.2	3.7
Be	ICP-MS	0.10	n.a.	n.a.	n.a.	n.a.	n.a.	n.a.	n.a.	n.a.	n.a.	n.a.
Hf	ICP-MS	0.10	b.d.	4.73	3.72	3.55	3.72	b.d.	4.02	b.d.	4.54	4.44
Y	ICP-MS	0.10	n.a.	n.a.	n.a.	n.a.	n.a.	n.a.	n.a.	n.a.	n.a.	n.a.
Ta	ICP-MS	0.10	0.61	0.79	0.56	0.53	0.58	0.7	0.89	0.59	0.95	0.84
Sc	ICP-MS	0.10	19.2	21.7	18	18	17	21	22	16	20	20
V	ICP-MS	8.00	140	163	161	150	164	165	181	143	162	187
Mo	ICP-MS	0.01	n.a.	n.a.	n.a.	n.a.	n.a.	n.a.	n.a.	n.a.	n.a.	n.a.
As	ICP-MS	0.1	n.a.	n.a.	n.a.	n.a.	n.a.	n.a.	n.a.	n.a.	n.a.	n.a.
Sb	ICP-MS	0.02	n.a.	n.a.	n.a.	n.a.	n.a.	n.a.	n.a.	n.a.	n.a.	n.a.
Te	ICP-MS	0.02	n.a.	n.a.	n.a.	n.a.	n.a.	n.a.	n.a.	n.a.	n.a.	n.a.

Appendix 1 (cont.): Goechemiscal dataset of rock types located within the Podolksy deposit and geochemical data collected from literature located within and around the Sudbury Structure. Major and trace element analyses (XRF and ICP-MS) characterizing the grey gabbro unit. Apprviations used are as follows: n.a. = not analysed; b.d. = below detection; Mg# = MgO/(MgO+FeO); ppm = parts per million; ppb = parts per billion; wt% = weight percent; * Carter et al. 2009; ** = Lightfoot and Farrow 2002; [3] = Lightfoot et al. 1997a; [9] = Ames 2014; WR-XRF = whole rock x-ray flouresence; ICP-MS = Inductively coupled plasma mass spectrometry; LLD = lower limits of detection; QD = Quartz diorite; LQD = Leucocratic quartz diorite; IQD = Inclusion quartz diorite;; FWBX = Footwall breccia; JL Intrusion = Joe Lake Intrusion.

wt. %	Method	LLD	** 94PCL-253	** 94PCL-3021	** 94PCL-3505	³ Creighton Mine Offset	³ Ministic Offset	³ Worthington Offset	³ Foy Offset	³ Copper Cliff Offset	³ Manchester Offset	³ Parkin Offset
			QD	QD	QD	QD	QD	QD	QD	QD	QD	QD
SiO_2	WR-XRF	0.10	52.8	57.5	55.7	55.07	58.93	55.53	59.31	56.42	59.57	58.7
TiO_2	WR-XRF	0.01	0.86	0.82	0.98	0.93	0.74	0.93	0.72	0.89	0.7	0.73
Al_2O_3	WR-XRF	0.01	12.7	14.8	14.2	14.9	14.6	14.41	14.92	15.03	14.27	14.86
Fe_2O_{3T}	WR-XRF	0.01	15.01	9.04	10.62	10.12	8.2	10.71	7.53	9.69	7.56	7.97
MgO	WR-XRF	0.01	3.79	4.26	4.34	4.42	4	4.4	3.75	4.22	3.89	3.71
MnO	WR-XRF	0.01	0.12	0.12	0.15	0.13	0.12	0.13	0.12	0.14	0.07	0.11
CaO	WR-XRF	0.01	5.39	6.08	6.43	6.84	4.79	5.98	5.18	6.4	4.08	4.73
Na_2O	WR-XRF	0.01	2.32	2.74	2.46	2.89	3.13	2.64	3.06	2.61	3.6	2.88
K_2O	WR-XRF	0.01	1.43	1.69	1.48	1.56	2.27	1.79	2.33	1.87	2.07	2.49
P_2O_5	WR-XRF	0.01	0.11	0.12	0.14	0.16	0.16	0.13	0.18	0.16	0.14	0.19
LOI			0.63	1.05	1.17	0.6	1.9	1.36	1.58	1.18	2.89	2.31
Total			95.1	98.2	97.6	97.62	98.85	98.02	98.68	98.62	98.84	98.68
TOT/C	LECO	0.02	b.d.	b.d.	0.16	0.11	0.28	0.33	0.39	0.29	1.03	0.32
FeO	S.E.-Assay	0.01	n.a.	n.a.	n.a.	7.37	5.31	7.19	4.87	6.83	4.75	4.51
TOT/S	LECO	0.02	3.4	0.18	0.51	0.41	0.19	0.72	0.13	0.22	0.07	0.23
ppb												
Se	ICP-MS	100.00	n.a.	n.a.	n.a.	b.d.	470	77	167	590	161	358
Au	ICP-MS	0.50	b.d.	b.d.	b.d.	n.a.	n.a.	n.a.	n.a.	n.a.	n.a.	n.a.
Pd	ICP-MS	10.00	b.d.	b.d.	b.d.	n.a.	n.a.	n.a.	n.a.	n.a.	n.a.	n.a.
Pt	ICP-MS	2.00	b.d.	b.d.	b.d.	n.a.	n.a.	n.a.	n.a.	n.a.	n.a.	n.a.
Ag	ICP-MS	2.00	n.a.	n.a.	n.a.	n.a.	n.a.	n.a.	n.a.	n.a.	n.a.	n.a.
Re	ICP-MS	1	n.a.	n.a.	n.a.	n.a.	n.a.	n.a.	n.a.	n.a.	n.a.	n.a.
ppm												
Cu	ICP-MS	0.01	5011	260	9	2974	297	1324	106	347	86	584
Ni	ICP-MS	0.10	5041	256	774	1381	203	1168	119	305	87	331
Co	ICP-MS	0.20	163	56	47	43	32	58	28	40	25	33
Cr	ICP-MS	0.50	189	208	177	177	169	187	161	170	164	162
Zn	ICP-MS	1.00	66	87	107	103	107	95	112	116	37	88
Sn	ICP-MS	1.00	n.a.	n.a.	n.a.	n.a.	n.a.	n.a.	n.a.	n.a.	n.a.	n.a.
Ga	ICP-MS	0.50	n.a.	n.a.	n.a.	n.a.	n.a.	n.a.	n.a.	n.a.	n.a.	n.a.
In	ICP-MS	0.02	n.a.	n.a.	n.a.	n.a.	n.a.	n.a.	n.a.	n.a.	n.a.	n.a.
Cd	ICP-MS	0.01	n.a.	n.a.	n.a.	n.a.	n.a.	n.a.	n.a.	n.a.	n.a.	n.a.
La	ICP-MS	0.10	33.4	35	31.4	40.23	36.64	32.44	36.37	32.56	32.19	38.16
Ce	ICP-MS	0.10	68	70.5	65.2	83.02	73.48	66.52	73.41	65.85	64.87	76.33
Pr	ICP-MS	0.02	8.1	8.7	8.1	10.53	8.84	8.12	8.85	7.94	7.74	0.07
Nd	ICP-MS	0.30	30.3	32.5	30.9	40.27	31.92	30.74	31.94	29.36	27.75	32.55
Sm	ICP-MS	0.05	5.69	6.06	6.12	8.22	5.87	5.96	5.82	5.86	5.2	5.93
Eu	ICP-MS	0.02	1.39	1.4	1.49	1.67	1.49	1.45	1.5	1.49	1.34	1.49
Gd	ICP-MS	0.05	5.68	5.66	5.84	7.79	4.95	5.67	4.9	5.53	4.57	4.95
Tb	ICP-MS	0.01	0.84	0.85	0.88	1.22	0.72	0.86	0.7	0.86	0.69	0.7
Dy	ICP-MS	0.05	4.73	4.93	5.25	7.45	3.85	4.98	3.69	4.97	3.75	3.68
Ho	ICP-MS	0.02	0.98	0.95	1.06	1.5	0.79	1.01	0.75	1.06	0.77	0.75
Er	ICP-MS	0.03	2.8	2.78	3	4.4	2.06	2.88	1.97	2.87	2.05	1.93
Tm	ICP-MS	0.01	0.41	0.39	0.43	0.65	0.31	0.41	0.29	0.45	0.31	0.29
Yb	ICP-MS	0.05	2.66	2.65	2.94	4.24	1.97	2.75	1.88	2.87	1.94	1.8
Lu	ICP-MS	0.01	0.4	0.4	0.45	0.64	0.31	0.41	0.3	0.44	0.29	0.27
Zr	ICP-MS	0.10	162	175	159	195	158	167	166	162	152	173
Ba	ICP-MS	1.00	474	567	434	523	779	515	719	500	452	755
Pb	ICP-MS	0.10	n.a.	n.a.	n.a.	n.a.	n.a.	n.a.	n.a.	n.a.	n.a.	n.a.
Th	ICP-MS	0.20	8.7	9.3	8.7	9.67	8.91	8.65	8.64	8.38	8.21	8.7
U	ICP-MS	0.10	2.21	2.15	2.18	2.14	1.85	2.06	1.68	1.96	2.09	1.68
Bi	ICP-MS	0.02	n.a.	n.a.	n.a.	n.a.	n.a.	n.a.	n.a.	n.a.	n.a.	n.a.
Rb	ICP-MS	0.10	64	85	73	72.9	83.8	70.3	79.6	91.8	74.8	83.3
Sr	ICP-MS	0.50	279	329	321	321	384	316	441	290	213	439
Nb	ICP-MS	0.10	10.5	10.7	11.4	16.82	8.83	10.59	8.62	10.27	8.49	8.69
Cs	ICP-MS	0.10	3.6	8.5	9.6	2.81	1.04	5.69	1.23	6.41	1.5	1.85
Be	ICP-MS	0.10	n.a.	n.a.	n.a.	b.d.	1.33	1.39	1.28	1.57	1.44	1.32
Hf	ICP-MS	0.10	4.15	4.45	4.18	2.38	3.84	4.11	4.4	3.84	3.33	3.95
Y	ICP-MS	0.10	n.a.	n.a.	n.a.	33.9	19.3	23.2	18	25.8	18.8	18.7
Ta	ICP-MS	0.10	0.71	0.67	0.73	0.89	0.53	0.69	0.51	0.71	0.56	0.52
Sc	ICP-MS	0.10	17	18	19	21	17	19	16	22	17	16
V	ICP-MS	8.00	158	149	180	172	132	173	137	178	133	128
Mo	ICP-MS	0.01	n.a.	n.a.	n.a.	n.a.	n.a.	n.a.	n.a.	n.a.	n.a.	n.a.
As	ICP-MS	0.1	n.a.	n.a.	n.a.	n.a.	n.a.	n.a.	n.a.	n.a.	n.a.	n.a.
Sb	ICP-MS	0.02	n.a.	n.a.	n.a.	n.a.	n.a.	n.a.	n.a.	n.a.	n.a.	n.a.
Te	ICP-MS	0.02	n.a.	n.a.	n.a.	n.a.	n.a.	n.a.	n.a.	n.a.	n.a.	n.a.

Appendix 1 (cont.): Goechemiscal dataset of rock types located within the Podolksy deposit and geochemical data collected from literature located within and around the Sudbury Structure. Major and trace element analyses (XRF and ICP-MS) characterizing the grey gabbro unit. Apprviations used are as follows: n.a. = not analysed; b.d. = below detection; Mg# = MgO/(MgO+FeO); ppm = parts per million; ppb = parts per billion; wt% = weight percent; * Carter et al. 2009; ** = Lightfoot and Farrow 2002; ³ = Lightfoot et al. 1997a; ᵠ = Ames et al. 2014; WR-XRF = whole rock x-ray flouresence; ICP-MS = Inductively coupled plasma mass spectrometry; LLD = lower limits of detection; QD = Quartz diorite; LQD = Leucocratic quartz diorite; IQD = Inclusion quartz diorite;; FWBX = Footwall breccia; JL Intrusion = Joe Lake Intrusion.

wt. %	Method	LLD	[3] Main Mass	[3] Main Mass	[φ] Copper Cliff	[φ] Copper Cliff	[φ] Trill	[φ] Trill	[φ] Podolsky-NZ	[φ] Segway	[φ] Worthington	[φ] Worthington
					EI-76-146	EI-70-07	05AV-32	05AV-33	02-AV-643	05AB-15	00AV-306	00AV-306A
			Mafic Norite	Felsic Norite	QD	QD	QD	QD quench	QD	QD	Ore	Ore
SiO_2	WR-XRF	0.10	55.78	56.47	54.00	54.90	60.20	60.80	61.80	56.10	55.50	60.40
TiO_2	WR-XRF	0.01	0.56	0.62	0.86	0.99	0.73	0.70	0.67	0.72	0.87	0.88
Al_2O_3	WR-XRF	0.01	11.71	16.3	13.50	14.40	14.90	15.00	14.60	15.30	14.80	15.00
Fe_2O_{3T}	WR-XRF	0.01	9.93	7.91	11.50	13.00	8.30	7.70	8.60	10.20	12.30	8.62
MgO	WR-XRF	0.01	10.61	4.95	4.79	5.01	3.73	3.74	3.62	4.64	3.47	3.64
MnO	WR-XRF	0.01	0.16	0.13	0.16	0.18	0.12	0.10	0.13	0.16	0.09	0.11
CaO	WR-XRF	0.01	4.54	6.38	5.82	6.89	5.54	5.78	3.09	6.90	4.11	5.47
Na_2O	WR-XRF	0.01	2.03	2.85	2.23	2.50	3.20	3.70	2.86	3.20	2.68	3.05
K_2O	WR-XRF	0.01	1.41	1.81	1.36	1.75	2.30	1.95	3.16	1.35	1.79	1.32
P_2O_5	WR-XRF	0.01	0.11	0.16	0.19	0.20	0.18	0.18	0.01	0.14	0.15	0.16
LOI			1.55	1.7	1.6	0.8	0.9	0.7	1.8	0.6	2.9	1.6
Total			98.38	99.26	95.50	100.40	100.6	100.8	100.60	100.30	100.50	101.30
TOT/C	LECO	0.02	0.2	0.32	0.10	0.10	0.1	0.1	0.20	0.30	0.10	0.10
FeO	S.E.-Assay	0.01	7.39	5.4	n.a.	n.a.	n.a.	n.a.	n.a.	n.a.	n.a.	n.a.
TOT/S	LECO	0.02	0.29	0.12	n.a.	n.a.	n.a.	n.a.	n.a.	n.a.	n.a.	n.a.
ppb												
Se	ICP-MS	100.00	419	230	300.0	300.0	2000	2000	300.0	2000.0	7000.0	3500.0
Au	ICP-MS	0.50	n.a.	n.a.	23	17	44	13	1	906	483	60
Pd	ICP-MS	10.00	n.a.	n.a.	b.d.	b.d.	268	3.9	5.0	2200.0	383.4	256.5
Pt	ICP-MS	2.00	n.a.	n.a.	b.d.	b.d.	154	1650	1.8	23.0	919.4	240.1
Ag	ICP-MS	2.00	n.a.	n.a.	1300.00	700.0	200.0	100.0	400.00	1400.0	9800.0	2200.0
Re	ICP-MS	1	n.a.	n.a.	n.a.	n.a.	n.a.	n.a.	n.a.	n.a.	n.a.	n.a.
ppm												
Cu	ICP-MS	0.01	358	155	650	470	368	128	603	1222	20800	5070
Ni	ICP-MS	0.10	341	126	750	470	168	73	232	82	418	495
Co	ICP-MS	0.20	60	33	58	45	24	23	20	31	24	38
Cr	ICP-MS	0.50	1690	213	200	82	131	149	184	195	206	246
Zn	ICP-MS	1.00	103	99	240	110	77	68	122	104	109	78
Sn	ICP-MS	1.00	n.a.	n.a.	2.5	3.9	1.4	3.4	3.0	30.0	1.0	1.2
Ga	ICP-MS	0.50	n.a.	n.a.	19.0	20.0	19.00	19.00	17.0	17.0	17.0	17.0
In	ICP-MS	0.02	n.a.	n.a.	0.03	0.03	0.05	0.06	0.06	0.20	0.03	0.03
Cd	ICP-MS	0.01	n.a.	n.a.	0.8	0.2	0.1	0.1	0.1	0.9	1.0	0.4
La	ICP-MS	0.10	27.12	30.6	31.0	29.0	37.0	39.0	36.0	29.0	28.0	26.0
Ce	ICP-MS	0.10	55.08	60.6	64.0	61.0	73.0	78.0	73.0	57.0	57.0	57.0
Pr	ICP-MS	0.02	6.14	7.29	7.70	7.10	8.60	8.90	8.40	6.80	6.50	6.60
Nd	ICP-MS	0.30	22.89	26	n.a.	n.a.	n.a.	n.a.	n.a.	n.a.	n.a.	n.a.
Sm	ICP-MS	0.05	4.13	4.9	5.80	5.70	5.50	5.80	5.20	5.20	4.20	4.10
Eu	ICP-MS	0.02	1.08	1.4	1.30	1.40	1.40	1.40	1.20	1.30	1.10	1.10
Gd	ICP-MS	0.05	1.85	4.49	5.20	5.70	4.70	4.60	4.30	4.70	3.40	3.40
Tb	ICP-MS	0.01	2.11	0.63	0.81	0.88	0.65	0.66	0.62	0.72	0.54	0.55
Dy	ICP-MS	0.05	2.8	3.41	5.00	5.10	3.70	3.60	3.50	4.40	3.20	3.40
Ho	ICP-MS	0.02	0.59	0.7	1.00	1.10	0.73	0.71	0.70	0.90	0.64	0.71
Er	ICP-MS	0.03	1.62	1.88	2.90	3.00	1.90	1.90	1.80	2.40	1.90	2.10
Tm	ICP-MS	0.01	0.25	0.29	0.47	0.50	0.30	0.30	0.28	0.39	0.30	0.33
Yb	ICP-MS	0.05	1.61	1.82	3.10	3.40	2.00	2.00	1.90	2.60	2.00	2.30
Lu	ICP-MS	0.01	0.25	0.28	0.44	0.50	0.30	0.30	0.29	0.39	0.32	0.36
Zr	ICP-MS	0.10	113	134	210.0	210.0	173.0	171.0	180.0	154.0	164.0	174.0
Ba	ICP-MS	1.00	492	622	460	550	884	887	1220	608	629	392
Pb	ICP-MS	0.10	n.a.	n.a.	67	23	15	12	17	1941	20	24
Th	ICP-MS	0.20	6.19	6.9	7.20	7.60	8.20	8.40	9.70	7.30	8.50	9.30
U	ICP-MS	0.10	1.24	1.5	1.60	1.90	1.80	2.10	2.20	1.90	1.90	2.10
Bi	ICP-MS	0.02	n.a.	n.a.	0.3	0.3	0.4	0.1	0.3	58.0	2.3	1.1
Rb	ICP-MS	0.10	50.7	60	68.00	87.00	72.00	62.00	68.00	41.00	64.00	50.00
Sr	ICP-MS	0.50	305	420	210	210	415	420	340	369	339	343
Nb	ICP-MS	0.10	6.44	7.5	10.0	9.6	8.70	8.70	8.7	8.8	12.0	11.0
Cs	ICP-MS	0.10	1.39	1.11	3.60	6.10	1.80	1.50	0.36	1.40	7.60	6.40
Be	ICP-MS	0.10	1.02	1.16	1.3	1.3	1.1	1.3	2.0	1.1	1.4	1.6
Hf	ICP-MS	0.10	2.8	3.57	5.20	5.20	4.20	4.20	4.70	3.80	3.90	4.30
Y	ICP-MS	0.10	15.2	16.5	28.0	30.0	22.00	21.00	20.0	27.0	20.0	21.0
Ta	ICP-MS	0.10	0.39	0.49	0.63	0.67	0.53	0.53	0.58	0.56	0.67	0.72
Sc	ICP-MS	0.10	21	19	25.0	27.0	14.0	15.0	16.0	23.0	21.0	22.0
V	ICP-MS	8.00	157	126	180	220	129	134	118	145	152	162
Mo	ICP-MS	0.01	n.a.	n.a.	0.90	1.0	1.0	1.2	1.40	1.9	2.1	1.2
As	ICP-MS	0.1	n.a.	n.a.	2.2	1.4	0.3	0.3	2.1	15.2	6.6	1.9
Sb	ICP-MS	0.02	n.a.	n.a.	0.5	0.7	0.1	0.8	0.1	0.6	0.1	0.1
Te	ICP-MS	0.02	n.a.	n.a.	0.2	0.1	0.3	0.1	0.1	24.0	1.3	0.5

Appendix 1 (cont.): Goechemiscal dataset of rock types located within the Podolksy deposit and geochemical data collected from literature located within and around the Sudbury Structure. Major and trace element analyses (XRF and ICP-MS) characterizing the grey gabbro unit. Apprviations used are as follows: n.a. = not analysed; b.d. = below detection; Mg# = MgO/(MgO+FeO); ppm = parts per million; ppb = parts per billion; wt% = weight percent; * Carter et al. 2009; ** = Lightfoot and Farrow 2002; [3] = Lightfoot et al. 1997a; [φ] = Ames et al. 2014; WR-XRF = whole rock x-ray flouresence; ICP-MS = Inductively coupled plasma mass spectrometry; LLD = lower limits of detection; QD = Quartz diorite; LQD = Leucocratic quartz diorite; IQD = Inclusion quartz diorite;; FWBX = Footwall breccia; JL Intrusion = Joe Lake Intrusion.

Mineral chemistry data for Felsic clots. All values are in combined element of oxygen.

	Na	K	Ca
Raster analysis of felsic clot	4.41	0	2.99
	4.26	0	2.61
	4.7	0	2.44
	4.48	1.27	1.97
	4.76	0	2.41
	4.2	0	2.86
	3.96	0	3.12
	4.1	0	3.09

	Na	K	Ca
Albite	6.42	0	0
	6.96	0	0
	7.55	0	0
	7.24	0	0
	6.58	0	1.14
	5.92	0	1.77
	6.88	0	0
	6.66	0	0
	6.79	0	0
	5.93	0	1.63
	5.82	0	1.58
	2.62	0	0.66
	0.46	0	0.19
	6.81	0	0.52
	7.27	0	0
	7.07	0	0
	1.13	0	0.46
	6.6	0	0
	6.71	0	0
	6.89	0	0

	Na	K	Ca
Alkali-Feldspar	0	7.32	0
	0	7.32	0
	1.08	5.11	0
	0	7.03	0
	0	6.45	0.28
	0	6.66	0
	0	7.37	0
	0	5.89	0
	3.80	1.52	0

	Na	K	Ca
Plagioclase	5.16	0	2.39
	4.75	0	2.75
	3.99	0	3.39
	4.56	0	3.13
	4.2	0	3.15
	4.76	0	2.41
	4.34	0	3.26
	4.19	0	3.05
	4.64	0	2.89
	4.45	0	2.95
	4.67	0	2.33
	4.56	0	2.78
	4.2	0	2.86
	4.56	0.5	2.53
	4.26	0	3.13
	3.8	0	2.97
	4.08	0.18	3.18
	4.17	0.1	3.18
	3.26	0	2.67
	4.8	0	2.92
	4.3	0	3.18
	4.36	0	2.89
	4.18	0	3.35
	4.27	0	2.95
	4.62	0	2.5
	3.94	0	3.11
	4.42	0	3.12
	3.96	0	3.12
	4.1	0	4.1
	4.8	0	2.56
	4.78	0	2.79
	3.12	0	1.74
	4.78	0	2.79
	4.17	0	3.06
	4.69	0	2.86
	4.29	0	2.88
	4.64	0	3
	4.41	0	2.99
	4.26	0	2.61
	4.7	0	2.44
	4.48	1.27	1.97
	4.49	0	3.04
	3.94	0	3.23
	4.25	0	2.72
	4.13	0	2.95
	4.29	0	2.95
	4.97	0	2.67
	4.36	0	3.21
	5.29	0	2.88
	3.99	0	3.41
	2.11	0	1.16
	5.47	0	2.2
	4.03	0	3.25
	3.76	0	3.53
	5.94	0	1.65
	4.21	0	3.24
	4.73	0	2.73

Appendix 2a: SEM-EDS felsic clot data summary

Mineral chemistry data for Mafic clots. All values are in combined element of oxygen.

	Mg	Ca	Fe
Raster analysis of mafic clot	8.56	6.23	3.17
	8.35	7.66	3.06
	8.6	8.19	3
	8.58	8.27	3
	7.49	7.61	3.06
	7.5	7.61	3.09
	9.58	6.24	3.67
	8.23	8.49	2.96
	11.36	1.17	4.77
	13.07		6.05
	11.32	1.36	4.79

	Mg	Ca	Fe
Amphibole	10.16	4.64	3.16
	9.78	4.49	3.01
	9.29	4.31	4.11
	9.63	4.84	2.98
	9.84	4.76	3.38
	9.7	4.44	3.25
	8.7	4.67	3.85
	9.18	5.16	3.64
	9.99	4.49	2.93
	9.81	5.04	2.87
	9.3	5.01	2.93
	9.47	4.48	2.63
	10.43	4.19	2.58
	9.45	4.8	3.63
	9.7	4.71	3.33
	9.2	4.79	3.69
	8.87	4.93	4.1
	9.45	4.64	3.25
	9.4	4.58	3.09
	8.6	4.89	3.96
	8.93	5.93	3.38
	9.47	4.95	3.48
	10.35	4.78	2.7
	10.16	4.5	3.42
	7.37	5.03	4.98
	8.26	5.18	3.99
	8.82	4.94	3.94
	8.15	5.06	4.48
	9.01	5.25	3.82
	8.52	5.06	4.29
	9.9	4.75	3.36
	8.43	5.11	3.84
	8.17	5.05	3.82
	8.97	5.34	4.08
	9.97	4.62	2.76
	8.95	4.96	4.03
	7.78	5.14	4.57
	4.44	5.16	4.44
	9.24	5.4	3.22
	6.12	5.38	18.87
	3.47	4.95	8.01
	3.3	4.93	8.19
	2.05	4.82	8.58
	4.04	4.91	7.57
	2.94	3.46	10.61
	2.8	4.87	8.64
	2.51	4.9	8.24
	3.65	4.82	7.14
	2.66	4.98	8.89
	2.67	5.02	7.76
	3.08	4.87	8.83
	2.38	4.84	8.95
	2.47	4.79	8.62
	2.7	4.87	8.75
	2.16	4.91	9.62
	3.68	4.97	8.04

	Mg	Ca	Fe
	4.5	4.48	5.99
	9.23	4.79	3.47
	6.71	4.86	6.11
	6.42	4.88	6.27
	6.84	4.99	5.95
	7.66	5.08	5.29
	7.5	5	5.31
	7.04	4.97	5.55
	6.74	5.05	5.48
	6.91	5.04	5.41
	10.6	4.83	2.63
	9.53	4.97	3.4
	6.91	5.04	5.41
	7.34	5.06	4.99
	7.09	5.15	5.27
	8.25	5.38	4.77
	3.53	4.97	1.12
	9.58	6.24	3.67
	10.24	6.1	2.56
	8.56	6.23	3.17
	7.44	6.63	3.7
	7.5	7.61	3.09
	8.35	7.66	3.06
	7.49	7.61	3.06
	8.82	8.09	2.39
	8.6	8.19	3
	8.58	8.02	2.4
	8.36	8.06	2.53
	8.58	8.27	3
	3.75	8.07	2.1
	8.27	8.11	2.41
	8.23	8.49	2.96
	8.22	8.53	2.62
	7.87	8.63	2.79
Pyroxene	8.26	8.56	2.75
	7.79	8.42	2.69
	7.53	8.49	2.62
	7.93	8.5	2.43
	7.09	9.16	2.38
	8.2	8.61	2.5
	8.23	8.82	2.6
	8.57	8.8	2.33
	8.37	8.86	2.19
	7.91	8.79	2.58
	8.28	9	2.29
	8.02	8.46	2.48
	8.1	8.55	2.83
	13.05		6.17
	13.58		5.63
	12.08		5.38
	13.16		5.31
	13.64		4.81
	12.15		4.06
	12.56		4.04
	12.29		3.78
	12.76		3.81
	12.29		3.39
	12.87		3.33
	12.3		3.37
	12.63		3.29
	12.99		3.32
	13.94		2.98
	13.56		2.65
	13.23		2.43
	13.68		2.31
	14.13		2.07
	11.83		1.95
	12.26		6.82
	12.06		3.98

Appendix 2b: SEM-EDS mafic clot data summary

Sample ID	Field of view	Target location	Mineral ID	Fe	O	Ti	Mn	Cr
LM-P-043G	SOI:13	Spectrum 1	Magnetite	74.53	22.96	1.35		0.64
LM-P-043G	SOI:13	Spectrum 5	Magnetite	76.42	22.51			0.7
LM-P-043G	SOI:14	Spectrum 2	Magnetite	73.5	23.25	2.15		0.55
LM-P-043G	SOI:15	Spectrum 2	Magnetite	73.95	23.09	2.03		0.57
LM-P-043G	SOI:22	Spectrum 1	Magnetite	76.79	22.47			0.35
LM-P-043G	SOI:22	Spectrum 2	Magnetite	77.73	22.27			
LM-P-055C	SOI:4	Spectrum 1	Magnetite	77.08	22.42	0.5		
LM-P-055C	SOI:7	Spectrum 2	Magnetite	77.73	22.27			
LM-P-055C	SOI:8	Spectrum 4	Magnetite	77.73	22.27			
LM-P-055C	SOI:9	Spectrum 2	Magnetite	73.9	23.15	2.13	0.31	
LM-P-019	SOI:1	Spectrum 1	Magnetite	74.25	23.02	2.36		
LM-P-019	SOI:1	Spectrum 2	Magnetite	77.39	22.35			
LM-P-019	SOI:5	Spectrum 1	Magnetite	77.73	22.27			
LM-P-019	SOI:5	Spectrum 3	Magnetite	77.73	22.27			
LM-P-019	SOI:14	Spectrum 1	Magnetite	76.08	22.65	1.28		
LM-P-019	SOI:16	Spectrum 1	Magnetite	77.73	22.27			
LM-P-019	SOI:21	Spectrum 5	Magnetite	76.79	22.53			
LM-P-019	SOI:21	Spectrum 6	Magnetite	77.73	22.27			
LM-P-019	SOI:21	Spectrum 7	Magnetite	76.91	22.37			
LM-P-019	SOI:22	Spectrum 2	Magnetite	77.73	22.27			
LM-P-019	SOI:22	Spectrum 3	Magnetite	76.2	22.6			
LM-P-019	SOI:24	Spectrum 7	Magnetite	77.73	22.27			
LM-P-019	SOI:25	Spectrum 5	Magnetite	76.63	22.4			
LM-P-019	SOI:27	Spectrum 4	Magnetite	77.73	22.27			
LM-P-019	SOI:27	Spectrum 5	Magnetite	76.19	22.39			
LM-P-019	SOI:32	Spectrum 1	Magnetite	77.73	22.27			
LM-P-019	SOI:34	Spectrum 1	Magnetite	75.38	22.81	1.81		
LM-P-007	SOI:1	Spectrum 2	Magnetite	77.73	22.27			
LM-P-007	SOI:1	Spectrum 3	Magnetite	77.73	22.27			
LM-P-007	SOI:5	Spectrum 1	Magnetite	76.33	22.59	1.08		
LM-P-007	SOI:5	Spectrum 2	Magnetite	77.12	22.41	0.47		
LM-P-007	SOI:5	Spectrum 3	Magnetite	77.29	22.32			0.39
LM-P-007	SOI:16	Spectrum 3	Magnetite	77.73	22.27			
LM-P-007	SOI:17	Spectrum 1	Magnetite	77.18	22.31			
LM-P-007	SOI:20	Spectrum 2	Magnetite	77.01	22.43	0.55		
LM-P-007	SOI:20	Spectrum 6	Magnetite	77.73	22.27			
LM-P-007	SOI:22	Spectrum 2	Magnetite	76.99	22.36			0.65
LM-P-007	SOI:24	Spectrum 1	Magnetite	77.01	22.35			0.63
LM-P-007	SOI:26	Spectrum 1	Magnetite	76.16	22.52	0.47		0.84
LM-P-007	SOI:29	Spectrum 1	Magnetite	75.65	22.63			1.19
LM-P-007	SOI:31	Spectrum 1	Magnetite	77.06	22.35			0.59

Appendix 2c: SEM-EDS magnetite data summary

Sample ID	Field of view	Target location	Mineral ID	Fe	O	Ti	Mn	Cr
LM-P-043G	SOI:14	Spectrum 1	Ilmenite	39	30.43	26.97	3.22	
LM-P-043G	SOI:15	Spectrum 1	Ilmenite	36.7	30.89	29.02	3.39	
LM-P-043G	SOI:22	Spectrum 3	Ilmenite	38.2	30.56	27.82	3.13	
LM-P-043G	SOI:24	Spectrum 4	Ilmenite	38.87	30.41	27.41	3.3	
LM-P-055C	SOI:8	Spectrum 5	Ilmenite	34.5	31.47	30.98	3.05	
LM-P-055C	SOI:9	Spectrum 1	Ilmenite	36.76	30.84	29.11	2.84	
LM-P-055C	SOI:10	Spectrum 2	Ilmenite	39.95	30.27	26.94	2.85	
LM-P-019	SOI:1	Spectrum 3	Ilmenite	34.02	31.52	31.02	2.96	
LM-P-019	SOI:14	Spectrum 3	Ilmenite	39.4	30.47	27.64	2.49	
LM-P-019	SOI:22	Spectrum 1	Ilmentite	35.45	31.4	30.76	2.39	
LM-P-019	SOI:25	Spectrum 4	Ilmenite	39.05	30.13	26.47	4.35	
LM-P-019	SOI:32	Spectrum 2	Ilmenite	40.89	29.89	25.67	3.55	
LM-P-019	SOI:32	Spectrum 3	Ilmenite	42.88	29.65	24.87	2.6	
LM-P-019	SOI:33	Spectrum 1	Ilmenite	43.75	29.54	23.84	2.38	
LM-P-019	SOI:34	Spectrum 2	Ilmenite	33.06	31.7	30.89	3.97	
LM-P-019	SOI:34	Spectrum 3	Ilmenite	44.22	29.3	23.36	2.22	
LM-P-007	SOI:18	Spectrum 1	Ilmentite	53.45	27.36	17.14	2.05	
LM-P-007	SOI:20	Spectrum 1	Ilmentite	38.2	30.62	28.13	3.04	
LM-P-007	SOI:21	Spectrum 2	Ilmentite	33.96	31.59	31.39	3.07	
LM-P-007	SOI:24	Spectrum 6	Ilmenite	38.06	30.72	28.46	2.76	
LM-P-007	SOI:27	Spectrum 3	Ilmenite	62.83	25.39	10.22	0.93	0.63

Appendix 2d: SEM-EDS ilmenite data summary

Chapter 3: The chemical fingerprint of alteration marginal to a sharp-walled Cu(-Ni)-PGE vein setting in the Sudbury ore district revealed from the Podolsky deposit, Sudbury, Ontario

Linette M. MacInnis[1], Daniel J. Kontak[1], Doreen E. Ames[2] and Nancy Joyce[2]

[1] Harquail School of Earth Sciences, Laurentian University, 935 Ramsey Lake Road, Sudbury, Ontario, P3E 2C6

[2] Geological Survey of Canada, 750-601 Booth Street, Ottawa, Ontario, K1A 0E8

Abstract

The nature of origin of an intense alteration zone's (i.e., epidote-actinolite) proximal to high-grade Cu-rich footwall's vein system located in Sudbury's world-class Ni-Cu-PGE mining district has been investigated by studying the Podolsky Cu(-Ni)-PGE deposit in the the North Range. Sharp-walled chalcopyrite veins are partly hosted in a relatively homogeneous gabbroic unit, which is referred to as the grey gabbro. This unit provides an excellent opportunity to constrain fluid:rock interaction and to assess the origin of fluids implicated in the alteration. Multiple 1 metre long transects adjacent to the sulfide veins combined with sampling intensely altered wall rock intervals of 2-3 cm adjacent the veins, provided the basis for a detailed petrographic, lithogeochemical, and isotopic (O, Sr, S) study. Petrographic observations indicate that although alteration related to mineralization is intense proximal (cm-scale) the veins, as manifested by an actinolite-epidote-quartz-chalcopyrite-magnetite assemblage, the alteration becomes cryptic (i.e., small clots and fracture-controlled alteration) and spatially diminishes over a distance of <1 m into the surrounding wall rock. Lithogeochemical traverses used to trace the alteration confirm its limited extent, with the exception of the LOI which relates to the formation

of hydrous alteration phases. Mass balance calculations indicate the most altered samples adjacent the veins record gains in LOI, S, Fe, Au, Pt, Pd, Ni, Cu, and Zn, which reflects invasion of sulfides into the wall rock, whereas minor losses in K, Rb, Sr, and Ba may reflect biotite altering to chlorite. The $\delta^{18}O$ and $^{87}Sr/^{86}Sr_{1850\ Ma}$ isotopic ratios for both least altered and altered whole-rock (i.e., grey gabbo) and an actinolite separate suggest a low fluid:rock ratio and rock-buffered system. The $\delta^{34}S$ signature of chalcopyrite (4.3 ± 0.3‰, n=15) is similar to other data for Sudbury ores and consistent with a crustal reservoir.

The study shows that where alteration is coincident with formation of the footwall Cu-rich sulfide vein systems, it is of very limited extent and thus not a viable vector for exploration. However, the detailed geochemical data suggest that crystallization of the sulfide melts in the footwall setting liberate an aqueous fluid and precious metals, which may be relevant to understanding the origin of the more distal low-sulfide type Au-PGE-rich systems in the footwall environments of the Sudbury mining district.

Introduction

The 1.85 Ga Sudbury Structure was historically mined for its relatively high-tonnage and moderate- to high-grade, contact- and offset-style magmatic sulfide deposits, which are located at the base of and in dikes associated with the Sudbury Igneous Complex (SIC), an impact melt sheet (Coats and Snajdr, 1984; Lightfoot et al., 1997; Rousell et al., 1997). A century of mining has begun to deplete many of the easily accessible (i.e., <2 km depth) traditional Ni-rich resources, thus in the past ~15-20 years the footwall rocks to the SIC have become a prime exploration target for new resources (Lightfoot, 2016). The footwall environment hosts a lower

tonnage of Cu, Ni and precious metals, but the ores have much higher grades which, along with the formerly high metal prices, made these resources attractive exploration targets.

The contact and offset deposits typically had low-Ni tenor ores (i.e., metals in 100% sulfides) averaging <5 % Ni_{100}, <5 % Cu_{100} and <1 g/t Au_{100}, Pd_{100}, and Pt_{100} (e.g., Naldrett and Pessaram, 1992; Farrow and Lightfoot, 2002; Ames and Farrow, 2007; Lightfoot, 2016). In contrast, footwall deposits contain higher tenor ores with >6.7 % Ni_{100}, >12.6 % Cu_{100} and >2.5 g/t Au_{100}, Pd_{100}, and Pt_{100} (e.g., Farrow and Lightfoot, 2002; Farrow et al., 2005; Ames et al., 2007).

The footwall ores typically underlie (or are interpreted to have once underlain) but are sometimes continuous with contact ores and appear to grade downward and outward from sharp-walled sulfide-rich veins and veinlets to stockworks and disseminations (e.g., Farrow et al., 2005; Stout, 2009; Nelles, 2012; Nelles et al., in review). Most workers have interpreted the footwall mineralization to be a Cu-Pd-Pt-Au-rich residual sulfide melt derived from the contact mineralization via fractionational crystallization of Ni-Co-Rh-Ru-Ir-rich monosulfide solid solution, (MSS; e.g., Keays and Crockett, 1970; Naldrett et al., 1999; Ballhaus et al., 2001; Barnes et al., 2001a, b; Mungall et al., 2004; Mungall, 2007; Dare et al., 2011). The aforementioned, albeit simplistic model, accounts for some but not all of the observed features of the high-grade footwall sulfide vein systems. In particular, the local formation of hydrous alteration assemblages (i.e., actinolite ± epidote ± chlorite ± magnetite) that occur at the interface of sulfide veins and wall rock and the associated haloes of F and Cl enrichment reported in a few deposit areas (e.g., Molnár et al., 2001; Péntek et al., 2008; Tuba et al., 2014). This alteration has been related to the formation of both the sulfide-rich footwall mineralization (e.g., Fraser deposit; Hanley and Mungall, 2003; Hanley and Bray, 2009) and the relatively sulfide-poor

zones characterized by higher PGE/S values (e.g., Farrow and Watkinson, 1992; Ames and Farrow, 2007; Tuba et al., 2014). The origin of the latter alteration and role in ore formation remains poorly quantified with respect to its relationship to fluids (e.g., Farrow and Watkinson, 1992; Hanley, 2005; Tuba et al., 2010, 2014; Hanley et al., 2011; Péntek et al., 2011; Lesher, 2017).

Farrow et al. (2005) provide a comprehensive review of the nature of the footwall vein-type mineralization styles. They concluded that deposits distal to the base of the SIC should be divided into a Cu-rich sharp-walled vein-style and PGE-rich (i.e., PPGE type) low-sulfide-type mineralization. The broad subdivision of these two ore types generally coincided with a separation of the two styles of mineralization into magmatic- and hydrothermally-related. The physical and chemical fingerprint of the hydrothermal alteration related to these footwall systems is observed throughout the Sudbury area with several detailed studies at a variety of settings indicating that multiple hydrothermal events likely occurred (e.g., Molnár et al., 2001; Péntek et al., 2008, 2011; Tuba et al., 2010, 2014; Hanley et al., 2011). In a more recent study of this ore environment, Tuba et al. (2014) examined the features of hydrothermal alteration types in footwall setting of the East Range, concluding that the observed low-sulfide PGE-rich zones originated from multiple fluid sources. The two important fluid sources identified were attributed to the contact zone at the base of the SIC and from granophyre that was generated in the footwall of the SIC due to partial melting.

The increasing demand for additional sulfide and PGE-rich deposits in the Sudbury area has provided the catalyst to improve both the conceptual understanding of deposit formation and models for footwall deposits in order to generate new exploration vectors. For example, the presence of hyper-saline fluid inclusions (e.g., Molnár and Watkinson, 2001; Péntek et al., 2008;

Tuba et al., 2014). Ni-Cu–rich amphibole (e.g., Hanley and Bray, 2009) at times appear to characterize footwall deposit setting. The focus of the current study follows this latter theme with the intent being to define the character and extent of alteration associated with the chalcopyrite-rich, sharp-walled footwall veins present in the recently mined Podolsky Cu(-Ni)-PGE, 2000 deposit (resource of 2.1 Mt of ore grading 4.55 % Cu, 0.4 % Ni, 0.139 oz./ton Pt+Pd+Au; 2007-2011; courtesy of KGHM, 2013), located in the Norman township, within the Whistle-Parkin radial offset of the Sudbury Structure.

In the Podolsky deposit, significant amounts of mineralization occur in a in a textural and compositionally relatively uniform gabbroic body which provides an opportunity to more effectively assess alteration. Such settings are not a common feature in the footwall environment of Sudbury where the rocks are generally geologically complex and therefore limits quantitative alteration studies. In the first part of this study (see Chapter 2), the host grey gabbro unit was fully characterized petrologically and forms the basis for the alteration study discussed here. Herein we present the results of detailed petrographic and SEM-EDS observations that are integrated with lithogeochemical profiles of the wall rock to the veins to assess elemental gains and losses. In order to fingerprint the fluid reservoirs, S, O, and Sr isotopic data were obtained for chalcopyrite veins and alteration minerals and rocks, respectively. Although microthermometric data were not collected, petrographic observations of quartz-hosted fluid inclusions in the alteration halo to veins were made to compare to similar observations in other studies. The results of study collectively indicate that intense fluid:rock interaction accompanied the mineralizing process, as also suggested by previous workers, this alteration was focused along the sulfide vein:wall rock contact and immediate wall rock halo (i.e., 10s cm). As such, the alteration is not a useful vector for exploration due to the limited scale of the alteration halo.

Geological Setting

Regional Geology

The Sudbury Structure (Fig. 1), which is located in the southern region of the Superior Province of the Precambrian Canadian Shield, hosts the product of an 1850 Ma bolide impact (e.g., Dietz 1960, 1964; Dressler, 1984; Krogh et al., 1982). This structure is located at the boundary of the ca. 2.7 Ga Superior Province (2711±7 Ma; Krogh et al., 1984) and the ca. 2.5 Ga Southern Province, the latter of which is dominated by the ca. 2.5 to 2.2 Ga Huronian Supergroup. The Sudbury Structure, which incorporates an impact-generated melt sheet and impact related geological features, is famous for the occurrence of a variety of magmatic Ni-Cu-PGE sulfide deposits that resulted from the formation of immiscible sulfide melt during the magmatic evolution of the SIC.

The Archean Superior Province located along the North and East ranges of the SIC (Fig. 1) consists of gneissic (i.e., Levack gneiss) and granitic units that record high-grade metamorphism and deformation at upper amphibolite to granulite facies (Ames and Farrow, 2007). Rare gabbroic bodies, such as the Joe Lake gabbro, intrude these basement rocks and their occurrence becomes relevant to this study as noted below. The Southern Province, which underlies the area south of the SIC (Fig. 1), is comprised of Paleoproterozoic Huronian Supergroup metasedimentary and metavolcanic rocks. These rocks were subjected to several periods of deformation and metamorphism; the Penokean Orogeny (ca. 1850 Ma; Mukwakwami et al., 2014) is likely the most intense. Ultramafic intrusive rocks of the East Bull Lake suite (2490-2470 Ma; Krogh et al., 1984) and the gabbroic rocks of the Nippising diabase suite (2210-

2217 Ma; Corfu and Andrews, 1986) intrude the South Range units and were an important part of the target rock sequence in the Sudbury area.

The Sudbury Structure is dominated by the 2.5-3 km thick Main Mass of the SIC, the crystallized product of the impact-generated melt sheet, which consists of a basal noritic unit and overlying granophyric unit that are separated by a thinner (10s m), transitional quartz gabbro unit. Also, part of the SIC are radial and concentric dike rocks and as part of the Sudbury Structure a variety of footwall breccia zones. The radial and concentric dike rocks consist of quartz diorite (QD) and inclusion-rich QD (IQD); the QD is considered to best approximate the initial composition of the melt sheet (Lightfoot et al., 1997, 2001). Breccia bodies associated with the SIC include footwall pseudotachylitic breccia (i.e., Sudbury breccia; Rousell et al., 2003), and inclusion-rich norites (i.e., the Sublary norite; Pattison, 1979; Naldrett, 1984), footwall anatectic and metabreccias (Lakomy, 1990; Lafrance et al., 2014) and overlying fall-back, suevitic, and phreatic breccias (i.e., Onaping Formation; Muir and Peredery, 1984; Ames et al., 2002; Grieve et al., 2010). The interior of the Sudbury Structure comprises a crater-fill sequence of fallback breccia material and eruptive units, already mentioned above, along with subsequent subaqueous sedimentary rocks that collectively make up the Whitewater Group. This group consists of the Onaping, Onwatin, and the Chelmsford formations, along with the discordant Vermilion Member that resides between the Onaping and Onwatin formations (e.g., Dressler, 1984; Krogh et al., 1984; Ames and Farrow, 2007).

Geology and mineralization of the Podolsky property

The Podolsky property occurs approximately 32 km NNE of the city of Sudbury, in Norman Township, where a NE-trending offset dike projects outward from the Whistle

embayment at the base of the SIC (Fig. 2A). This radial offset dike, which is referred to as the Whistle dike, crosscuts ca. 2.7 Ga Levack gneiss that is part of the Superior Province. The Whistle embayment is ~350-500 m wide, funnel-shaped, and is dominated by mafic norite that is bordered by sublayer norite along its base (Pattison, 1979; Giroux and Benn, 2005; Fig 2A). The Whistle offset dike extends from the base of the Whistle embayment, and at this latter point is ~2 km in length, ~100 m wide and distally narrows to a width of ~15 m (Carter et al, 2009). In the context of this study, the dike is important as it is host to the Podolsky Cu(-Ni)-PGE sulfide deposit (Fig. 2B). Between 2009 and 2011, the deposit produced 1.502 Mt of ore at 4.29 wt. % Cu, 0.38 wt. % Ni, and 0.139 oz./t TPMs (Pt+Pd+Au) (data courtesy of KGHM; see Fig. 2B). The deposit was put on care and maintenance in March 2013.

The offset dike is is composite with two main constituents, an inclusion quartz diorite (IQD) unit and a breccia unit. The IQD unit consists of a matrix of variably textured diorite within which there are a range of inclusions that include Levack gneiss, diabase dike, Matachewan diabase dike, quartz diorite, leucocratic quartz diorite, Sudbury breccia, metagabbro, grey gabbro, and pegmatitic rocks (see Chapter 2). The breccia unit is characterized by its recrystallized matrix; hence it is referred to informally as a metabreccia (MTBX); this recrystallized feature is attributed to conductive heat transferred from the cooling of the overlying superheated melt sheet. The breccia component of this unit contains a fine-grained, igneous textured matrix surrounding Archean basement clasts (Lafrance et al., 2014). As noted above, the offset dike hosts a wide variety of xenoliths that range in size (cm to m scale), have variable shapes, and are informally referred to by mine and exploration geologists (e.g., KGHM) as pods, (i.e., breccia components).

The Whistle embayment was the locus of contact-style massive sulfide ore that formed the Whistle mine. The disseminated, pyrrhotite-rich mineralization (5.7 Mt grading 0.33 % Cu and 0.95 % Ni; Farrow et al., 2005) was hosted by sublayer norite at the base of the embayment (Fig. 2A). Approximately 300 m below the base of the SW plunging embayment and ~650 m below the present surface resides the Podolsky 2000 deposit (Fig. 2B), which is a rare example of a "hybrid"–style deposit sharing characteristics of both sharp-walled vein and low-sulfide types of mineralization (Farrow and Lightfoot, 2002).

The majority of the hybrid mineralization in the Podolsky 2000 deposit resides in a breccia-hosted (MTBX-IQD) unit containing Cu(-Ni)-PGE veins and stockwork, but a significant component also resided at the time of mining in the grey gabbro (GG) unit, a fragment (~230 m x 90 m x 275 m) of dislodged gabbro transported to its present site during emplacement of the offset dike. The GG contains sharp-walled sulfide veins which forms the focus of this study. A plan map in Figure 3A shows the geology of the 1850 level, as mapped by Podolsky mine geologists, with the extent of the GG outlined and distribution of the sharp-walled sulfide veins shown. Within this area the GG is generally homogeneous but see below for further discussion as pertains to this study. Visual examples of the various sharp-walled sulfide veins and their contacts with wall rock (GG unit) are shown in Figures 3B-D. The alteration of the wall rock (GG unit) leading up to the sharp-walled sulfide veins is shown in Figure 3E, whereas examples of the hydrous alteration minerals observed along the contact of these sharp-walled sulfide veins and the wall rock are shown in Figures 3F-H.

Actinolite fiber veins

A local feature to some of the sharp-walled sulfide veins in the Podolsky deposit is the occurrence of narrow (<2-3 cm) actinolitic fiber veins. Fibrous monomineralic actinolite grains are observed along the contact between the GG and the sharp-walled sulfide vein (Figs. 3F,G). These grains are oriented perpendicular to the contact, except Figure 3G, shows a shear fabric, and is also observed as dislodged grains within the sulfide vein (Fig. 3G). Figure 3H is a closer image of the fibrous actinolite grains which contain L-V aqueous fluid inclusions.

Sampling and Analytical Methods

Thirty whole-rock samples of GG were collected from a variety of settings in the deposit area that included underground workings (see Fig. 3A), drill core, and transects marginal to the sulfide veins (Fig. 3B-D). Underground samples came from the 1700 (2), 1850 (2), 1925, and 2225 levels, whereas drill core material came from drill holes FNX4306, FNX4307, and FNX4938. For several samples detailed transects were made to assess alteration which included: (1) a detailed transect with 16 samples (LM-P-043A to LM-P-043P); (2) a minor transect of 4 samples (LM-P-055A to LM-P-055D); (3) 2 sets of paired samples against sharp-walled sulfide veins (LM-P-060A and LM-P-060B; LM-P-039A and LM-P-039B); (4) 3 intensely altered samples from against sulfide veins (LM-P-026, LM-P-027, LM-P-031) ; and (5) 3 least altered samples from various locations in the GG unit (LM-P-007, LM-P-021, LM-P-025). All the data are reported in Tables 1 and 2.

Tabular actinolite crystals, which form part of fiber veins localized to the contact of the GG and sharp-walled sulfide veins (Fig. 3E-G), were collected from one locality (Fig. 3H) for a variety of studies (Fig. 3H), including Ar-Ar dating and isotopic analysis (Sr,O). These samples

were prepared by crushing and sieveing and handpicking in alcohol using a binocular microscope to generate a high quality separate.

The thirty GG samples were analyzed for a complete package of major, minor and trace elements, which also included a suite of ore metals (e.g., Cu, Ni, Pt, Pd, Au, Ag, etc.) and volatiles (F, Cl, H_2O); the data are summarized in Tables 1 and 2. Two commercial laboratories (Actlabs and Acme) carried out these analyses and the analytical details are provided on the respective company websites (Actlabs, 2013; Acme, 2012). This data, along with the complementary analyses for the 23 samples of least altered GG, are provided in MacInnis et al. (2014).

Samples were studied petrographically, in both transmitted and reflected light modes, and with a JEOL 6400 scanning electron microscope (SEM) with an INCA energy dispersive spectrometer (EDS) in the Mineral Analytical Centre (MAC), at Laurentian University, Sudbury, Ontario. Operating conditions were: accelerating voltage of 20 keV, 1.005 ηA beam current, acquisition count times of 5-10 seconds, and a working distance of 15 mm. Well characterized standards (jadeite, diopside, orthoclase, corundum, quartz, chalcopyrite, pyrophanite) were used to calibrate the instrument. The detection limits for elements are estimated at about 0.15 wt. %.

Trace-element analyses of chalcopyrite grains from five polished thin-sections representing increasing distance along a sharp-walled chalcopyrite vein from the 2225 level of the 2000 deposit were obtained (Appendix 1). These analyses were done at the Chemical Fingerprinting Laboratory at Laurentian University, Sudbury, Ontario, using a 192 nm excimer laser (Resonetics RESOlution M-50) coupled to a quadrupole ICP-MS (Thermo X Series II). Approximately twenty grains per thin-section were ablated using a 10 to 14 μm beam size and repetition rate of 4 Hz. For each ablation, Cu was used as the internal standard assuming

stoichiometric chalcopyrite. Elements analyzed included Co, Ni, Zn, As, Se, Pd, Ag, Cd, In, Sb, Sn, Bi, Pt, and Au. The external standard used was NIST-610 glass.

Oxygen isotopic analyses of selected whole-rock samples along with both oxygen and deuterium isotopic analyses of a single actinolite separate were done at the Queen's Facility for Isotope Research (QFIR) in Kingston, Ontario. Standard procedures were used for extraction and isotopic ratios were determined using a Thermo-Finnigan MAC 253 and a DELTA^{PLUS}XP mass spectrometers; full analytical procedures are given in Kontak and Kyser (2011). The $\delta^{18}O$ data are reported in the standard notation of $\delta^{18}O$ relative to VSMOW and reported in per mil (‰) values; the analytical uncertainty is less than ± 0.1‰ and sample reproducibility is estimated at ± 0.2‰ (see Tables 1 and 2).

Three samples, two powdered GG rocks and one actinolite separate, were analyzed for $^{87}Rb/^{86}Sr$ and $^{87}Sr/^{86}Sr$ ratios at the Carleton University Isotope Geochemistry and Geochronology Research Centre (IGGRC) in Ottawa, Ontario. The samples were dissolved in 2.5 N HCl, pipetted in to a 14-ml Bio-Rad borosilicate glass chromatography column containing 3.0 mL of Dowex AG50-X8 cation resin. The solution was dried down and the residue dissolved in 0.26 HCl with the strontium then loaded onto a single Ta filament with H_3PO_4 and run at filament temperatures of 1350-1500°C on a ThemoFinnigan Triton Tl thermal ionization mass spectrometer. Two standards were run with the analysis – NIST SRM987 and the Eimer and Amend (E&A) – and the isotope ratios are normalized to $^{86}Sr/^{87}Sr = 0.11940$ to correct for fractionation (see Tables 1 and 2). Initial age-corrected $^{87}Sr/^{86}Sr_{1850\ Ma}$ ratios (i.e., $^{87}Sr/^{86}Sr_i$) ratios were calculated using using a decay constant of $1.42 \times 10^{-11}\ y^{-1}$. Four samples of sharp-walled chalcopyrite vein material collected from former underground workings of the mine (1700L, 1850L, 1900L, 2225L) were selected for sulfur isotopic analysis. These veins locally

contain angular GG clasts (Fig. 3B-D), have sharp contacts, and typically have narrow, actinolite-rich alteration selvages along their contacts (Fig. 3E-G). From these large samples, three sites (left edge, middle, right edge) across the <1 m width of five chalcopyrite veins were prepared for analyses. The material was pulverized to <1 mm size fragments and pure chalcopyrite separates handpicked using a binocular microscope; sample descriptions are given in Table 3. Sulfur isotopic analyses were done at the G.G. Hatch isotope laboratories, University of Ottawa, Ottawa, Ontario. Sulfide was pulverized in an agate and mortar pestle, mixed in tin capsules with equal or greater amounts of tungstic oxide and then loaded into a vario El cube elemental analyser (Elemantar, Germany) and flash combusted at 1800°C. The resultant gasses were released and carried by helium through the analyser to be cleaned, and then separated by chemical absorption "trap and purge" method. Sulfur dioxide gas was carried into a DeltaPlus XP isotope ratio mass spectrometer (ThermoFinnigan, Germany) coupled with a ConFlo IV for analysis. The results are reported in the standard notation of $\delta^{34}S$ relative to the Vienna Canon-Diablo Troilite scale (VCDT) and reported as per mil (‰) values; analytical uncertainty is estimated at less than ± 0.2‰ and sample reproducibility is estimated at ± 0.1‰ (see Table 3).

The same sample of hydrothermal actinolite used above for oxygen and strontium isotopic analysis was also used for $^{40}Ar/^{39}Ar$ geochronology (Fig. 3H). Pulverized and sieved (-60/+80 fraction) material was purified using heavy liquids (methylene iodide) and from the concentrate inclusion free, pure grains of 600-800 μm were handpicked for analysis; these grains were then rinsed for 15-minutes in an ultrasonic bath of acetone, followed by several rinses with deionized water and ethyl alcohol to remove all traces of methylene iodide. Samples were irradiated for 960 MWH in the medium flux position 8C (cadmium-shielded) at the research nuclear reactor of McMaster University (MNR) in Hamilton, Ontario. These mineral grains were

then conventionally step-heated (McDougall and Harrison, 1999) and analyzed with a Noblesse multi-collector noble gas mass spectrometer (Nu Instruments) at the Geological Survey of Canada. Further details of data acquisition and its processing are given in MacInnis et al. (2014).

Analytical Results

Petrographic features of the altered grey gabbro marginal the sharp-walled veins

To summarize the increasing degree of alteration of the GG unit towards the sharp-walled sulfide veins, a compilation of observations from multiple transects from the least altered to the most altered GG, as observed petrographically along with SEM-EDS observations, were used to prepare the summary diagram in Figure 4. To construct this diagram, an average distance correlation point was assessed based on each transect to determine when minerals appeared or were no longer present. In essence, this transect summarizes the degree of reaction or equilibration of the host rock (stage 1) with another medium, which is herein interpreted to be an incoming fluid, to form the most altered sample marginal to the sharp-walled vein (stage 5).

In Figure 4, the y-axis is a summary of the mineral phases present in the GG whereas the x-axis shows their relative abundance and extent in the traverse. In order to show the relative appearance of the mineral phase(s) that occur multiple times, their sequential appearance is represented by the numerals 1, 2 and 3. In this figure, it is inferred that the least altered or pre-impact unit is stage 1 (the GG) with subsequent numbers reflecting the later development of increasing degrees of alteration towards the sharp-walled sulfide vein. In this regard, it is noted that stage 1A, considered to be the original composition of the GG, and 1B, the GG prior to the bolide impact, are inferred to have been present in the GG but are not observed, and stage 1C represents the least altered GG observed. Some minerals present in stage 1, such as plagioclase

(i.e., primary magmatic), are not present in their original state but are included for the sake of completeness. Figure 4 also contains asterisks that represent inferred phases of the GG unit that were not observed in thin-section. The section below describes the petrographic features of the least altered GG, through the alteration of this unit towards the sharp-walled vein, and finally the most intensely altered GG.

Petrographic features of the least altered grey gabbro and the vein alteration halo

A detailed petrological study of the least altered GG unit is presented elsewhere (see Chapter 2) and is here summarized to provide context for the present study. The GG was originally an ophitic-textured gabbro dominated by calcic plagioclase and augitic pyroxene with minor quartz, orthopyroxene, hornblende, ilmenite and biotite, and accessory apatite and zircon. Due to the combined effects of the 1850 Ma impact event and, shortly thereafter, conductive heat transfer from the crystallization of the superheated melt sheet (i.e., SIC unit), the primary assemblage equilibrated during isochemical metamorphism. The secondary phases formed were dominated by the formation of granoblastic plagioclase and secondary actinolite (1) and biotite (2) after augitic pyroxene (CPX). Later modification of the GG relates to the influx of hydrothermal fluids possibly at the time of formation of the sharp-walled sulfide veins. This alteration occurs as clots where the GG is dissolved or vein formation where brittle features were present. This alteration increases in its intensity towards the sharp-walled veins, but there is a marked break in the development of the most intense alteration within a few cms of these veins (see Fig. 4). This fracture-controlled style of alteration is present in varying amounts of intensity and has been noted elsewhere proximal to other sharp-walled sulfide veins (e.g., Péntek et al., 2011; Tuba et al., 2014).

Petrographic evidence for the alteration sequence discussed and summarized in Figure 4 is shown in Figure 5, a 60 cm long transect through the GG towards a sharp-walled sulfide vein located on the 2225 level of the Podolsky deposit (Fig. 5A). The accompanying photomicrographs provide a summary of petrographic features in the least altered (stage 1) to the most altered (stage 5) GG unit. In stage 1 the granoblastic textured calcic plagioclase (Fig. 5B, D) and modified augitic pyroxene occurs (Fig. 5C, E). When observed in cross-polarized light, it is apparent that the minerals represent the relics of a fresh ophitic-textured gabbroic rock.

Alteration phase 1 (middle part of Fig. 4) represents hydrothermal alteration that is not associated with sulfide mineralization, which is discussed in detail below, but is instead related to the impact event and the ensuing high pressure-high temperature event that overprinted the GG unit. The granoblastic (mosaic) texture of plagioclase occurs in the relic or primary plagioclase (1) whereas formation of small equigranular and unzoned laths of plagioclase of An_{50} composition represent the second stage of plagioclase (2) in Figure 4. The latter plagioclase is then altered along grain boundaries to a third plagioclase (3) of An_{20} or albite (An_0) composition that occurs with quartz (2) and epidote (1) (Fig. 5D). Sericitization commonly occurs in the plagioclase domains and becomes more abundant toward the contact of the sharp-walled sulfide vein. Alkali feldspar and quartz (3) are observed as angular clasts with a granophyric texture. Fibrous actinolite (1) is often observed within relic augitic pyroxene crystals (CPX; Fig. 5E), whereas actinolite, and/or chlorite exist along the contacts of these relic pyroxenes. Euhedral crystals of biotite (2) lack the Fe-Ti-rich phases that are often present in biotite (1); as the latter is considered to be impact related (see Chapter 2) it suggests that biotite (2) has been generated post impact, thus part of alteration phase 1. Alteration of the augitic pyroxene typically increases towards the contact of the sharp-walled sulfide vein.

Petrographic evidence for the presence of hydrothermal alteration/mineralization of phase 2 (bottom part of Fig. 4) is most abundant <30 cm from the sharp-walled sulfide vein (see Fig. 4). The hydrothermal minerals are most commonly observed as alteration clots or dissolution features (Fig. 5F, G), and also as micro-veinlets (Fig. 5H, I) that likely exploited brittle fractures. The clots and micro-veinlets are commonly comprised of chlorite ± epidote (2) ± quartz (2) ± actinolite (3) ± calcite ± pyrite ± magnetite ± chalcopyrite; all the phases are subhedral to euhedral. Additionally, sericite is also present in this stage and although it occurs throughout the GG as an alteration of plagioclase, it is most abundant near the sharp-walled veins (see Fig. 5H) and marginal to carbonate veinlets that also are more common near the sulfide veins. Actinolite (2), as monomineralic fiber veins that resides along the contact of the GG unit and sharp-walled sulfide veins, are <1 to 2 cm wide, with the crystals oriented perpendicular to the vein walls (Fig. 5J-K). Actinolite (2) is interpreted to represent a different event compared to actinolite (1) based on its occurrence and the fact it is a monomineralic veinlet (Fig. 5J-K). The 'mineralization' proportion of phase 2 (Fig. 4) represents sulfides present within the clots, micro-veinlets, and the sharp-walled veins. Chalcopyrite, the most common sulfide, occurs in minor amounts throughout the GG and is often associated with magnetite replacing earlier ilmenite. Pyrite also occurs but it is a minor component. As the sharp-walled sulfide vein is approached, the amount of chalcopyrite increases.

Features of the most altered grey gabbro

The most altered proportion of the GG unit occurs within several cms (i.e., <5 cm) of its contact with the sharp-walled vein (Fig. 6) and is shown as stages 4 and 5 in Figure 4. This section of the GG is pervasively altered as a result of interaction with hydrothermal fluids that

presumably relate to mineralization. The minerals present in this zone are dominated by hydrothermal alteration/mineralization phase 2, in particular epidote, actinolite and chlorite with quartz and calcite also present. Figure 6A shows varying phases of alteration as the sharp-walled chalcopyrite vein that hosts subhedral silicate clasts is approached. In this sample thin bands of altered rock enriched in chlorite ± epidote (2) ± actinolite (3) ± quartz (3) ± calcite is interlayered in the wall rock (GG unit). Alteration clots leading up to these sharp-walled veins are comprised of euhedral to subhedral chlorite ± epidote (2) ± actinolite (3) and cored by magnetite ± pyrite (Fig. 6B-H). Varying proportions of chlorite ± epidote (2) ± actinolite (3) are present throughout these intensely altered halos to the veins and are commonly observed as mineral aggregates inside the sharp-walled sulfide veins (Fig. 6A, I, J).

Sulfide mineralization in the grey gabbro and sharp-walled veins

Sulfide mineralization, as sharp-walled veins, occurs throughout the GG with massive chalcopyrite dominating; minor amounts of magnetite, millerite, bornite, pyrite, and cubanite are present and most commonly observed close to vein margins (Fig. 7A-C). Spatially associated with the vein margins are fragments of hydrothermal minerals related to phase 2 of the alteration paragenesis (see Fig. 4); included as fragments are actinolite, epidote, chlorite, quartz and carbonate (Fig. 7D-F). Within the host rock, micro-veins also occur and consist of chlorite, quartz, epidote, actinolite and carbonate with variable chalcopyrite, magnetite and pyrite (Fig. 7G-I). Dissolution features also form in the adjacent wall rock and are lined by euhedral phases of the same assemblage just mentioned (Fig. 7J-O).

Petrographic features of fluid inclusions

Here is summarized the petrographic observations of fluid inclusions hosted by hydrothermal quartz from a sample marginal to a sharp-walled vein. This is the same sample from which the actinolite was sampled for isotopic study (see Fig. 3G, H, for location). These observations are provided due to the significance of fluid inclusions in the context of the origin of footwall vein systems, in particular the low-sulfide, PGE-rich systems (e.g., Farrow and Watkinson, 1992; Molnár et al., 1997, 1999, 2001; Hanley et al., 2005, Péntek et al., 2008; Hanley and Bray, 2009; Hanley et al., 2011; Tuba et al., 2014).

In the sample studied, the quartz was clear, lacked textural evidence of post-formation recrystallization and contained abundant fluid inclusions present either as isolated groups or along healed fracture planes (Fig. 8A); both groups observed are considered examples of fluid inclusions assemblages (FIA; Goldstein and Bodnar, 1994). As the former FIA could not be related to primary growth features in the host quartz, it is considered indeterminate in origin and may therefore still represent primary inclusions (e.g., Bodnar and Vityk, 1994; Bodnar, 2003). In contrast, the second type could be considered as either pseudosecondary or secondary in origin.

The fluid inclusions observed were in all cases aqueous (L_{H2O}-V) with the vapour phase occupying <5-10 % volume % of the inclusions (Fig. 8B, C). In addition, all the inclusions contained multiple solid phases, but the number, proportions and types of solid phases varied; for example, compare the fluid inclusions in Figures 8B and C. The latter feature has been reported in other studies of low-sulfide mineralization in Sudbury (e.g., Hanley et al., 2005, 2011). Thus, the inclusions present compare in their petrographic features to other fluid inclusions reported in similar settings in the Sudbury ore environments and therefore suggest that fluids of comparable bulk chemistry are represented in the alteration zones at Podolsky.

Whole-rock geochemistry

Examination of the whole rock data indicate similar elemental behavior in all the altered wall rock samples analyzed, as a result only some of the data is discussed in detail below in order to highlight the significance of the results; including the more detailed transect located on the 2225L (i.e., sample set LM-P-043; see Table 1) and the most intensely altered samples from against the sharp-walled veins (see Table 2). Detailed discussion of the remaining data is deemed redundant, but the data are included here to document the uniformity of the alteration.

Figure 9 summarizes the trace-and rare earth (REE) element data from the detailed transect; the complete data set is discussed separately below. In this figure, the results for five samples from distal to proximal (i.e., LM-P-043P to 043B) the sharp-walled sulfide vein are shown normalized against primitive-mantle and chondrite values. In order to compare and contrast with the transect samples the plots include the average value for the least altered GG (n = 3; red line). As observed in these normalized plots, there is only very slight variation in the datasets; the single exception is for sample LM-P-043D whose depleted values are attributed to the presence of calcite-rich micro-veins. As seen in the normalized plots, the carbonate veins have diluted the abundance of other elements in this sample.

Examining the results in more detail, the normalized data show in general there is only a slight departure from the average data for the least altered GG unit, with the large ion lithophile elements (LILE; K, Cs, Rb, Ba, Th, and U) showing the largest degree of departure. For the REE, the normalized plots essentially overlap, except for the carbonate-veined sample (LM-P-043D). Hence even for the REEs, which are sometimes sensitive to alteration, there is an absence of modification.

In order to assess in detail, the chemical variation in the detailed transect over 60 cm that used 16 samples, all the data are plotted in line traverses in Figures 10 to 13; note that each transect begins with the average composition for the least altered GG (Table 2), which has been shown to be very uniform chemically (see Chapter 2). Examining first the major and minor elements (Fig. 10, top to bottom), the transect profile shows that the unit remains chemically homogeneous throughout for many elements as the sharp-walled vein is approached, hence lack of mobility of Si, Al, Na, K, P and Ti. There are, however, some exceptions:(1) both TiO_2 and P_2O_5 show an abrupt drop of 0.2 wt. % at the beginning of the transect, which may reflect original differences for these elements in the GG; (2) both forms of iron, that is reduced (FeO) and oxidized (Fe_2O_3), and total iron change towards the vein with an overall increase in FeO and $FeO_{(total)}$ by 3-4 wt. %. Note that these changes are most dramatic for the five samples nearest the vein; (3) MgO shows a slight increase except for the central part of the traverse and the last 2 samples nearest the vein; (4) CaO is uniform along the traverse but drops by >1 wt. %, again over the last 5 samples; and (5) there is an irregular profile for both Al_2O_3 and S. As noted above, the only apparent exception to the trends is for sample LM-P-043D, which is attributed to the presence of carbonate ± quartz micro-veinlets; this is best indicated by the sharp increases in LOI and SiO_2. Lastly it is noted that for most of the elements there is a downward deflection in the trends over the last three samples nearest the vein that is likely due to mass gains and attributed to the addition of Fe, S and LOI, all of which show upward or increasing trends.

As for the trace elements in this 60 cm transect, the profiles generally remain uniform with similar elemental abundances as the least altered GG until proximal the vein, at which point there are subtle but sudden increases (e.g., Zr, Nb, Y) followed by depletion over the last three samples (Fig. 11). Again, the exception to this trend is for sample LM-P-043D in which variable

elemental enrichment and depletion occur. Also noted is the behavior of Ta, which shows a systematic depletion across the traverse.

The behavior of the REEs is summarized in Figure 12. In this plot it is seen that $(Eu/Eu^*)_N$, a good index of alteration since plagioclase is the main repository for Eu, is uniform, whereas a slight increase occurs in the total REEs and a notable fractionation of the REEs as indicated by increases in $(La/Lu)_N$, $(La/Sm)_N$, and $(Gd/Lu)_N$.

Figure 13 shows the abundances of metals, including the base- and precious- (Au, Ag, PGEs) metals. The following points are noted: (1) Cu is well above the average for the GG (i.e., ~2000 ppm) and is variably enriched across this transect, but with a maximum concentration at the sulfide vein contact; (2) Ni, Au, Pd and Pt generally follow the trend for Cu, including at the beginning of the transect and near the sulfide vein; (3) several elements (Co, Cr, Ag, Mn) show a similar uniform trend across the transect with a sudden decrease for the last five samples; and (4) there is generally uniform profile for Zn, but less so for Pb, which shows an overall convex upwards profile. In addition, both elements decrease over the last three samples, as noted before for other elements (Figs. 10-12).

In Figure 14, the average values of the three most intensely altered GG samples adjacent sharp-walled sulfide veins are compared to the average data for the least altered GG. In the normalized plot (Fig. 14A, B) a similarity of the profiles for the most altered and least altered samples of GG is observed, as noted above for samples from the detailed transect. There does appear, however, to be more departure of the average values with variable relative enrichment (K, Rb, Pb, Ba) and depletion (Th, U, Nb) for elements on the left of the spider diagram. In the chondrite normalized REE plot (Fig. 14B), there is near overlap of the two profiles, both being strongly fractionated, apart from Eu, which is clearly depleted in the most altered GG material.

As previously observed, there is a consistent relative depletion of the LREE in this diagram that suggests some mass gain.

In order to assess in detail whether there is much elemental variation due to mass change, either gains or losses, in the altered GG unit marginal to the sulfide vein, the Grant (1986) method was used to assess both the detailed transect and the most altered samples. For the detailed transect (sample LM-P-043), samples were compared sequentially commencing with the most distal sample (LM-P-043P) which was compared to the average least altered GG; the results are summarized in Appendix 2 (note the omission of sample LM-P-043D for reasons noted above). As the summary table shows, the major-, trace-, and REE elements show consistent values as sharp-walled sulfide veins are approached (i.e., no gains or losses), whereas the some base (Ni, Cu) and precious (i.e., Cu, Ni, Pd, Au, and Pt) metals show enrichment as the sharp-walled vein is approached, with highest values <5 cm from the veins.

In contrast to the transect data, results for the most intensely altered GG samples, based on an average of the three analyses, show mass gain and significant gains and losses (Fig. 14C). using the average of these data (n=3; Fig. 14C). In the latter plot, the mass factor used is based on the behavior of the LREE, which are all similar to the average GG, in addition to Al_2O_3 and SiO_2; we do however highlight the unusual apparent enrichment, and therefore mobility, of Zr, Hf and HREE based on this choice. A summary of the calculated gains and losses is presented in Figure 14D. We note for the major elements enrichment of Fe (40 %) and LOI (400 %) and loss of K (-60%), Na (-20 %) and K (-60 %), whereas for the trace elements most notable is the variable enrichment in a wide range of metals (Ni, Cu, Pt, Pd, Au, Ag, As, Bi, Sn, Zn), all of which exceed +200 %.

Trace-element geochemistry of chalcopyrite

Results for 16 trace elements determined in chalcopyrite from five samples along the detailed transect (LM-P-043) are summarized in Appendix 1, and shown graphically for each location in Figure 15, where each bar represents a single point analysis. The following points are first noted with regards to the data: 1) Ag, Ni, Zn, Se, Co, Pb, As, Bi, Sn, and In values are in the range of ppm, whereas Au and Pd are in the ppb range; 2) Sample A represents the sample proximal to the sharp-walled sulfide vein (>5 cm) whereas sample P represents the most distal sample to the vein (~60 cm); 3) Pt is below detection limits; and 4) each element is represented in log scale format. The following is a summary of the actual results:

1) Consistent levels in Ag, Ni, and Zn, regardless of the proximity of the sharp-walled sulfide vein, although Ag appears to be enriched to near 100 ppm near the vein;

2) Se contains high (>10 to 100 ppm) and consistent ppm values throughout the transect with a notable enrichment to >100 ppm proximal to the vein;

3) Cobalt, and Pb both show an irregular pattern throughout the transect with more regular enrichment near the vein;

4) As and Bi appear to be correlated throughout the transect and are relatively consistent in elemental abundances distal to the vein;

5) Sn and In show a very strong correlation throughout the transect with the highest values (>10 to 100 ppm) closest to the vein and much lower values (<5-10 ppm) distally. These two elements show a weak correlation with Se in terms of their enrichment proximal to the vein;

6) Relative to their vein location, Pd and Au, both in ppb values, generally show no correlation of their enrichment (10 to 100 ppb; Au to 1000 ppb) or depletions, although there is a

more consistent enrichment near the vein, and they behave similarly throughout the transect. A weak correlation is observed between these two elements and Ag, Ni, and Zn, with respect to their lack of enrichment/depletion relative to the vein.

Stable (O, S) and radiogenic (Sr) isotopic data

Results for 17 whole rock $\delta^{18}O$ analyses of the GG (Tables 1) from the detailed transect (LM-P-043; n=6), the most intensely altered GG samples (n=3), the shorter transects (n=7) range from +6.3 to +12.7‰. The sample (LM-P-043E) with the highest values contains a carbonate micro-veinlets and is thus excluded from the calculated average for altered GG samples of +7.0 ± 0.6‰ (n=16). Of the next most enriched samples, with values of +8.0‰ and +8.2‰, these either have micro-veinlets of carbonate or is one of the most intensely altered samples from adjacent a sharp-walled vein, respectively. In addition, no spatial correlation of the data is noted relative to either the sharp-walled sulfide veins or simple indices of alteration, such as values of LOI versus $\delta^{18}O$. Lastly, the three samples of most altered GG, which come from adjacent sharp-walled sulfide veins, average +6.6‰; exclusion of these samples would result in an average $\delta^{18}O$ of +7.3 ± 0.6‰ for the transect samples. For the two least altered GG samples values, $\delta^{18}O$ values of +6.9 and +7.7‰ were obtained.

An actinolite separate taken from the contact of the GG with the sharp-walled vein (LM-P-060; Fig. 3G, H) has a $\delta^{18}O$ value of +5.0‰ (Table 2). This value is abnormally low compared to the average value of +7.4 ± 0.5‰ for the GG and is discussed in more detail later.

Results of $\delta^{34}S$ analyses for fifteen chalcopyrite separates across four sharp-walled sulfide veins (Table 3) yielded values range from +3.4 to +4.5‰ with an average of +4.3 ±

0.3‰. A single analysis (LM-PRC-01.3B, +3.4‰) departed slightly from the otherwise tight clustering at +4.3‰.

Whole-rock strontium isotopic data were determined on one sample of least-altered GG (LM-P-007) one sample of altered GG (LM-P-043G) and the actinolite separate (LM-P-060); the data are given in Tables 1 and 2. The age-corrected initial $^{87}Sr/^{86}Sr$ ratios (Sr_i) for the whole rock samples are uniform with values of 0.70199 and 0.70092 at 2714 Ma, the inferred age of crystallization of the GG (see Chapter 2), and 0.703422 and 0.703050 at 1850 Ma, the time of the SIC impact event. The actinolite separate has a Sr_i value of 0.703054 at 1850 Ma, which is the same value for the GG at this time.

$^{40}Ar/^{39}Ar$ dating of actinolite

The results of step-heating experiments on five aliquots from a single actinolite separate collected at the contact of a sharp-walled sulfide vein are summarized in Figure 16. Also shown with the age spectra are the Ca/K and Cl/K profiles which monitor the chemical uniformity of the phase being analyzed. It is noted that aliquots 1 and 2 (Fig. 16A, B) represent single grains, whereas for aliquots 3, 4, and 5 (Fig. 16C-E) multiple grains were heated simultaneously (i.e., 4, 4, and 5 grains, respectively) in an attempt to increase the signal intensity and reduce the uncertainty of the ages. In all the analyses, the gas-release (i.e., $\%^{40}Ar/^{39}Ar$), Ca/K, and Cl/K patterns are sufficiently different for each aliquot such that none of the aliquots produced a plateau from which a robust age could be determined. These phenomena probably reflect intra- and intergrain compositional heterogeneity, and/or degassing of hydrothermal fluid inclusions of varying composition and abundance, which is possible based on the petrographic observations noting the nature of fluids inclusions (Fig. 8). Furthermore, the scatter of the data on the inverse

isochron plot (Fig. 16F) also indicates that there are multiple compositions of excess argon with no justification for choosing one regression over another in order to assign an inverse isochron age.

In a final attempt to resolve the scattered age results, single fusions of 14 single-grain aliquots were carried out. Integrated ages from aliquots 6 through 20 are presented in the age-probability plot in Figure 17 from which a weighted mean age of 1850 ± 30 Ma was calculated based on 10 grains (MSWD=1.08). Although the 10 grains used for this age calculation contained varying amounts of excess ^{40}Ar (see inset isochron plot in Fig. 17), a regression through the analyses was done that yielded an imprecise age of 1820 ± 40 Ma (corrected for excess ^{40}Ar), which is within error of both the weighted mean age and accepted age for the Sudbury impact event (1849.53 ± 0.21 Ma; Davis, 2008).

Discussion

Paragenetic evolution of the grey gabbro unit

The petrological signature of the least altered GG suggests some alteration prior to emplacement of the sharp-walled sulfide veins. Localized patches of intense alteration close (<10 cm) to the sharp-walled sulfide veins strongly implicates ingress of hydrothermal fluids at the time sulfide veins formed. The evidence supporting this interpretation is discussed below, but in an attempt to summarize the nature of the alteration and mineralization in the GG as sharp-walled veins are approached, the relevant information is presented graphically in Figure 18 and broken into three sections: A) a schematic diagram summarizing all of the relevant petrographic features; B) photomicrographs representative of the critical petrographic observations; and C) a paragenesis summarizing sequentially the development of the events.

Section (A) of Figure 18 is color coded and the following is noted: (1) blue is the least altered homogeneous GG; (2) red is a sharp-walled chalcopyrite-rich vein; (3) green circles are alteration clots with size proportional to proximity to the sharp-walled veins; (4) black lines are stringers of either alteration or micro-veinlets that often host sulfides; (5) beige are areas of most intensely altered GG; and (6) green hachured lines represent monomineralic actinolite fibers.

In section (B) of the figure, petrographic evidence supportive of the schematic drawing is shown with insert number referring to the sequence of events noted above: (1) least altered GG in both plane polarized light (PPL) and cross-polarized light (CPL) which highlights development of the subgrain or mosaic textured plagioclase domains; (2) most altered GG in PPL and CPL; (3) development of the actinolite fibers at the contact of GG and sulfide vein in combined CPL and reflected light (RL); (4) chlorite-rich alteration stringer in CPL; (5) actinolite-rich alteration clot with chalcopyrite in PPL-RL; and (6) a sulfide-rich sharp-walled vein in RL. Lastly, section (C) is a paragenetic summary of events, as represented by numbers inserted, recorded by the GG along with the relationship between alteration and mineralization.

Petrologic feature in the least altered grey gabbro

Detailed petrography complemented with SEM-EDS analyses and imaging indicate the GG unit records a complex, multi-stage history commencing with a primary assemblage of clinopyroxene, plagioclase, and minor amounts of orthopyroxene, biotite, magnesiohornblende, ilmenite, zircon, and quartz (Fig. 4). This assemblage was greatly modified due to a protracted post-crystallization history involving regional deformation prior to and after bolide impact (e.g., Card et al., 1984; Card, 1994; Ames et al., 2008), in addition to several events related to the

impact itself. For this study, we focus on those textures that first resulted from the impact event and subsequently discuss those textures that can be related to mineralization.

As summarized above and in detail in Chapter 2, the GG represents part of a composite fragment dislodged from a mafic intrusion similar to the Joe Lake gabbro hosted in Levack gneiss and sourced in the North Range. The presence of planar deformation features (PDF) in zircon in this unit implies excessive shock-induced pressure, which means other minerals must also have been texturally modified given the more robust nature of zircon. The lack of shock-induced features (e.g., PDFs, glasss) preserved in the quartz and plagioclase may reflect thermal annealing during conductive heat transfer from the cooling of the overlying SIC melt sheet, which has been speculated to have attained 2000ºK (e.g., Grieve et al. (2010) and references therein). This event is therefore considered responsible for the granoblastic or mosaic texture observed in relict plagioclase crystals (Fig. 18B (1)), presence of unusual K-feldspar ($Or_{96}An_4Ab_1$) locally enriched in Ba (i.e., ~1.7 wt. % BaO), and lack of shock features in quartz.

Petrological features of altered grey gabbro

The inferred hydrothermal alteration shown in Figure 18B depicts formation of the actinoite fibers (3), chlorite-rich micro-vein (4), and actinolite-rich micro-clots (5); the latter two features are common in the GG. These intensely altered areas contain actinolite ± epidote ± chlorite ±calcite ± quartz ± pyrite ± chalcopyrite. Micro-clots are observed throughout the GG but diminish in size distal to the sharp-walled sulfide vein. Micro-veins are also observed throughout the GG but do not appear to be spatially controlled. These features have been interpreted to provide a network for fluids to migrate into the GG.

In summary, petrography and imaging analysis reveal: (1) development of actinolite fibers prior to vein emplaced which grew in dilated fractures cutting the GG. The fluids responsible for these veins are discussed below in the context of isotopic data; and (2) intense alteration of the GG via coupled dissolution-precipitation to form new mineral phases (quartz-actinolite-epidote-magnetite-chalcopyrite). This alteration occurs distally (cms) as clots and intense replacement zones near the vein-GG contact. The presence of the clots and micro-veinlets of this same assemblage represents advancement of this alteration into the GG away from the sharp-walled vein.

Implications of the whole-rock geochemistry

Transect of the grey gabbro unit marginal to the sharp-walled vein

Detailed geochemical traverses in the GG have shown a lack of significant chemical gains and losses until proximal the vein (<10 cm) where the most intense alteration occurs (Fig. 9). The only exception to this trend is noted for a single sample (LM-P-043D) which is attributed to small carbonate veins. In the most detailed traverse (Figs. 10 to 13), the most significant change note was for Fe and LOI nearest the vein (<10 cm), although it was noted that LOI was elevated across the transect. The latter enrichments may account for the general decrease of many elements (TiO_2, FeO_T, CaO, P_2O_5, S; see Fig. 10) due to dilution, whereas the elevated LOI accounts for the presence of a variety of volatile-bearing phases (i.e., actinolite, epidote, carbonate) in the analysed samples. The overall increase in FeO_T is attributed to the addition of Fe^{2+} given that the amount of Fe^{3+} remains constant. Hence the latter reflects the presence of chalcopyrite, epidote and actinolite; although magnetite is present, its abundance (<1 %) was

insufficient to greatly affect the amount of ferric Fe. As noted, this increase in Fe, which would have increased the mass of the altered rock, likely contributed to the decrease in the relative abundance of some of the major (MgO, CaO, K_2O) and trace (Rb, Sr, REEs, Zr, Nb, Ta, Pb, Zn; see Fig. 11) elements. The gradual depletion of Ta proximal to the sharp-walled sulfide vein is attributed to replacement of ilmenite with magnetite. Surprisingly, S shows little variation in the chemical profile except over the last ~5 cm towards the vein in addition to samples at ~28 cm (LM-P-043H) and ~50 cm (LM-P-043N) from the vein; in all these cases this correlates with the presence of small micro-veins with alteration halos, presence of hydrothermal minerals, and chalcopyrite.

There is a slight increase in ∑REE across the transect (see Fig. 12), which is matched with increases in $(La/Lu)_N$, $(La/Sm)_N$, and $(Gd/Lu)_N$, but $(Eu/Eu^*)_N$ values remain uniform. These trends, coupled with the lack of any progressive mass changes, suggest that the observed changes in the REEs are fluid related and that the hydrothermal phases that were formed, such as actinolite and epidote (e.g., Tuba et al., 2014), were able to sequester any REEs liberated during alteration. The fact that there is a preference increase in the LREE, as the $(La/Sm)_N$ profile shows, suggests preferential uptake of these elements which is tentatively attributed to the presence of allanite. As for Eu, the lack of any anomaly, either positive or negative, suggests that during alteration there was no apparent change in fO_2 that would have mobilized Eu^{2+} or stabilized Eu^{3+}.

Of particular note for the detailed traverse are elemental profiles for the metals (Fig. 13). The most significant enrichment is for Au, Pd, Pt, and Cu, all of which show geochemical coupling and enrichment both nearest to the vein and distally. Copper is the only metal of interest to show a consistent enrichment above background values in the GG across the entire

profile. Although these samples were studied with the SEM-EDS, no PGE-bearing phases were identified, which means that when coupled with the low Pt and Pd values for chalcopyrite from LA ICP-MS analysis, it is not possible to say where these elements reside. The only other metal of interest that shows enrichment is Sn but has only slightly above values for least altered GG. Lastly, both Zn and Pb decrease in values near the vein, which is related, as noted above, to the addition of Fe to the rock, thus these elements are not coupled to Cu and the precious metals.

Mineralogical and geochemical signature of the most altered grey gabbro

The most intensely altered GG is dominated by hydrothermal alteration/mineralization phase 2 (Fig. 4) which include euhedral to subhedral chlorite ± sericite ± calcite ± epidote (2) ± actinolite (3) and cored by magnetite ± pyrite. The geochemical signature of the most intense alteration related to sharp-walled sulfide vein formation was determined by comparing the average of the three such samples to the average least altered GG (Fig. 14A, B). The derived isocon plot for these samples (Fig. 14C) indicates that the alteration involved some mass gain (i.e., 10 %). Using the mass factor defined by the isocon, gains and losses were estimated (Fig. 14D) and, as with the detailed transect, the largest gains were for both FeO_T and LOI, which were inferred to be about 37 % and 430 %, respectively, with mass losses for CaO (-28 %), Na_2O (-19 %), MgO (-3 %), and K_2O (-57 %). The gains of FeO_T and LOI are consistent with the alteration mineral assemblage noted above (i.e., epidote, actinolite, chlorite, magnetite). For the trace elements, the largest losses are noted for Ba, Rb, and Sr, all of which are similar and match that of K_2O, suggesting it reflects the breakdown of biotite. In contrast to the transect samples discussed above, there is notable loss of Eu (-20 %) which may reflect one or more of the

destruction of plagioclase in this zone, presence of quartz (i.e., cannot sequester REE) in the new assemblage, and a change in fO_2 and hence the ratio of Eu^{3+}/Eu^{2+}. Lastly, there is minor enrichment noted for some of the HFSE (Ta, Nb, Zr, Hf), which are generally noted to be immobile during hydrothermal alteration. This modest enrichment contrasts with the decrease of these elements in the detailed transect, in particular for the most intensely altered part, proximal the vein (Fig. 11). As a result, the alteration may in part relate to some combination of the variable and low abundances of these elements in the GG, as seen in some of the irregular profiles in Figure 11 (e.g., Zr, Ta, Nb).

In contrast to the above trace elements, there is a consistent trend of elemental gains for metals (Ni, Cu, Pt, Pd, Au, Ag, As, Bi, Sn, Zn), all of which exceed +200 %. This observation is further supported by the chemistry of chalcopyrite, discussed separately below. Metal enrichment is limited in its extent proximal to the wall rock and relates to fluid ingress, as documented by clot formation (Fig. 18A, B). The timing of this fluid ingress is considered to represent the terminal stage in the formation and crystallization of the sulfide vein with enrichment of metals having a low partition coefficient for chalcopyrite (i.e., intermediate solid solution or ISS). This metal enrichment in the alteration zone is similar to low sulfide PGE zones and has been previously documented (e.g., Farrow et al., 2005; Péntek et al., 2008; Tuba et al., 2010). The very limited extent of the alteration halos indicate that this zone experiences high fluid:rock ratios, the amount of fluid must have been low compared to the volume of the sulfide melt (e.g., Péntek et al., 2008; Tuba et al., 2014).

Implications of LA ICP-MS analysis of chalcopyrite

The LA ICP-MS analyses of chalcopyrite (Fig. 15) indicate variable enrichment (to >100 ppm) for Ag, Ni, Zn, Se, Co, Pb, As, Bi, Sn, and In and also Au and Pd (to >100 ppb). In addition, the data reflects an element zonation with variable enrichment of metals such that Sn and In, and to some extent Se and Co, are most enriched near the vein; Pb, As and Bi in contrast are generally most enriched distal to the vein. The values of the precious metals (Au, Pd) are also most enriched near the vein if averages are used. These results are somewhat similar to those of the mass balance for the most altered wall rock samples, thus it can be inferred that the fluid responsible for the alteration and metal enrichment was the same. The chemistry of chalcopyrite also provides more convincing for fluid ingress and metal enrichment into the wall rock that the detailed lithogeochemical transects suggest (Fig.13). In addition, assuming that transport was via a fluid phase, the variation in abundances for some of the metals suggests either a thermal or chemical gradient away from the sulfide vein.

The trace-element data for chalcopyrite, which strongly suggests evidence of metal transport via a fluid phase, thus provides an analogy to the formation of low-sulfide PGE type mineralization in the Sudbury footwall environment (e.g., Li and Naldrett, 1993; Péntek et al., 2008; Tuba et al., 2010, 2014), Although a detailed study of the fluid inclusions observed in the alteration halo to the sulfide vein (Fig. 8) was not part of this study, the fact that they are multi-solid, high-salinity types provides additional supporting evidence of similarity with fluids identified in the low-sulfide, PGE-rich footwall settings (e.g., Farrow et al., 1994; Molnár et al., 2001; Hanley, 2005). As a result, there is compelling evidence from both the trace-element enrichment and the fluid chemistry to suggest the fluids exsolved from the sharp-walled veins relate to those implicated in low sulfide-type mineralization.

Chemical signature of the altering fluid

The mass balance inferred from the isocon plot for the most intensely altered GG samples can be used to best infer the chemical fingerprint of the altering fluid. Based on this, the fluid is characterized as being enriched in Fe and S in addition to a variety of metals, the most important being Cu, Au, Pd, Pt, Ni, and Ag, but also Sn, Bi, As, Mn and Zn. This signature would be consistent a fluid originating within the sulfide melt that formed the sharp-walled sulfide veins. The extent of alteration noted is limited to the immediate contact zone indicates the mass of fluid released during solidification of the sulfide vein was low compared to the mass of the sulfide melt.

Whole-rock geochemistry (Table 2) shows increases in FeO_T, CO_2, S, Cl, and LOI, and no significant change in the amount of fluorine present relative to the least and most altered GG samples. Previous authors (e.g., Li and Naldrett, 1993; Farrow et al., 1994; and Hanley, 2005) have suggested that Cu, Au, Pd, and Pt were liberated from the contact-style deposits and transported into the footwall and 'hybrid' deposits. As mentioned above, hydrothermal fluids associated with mineralization in the Podolsky setting formed halos around sharp-walled sulfide veins, clots in the wall rock GG, and produced smaller unmineralized veins, as summarized in Figure 18. Varying phases of alteration are present within these hydrothermal areas and are enriched in chlorite ± epidote ± actinolite ± quartz ± calcite.

Implications of the actinolite fiber veins

Locally the contact between the GG and the sharp-walled sulfide veins is marked by the presence of narrow (<1-2 cm) zones of monomineralic, fibrous actinolite oriented perpendicular

to the contact (Fig. 3F, G), except where it is subsequently sheared. This actinolite is also present as dislodged grains or aggregates in the sulfide vein (Fig. 3E, G). We note in these grains the rare presence of two phase, high temperature (i.e., ca. 350°C) L-V aqueous fluid inclusions, the latter temperature based on their phase ratios.

The occurrence of this actinolite, plausibly representing a pre-sulfide vein hydrothermal event, indicates that pre-existing fractures in the GG unit were dilated and infilled (Fig. 18C). The latter may reflect post-impact adjustment of this area related to formation of the Sudbury Structure, as suggested by several other workers (e.g., Farrow et al., 1994; Farrow et al., 2005; and Péntek et al., 2008). Importantly, these dilational fractures are also noted in other deposits in the North Range (e.g., McCreedy West, Broken Hammer; Farrow et al., 2005; Péntek et al., 2008; Tuba et al., 2014) and are preferentially oriented northeastwards (e.g., Farrow et al., 1994; Hanley and Mungall, 2003; Farrow et al., 2005; Péntek et al., 2008). These fiber veins indicate therefore that, in at least some cases, sharp-walled sulfide vein formation exploited pre-existing structural features, an observation that is important in the context of deposit formation.

Implications of isotopic data (O, S, Sr)

The results for $\delta^{18}O$ analyses of the GG did not indicate a strong spatial correlation that can be related to the sharp-walled sulfide veins as the average value for all the transect samples of +7.0 ± 0.6‰ is similar to the average value of 7.3‰ for least altered GG. The only departure from this was for a sample with micro-veinlets of carbonate for which its anomalously high $\delta^{18}O$ value of +12.7‰ reflects the high mineral-H_2O fractionation factor for carbonate. With regards to the data for the three intensely altered samples that average +6.6 ± 0.6‰, this is only slightly less than the average (+7.3‰) for the least altered GG. This minor variation indicates no

significant modification of the $\delta^{18}O$ signature of the GG due to vein-related fluid infiltration which we attribute to two factors: 1) the alteration phases (act-epid-chl) have an aggregate mineral-H_2O fractionation factors at 350-450°C of -0.4 to -1.0; and 2) the alteration was rock buffered or low fluid:rock system.

The actinolite separate has a $\delta^{18}O$ value of 5.0‰, which equates to a $\delta^{18}O_{H2O}$ value between +6.1 to +6.9‰ for mineral-H_2O fractionation between 400°C to 600°C (Zheng, 1993). Again, this data suggests that the actinolite grew from a fluid with a magmatic signature or one that had equilibrated with the GG at a low fluid:rock ratios at high temperature and consistent with data for altered GG.

In terms of sourcing this fluid, the Superior Province basement rocks in the area, which are dominated by felsic and intermediate gneiss, have $\delta^{18}O$ values between 6.9 to 8.4‰ (Shieh and Schwarcz, 1978). This value range means that any fluid contribution from this source would most likely be undetected and excludes the possibility of the fluid signature having a high- or low- $\delta^{18}O$ signature relative to the average GG value. The strontium isotope data discussed below is consistent with this interpretation.

Sulfur isotopic data for sharp-walled sulfide veins are uniform +4.5 ± 0.5‰. This value is comparable to values for sulfide mineralization in the North Range area versus the South Range (Ripley et al., 2015) and consistent with derivation of S from a magmatic reservoir (i.e., the SIC). These values also suggest that these sulfides, both at Podolsky and elsewhere, were deposited under similar physio-chemical conditions since no fractionation is recorded as would be expected if there had been changes in intensive parameters such as T and fO_2 (i.e., SO_4/H_2S; e.g., Ohmoto and Rye 1979; Ohmoto, 1986; Taylor, 1986).

Strontium isotopic data obtained for two least altered GG samples and a fibrous actinolite sample adjacent a sulfide vein provide similar Sr_i values at 1850 Ma, these being 0.703422 and 0.703050 versus 0.703054, respectively. These results are strongly suggestive that the actinoite formed in rock buffered, low flud:rock system. The data are also consistent with inferences based on the $\delta^{18}O$ data.

$^{40}Ar/^{39}Ar$ dating

Dating of fibrous actinolite from adjacent a sharp-walled sulfide vein gave variable results with the most reliable yielding a mean age of 1850 ± 30 Ma based on results for 10 total fusion analyses (Fig. 16). This age, interpreted to represent the time actinolite cooled below its blocking temperature of 350-400°C (McDougall and Harrison, 1999). The age for both total fusion and step-heating are therefore consistent with the the 1850 Ma Sudbury impact event (Krogh et al., 1984; Davis, 2008). The coincidence of these ages and the flat age spectra strongly suggest therefore that, within error, the actinolite did not experience a later heating event that approached its blocking temperature. The age dating precludes therefore ingress of heated fluids post the mineralizing event and contrast with the younger 1477 ± 8 Ma Ar-Ar biotite ages recorded for samples from mineralized zones in the South Range (Bailey et al., 2004). The results further suggest that latter thermal events in the area were not homogeneous in nature.

Conclusions

Footwall Cu-PGE-rich sulfide deposits in the Sudbury Structure have in recent years become prime exploration targets in this mature mining district. Thus, understanding the nature and origin of alteration proximal to these sulfide zones have the potential to provide useful

exploration indicators for further discoveries. Based on the present study, such alteration appears to be limited in its scale only to proximal the sharp-walled sulfide veins hosted by the grey gabbro unit in the Podolsky footwall sulfide system and thus are of limited use as an exploration vector. This study did however prove useful when furthering our understanding of footwall mineralized environments in the Sudbury Structure, most notably the deposits located in the North Range. In this context the most relevant outcomes are as follows: (1) defining the extent of the development of intense and more cryptic alteration marginal the sharp-walled sulfide veins, which appear to be a few cms to 10s cm, respectively, which reflects mainly the formation of epidote, actinolite, quartz, chlorite, chalcopyrite and magnetite; (2) constraining element mobility in the alteration zones, which is limited mainly to LOI and FeO for the major elements. In addition, there are noted gains, as expected, for the ore metals (e.g., Au, Pd, Pt, Cu, Ni), as seen in both whole-rock data and in situ LA ICP-MS analysis of chalcopyrite; 3) the source of the fluid is likely sourced in the crystallizing sulfide melt, as constrained from the mass balance and supporting data from O, Sr and S isotopes; and 4) formation of actinolite fibers lining the sharp-walled sulfide veins, which are constrained to forming at ca. 1850 ± 30 Ma based on $^{40}Ar/^{39}Ar$ dating, provide evidence for a fluid front to the sulfide melt which following pre-existing brittle pathways in the footwall setting and which were subsequently exploited to form the sulfide bodies.

Thus, whereas alteration halos related to formation of footwall sulfide veins at the Podolsky deposit are present they are limited in scale to proximal ore systems and as a result, are not a useful exploration tool. However, a detailed study of the geochemical features of these alteration zones provided important data relevant to advancing our understanding of the

evolution of the sulfide melts as they crystallized to generate Cu-rich footwall veins and PGE-rich low-sulfide ore systems.

References

Acme Analytical Laboratories, 2012, Acme Price Brochure (www.acmelab.com/pdfs/FeeSchedule-2015.pdf).

Actlabs, 2013.Actlabs Price Brochure, (actlabs.com/filed/Canada/2015.pdf).

Ames, D.E., and Farrow, C.E.G., 2007, Metallogeny of the Sudbury mining camp, Ontario, *In* Goodfellow W.D., ed., Mineral deposits of Canada: A synthesis of major deposit-types, district metallogeny, the evolution of geological provinces, and exploration methods: Geological Association of Canada, Mineral Deposits Division, Special Publication, 5, p. 329-350.

Ames, D.E., Golightly, J.P., Lightfoot, P.C., and Gibson, H.L., 2002, Vitric compositions in the Onaping Formation and their relationship to the Sudbury Igneous Complex, Sudbury Structure: Economic Geology, v. 97, p. 1541-1562.

Ames, D.E., McClenaghan, M.B., and Averill, S., 2007, Footwall-hosted Cu-PGE (Au, Ag), Sudbury Canada: Towards a new exploration vector: Geochemical Case Histories and Geochemical Exploration Methods, Paper, 87, p. 1-5.

Ames, D.E., Davidson, A., and Wodicka, N., 2008, Geology of the Giant Sudbury Polymetallic Mining Camp, Ontario, Canada: Economic Geology, v. 103, p. 1057-1077.

Bailey, J., Lafrance, B., McDonald, A.M., Fedorowich, J.S., Kamo, S., and Archibald, D.A., 2004, Mazatzal-Labradorian-age (1.7-1.6 Ga) ductile deformation of the South Range Sudbury impact structure at the Thayer Lindsley mine, Ontaro: Canadian Journal of Earth Sciences, v. 41, p. 1491-1505.

Ballhaus, C., Tredoux, M., and Spath, A., 2001, Phase relations in the Fe-Ni-Cu-PGE-S system at magmatic temperature and application to massive sulphide ores of the Sudbury Igneous Complex: Journal of Petrology, v. 42, p. 1911-2026.

Barnes, S.-J., Melezhik, V.A., Sokolov, S.V., 2001a, The composition and mode of formation of the Pechenga nickel deposits, Kola Peninsula, Northwestern Russia: Canadian Mineralogy, v. 39, p. 447-471.

Barnes, S.-J., van Achterbergh, E., Makovicky, Li., 2001b, Proton microprobe results for the partitioning of platinum-group elements between monosulphide solid solution and sulphide liquid: South African Journal of Geology, v. 104, p. 275-286.

Bodnar, R.J., 2003, Introduction to Fluid Inclusions, i*n* Samson, I., Anderson, A., and Marshall, D., eds., Fluid Inclusions Analysis and Interpretation: Mineral Association of Canada, Short Course, 32, 1-8.

Bodnar, R.J., and Vityk, M.O., 1994, Interpretation of microthermometric data for H_2O-NaCl fluid inclusions, *in* De Vivo, B., and Frezzotti, M.L., eds., Fluid inclusions in minerals: Methods and Applications: Short Course of the Working Group (IMA) "Inclusions in Minerals", p. 117–130.

Card, K.D., 1994, Geology of the Levack gneiss complex, the northern footwall of the Sudbury structure, Ontairo: Geological Survey of Canada, Current Research 1994, p. 269-278.

Card, K.D., Gupta, V.K., McGrath, P.H., and Grant, F.S., 1984, The Sudbury Structure: Its regional geological and geophysical setting, *in*Pye, E.G., Naldrett, A.J., Giblin, P.E., eds., Geology and Mineral Deposits of the Sudbury Structure: Ontario Geological Survey, Special Volume, 1, p. 25-44.

Carter, W.M., Watkinson, D.H., Ames, D.E., and Jones, P.C., 2009, Quartz diorite magmas and

Cu(-Ni)-PGE mineralization, Podolsky Deposit, Whistle offset structures, Sudbury, Ontario: Geological Survey of Canada, Open File, 6134.
Coats, C.J.A., and Snajdr, P., 1984, Ore deposits of the North Range, Onaping-Levack area, Sudbury, Ontario: Geological Survey, special volume 1, p. 327-346.
Corfu, F., and Andrews, A.J., 1986, A U-Pb age for mineralized Nippissing diabase, Gowganda, Ontario: Canadian Journal of Earth Sciences, v. 23, p. 107-109.
Dare, S.A.S., Barnes, S.-J., Prichard, H.M., Fisher, P.C., 2011, Chalcophile and platinum-group element (PGE) concentrations in the sulfide minerals from the McCreedy East deposit, Sudbury, Canada, and origin of the PGE in pyrite: Mineralium Deposita, v. 46, p. 381-407.
Davis, D., 2008, Sub-million-year age resolution of Precambrian igneous events by thermal extraction-thermal ionization mass spectrometer Pb dating of zircons: Application to crystallization of the Sudbury impact melt sheet: Geology, v. 36, p. 383-386.
Dietz, R., 1960, Meteorite impact suggested by shatter cones in rock: Science, v. 131(3416), p. 1781-1784.
Dietz, R.S., 1964, Sudbury structure as an astrobleme: Journal of Geology, v. 72(4), p. 412-434.
Dressler, B.O., 1984, General Geology of the Sudbury Area, *in* Pye, E.G., Naldrett, A.J., Giblin, P.E., eds., Geology and Mineral Deposits of the Sudbury Structure: Ontario Geological Survey, Special Volume, 1, p. 57-82.
Farrow, C.E.G., and Lightfoot, P.C., 2002. Sudbury PGE revisited, Towards an Integrated Model, *in* Cabri, L.J., ed., The Geology, Geochemistry, Mineralogy and Mineral Beneficiation of Platinum-Group Elements: Canadian Institute of Mining, Metallurgy and Petroleum, Special Volume, v. 54, p. 273-298.
Farrow, C.E.G., and Watkinson, D.H., 1992, Alteration and the role of fluids in Ni, Cu and platinum-group element deposition, Sudbury Igneous Complex contact, Onaping-Levack area, Ontario: Mineralogy and Petrology, v. 46, p. 67-83.
Farrow, C.E.G., Watkinson, D.H., and Jones, P.C., 1994, Fluid inclusions in sulfides from North and South range Cu-Ni-PGE deposits, Sudbury Structure, Ontario: Economic Geology, v. 89, p. 647-655.
Farrow, C.E.G., Everest, O.J., King, D.M., Jolette, C., 2005, Chapter 8: Sudbury Cu(-Ni)-PGE systems, Refining the classification using McCreedy West Mine and Podolsky project case studies, *in* Mungall, J.M., ed., Exploration for Platinum-Group Elements Deposits: Mineralogical Association of Canada, Short Course, 35, p. 163-180.
Giroux, L.A., and Benn, K., 2005, Emplacement of the Whistle dike, the Whistle embayment and hosted sulfides, Sudbury impact structure, based on anisotropies of magnetic susceptibility and magnetic remanence: Economic Geology, v. 100(6), p. 1207-1227.
Goldstein, R.H., and Reynolds, T.J., 1994, Chapter 2: Fluid inclusions in their origin, *in* Goldstein, R.H., and Reynolds, T.J, eds., Systematics of fluid inclusions in diagenetic minerals: The Society for Sedimentary Geology, Short Course 31, p. 5-21.
Grant, J.A., 1986, The isocon diagram – a simple solution to gresens' equation for metasomatic alteration: Economic Geology, v. 81, p. 1976-1982.
Grieve, R.A.F., Ames, D.E., Morgan, J.V., and Artemieva, N., 2010, The evolution of the Onaping Formation at the Sudbury Impact Structure: Meteoritics and Planetary Science, v. 45, p. 759-782.

Hanley, J.J., 2005, Chapter 2: The aqueous geochemistry of the platinum-group elements (PGE)

in surficial, low-T hydrothermal and high-T magmatic-hydrothermal environments, *in*, Mungall, J.E., ed., Exploration for Platinum-Group Element deposits: Mineralogical Association of Canada, Short Course Series, v. 35, p. 35-56.
Hanley, J.J., and Bray, C.J., 2009, The trace metal content of amphibole as a proximity indicator for Cu-Ni-PGE mineralization in the footwall of the Sudbury Igneous Complex, Ontario, Canada: Economic Geology, v. 104(1), p. 113-125.
Hanley, J.J., and Mungall, J.E., 2003, Chlorine enrichment and hydrous alteration of the Sudbury breccia hosting footwall Cu-Ni-PGE mineralization at the Fraser Mine, Sudbury, Ontario, Canada: The Canadian Mineralogist, v. 41(4), p. 857-881.
Hanley, J.J., Mungall, J.E., Pettke, T. Spooner, E.T.C., and Bray, C.J., 2005, Ore metal redistribution by hydrocarbon-brine and hydrocarbon-halide melt phases, North Range footwall of the Sudbury Igenous Complex, Ontario, Canada: Mineralium Deposita, v. 40, p. 237-256.
Hanley, J., Ames, D., Barnes, J., Sharp, Z., and Guillong, M., 2011, Interaction of magmatic fluids and silicate melt residues with saline groundwater in the footwall of the Sudbury Igneous Complex, Ontario, Canada: new evidence from bulk rock geochemistry, fluid inclusions, and stable isotopes: Chemical Geology, v. 281(1-2), p. 1-25.
Keays, R.R., and Crocket, J.H., 1970. A Study of Precious Metals in the Sudbury Nickel Irruptive Ores: Economic Geology. v. 65, p. 438–450.
Kontak, D.J., and Kyser, K., 2011, A fluid inclusion and isotopic study of an intrusion-related gold deposit (IRGD) setting in the 380 Ma South Mountain Batholith, Nova Scotia, Canada: evidence for multiple fluid reservoirs: Miner Deposita, v. 46, p. 337-363.
Krogh, T.E., McNutt, R.H., and Davis, G.L., 1982, Two high precision U-Pb zircon ages for the Sudbury Nickel Irruptive: Canadian Journal of Earth Sciences, v. 19(4), p. 723-728.
Krogh, T.C., Davis, D.W., and Corfu, F., 1984, Precise U-Pb zircon and baddeleyite ages for the Sudbury Structure, *in* Pye, A.J., Naldrett, A.J., and Giblin, P.E., eds., The Geology and Ore Deposits of the Sudbury Structure: Ontario Geological Survey, Special Volume, 1, p. 431-446.
Lafrance, B., Bygnes, L., and McDonald, A.M., 2014, Emplacement of metabreccia along the Whistle offset dike, Sudbury: implications for post-impact modification of the Sudbury impact structure: Canadian Journal of Earth Sciences, v. 51(5), p. 466-484.
Lakomy, R., 1990, Implications for cratering mechanics from a study of the Footwall Breccia of that Sudbury impact structure, Canada: Meteoritics & Planetary Science, v. 25(3), p. 149-243.
Lesher, C.M., 2017, Roles of Xenomelts, Xenoliths, Xenocrysts, Xenovolatiles, Residues, and Skarns in the Genesis, Transport, and Localization of Magmatic Fe-Ni-Cu-PGE Sulfides and Chromite: Ore Geology Reviews, v. 90, p. 465-484.
Li, C., and Naldrett, A.J., 1993, Sulfide capacity of magma: a quantitative model and its application to the formation of sulfide ores at Sudbury: Economic Geology, v. 88, p. 1253-1260.
Lightfoot, P.C., 2016, Nickel Sulfide Ores and Impact Melts: Origin of the Sudbury Igneous Complex, 1st Edition. Elsevier, Cambridge, MA.
Lightfoot, P.C., Keays, R.R., and Doherty, W., 2001, Chemical evolution and origin of the nickel sulfide mineralization in the Sudbury Igneous Complex, Ontario, Canada: Economic Geology, v. 96 (8), p. 1855-1875.
Lightfoot, P.C., Keays, R.R., Morrison, G.C., Bite, A., and Farrel, K.P., 1997. Geochemical

relationships in the Sudbury Igneous Complex: Origin of the main mass and offset dikes. Economic Geology, v. 92(3), p. 289-307.
MacInnis, L.M., Kontak, D.J., Ames, D.E., and Joyce, N.L., 2014, Alteration proximal to the sharp-walled Cu-(Ni)-PGE vein footwall mineralization of the Podolsky deposit, Sudbury, Ontario: Geological Survey of Canada, Open File, 7666.
McDonough, W.F., and Sun, S.-s., 1995, The composition of the Earth: Chemical Geology, v. 120(3-4), p. 223-253.
McDougall, I., and Harrison, T.M., 1999, Geochronology and Thermochronology by the $^{40}Ar/^{39}Ar$ Method. New York, Oxford University Press.
Muir, T.L., and Peredery, W.V., 1984, The Onaping Formation: in Pye, E.G., Naldrett, A.J., Giblin, P.E. (Eds.), The Geology and Ore Deposits of the Sudbury Structure. Ontario Geological Survey Special Volume 1, p. 234.
Molnár, F., Watkinson, D.H., Jones, P.C., Gatter, I., 1997, Fluid inclusion evidence for hydrothermal enrichment of magmatic ore at the contact zone of the Ni-Cu-platinum group element 4b deposit, Lindsley mine, Sudbury, Canada: Economic Geology, v. 92, p. 674-685.
Molnár, F., Watkinson, D.H., Everest, J.O., 1999, Fluid-inclusion characteristics of hydrothermal Cu-Ni-PGE veins in granitic and metavolcanic rocks at the contact of the Little Stobie deposit, Sudbury, Canada: Chemical Geology, v. 154, p. 279-301.
Molnár, F., and Watkinson, D.H., 2001, Fluid-inclusion data for vein-style Cu-Ni-PGE footwall ores, Sudbury Igneous Complex and their use in establishing an exploration model for hydrothermal PGE-enrichment around mafic-ultramafic intrusions: Exploration and Mining Geology, v. 10(1-2), p. 125-141.
Molnár, F., Watkinson, D.H., and Jones, P.C., 2001, Multiple hydrothermal processes in footwall units of the North range, Sudbury Igneous Complex, Canada, and implications for the genesis of vein-type Cu-Ni-PGE deposits: Economic Geology, v. 96(7), p. 1645-1670.
Mukwakwami, J., Lafrance, B., Lesher, C.M., Tinkham, D.K., Rayner, N.M., and Ames, D.E., 2014, Deformation, metamorphism, and mobilization of Ni-Cu-PGE sulfide ores at Garson mine, Sudbury: Mineralium Deposita, v. 49, p. 175-198.
Mungall, J.E., 2007, Crystallization of magmatic sulfides: An empirical model and application to Sudbury Ores: Science Direct, v. 71(11), p. 2809-2819.
Mungall, J. E., Ames, D.E., and Hanley, J.J., 2004, Geochemical evidence from the Sudbury structure for crustal redistribution by large bolide impacts: Nature, v. 429, p. 546-548.
Naldrett, A.J., 1984. Introduction to the geology of the Sudbury Igneous Complex. *in* Pye, E.G., Naldrett, A.J., Giblin, P.E. (Eds.), The Geology and Ore Deposits of the Sudbury Structure. Ontario Geological Survey Special Volume 1, p. 234.
Naldrett, A.J., and Pessaram, A., 1992, Compositional variation in the Sudbury ores and prediction of the proximity of footwall copper-PGE ore bodies: Ontario Geological Survey, Miscellaneous Paper, 159, p. 47-62.
Naldrett, A.J., Asif, M., Schandl, E., Searcy, T., Morrison, G.G., Binney, W.P., and Moore, C., 1999, Platinum group elements in the Sudbury ores: Significance with respect to the origin of different ore zones and to the exploration for footwall ores: Economic Geology, v. 94, p. 185-210.
Nelles, E., 2012. Genesis of Cu-PPGE-rich veins and Au-Pd-Pt-Ni-Te-rich disseminated footwall mineralization in the Sudbury Igneous Complex, unpublished MSc thesis, Laurentian University, Sudbury.

Nelles, E., Lesher, C.M., in revision. Genesis of Cu-PGE-rich Footwall-Type Mineralization in the Morrison Deposit, Sudbury: Economic Geology.
Ohmoto, H., 1986, Stable isotope geochemistry of ore deposits, *in* J.W. Valley, H.P. Taylor, Jr., and R. O'Neil, eds., Stable isotopes in high temperature geological processes: Reviews in Mineralogy, v. 16, p. 491-560.
Ohmoto, H. and Rye, R.O., 1979, Isotopes of sulfur and carbon, *in* H.L. Barnes, ed., Geochemistry of Hydrothermal Ore Deposits: John Wiley and Sons, New York, p. 509-567.
Pattison, E.F., 1979. The Sublayer: its characteristics and relationship to the Main Mass of the Sudbury irruptive. Canadian Mineralogist, v. 17, p. 257–274.
Péntek, A., Molnár, F., Watkinson, and D.H., Jones, 2008, Footwall-type Cu-Ni-PGE mineralization in the Broken Hammer area, Wisner township, North Range, Sudbury structure: Economic Geology, v. 103(5), p. 1005-1028.
Péntek, A., Molnár, F., Watkinson, D.H., Jones, P.C., and Mogessie, A., 2011, Partial melting and melt segregation in footwall units within the contact aureole of the Sudbury Igneous Complex (North and East Ranges, Sudbury structure), with implications for their relationship to footwall Cu-Ni-PGE mineralization: International Geology Review, v. 53(2), p. 291-325.
Ripley, E. M., Lightfoot, P.C., Stifter, E.C., Underwood, B., Taranovic, B., Dunlop, M., and Donoghue, K.A., 2015, Heterogeneity of S isotope compositions recorded the Sudbury Igneous Complex, Canada: Significance to formation of Ni-Cu sulfide ores and the host rocks. Economic Geology, v. 110, p. 1125-1135.
Rousell, D.H., Gibson, H.L., and Jonasson, I.R., 1997, The tectonic, magmatic, and mineralization history of the Sudbury Structure: Exploration and Mining Geology, v. 6, p. 1-22.
Rousell, D.H., Fedorowich, J.S., and Dressler, B.O., 2003. Burkhard, O., 2003, Sudbury Breccia (Canada): a product of the 1850 Ma Sudbury Event and host to footwall Cu–Ni–PGE deposits. Earth Science Reviews, v. 60, p. 147-174. Shieh, Y-N., and Schwarcz, H.P., 1978, The oxygen isotope composition of the surface Crystalline rocks of the Canadian Shield: Canadian Journal of Earth Sciences, v. 15, p. 1773-1782.
Shieh, Y., and Schwarcz, H.P., 1978, The oxygeb isotope composition of the surface of the Canadian Shield: Canadian Journal of Earth Sciences, v. 15, p. 1773-1782.
Stout, A.E., 2009. Geology, Mineralogy, and Geochemistry of the McCreedy East 153 Cu-Ni-PGE Deposit, Sudbury, Ontario: Unpublished M.Sc. Thesis, Utrecht, The Netherlands, Utrecht University.
Taylor, B.E., 1986, Stable isotope geochemistry of ore-forming fluids. *in* T.K. Kyser, ed., Stable isotope geochemistry of low temperatures fluids: Mineralogical Association of Canada, Short Course Handbook, v. 13, p. 337-445.
Tuba, G., Molnár, F., Watkinson, D.H., Jones, P.C., and Mogessie, A., 2010, Chapter 30: Hydrothermal vein and alteration assemblages associated with low-sulfides footwall Cu-Ni-PGE mineralization and regional hydrothermal processes, North and East Ranges, Sudbury Structure, Canada, *in* Goldfarb, R.J., Marsh, E.E., and Monacke, T., eds., The Challenge of Finding New Mineral Resources: Golobal Metallogeny, Innovative Exploration, and New Discoveries, Volume I: Gold, Silver, and Copper-Molybdenum: Society of Economic Geologists, Special Publication, 15, v. 1, p. 573-598.
Tuba, G., Molnár, F., Ames, D.E., Péntek, A., Watkinson, D.H., and Jones, P.C., 2014, Multi-

stage hydrothermal processes involved in “low-sulfide” Cu(-Ni)-PGE mineralization in the footwall of the Sudbury Igneous Complex (Canada): Amy Lake PGE zone, East Range: Miner Deposita, v. 49, p. 7-47.
Zheng, Y-.F., 1993, Calculation of oxygen isotope fractionation in hydroxyl-bearing silicates: Earth and Planetary Science Letters, v. 120(3-4), p. 247-263.

Tables:

	2225L-9450 Drift							
	LM-P-043A	LM-P-043B	LM-P-043C	LM-P-043D	LM-P-043E	LM-P-043F	LM-P-043G	LM-P-043H-1
Distance from Vein	~2.5 cm	~5.5 cm	~9 cm	~12.5 cm	~16 cm	~19.5 cm	~23 cm	~26.5 cm
SiO_2	51.5	51.6	51.3	53.5	51.5	50.97	50.99	50.97
TiO_2	0.82	0.82	0.84	0.68	0.81	0.839	0.819	0.798
Al_2O_3	15.56	15.84	15.69	15.92	15.63	15.54	15.82	15.69
FeO_T	10.11	9.24	9.24	8.54	9.04	7.61	7.68	7.46
FeO	9.77	8.93	8.94	8.25	8.74	7.3	7.5	7.1
Fe_2O_3	1.09	0.99	0.96	0.92	0.97	1.01	0.58	1.17
MgO	6.99	7.19	7.27	5.92	7.21	7.08	6.82	6.57
MnO	0.16	0.15	0.15	0.27	0.15	0.147	0.145	0.148
CaO	6.86	7.35	7.57	7.07	7.55	8	8.02	7.85
Na_2O	3.26	3.37	3.39	2.79	3.3	3.16	3.2	3.17
K_2O	1.55	1.77	1.91	1.02	1.77	1.85	1.86	1.67
P_2O_5	0.38	0.39	0.4	0.19	0.38	0.4	0.4	0.37
LOI	1.81	1.67	1.6	2.42	1.65	1.65	1.63	1.76
Total	99.83	100.18	99.85	98.99	99.74	98.77	98.62	98.04
C-Total	0.03	0.11	0.04	0.2	0.05	0.07	0.05	0.06
FeO	8.64	7.67	7.51	6.53	7.59	7.3	7.5	7.1
Total S	0.23	0.13	0.15	0.09	0.2	0.17	0.16	0.21
Cl	n.a.	n.a.	n.a.	n.a.	n.a.	0.09	0.09	0.08
F	n.a.	n.a.	n.a.	n.a.	n.a.	0.07	0.07	0.06
ppm								
B	1	2	1	2	1	17	12	10
Li	20.5	21.8	23.5	11.8	24.1	26	26	25
ppb								
Au	166.4	41.2	12.9	5.1	14.8	2	b.d.	4
Pd	135	16	b.d.	b.d.	25	2	1	6
Pt	230	274	55	b.d.	22	b.d.	b.d.	15
ppm								
Cu	2099.69	902.49	653.19	248.27	1496.36	170	550	1570
Ni	199.8	121	135	70.2	672.4	100	90	150
Co	34.3	32.5	35.7	20	32.1	45.5	44.9	38.5
Cr	110	109.2	106.9	73.1	99	170	170	160
Mn	399	341	333	591	371	1150	1120	1130
Zn	111	239	653	63	112	245	255	157
Sn	4	2	1	2	2	b.d.	b.d.	3
Ga	17.5	16.7	17.6	15.6	17.6	18	18	18
Ge	0.1	0.1	b.d.	b.d.	b.d.	1.6	1.5	1.5
In	0.03	0.02	0.02	0.04	b.d.	b.d.	b.d.	b.d.
Cd	1.3	7.58	25.9	1.17	1.96	4.5	4.6	0.9
Zr	186.4	230.4	265.6	85.8	220.5	214	209	213
Ag	2.11	1.391	1.187	0.239	1.138	4.8	3.7	3.4
Ba	960	958	1053	423	897	961	952	1002
Pb	29.3	52.3	69.9	9.6	31.8	108	122	40
Th	3.2	3.2	3.2	2.2	4.2	2.78	2.83	3.12
U	0.4	0.1	0.3	0.9	0.9	0.15	0.14	0.5
Bi	1.33	1.71	1.04	0.32	0.57	0.6	1	0.6
Tl	0.49	0.33	0.35	0.13	0.39	0.48	0.55	0.58
Rb	43.1	50.1	60.7	30.4	56.1	56	57	54
Sr	765.1	805.4	854.4	438	835.1	892	910	915
Nb	6.5	6.8	7.2	3.5	8	6.7	6.6	6.7
Cs	0.8	0.7	0.8	2.9	0.9	0.6	0.7	0.8
Be	0.2	0.2	0.2	0.2	0.2	1	2	2
Hf	4.1	5.4	5.9	2.6	5	4.7	4.5	4.8
Y	17.7	17.3	18.8	13.3	19.3	16.7	16.4	15.5
Ta	0.2	0.2	0.3	0.2	0.3	0.58	0.71	0.85
Sc	16	14	15	4.4	19	20	20	19
V	126	118	130	191	121	133	133	129
As	0.3	0.2	b.d.	1.1	0.3	b.d.	b.d.	b.d.
Mo	0.4	0.2	0.2	0.8	0.5	b.d.	2	b.d.
Sb	b.d.	b.d.	b.d.	0.14	b.d.	b.d.	b.d.	b.d.
W	b.d.	b.d.	b.d.	0.1	b.d.	n.a.	n.a.	n.a.
Hg	b.d.	b.d.	0.01	b.d.	0.01	n.a.	n.a.	n.a.
Te	0.33	0.17	0.06	0.07	0.13	n.a.	n.a.	n.a.
La	64.1	65.7	68.8	18	65	62	62.5	60.8
Ce	124	128.1	135.1	35.9	129	128	128	122
Pr	14.84	14.93	15.54	4.48	15.3	14.3	14.2	13.6
Nd	57.6	55.2	58.1	18.4	56	53.4	53.8	51
Sm	8.68	8.4	9.03	3.46	9.02	8.81	9.08	8.65
Eu	2.23	2.1	2.14	0.99	2.15	2.11	2.08	2.05
Gd	6.3	5.89	6.53	3.2	6.22	5.87	5.86	5.37
Tb	0.69	0.66	0.7	0.4	0.71	0.69	0.69	0.68
Dy	3.67	3.43	3.79	2.46	3.81	3.5	3.55	3.4
Ho	0.6	0.57	0.59	0.46	0.63	0.63	0.64	0.58
Er	1.7	1.59	1.77	1.46	1.76	1.7	1.71	1.59
Tm	0.22	0.22	0.23	0.2	0.23	0.237	0.235	0.219
Yb	1.44	1.39	1.46	1.32	1.56	1.44	1.48	1.44
Lu	0.21	0.18	0.21	0.18	0.22	0.218	0.222	0.227
Mg#	55.2	58.1	58.4	55.3	58.7	62.4	61.3	61.1
$\delta^{18}O$	6.7		7.1		12.7		6.6	
$^{87}Sr/^{86}Sr$							0.703050	

Table 1: Geochemical dataset of 2225L Transect, LM-P-043. b.d. = below detection; Mg# = MgO/Mg+FeO; $\delta^{18}O$ – oxygen isotope values; $^{86}Sr/^{87}Sr$ = strongtium isotope values.

	2225L-9450 Drift							
	LM-P-043I	LM-P-043J	LM-P-043K	LM-P-043L-1	LM-P-043M	LM-P-043N	LM-P-043O-1	LM-P-043P
Distance from Vein	~30 cm	~33.5 cm	~37 cm	~40.5 cm	~44 cm	~47.5	~51 cm	~54.5 cm
SiO_2	51.13	50.87	51.29	51.01	50.57	51.41	51.17	51.82
TiO_2	0.818	0.825	0.837	0.79	0.821	0.793	0.82	0.81
Al_2O_3	15.5	15.5	15.35	15.54	15.88	15.45	15.8	15.74
FeO_T	7.44	7.38	7.23	7.17	7.38	7.48	7.74	7.23
FeO	7.1	7	6.8	6.8	6.9	6.9	7.6	6.7
Fe_2O_3	1.1	1.21	1.39	1.19	1.54	1.88	0.46	1.72
MgO	6.81	6.87	7.05	6.78	6.71	6.74	6.84	6.81
MnO	0.146	0.143	0.143	0.142	0.148	0.142	0.139	0.142
CaO	7.92	8.01	7.93	7.97	7.75	7.76	7.79	7.74
Na_2O	3.25	3.2	3.19	3.22	3.05	3.11	3.28	3.22
K_2O	1.89	1.9	1.92	1.81	1.81	1.69	1.82	1.83
P_2O_5	0.38	0.39	0.4	0.4	0.39	0.39	0.38	0.38
LOI	1.8	1.68	1.87	1.66	1.9	2	1.84	2.05
Total	98.63	98.39	98.94	98.07	98.25	99.05	98.79	99.73
C-Total	0.07	0.05	0.06	0.06	0.04	0.05	0.05	0.08
FeO	7.1	7	6.8	6.8	6.9	6.9	7.6	6.7
Total S	0.16	0.19	0.18	0.17	0.18	0.32	0.14	0.18
Cl	0.09	0.1	0.08	0.08	0.07	0.08	0.1	0.1
F	0.07	0.06	0.07	0.07	0.07	0.06	0.06	0.06
ppm								
B	6	b.d.	6	10	12	14	17	12
Li	26	21	23	23	27	27	31	32
ppb								
Au	b.d.	b.d.	b.d.	2	6	18	2	53
Pd	b.d.	b.d.	b.d.	b.d.	7	137	b.d.	41
Pt	b.d.	b.d.	3	b.d.	48	201	b.d.	33
ppm								
Cu	510	100	210	1230	1500	1980	870	1220
Ni	90	100	100	100	250	510	140	360
Co	45.6	45	47	43.1	47.1	43.5	44.5	51.1
Cr	170	170	170	160	160	160	160	160
Mn	1190	1070	1040	1120	1160	1130	1160	1190
Zn	337	203	244	163	157	176	242	296
Sn	b.d.	b.d.	b.d.	b.d.	2	4	b.d.	1
Ga	18	18	18	18	18	18	18	18
Ge	1.5	1.5	1.4	1.5	1.3	1.5	1.5	1.4
In	b.d.	b.d.	b.d.	b.d.	b.d.	b.d.	b.d.	b.d.
Cd	6.7	3.2	5	1.3	0.5	1	3.9	4.7
Zr	213	217	189	203	196	199	215	206
Ag	3.2	2.8	2.4	3.2	2.7	2.7	2.6	2.4
Ba	994	994	985	930	1040	922	944	953
Pb	124	120	124	44	36	70	55	49
Th	2.85	2.84	4.06	3.46	3.17	3.71	2.77	3.17
U	0.15	0.15	1.36	0.92	0.53	1.15	0.15	0.5
Bi	0.9	0.3	0.4	0.4	0.6	1	0.6	0.6
Tl	0.53	0.52	0.53	0.57	0.59	0.59	0.54	0.53
Rb	60	60	63	60	62	59	58	58
Sr	891	899	880	922	897	884	919	894
Nb	6.7	6.7	7.9	7.5	7.1	7.7	6.7	6.9
Cs	0.8	0.8	1.1	1.1	1.1	1	0.7	0.8
Be	2	2	2	2	2	2	2	2
Hf	4.7	4.8	4.2	4.5	4.5	4.5	4.6	4.7
Y	16.2	16.1	19.1	17.9	16.5	18.3	16.1	16.1
Ta	0.65	0.68	0.99	0.83	0.92	0.9	0.75	1.03
Sc	20	20	20	20	19	20	20	19
V	134	132	134	128	129	128	128	129
As	b.d.	b.d.	b.d.	b.d.	b.d.	b.d.	b.d.	b.d.
Mo	b.d.	b.d.	b.d.	b.d.	b.d.	b.d.	2	b.d.
Sb	b.d.	b.d.	b.d.	b.d.	b.d.	b.d.	b.d.	b.d.
W	n.a.	n.a.	n.a.	n.a.	n.a.	n.a.	n.a.	n.a.
Hg	n.a.	n.a.	n.a.	n.a.	n.a.	n.a.	n.a.	n.a.
Te	n.a.	n.a.	n.a.	n.a.	n.a.	n.a.	n.a.	n.a.
La	63.3	62.4	59.9	61.5	60.9	61.3	62.3	60.4
Ce	127	128	124	125	124	121	125	122
Pr	14.3	14.2	14.2	14	13.8	13.5	14	13.4
Nd	53.1	53.5	52.4	52.2	52.1	51.4	52.5	50.1
Sm	8.89	8.63	8.81	8.81	8.81	8.54	8.8	8.27
Eu	2.11	2.12	2.08	2.13	2.11	2.1	2.09	2.01
Gd	5.65	5.68	5.77	5.56	5.6	5.71	5.62	5.42
Tb	0.7	0.72	0.75	0.75	0.68	0.77	0.67	0.71
Dy	3.43	3.37	3.84	3.78	3.52	3.87	3.45	3.63
Ho	0.62	0.59	0.69	0.69	0.62	0.68	0.62	0.63
Er	1.66	1.57	1.89	1.87	1.68	1.88	1.73	1.7
Tm	0.225	0.22	0.266	0.259	0.24	0.27	0.246	0.24
Yb	1.49	1.44	1.7	1.68	1.54	1.68	1.51	1.5
Lu	0.231	0.232	0.27	0.266	0.242	0.256	0.228	0.238
Mg#	62.0	62.4	63.5	62.8	61.8	61.6	61.2	62.7
$\delta^{18}O$			8.0					7.1
$^{87}Sr/^{86}Sr$								

Table 1 (cont.): Geochemical dataset of 2225L Transect, LM-P-043. b.d. = below detection; Mg# = MgO/Mg+FeO; $\delta^{18}O$ – oxygen isotope values; $^{86}Sr/^{87}Sr$ = strongtium isotope values.

	1700-RMK (Haulage)			DDH4938			
	LM-P-060	LM-P-060A	LM-P-060B	LM-P-055A	LM-P-055B	LM-P-055C	LM-P-055D
Distance from Vein	Actinolite Crystals along contact (0 cm)	~3.5 cm	~5 cm	~3.5 cm	~7 cm	~10.5 cm	~14 cm
SiO_2		52.34	51.15	57.1	51.56	51.5	51.21
TiO_2		0.799	0.822	0.829	1.199	1.219	1.209
Al_2O_3		14.08	15.26	15.43	16.58	16.39	16.25
FeO_T		9.66	8.73	6.12	7.36	7.39	7.47
FeO		8.8	8.1	5.3	6.6	6.5	6.6
Fe_2O_3		2.77	2.03	2.63	2.46	2.86	2.81
MgO		6.93	6.45	3.46	5.26	5.25	5.49
MnO		0.153	0.147	0.084	0.13	0.136	0.135
CaO		5.3	6.41	4.51	7.42	7.64	7.94
Na_2O		3.73	3.97	3.55	3.57	3.63	3.51
K_2O		0.54	0.73	1.77	1.97	1.94	1.96
P_2O_5		0.37	0.4	0.45	0.66	0.73	0.68
LOI		2.93	2.77	1.86	1.49	1.64	1.49
Total		99.73	99.14	97.59	99.63	100.2	100
C-Total		0.01	0.04	0.04	0.03	0.06	0.03
FeO		8.8	8.1	5.3	6.6	6.5	6.6
Total S		0.42	0.08	0.27	0.16	0.19	0.19
Cl		0.08	0.08	0.11	0.07	0.07	0.08
F		0.07	0.07	0.05	0.07	0.07	0.08
ppm							
B		7	8	b.d.	8	7	17
Li		19	23	25	24	22	22
ppb							
Au		168	39	327	2	b.d.	b.d.
Pd		107	4	818	2	b.d.	b.d.
Pt		343	20	194	b.d.	b.d.	b.d.
ppm							
Cu		2790	920	2010	1100	910	110
Ni		3530	1670	250	60	70	60
Co		42.3	45	49.1	40.3	37.3	43.5
Cr		190	210	60	90	90	100
Mn		1090	1130	649	983	1010	991
Zn		241	235	171	167	166	171
Sn		15	6	7	2	1	1
Ga		15	17	19	20	20	20
Ge		1.2	1.8	1.3	1.3	1.5	1.2
In		0.6	0.3	b.d.	b.d.	b.d.	b.d.
Cd		0.6	0.8	b.d.	0.4	0.5	0.6
Zr		171	205	245	237	243	244
Ag		2.2	2.8	3.3	2.5	2.7	2.7
Ba		381	585	902	1189	1217	1151
Pb		34	42	138	39	31	27
Th		3.8	2.33	13.3	2.76	1.8	1.49
U		0.32	0.19	4.52	0.45	0.13	0.12
Bi		2.1	2.8	1.6	0.3	0.3	0.2
Tl		0.2	0.16	0.74	0.53	0.39	0.38
Rb		16	20	73	54	48	51
Sr		515	746	748	974	1012	1006
Nb		6.3	7.1	10.7	9.5	9.5	8.7
Cs		0.4	0.5	1.4	0.8	0.6	0.6
Be		1	2	2	2	2	2
Hf		3.9	4.6	5.7	5.3	5.4	5.6
Y		13.9	15.8	17.4	20.7	21.3	21.4
Ta		0.53	0.75	1.68	0.88	0.87	0.73
Sc		22	22	13	18	18	19
V		123	139	118	174	178	175
As		b.d.	b.d.	b.d.	b.d.	b.d.	b.d.
Mo		b.d.	b.d.	1	b.d.	b.d.	b.d.
Sb		b.d.	b.d.	b.d.	b.d.	b.d.	b.d.
W		n.a.	n.a.	n.a.	n.a.	n.a.	n.a.
Hg		n.a.	n.a.	n.a.	n.a.	n.a.	n.a.
Te		n.a.	n.a.	n.a.	n.a.	n.a.	n.a.
La		45.3	57.4	75.3	73.6	76.3	70.7
Ce		98.8	117	150	156	164	152
Pr		11.4	14	16.1	18	19	17.7
Nd		43.7	49.2	58.5	68	72	68.1
Sm		7.58	8.04	9.28	11.3	12	11.4
Eu		1.34	1.7	2.12	2.61	2.69	2.65
Gd		4.77	5.98	6.02	7.17	7.19	7.36
Tb		0.62	0.69	0.74	0.88	0.9	0.93
Dy		3	3.49	3.68	4.33	4.36	4.65
Ho		0.51	0.58	0.64	0.74	0.77	0.83
Er		1.4	1.6	1.73	1.99	2.11	2.24
Tm		0.196	0.228	0.237	0.281	0.29	0.311
Yb		1.26	1.41	1.5	1.76	1.87	1.91
Lu		0.201	0.208	0.251	0.264	0.292	0.292
Mg#		56.1	56.8	50.2	56.0	55.9	56.7
$\delta^{18}O$	5.0	6.4	7.3	8.2	6.7	7.2	6.5
$^{87}Sr/^{86}Sr$	0.703054						

Table 2: Geochemical dataset of the transects, most altered samples used for most altered average, and least altered samples used for least altered average. b.d. = below detection; Mg# = MgO/Mg+FeO; $\delta^{18}O$ – oxygen isotope values; $^{86}Sr/^{87}Sr$ = strongtium isotope values.

	DDH4306		Most Altered Grey Gabbro Samples			Least Altered Grey Gabbro Samples		
	LM-P-039A	LM-P-039B	LM-P-026	LM-P-027	LM-P-031	LM-P-021	LM-P-025	LM-P-007
Distance from Vein	~3.5 cm	~7 cm	~1 cm	~1 cm	~1 cm	N/A	N/A	N/A
SiO_2	49.5	47.5	48.22	49.82	42.96	51.30	51.10	51.4
TiO_2	1.42	1.46	1.128	1.058	1.463	1.07	1.00	0.883
Al_2O_3	16.38	16.24	14.29	14.33	15.11	16.83	16.15	14.79
FeO_T	9.92	10.76	9.96	8.32	13.60	9.33	9.34	7.1
FeO	9.59	10.4	9	7.3	11.6	9.02	9.03	6.7
Fe_2O_3	1.07	1.16	3.08	3.29	6.44	1.00	1.00	1.29
MgO	5.93	5.13	6.5	6.41	5.75	5.91	6.61	7.57
MnO	0.16	0.13	0.134	0.172	0.179	0.13	0.15	0.145
CaO	7.57	10.1	5.05	7.56	3.8	8.40	8.30	8.51
Na_2O	4.23	3.56	2.38	3.26	2.11	3.94	3.50	3.22
K_2O	0.76	0.28	1.07	0.59	0.07	1.31	1.74	1.41
P_2O_5	0.81	0.84	0.54	0.53	0.7	0.66	0.52	0.48
LOI	2.41	2.53	4.3	3.31	5.97	0.84	1.03	0.98
Total	99.89	99.37	96.7	98.44	97.47	99.57	99.09	98.91
C-Total	0.03	b.d.	0.03	0.09	0.07	0.02	0.03	0.06
FeO	7	5.96	9	7.3	11.6	5.70	6.14	7.4
Total S	0.2	0.54	1.22	0.34	0.61	0.21	0.21	0.23
Cl	n.a.	n.a.	0.11	0.05	0.08	n.a.	n.a.	0.04
F	n.a.	n.a.	0.06	0.06	0.06	n.a.	n.a.	0.06
ppm								
B	1	1	1	b.d.	b.d.	b.d.	b.d.	b.d.
Li	14.3	13.4	46	32	28	18.2	20.7	22
ppb								
Au	2	6.2	94	160	17100	b.d.	b.d.	b.d.
Pd	b.d.	b.d.	109	237	2330	b.d.	b.d.	1
Pt	b.d.	b.d.	401	58	119	b.d.	b.d.	b.d.
ppm								
Cu	1525.95	5318.47	7250	2550	5330	49.00	47.20	50
Ni	54.8	49.3	9260	2590	6400	63.20	70.00	120
Co	36.8	29.7	82.9	54	57.1	34.00	37.10	68
Cr	59.3	47.1	170	130	60	80.80	84.60	220
Mn	528	412	982	1390	1330	178	236	1130
Zn	112	90	256	261	261	65.00	86.00	125
Sn	b.d.	2	17	21	18	1	1	b.d.
Ga	18.6	21.5	15	17	21	19.4	18.8	18
Ge	0.1	0.1	1.3	1.7	1.3	0.1	b.d.	1.7
In	b.d.	b.d.	1	0.9	0.6	b.d.	b.d.	b.d.
Cd	0.12	0.09	1.2	0.2	0.3	0.56	1.03	b.d.
Zr	310.4	329.3	296	217	258	215.60	224.80	208
Ag	1.09	0.383	3.7	5.5	15.7	209	297	2300
Ba	842	154	546	423	58	960.00	1003.00	940
Pb	6.4	16.4	36	13	19	23.90	55.10	15
Th	4	3.5	7.7	1.76	3.01	1.80	1.90	2.23
U	0.2	0.2	0.55	0.19	0.41	0.20	0.10	0.21
Bi	b.d.	b.d.	16.1	8.5	3.2	b.d.	0.09	b.d.
Tl	0.07	0.05	0.41	0.15	0.06	0.17	0.3	0.38
Rb	19.1	8.1	35	15	2	29.50	41.60	39
Sr	829.5	1341.8	679	872	328	1030.80	957.20	882
Nb	8.3	10.2	10.7	7.3	9.3	8.10	7.30	7.1
Cs	0.4	0.3	0.8	0.3	b.d.	0.20	0.50	0.5
Be	0.2	0.3	b.d.	1	b.d.	0.20	0.10	2
Hf	6.9	7.1	6.4	4.9	5.7	5.10	5.20	4.6
Y	24.7	26.1	15.5	16.7	19.9	19.90	19.40	18.5
Ta	0.3	0.3	1.17	1.01	1.18	0.30	0.30	1.71
Sc	1.6	2.5	16	19	17	1.80	1.90	23
V	197	217	136	147	206	169.00	158.00	147
As	0.6	1	6	b.d.	b.d.	0.1	0.7	b.d.
Mo	0.2	0.5	b.d.	b.d.	b.d.	0.19	0.16	b.d.
Sb	0.02	0.09	b.d.	b.d.	b.d.	b.d.	b.d.	b.d.
W	b.d.	b.d.	n.a.	n.a.	n.a.	b.d.	b.d.	n.a.
Hg	b.d.	b.d.	n.a.	n.a.	n.a.	b.d.	b.d.	n.a.
Te	b.d.	b.d.	n.a.	n.a.	n.a.	b.d.	b.d.	n.a.
La	95.8	98.3	62.5	58.7	72.1	76.40	68.00	65
Ce	189.6	198.2	137	127	154	154.00	134.90	137
Pr	22.66	23.39	15.3	14.6	17.5	17.77	16.38	15.6
Nd	83.5	88.9	57.5	55.4	65.8	67.10	65.60	59.6
Sm	13.15	13.62	8.88	9.44	10.3	10.48	9.77	9.85
Eu	2.72	3.56	1.61	1.69	1.85	2.47	2.47	2.27
Gd	9.05	9.7	5.7	6.08	6.67	7.30	6.83	6.5
Tb	1	1.04	0.66	0.72	0.83	0.80	0.76	0.8
Dy	5.09	5.12	3.33	3.6	3.99	3.82	3.99	3.84
Ho	0.78	0.86	0.58	0.63	0.72	0.68	0.70	0.68
Er	2.21	2.42	1.65	1.73	1.99	1.75	1.91	1.82
Tm	0.28	0.33	0.243	0.243	0.279	0.25	0.23	0.261
Yb	1.86	2	1.54	1.54	1.78	1.48	1.54	1.63
Lu	0.25	0.27	0.237	0.236	0.28	0.21	0.21	0.242
Mg#	51.6	45.9	53.8	57.9	43.0	53.0	55.8	65.5
$\delta^{18}O$			7.2	6.3	6.3		7.7	6.9
$^{87}Sr/^{86}Sr$								0.73054

Table 2 (cont.): Geochemical dataset of the transects, most altered samples used for most altered average, and least altered samples used for least altered average. b.d. = below detection; Mg# = MgO/Mg+FeO; $\delta^{18}O$ – oxygen isotope values; $^{86}Sr/^{87}Sr$ = strontium isotope values.

Sample ID	Mineralogy	$\delta^{34}S$ value	Location	Host Rock	Mineral Texture	Comments
LM-PRC-01.1	cpy	4.37	1700-550 drift	Grey Gabbro	primary	sampled at beginning of sharp walled chacopyrite vein; trace amounts of actinolite present
LM-PRC-01.2	cpy	4.43	1700-550 drift	Grey Gabbro	primary	sampled at end of sharp walled chacopyrite vein; trace amounts of actinolite present
LM-PRC-01.3A	cpy	4.29	1700-550 drift	Grey Gabbro	primary	sampled at end of sharp walled chacopyrite vein; trace amounts of actinolite present
LM-PRC-01.3B	cpy	3.44	1700-550 drift	Grey Gabbro	primary	sampled at end of sharp walled chacopyrite vein; trace amounts of actinolite present
LM-PRC-02.1	cpy	4.35	1850-400 drift	Grey Gabbro	primary	sampled at beginning of sharp walled chacopyrite vein; trace amounts of magnetite present
LM-PRC-02.2	cpy	4.3	1850-400 drift	Grey Gabbro	primary	sampled in middle of sharp walled chacopyrite vein; trace amounts of magnetite present
LM-PRC-02.3	cpy	4.39	1850-400 drift	Grey Gabbro	primary	sampled at end of sharp walled chacopyrite vein; trace amounts of magnetite present
LM-PRC-03.1	cpy	4.5	1925-Haulage	Grey Gabbro	primary	sampled at beginning of sharp walled chacopyrite vein; trace amounts of magnetite present
LM-PRC-03.2	cpy	4.42	1925-Haulage	Grey Gabbro	primary	sampled in middle of sharp walled chacopyrite vein; trace amounts of magnetite present
LM-PRC-03.3	cpy	4.45	1925-Haulage	Grey Gabbro	primary	sampled in middle of sharp walled chacopyrite vein; trace amounts of magnetite present
LM-PRC-04.1A	cpy	4.32	2225-9450 drift	Grey Gabbro	primary	sampled at end of sharp walled chacopyrite vein; trace amounts of magnetite present
LM-PRC-04.1B	cpy	4.3	2225-9450 drift	Grey Gabbro	primary	sampled at beginning of sharp walled chacopyrite vein; trace amounts of magnetite present
LM-PRC-04.2	cpy	4.51	2225-9450 drift	Grey Gabbro	primary	sampled in middle of sharp walled chacopyrite vein; trace amounts of magnetite present
LM-PRC-04.3	cpy	4.28	2225-9450 drift	Grey Gabbro	primary	sampled in middle of sharp walled chacopyrite vein; trace amounts of magnetite present
LM-PRC-04.4	cpy	4.2	2225-9450 drift	Grey Gabbro	primary	sampled at end of sharp walled chacopyrite vein; trace amounts of magnetite present

Table 3: Sulfur isotope dataset of sharp-walled sulfide veins.

Figures:

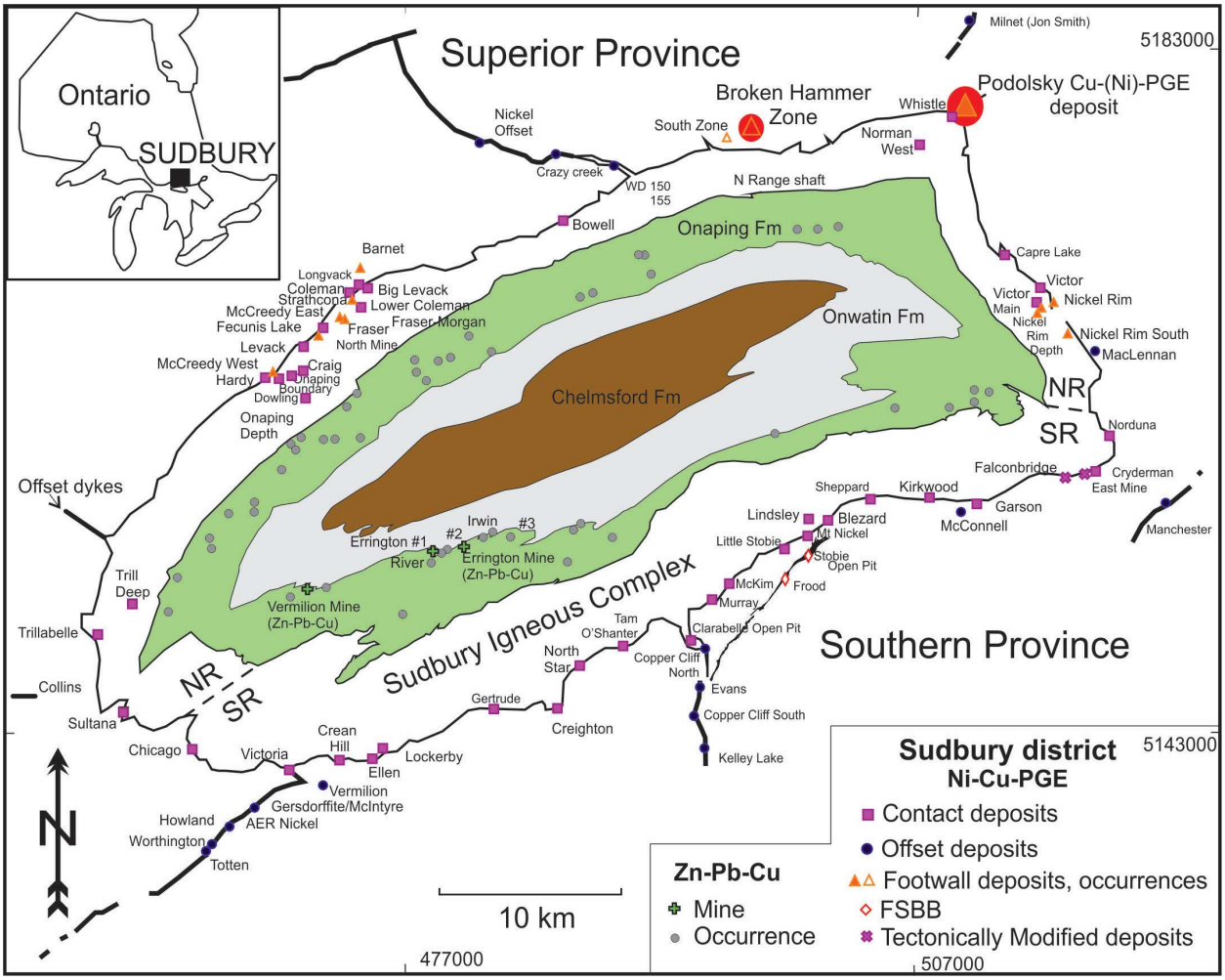

Fig. 1: Geological map of the Sudbury mining district (modified after Ames and Farrow, 2007) showing the outline of the SIC, the crater-fill sequence and locations of the various sulfide deposit types related to the SIC (i.e., magmatic sulfide deposits; contact, footwall, offset) and the crater fill sequence (i.e., Zn-Pb-Cu deposits). The area of interest for this study, the Podolsky Cu(-Ni)-PGE deposit, is located in the northeast part of the map area and is highlighted in red.

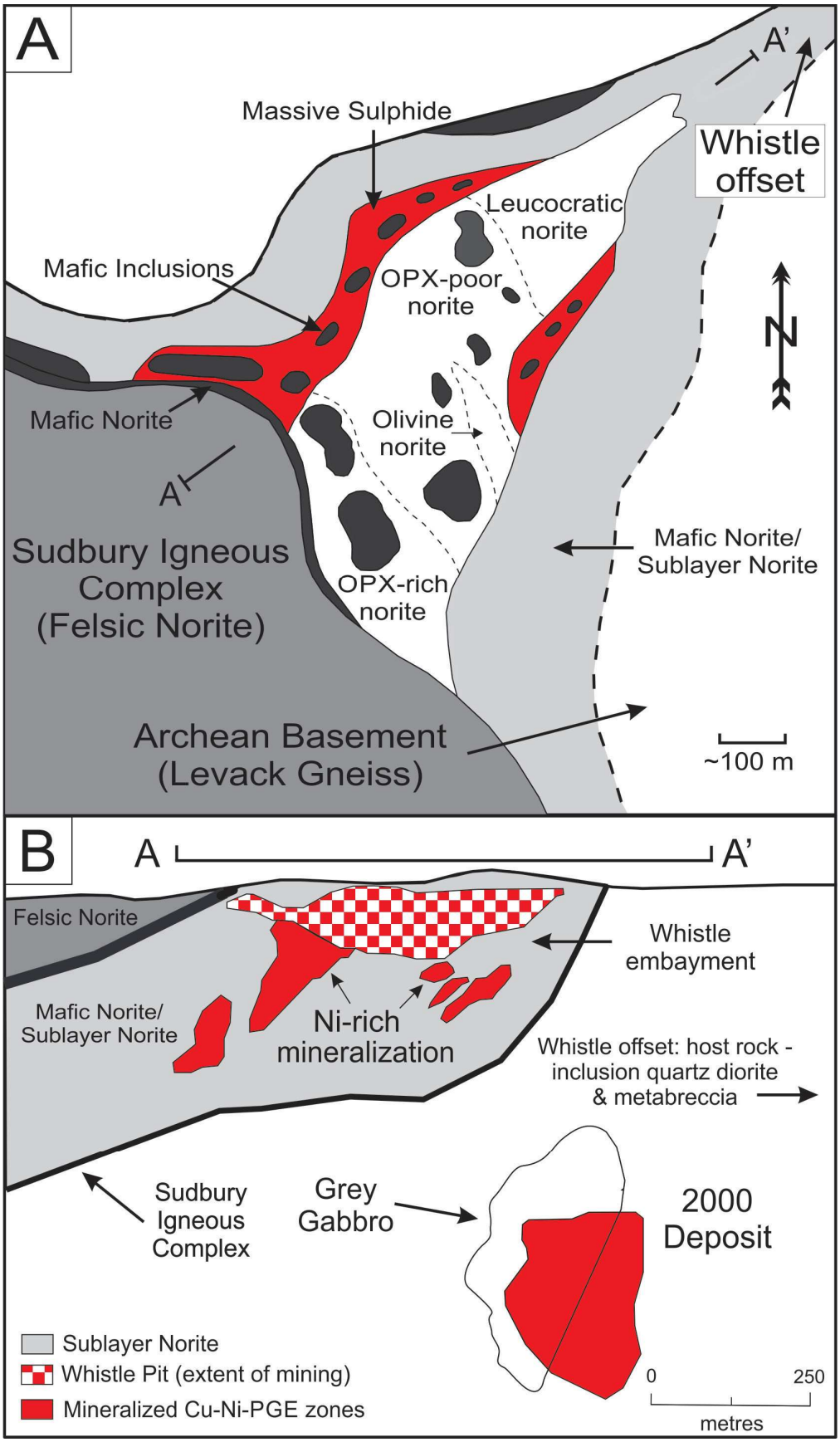
A
A'
Massive Sulphide
Whistle offset
Leucocratic norite
Mafic Inclusions
OPX-poor norite
N
Mafic Norite
Olivine norite
A
Sudbury Igneous Complex (Felsic Norite)
Mafic Norite/ Sublayer Norite
OPX-rich norite
Archean Basement (Levack Gneiss)
~100 m
B
A
A'
Felsic Norite
Whistle embayment
Mafic Norite/ Sublayer Norite
Ni-rich mineralization
Whistle offset: host rock - inclusion quartz diorite & metabreccia
Sudbury Igneous Complex
Grey Gabbro
2000 Deposit
Sublayer Norite
Whistle Pit (extent of mining)
Mineralized Cu-Ni-PGE zones
0
250
metres

Fig. 2: An overview of the geology of the Whistle embayment area of the SIC (see Fig. 1 for location): A) A schematic map in plan-view showing the relationship between the main rock types of the SIC and those of the offset structure; note the presence of the Levack gneiss, which is the basement rock in this area. Also present in the map area is contact-type ore in the Whistle embayment, which was mined by INCO for its Ni content ('Whistle Pit"). Map has been modified from Lightfoot et al. (1997); B) Cross section of Whistle embayment along line A-A' in Figure 2A, which shows the base of the SIC and its contained Ni-rich contact ore, the Whistle embayment structure, and the outline of the grey gabbro fragment that hosts a proportion of the Podolsky Cu(-Ni)-PGE sulfide deposit. The figure has been modified from Farrow et al. (2005).

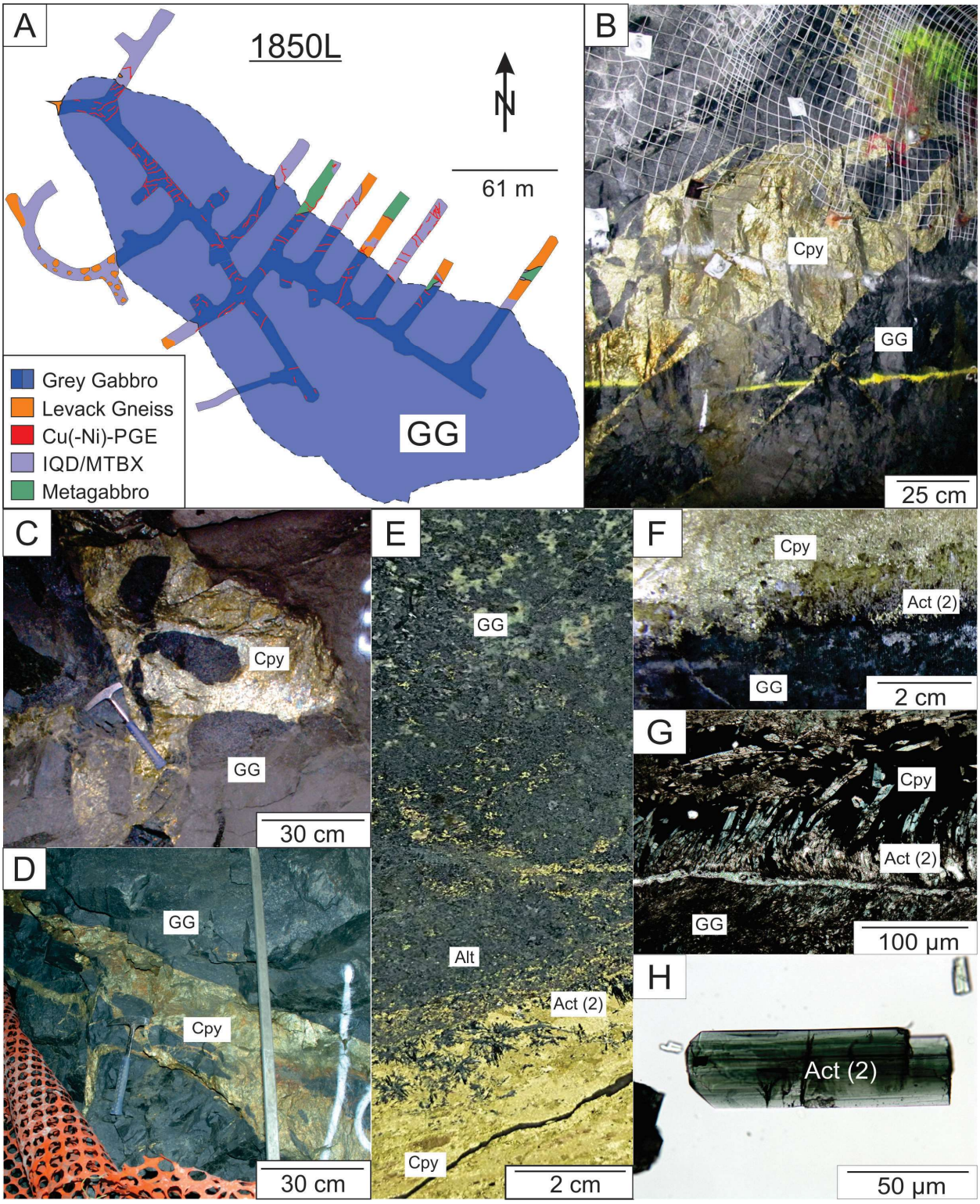
A
1850L
N
61 m
Grey Gabbro
Levack Gneiss
Cu(-Ni)-PGE
IQD/MTBX
Metagabbro
GG
B
Cpy
GG
25 cm
C
Cpy
GG
30 cm
D
GG
Cpy
30 cm
E
GG
Alt
Act (2)
Cpy
2 cm
F
Cpy
Act (2)
GG
2 cm
G
Cpy
Act (2)
GG
100 µm
H
Act (2)
50 µm

Fig. 3: Overview of the geological setting and features of the sharp-walled sulfide veins hosted by the grey gabbro (GG) unit of the Podolsky deposit: A) Plan map on the 1850 level of the 2000 ore zone of the Podolsky deposit. The dark blue color represents grey gabbro that was mapped along haulages and drifts and the lighter blue represents the inferred outline of GG. In red is shown the extent of the Cu(-Ni)-PGE sharp-walled sulfide veins. Abbreviations are: IQD – inclusion quartz diorite; MTBX – metabreccia; B) A sharp-walled sulfide vein of chalcopyrite (Cpy) hosted in GG; note the presence of angular clasts of the host rock gabbro in the sulfide vein; C) A sulfide-rich vein in the GG with rounded clasts of the GG; D) Sharp-walled chalcopyrite-rich sulfide vein hosted in GG with a series of small splays also composed of chalcopyrite; E) Cut slab of sample LM-P-060 collected from the 1700 level of the deposit, which shows the contact between a sharp-walled sulfide vein and GG. Note the presence of actinolite crystals (Act (2)) along the contact between the sulfide vein (Cpy) and GG and the alteration halo (Alt); F) Drill core from hole FNX40272 showing the contact relationship of the GG, actinolite fibers (Act (2)), and the sharp-walled chalcopyrite vein (Cpy); G) A plane-polarize light photomicrograph of sample LM-P-005 showing the contact relationship between the chalcopyrite vein (Cpy) and the GG with the development of actinolite (Act (2)). Note the actinolite has a fibrous texture, shows a shear fabric, and occurs as inclusions in the sulfide vein; H) Photo of actinolite crystal from sample LM-P-060 taken in plane-polarized light with it immersed in oil.

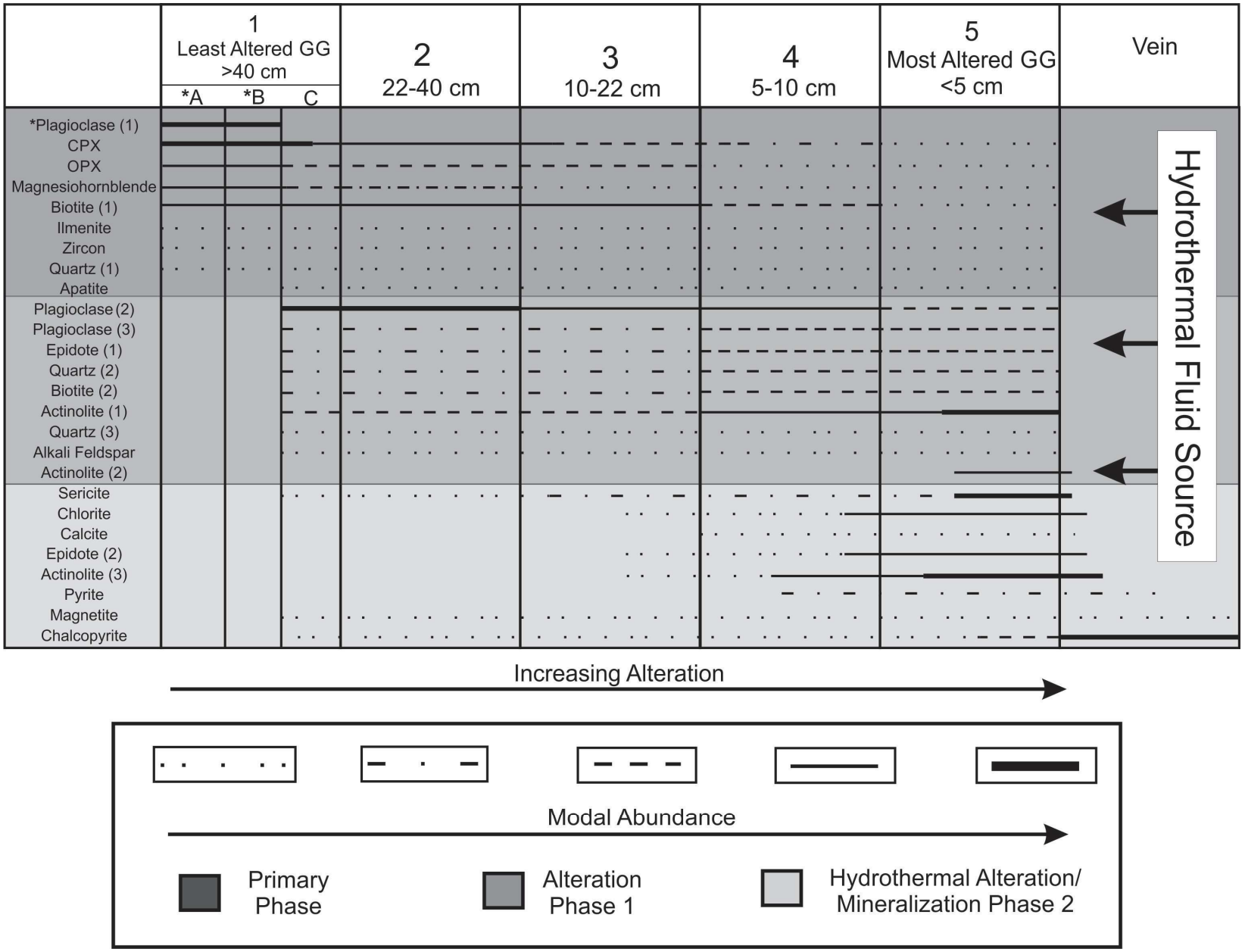
1
Least Altered GG
>40 cm
*A
*B
C
2
22-40 cm
3
10-22 cm
4
5-10 cm
5
Most Altered GG
<5 cm
Vein
*Plagioclase (1)
CPX
OPX
Magnesiohornblende
Biotite (1)
Ilmenite
Zircon
Quartz (1)
Apatite
Plagioclase (2)
Plagioclase (3)
Epidote (1)
Quartz (2)
Biotite (2)
Actinolite (1)
Quartz (3)
Alkali Feldspar
Actinolite (2)
Sericite
Chlorite
Calcite
Epidote (2)
Actinolite (3)
Pyrite
Magnetite
Chalcopyrite
Hydrothermal Fluid Source
Increasing Alteration
Modal Abundance
Primary Phase
Alteration Phase 1
Hydrothermal Alteration/ Mineralization Phase 2

Fig. 4: A summary of the mineral paragenesis for samples of the grey gabbro host rock and samples collected from varying distances from the sharp-walled vein mineralization. Note that samples have been arranged from the least altered GG to the most altered GG located proximal to the sharp-walled sulfide vein, as indicated along the top (point 1 is the most distal). Also note that the minerals present, as shown on the vertical axis, represent three different stages, as shown in grey shading, in the development of the altered and mineralized system: the primary mineral assemblages of the grey gabbro (GG), alteration phase one GG, and hydrothermal alteration/mineralization phase 2 related to the sharp-walled veins. Note that the least altered GG is broken into three sections:1A: Original composition of GG, which is not observed; 1B: GG prior to the bolide impact event at ca.1850 Ma, not observed;1C: Least altered GG, as observed today.

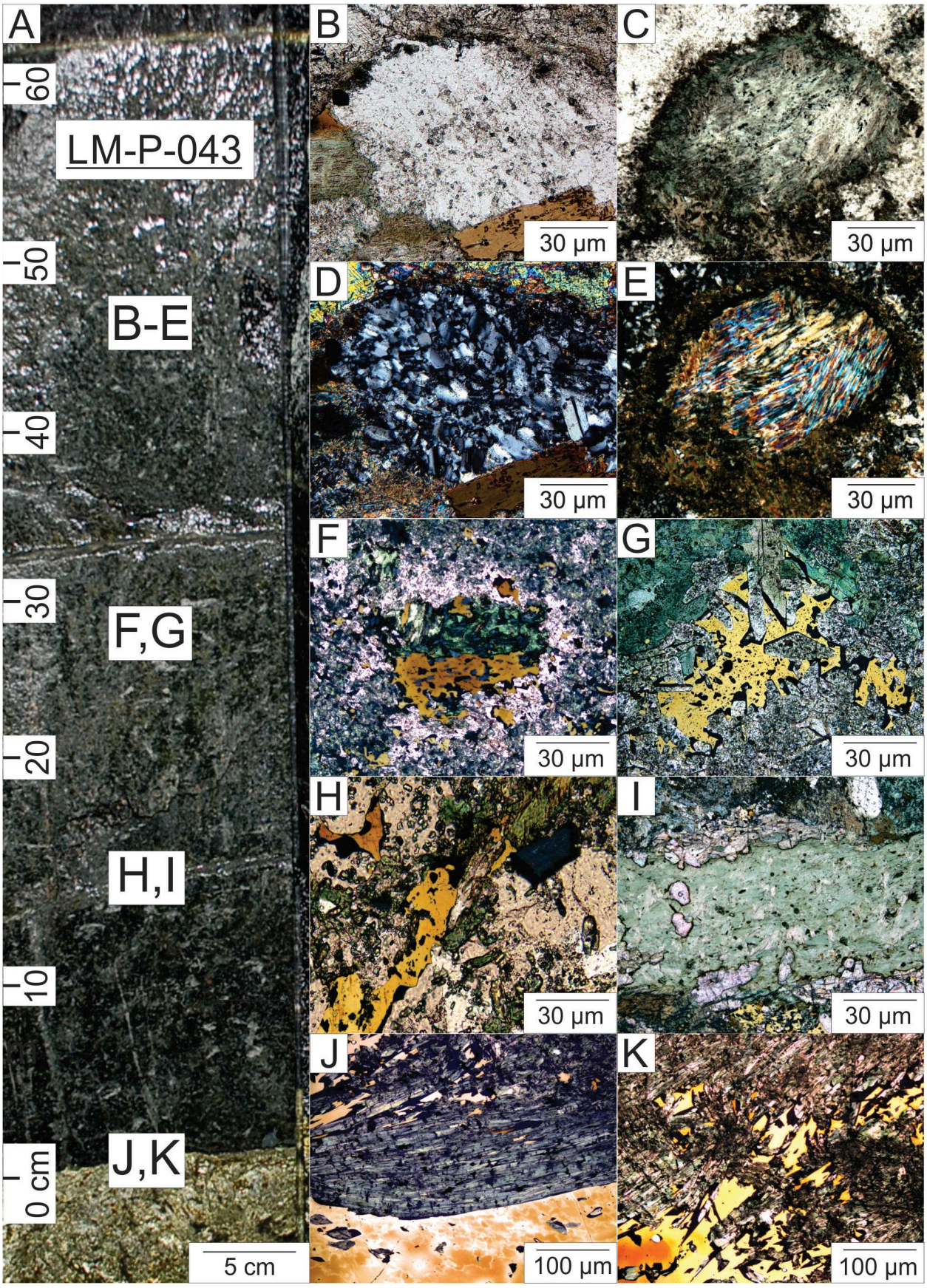
A
60
LM-P-043
50
B-E
40
30
F,G
20
H,I
10
J,K
0 cm
5 cm
B
30 µm
C
30 µm
D
30 µm
E
30 µm
F
30 µm
G
30 µm
H
30 µm
I
30 µm
J
100 µm
K
100 µm

Fig. 5: A summary of petrographic observations along a transect in the grey gabbro (GG; sample LM-P-043, 2225 level) perpendicular to a sharp-walled sulfide vein observed in plane-polarized light (PPL), cross-polarized light (CPL) and combined reflected light (RL) and PPL. A) A 60 cm long cut of sample LM-P-043 showing GG and sulfide vein showing the location of photos B-K away from the sharp-walled vein; B) Least altered GG showing a plagioclase crystal surrounded by biotite, apatite and pyroxene; C) Least altered GG with an altered subhedral clinopyroxene grain surrounded by plagioclase; D) Image in B in CPL to highlight the granoblastic (mosaic) texture of the plagioclase; E) Image in C in in CPL to highlight the clinopyroxene replacement by actinolite; F) Alteration clot in the GG hosted by plagioclase and lined by actinolite, chlorite, chalcopyrite, and magnetite; G) Alteration clot with epidote, chlorite, chalcopyrite, chalcopyrite, and actinolite; H) Micro-veinlet of chlorite and chalcopyrite with a halo of chalcopyrite, chlorite, actinolite and sericite; I) Micro-veinlet of chlorite with subhedral grains of epidote with a halo of chalcopyrite, biotite, actinolite, and apatite; J) Actinolite crystals (green) in chalcopyrite along the contact of a sharp-walled sulfide vein and the GG; K) Contact of the sharp-walled sulfide vein showing chalcopyrite extending into the GG wall rock that has been altered to actinolite and epidote.

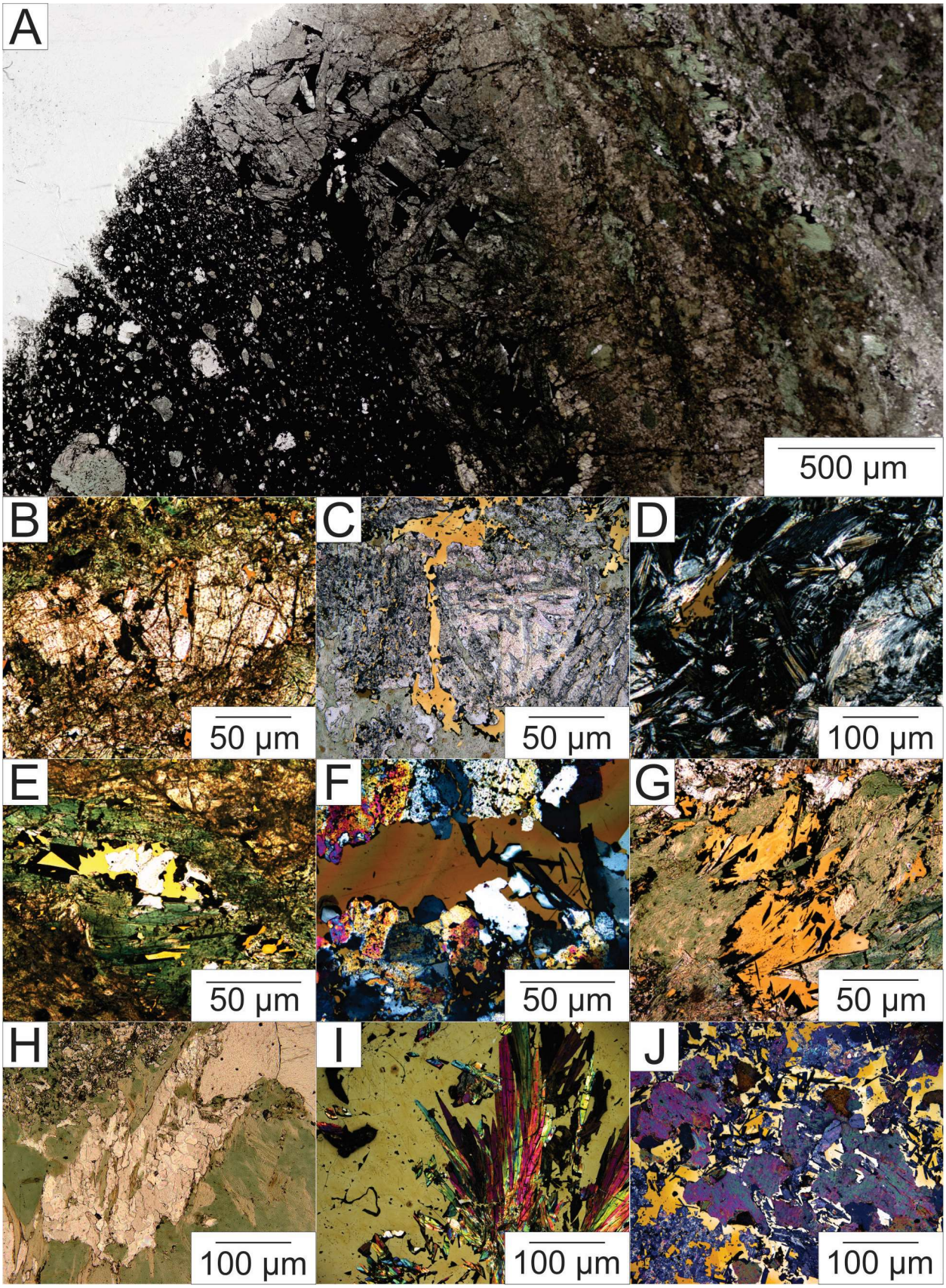
A
500 µm
B
50 µm
C
50 µm
D
100 µm
E
50 µm
F
50 µm
G
50 µm
H
100 µm
I
100 µm
J
100 µm

Fig. 6: Images of the most altered grey gabbro (GG) next to sharp-walled sulfide veins. A) Plane-polarized (PPL) scanned thin-section of sample LM-P-027. The black represents a sulfide-rich area (left side) and light areas (right side) a silicate-rich area. Note the layered structure away from the sulfide-rich vein; B) Micro-vein, as seen in both reflected light (RL) and PPL, with epidote, chalcopyrite, and a halo of actinolite, chlorite, magnetite, and chalcopyrite; C) Alteration clot, as seen in combined RL and PPL with epidote, biotite, chlorite, actinolite, magnetite, and chalcopyrite. Note the chalcopyrite infilling pore space; D) Micro-vein, as seen in combined cross-polarized light (CPL) and RL, of coarse-grained chlorite (black to white) with chalcopyrite (rusty yellow); E) Alteration clot, as seem in combined RL and PPL, with actinolite, epidote, quartz, magnetite, and chalcopyrite, with a halo of sericite, actinolite, and biotite; F) Micro-vein of chalcopyrite with a halo of quartz, feldspar, apatite, clinopyroxene, and actinolite. Image taken in combined RL an CPL; G) Alteration clot, as seen in combined RL and PPL comprised of actinolite, chlorite, and chalcopyrite; H) PPL image of a coarse-grained calcite-rich micro-vein surrounded by chlorite; I) Combined CPL and RL image of chalcopyrite with inclusions of radiating actinolite fibers; J) Combined CPL and RL image of epidote, actinolite, biotite, and calcite inclusions in in chalcopyrite.

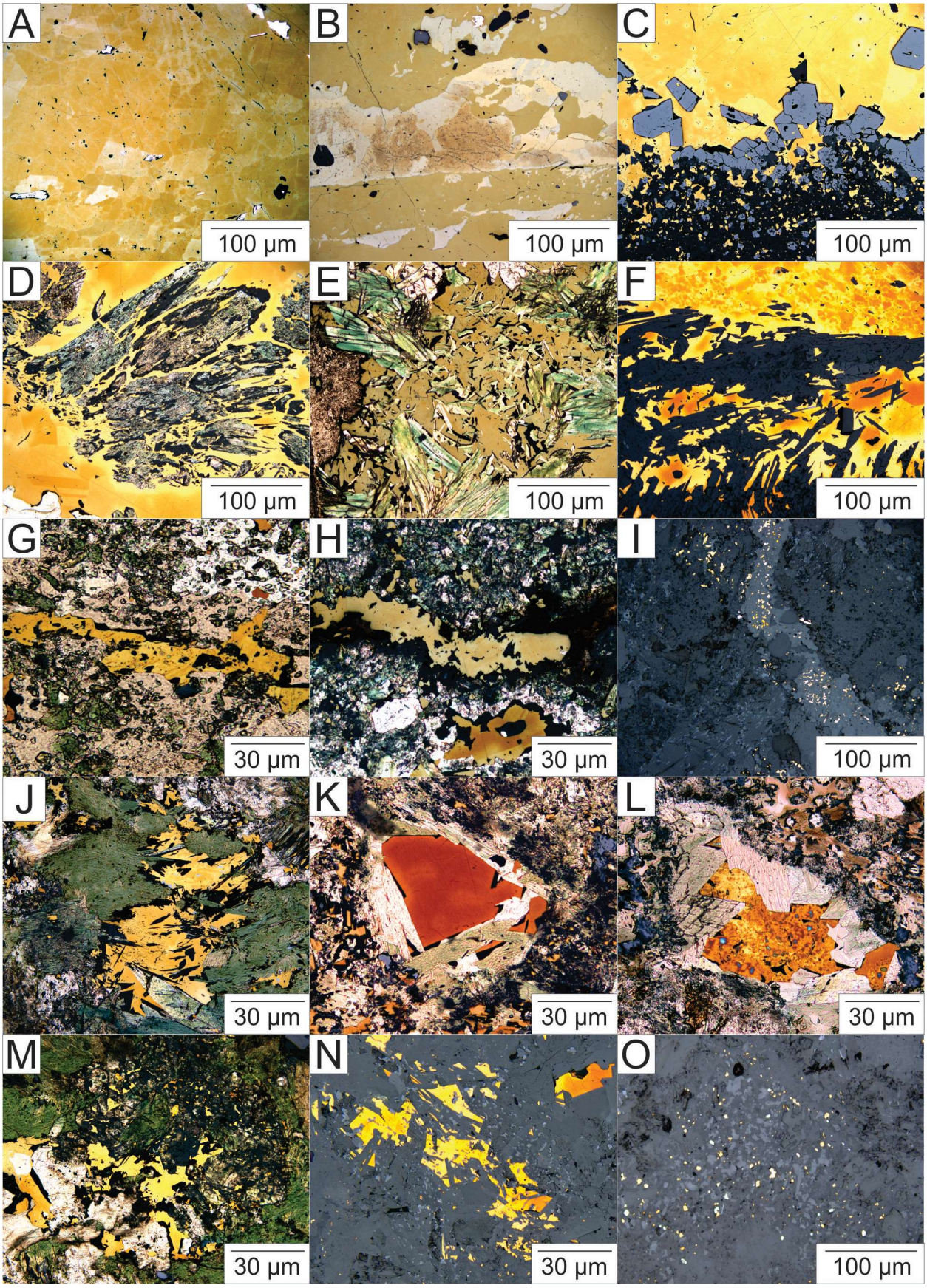
A
100 µm
B
100 µm
C
100 µm
D
100 µm
E
100 µm
F
100 µm
G
30 µm
H
30 µm
I
100 µm
J
30 µm
K
30 µm
L
30 µm
M
30 µm
N
30 µm
O
100 µm

Fig. 7: Different styles of sulfide mineralization that occur in the grey gabbro (GG) unit. Area within the sharp-walled sulfide vein (A, B) that gives way to the contact of sharp-walled sulfide vein (C, D, E, F, G) and then as micro-veins in the GG (H, I), and finally to alteration clots present in the grey gabbro (J, K, L, M). Lastly are images of chalcopyrite grains located throughout the host rock: A) Reflected light (RL) image of massive chalcopyrite with minor inclusions of gabbroic material; B) RL image of massive chalcopyrite with minor amounts of cubanite (bluish-grey), magnetite (dark grey), and millerite (light yellow); C) RL image along the contact of the sharp-walled sulfide vein showing euhedral magnetite in chalcopyrite, silicates are in black (grey gabbro); D) Combined plane-polarized (PPL) and RL image of chalcopyrite hosting acicular actinolite crystals; E) Combined PPL and RL image of chalcopyrite hosting actinolite crystals along the contact of the GG and the sharp-walled sulfide vein; F) Combined CPL and RL image of actinolite crystals at contact of the chalcopyrite-rich sulfide vein and GG; G) Combined PPL and RL image of a micro-vein hosted in GG; H) Combined PPL and RL image of a micro-vein hosting abundant chalcopyrite; I) RL image of a micro-vein showing chalcopyrite (yellow), magnetite (blue-grey) and pyrite (pinkish-white) which occur in the vein and gabbro host; J) Combined PPL and RL image of a clot comprised of intergrown chlorite and chalcopyrite; K) Combined PPL and RL image of chalcopyrite rimmed by actinolite crystals; L) Combined PPL and RL image of an alteration clot dominated by epidote and actinolite and cored by chalcopyrite; M) Combined PPL and RL image showing chalcopyrite in GG that is often associated with hydrothermal phases, in this case chlorite; N) RL image of chalcopyrite (yellow) and magnetite (bluish-grey) in GG; O) RL image of a disseminated chalcopyrite (yellow), magnetite (blue-grey) and pyrite (pinkish-white) that in the GG.

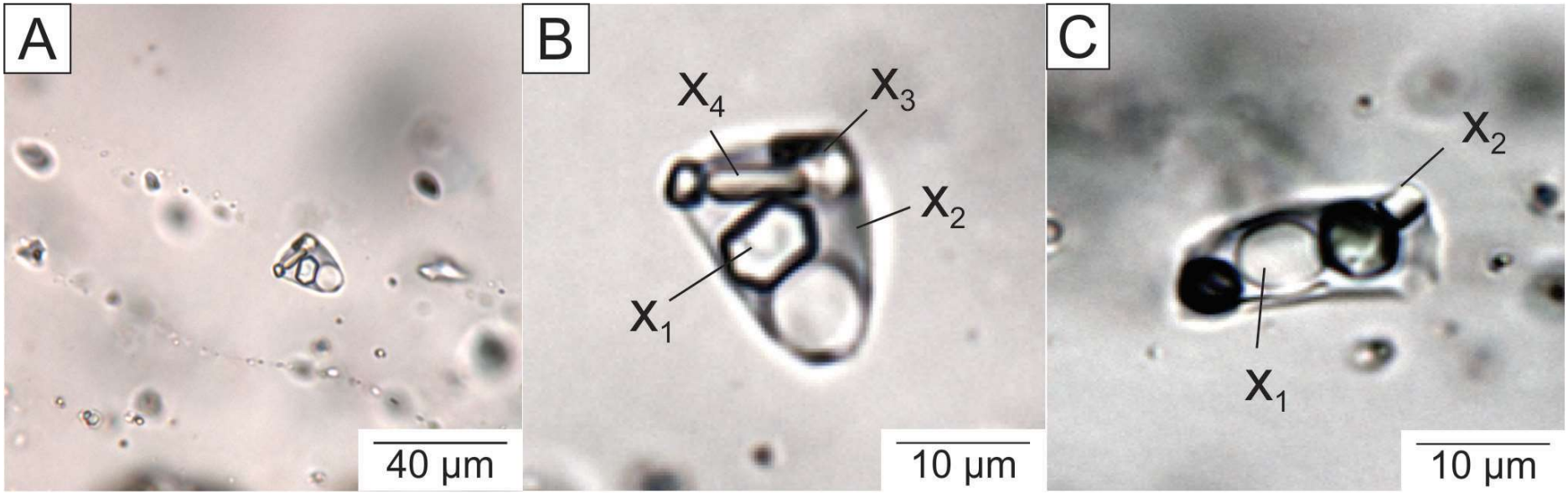

Fig. 8: Representative examples of quartz-hosted fluid inclusions from a quartz-actinolite-epidote-magnetite alteration halo in the grey gabbro unit marginal to a sharp-walled sulfide veins. Note there is not significance to the labeling other than to highlight the presence of abundant and different solid phases in the inclusions. A, B) Low- and high-magnification images of a multi-solid fluid inclusion with at least 4 solid phases; note the presence of an aqueous vapor phase in the upper left corner. In image A, note the inclusions are aligned on steeply dipping fracture planes cutting the host quartz; C) Fluid inclusion with at least two solid phases and apparently two aqueous (?) vapor phases.

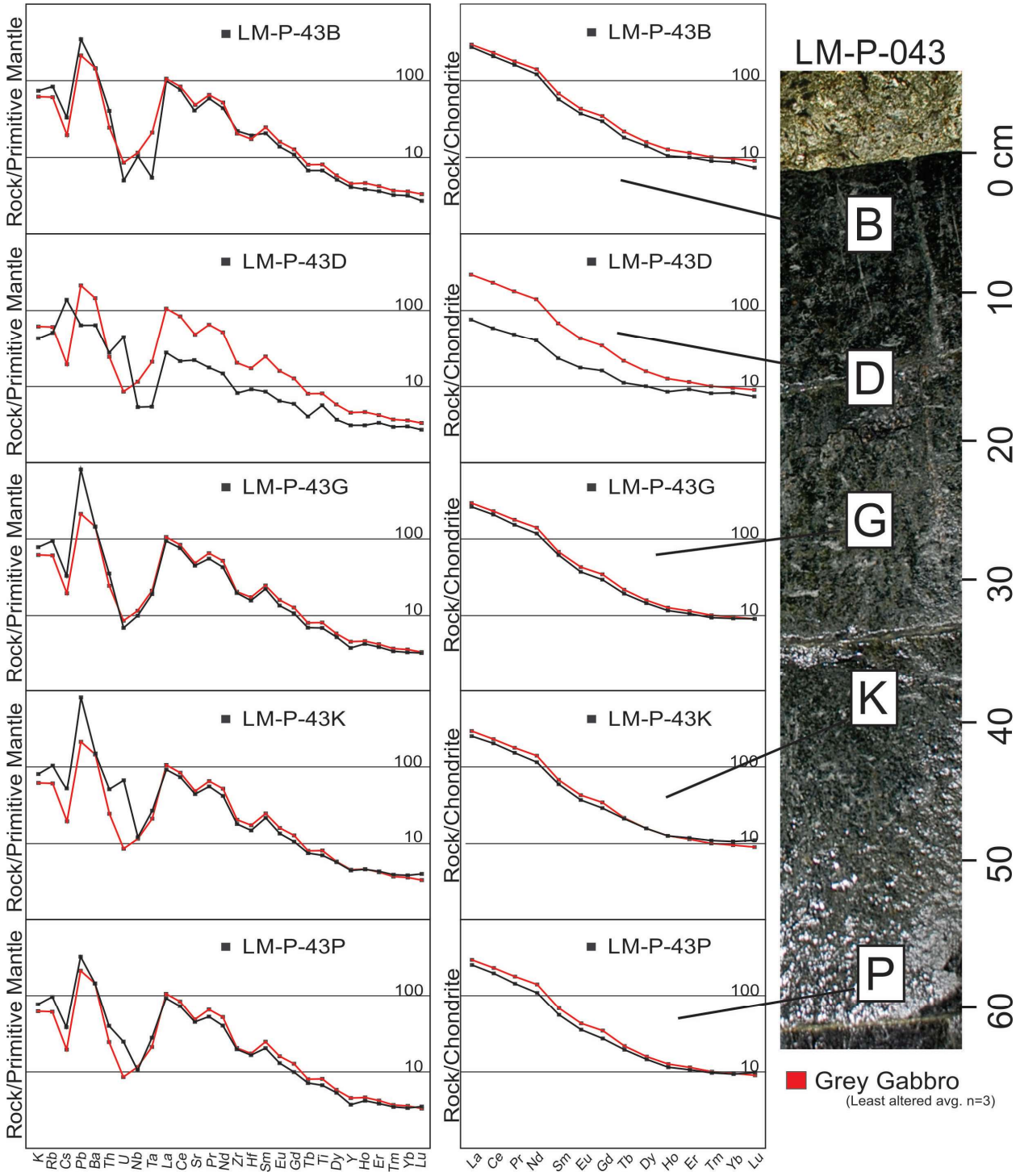
LM-P-43B
LM-P-43D
LM-P-43G
LM-P-43K
LM-P-43P
Rock/Primitive Mantle
Rock/Chondrite
100
10
K Rb Cs Pb Ba Th U Nb Ta La Ce Sr Pr Nd Zr Hf Sm Eu Gd Tb Ti Dy Y Ho Er Tm Yb Lu
La Ce Pr Nd Sm Eu Gd Tb Dy Ho Er Tm Yb Lu
LM-P-043
B
D
G
K
P
0 cm
10
20
30
40
50
60
Grey Gabbro
(Least altered avg. n=3)

Fig. 9: A summary of the whole-rock geochemistry of representative samples from a traverse in sample LM-P-043. The data have been plotted in primitive-mantle and chondrite-normalized diagrams using factors in McDonough and Sun (1995). The red line in each plot represents an average value for least altered grey gabbro (n=3; see Table 2). Note that samples are located proximal to distal from the sulfide vein as follows: LM-P-043B (~5.5 cm, from the sharp-walled sulfide vein), LM-P-043D (~12.5 cm), LM-P-043G (~23 cm), LM-P-043K (~37 cm), and LM-P-043P (~54.5 cm). See text for detailed discussion of the data.

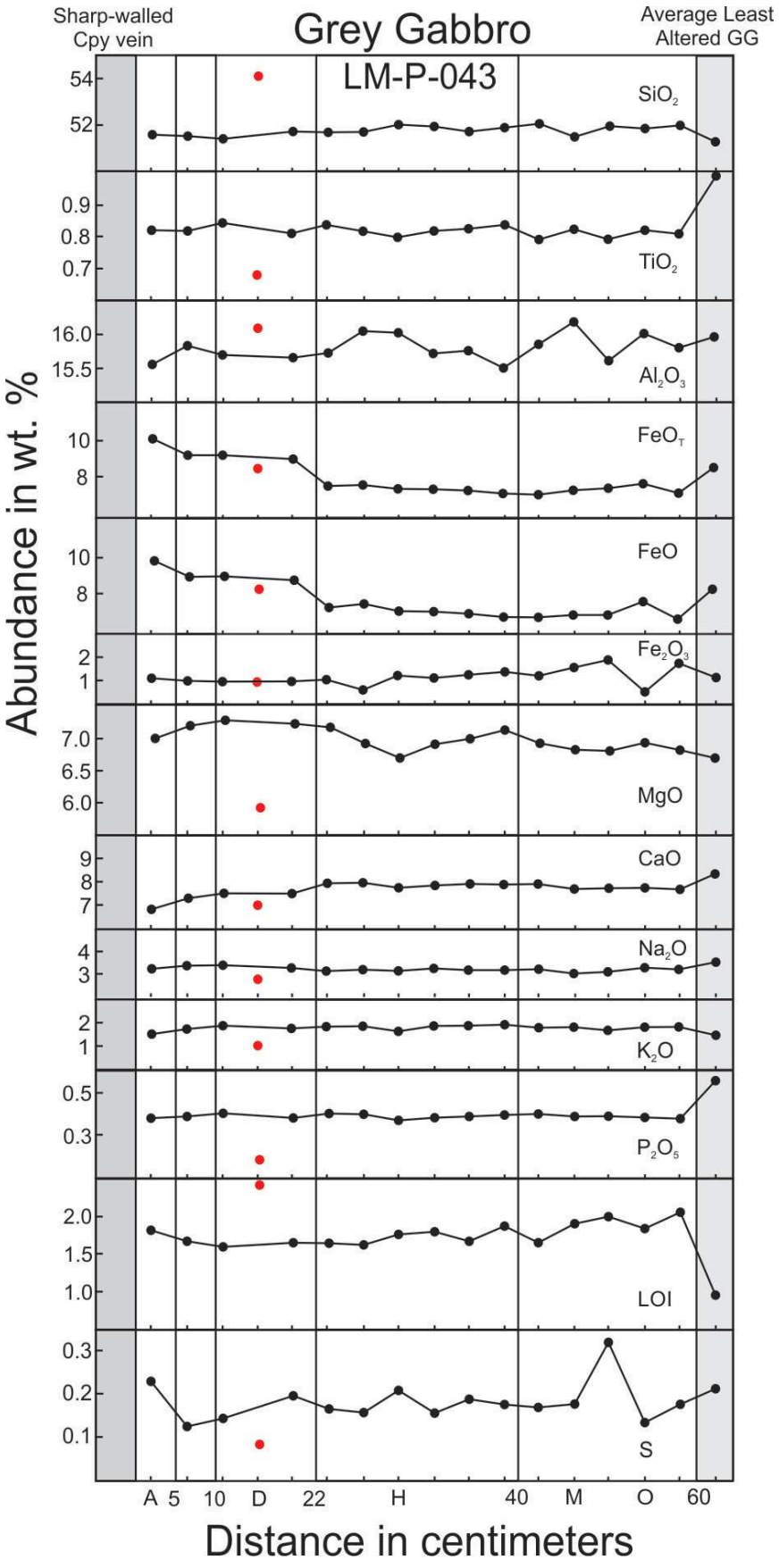
Sharp-walled
Cpy vein
Grey Gabbro
LM-P-043
Average Least
Altered GG
SiO2
TiO2
Al2O3
FeOT
FeO
Fe2O3
MgO
CaO
Na2O
K2O
P2O5
LOI
S
Abundance in wt. %
A 5 10 D 22 H 40 M O 60
Distance in centimeters

Fig. 10: A summary of the major-element chemistry of whole-rock samples along a transect in sample LM-P-043 from distal to proximal the sharp-walled sulfide vein (right to left). The first sample plotted is the average for the least altered grey gabbro (n=3; see Table 2). Note that sample LM-P-043D is shown in red and is omitted from the trend line drawn in black due to the presence of a calcite-rich micro-vein that contaminated the sample.

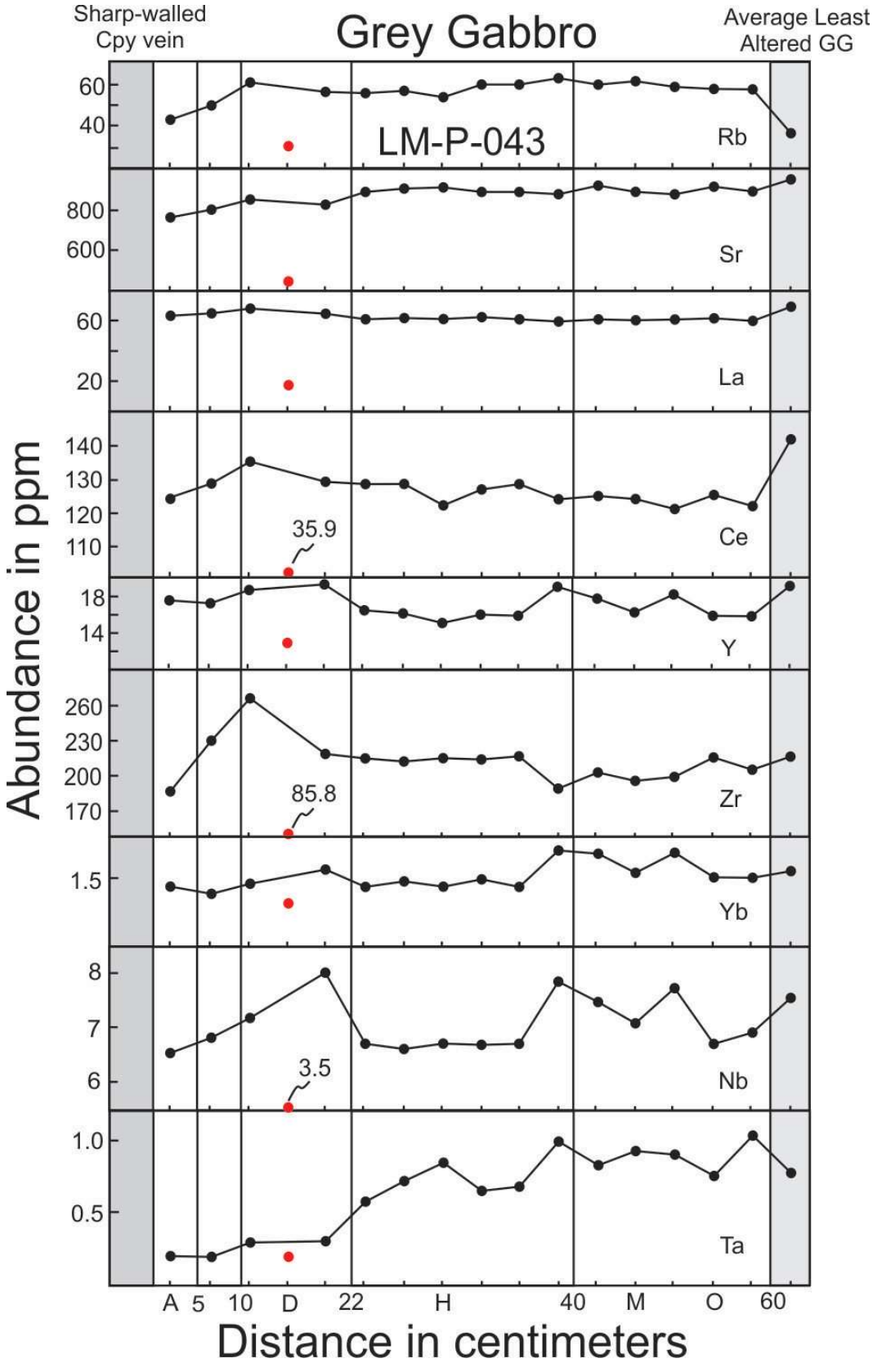
Sharp-walled
Cpy vein
Grey Gabbro
Average Least
Altered GG
LM-P-043
Rb
Sr
La
Ce
Y
Zr
Yb
Nb
Ta
35.9
85.8
3.5
Abundance in ppm
Distance in centimeters
A 5 10 D 22 H 40 M O 60

Fig. 11: A summary of the trace-element chemistry for whole-rock samples along a transect in sample LM-P-043 from distal to proximal the sharp-walled sulfide vein (right to left). The first sample plotted is the average for the least altered grey gabbro (n=3; see Table 2). Note that sample LM-P-043D is shown in red and is omitted from the trend line drawn in black due to the presence of a calcite-rich micro-vein that contaminated the sample.

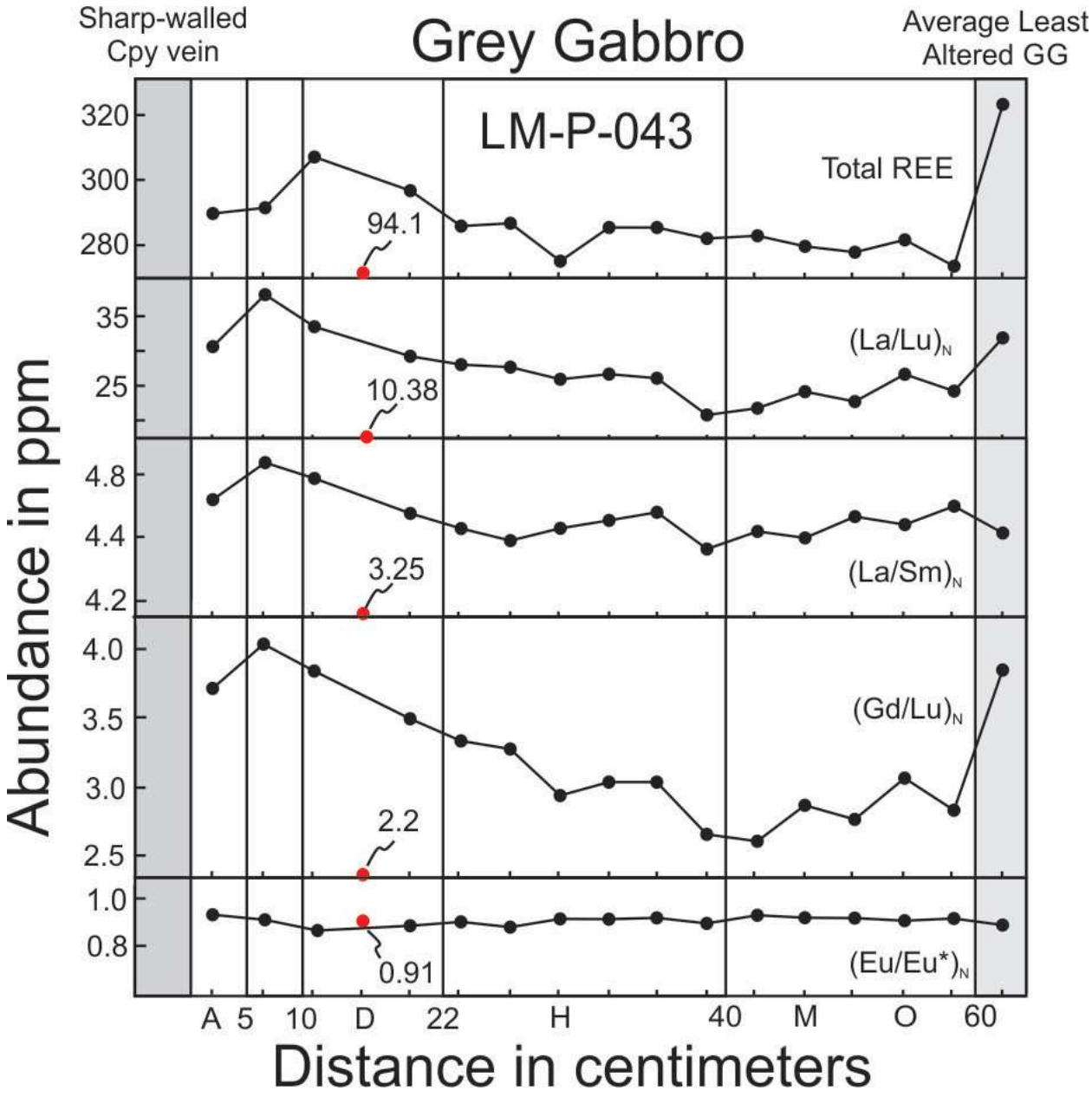

Fig. 12: A summary of the rare earth element chemistry of whole-rock samples along a transect in sample LM-P-043 from distal to proximal the sharp-walled sulfide vein (right to left). The first sample plotted is the average for the least altered grey gabbro (n=3; see Table 2). Note that sample LM-P-043D is shown in red and is omitted from the trend line drawn in black due to the presence of a calcite-rich micro-vein that contaminated the sample. Shown in the diagram are values for ΣREEs, overall fractionation of the REEs by $(La/Lu)_N$; fractionation of the LREEs by $(La/Sm)_N$; fractionation of the HREEs by $(Gd/Lu)_N$; and indication of the Eu anomaly by (Eu_N/Eu^*).

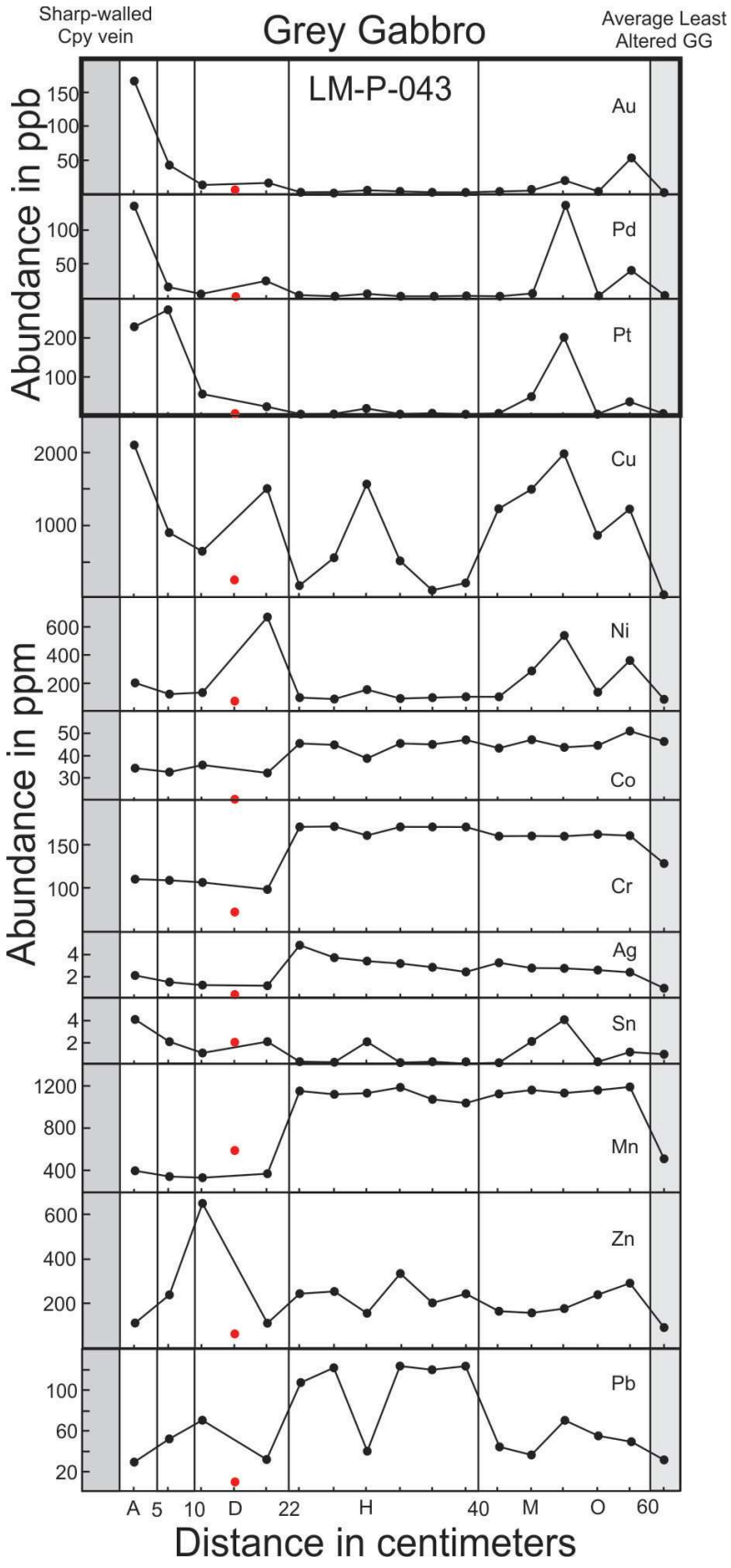
Sharp-walled
Cpy vein
Grey Gabbro
Average Least
Altered GG
LM-P-043
Au
Pd
Pt
Cu
Ni
Co
Cr
Ag
Sn
Mn
Zn
Pb
Abundance in ppb
Abundance in ppm
A 5 10 D 22 H 40 M O 60
Distance in centimeters

Fig. 13: A summary of metal abundance in whole-rock samples along the transect in sample LM-P-043 from distal to proximal the sharp-walled sulfide vein (right to left). Note that Au, Pd and Pt are in ppb and the other elements are in ppm. The first sample plotted is the average for the least altered grey gabbro (n=3; see Table 2). Note that sample LM-P-043D is shown in red and is omitted from the trend line drawn in black due to the presence of a calcite-rich micro-vein that contaminated the sample.

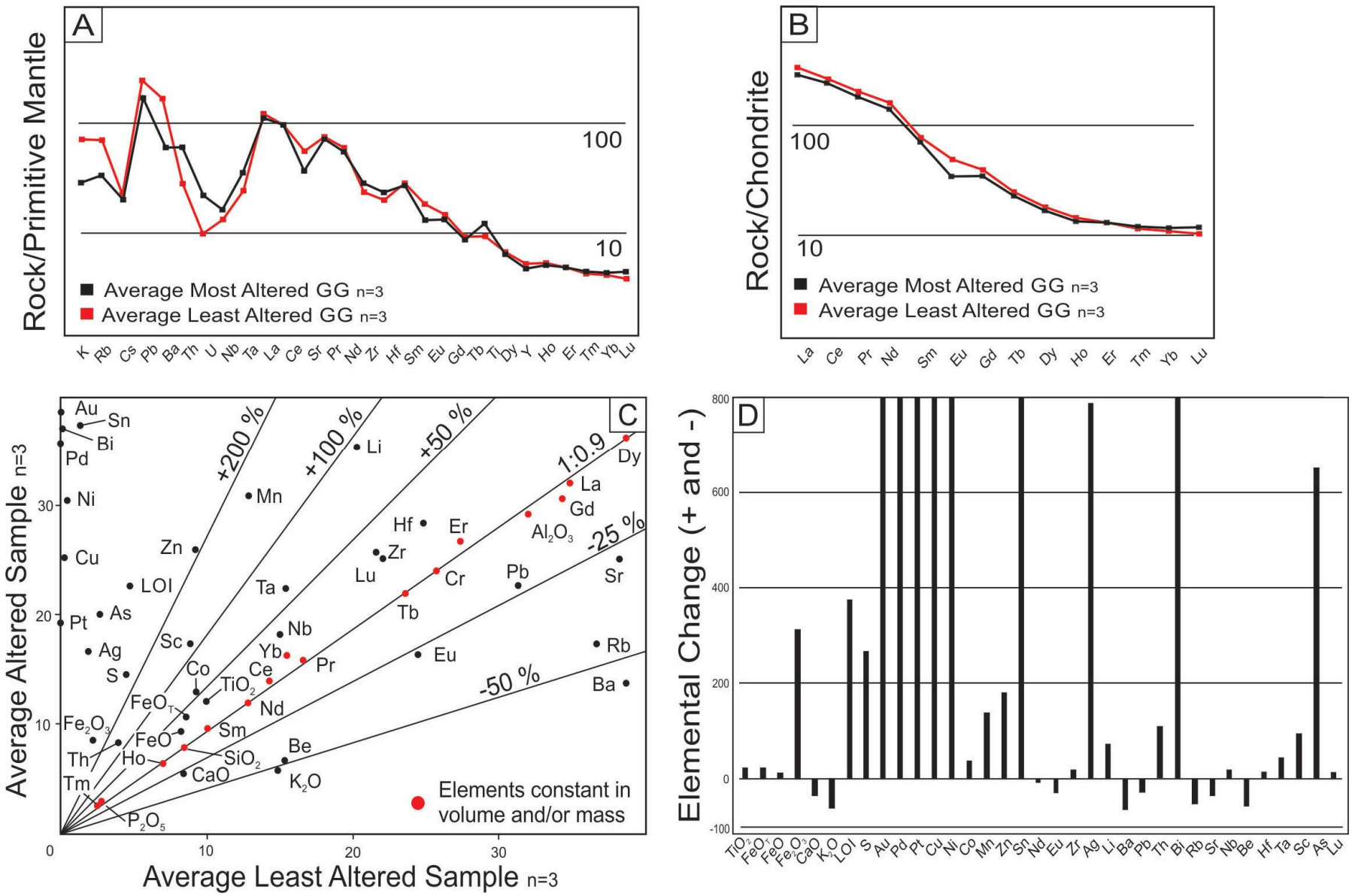
A
Rock/Primitive Mantle
100
10
Average Most Altered GG n=3
Average Least Altered GG n=3
K Rb Cs Pb Ba Th U Nb Ta La Ce Sr Pr Nd Zr Hf Sm Eu Gd Tb Ti Dy Y Ho Er Tm Yb Lu
B
Rock/Chondrite
100
10
Average Most Altered GG n=3
Average Least Altered GG n=3
La Ce Pr Nd Sm Eu Gd Tb Dy Ho Er Tm Yb Lu
C
Average Altered Sample n=3
Average Least Altered Sample n=3
+200 %
+100 %
+50 %
1:0.9
-25 %
-50 %
Elements constant in volume and/or mass
D
Elemental Change (+ and -)
800
600
400
200
0
-100

Fig. 14: Diagrams comparing the average (n=3; LM-P-026, LM-P-027, and LM-P-031) composition for the most intensely altered grey gabbro (black line; GG) from against sharp-walled sulfide veins to the average (n=3; LM-P-007, LM-P-021, and LM-P-025) composition of the least altered GG (red line). A) Plot of average least altered GG normalized to primitive mantle versus the same for the average least altered GG; B) The same data in the previous plot normalized to chondrite; C) A Grant (1986) – type isocon plot comparing the average for most altered GG against the average for least altered GG. Note that elements in red were inferred to have been conserved and define the isocon line which has a slope of 0.9, hence there has been some mass gain recorded by the alteration; D) Plot of the relative elemental gains (%) for the average of the most altered GG samples versus the least altered GG. Note that the only the results for the significant major and minor elements are plotted. Normalizing values in plot A and B are from McDonough and Sun (1995). See Table 2 for more details.

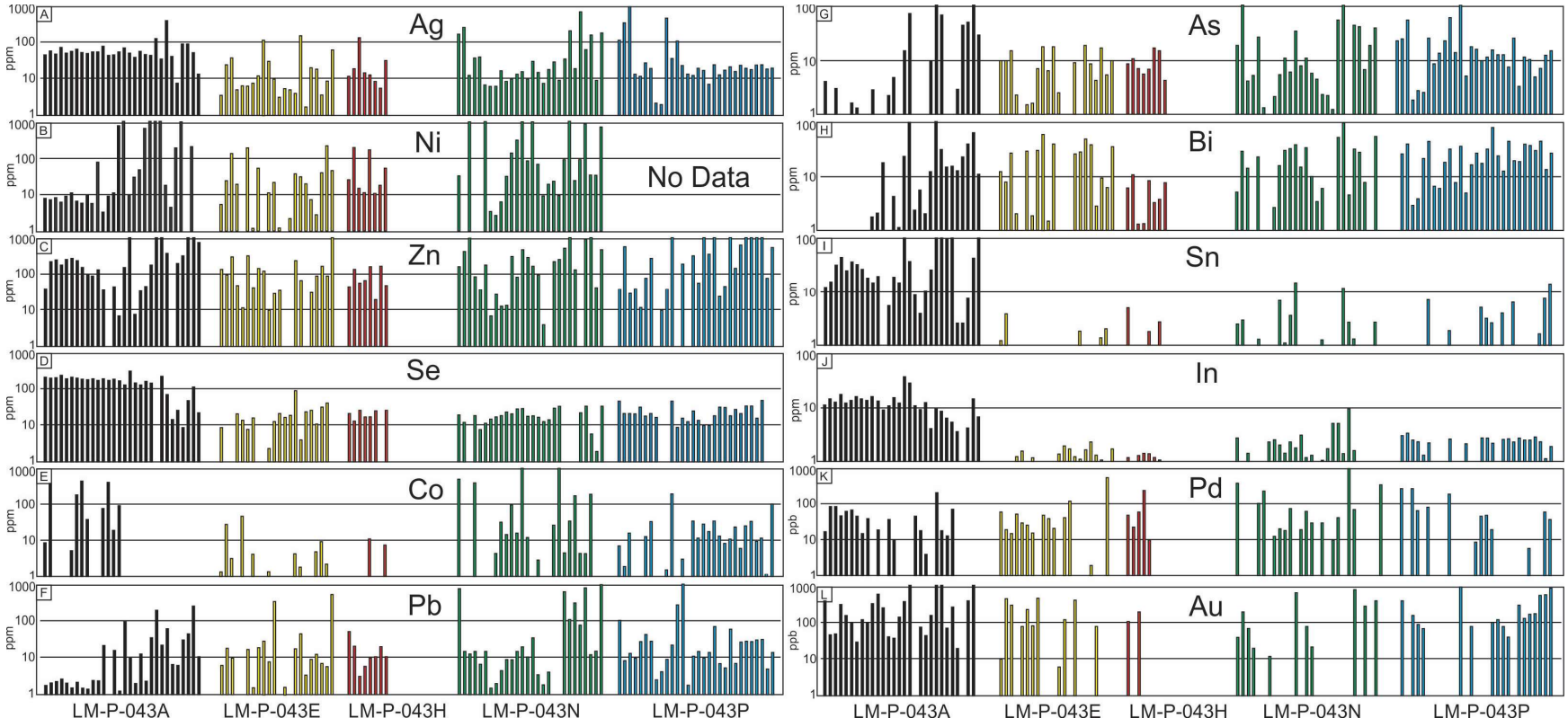
A
Ag
B
Ni
No Data
C
Zn
D
Se
E
Co
F
Pb
G
As
H
Bi
I
Sn
J
In
K
Pd
L
Au
ppm
ppb
1000
100
10
1
LM-P-043A
LM-P-043E
LM-P-043H
LM-P-043N
LM-P-043P

Fig. 15: A summary of element abundances in chalcopyrite associated with disseminated type mineralization measured in situ using LA ICP-MS in five polished thin sections from the transect in sample LM-P-043: LM-P-043A (black; <~2.5 cm; distance from vein contact for this and others to follow), LM-P-043E (yellow; ~16 cm), LM-P-043H (red; ~26.5 cm), LM-P-043N (green; ~47.5 cm), and LM-P-043P (blue; ~54.5 cm). Note that Ag, Ni, Zn, Se, Co, Pb, As, Bi, Sn, and In are in ppm whereas Pd and Au are in ppb.

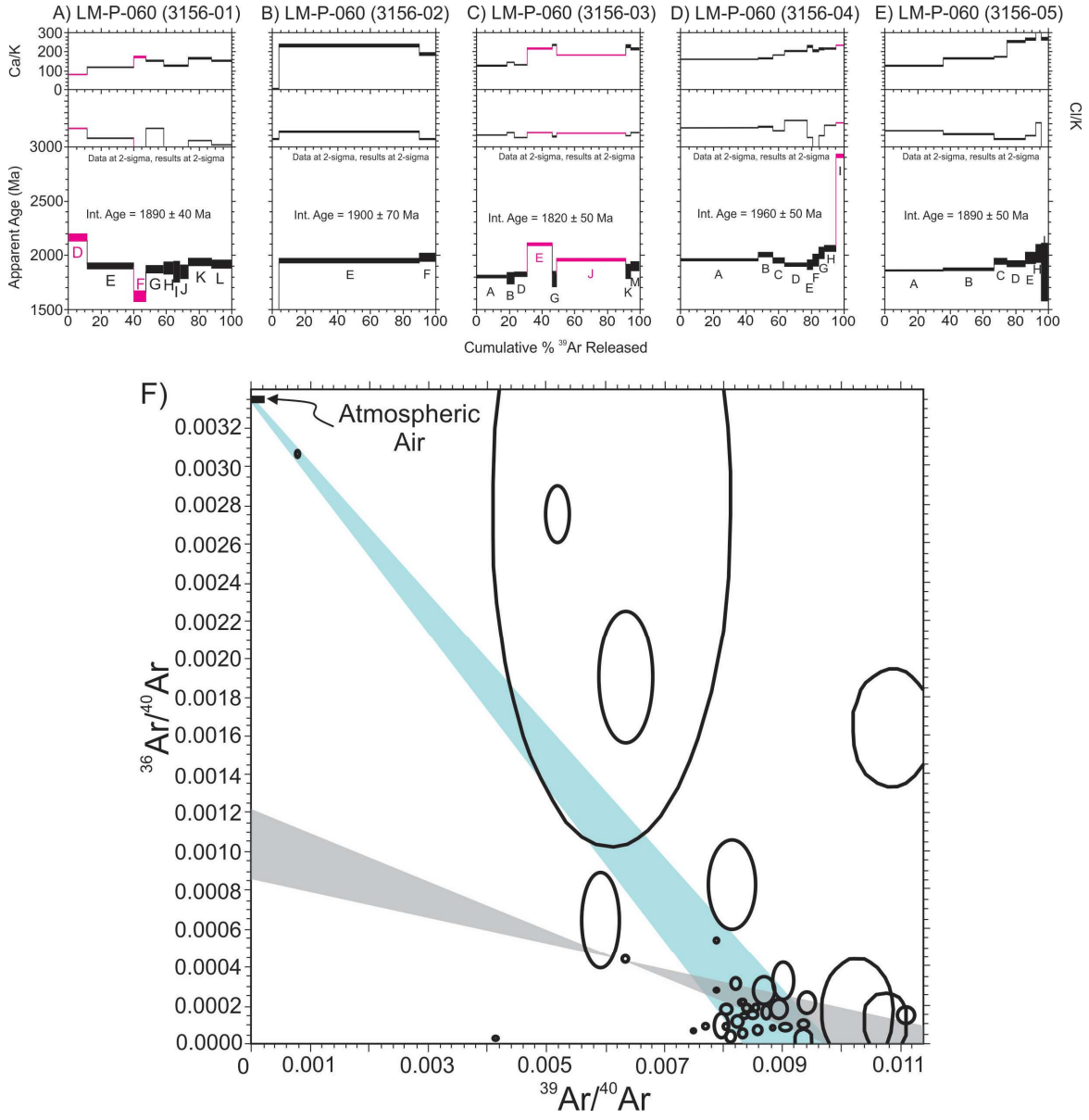

Fig. 16: (A) to (E) Argon gas-release age spectra for five aliquots of actinolite from sample LM-P-060 analysed for $^{40}Ar/^{39}Ar$ dating. Note that only gas steps comprising >2 % of the total ^{39}Ar released are plotted. Integrated ages are shown for each aliquot but do not include steps that are shown as unfilled boxes (or plot off-scale of the diagram which step A does in Aliquot 2). (F) Inverse argon isochron plot showing data points for all five step-heated aliquots with error ellipses shown for 2σ. The aqua band shows a range of possible regressions anchored by a single near-atmospheric data point in the upper left. Ages derived from the $^{39}Ar/^{40}Ar$ x-intercepts range from ca. 1812 to 1990 Ma. The grey shaded areas are fields that fall between two example regressions for the data points containing excess ^{40}Ar; ages derived from these $^{39}Ar/^{40}Ar$ x-intercepts (corrected for excess ^{40}Ar) and range from ca. 1510 to 1800 Ma (with $^{40}Ar/^{36}Ar$ compositions of 1160 ± 160 Ma and 820 ± 90 Ma, respectively). Note that the diagram is unmodified as presented in MacInnis et al. (2014).

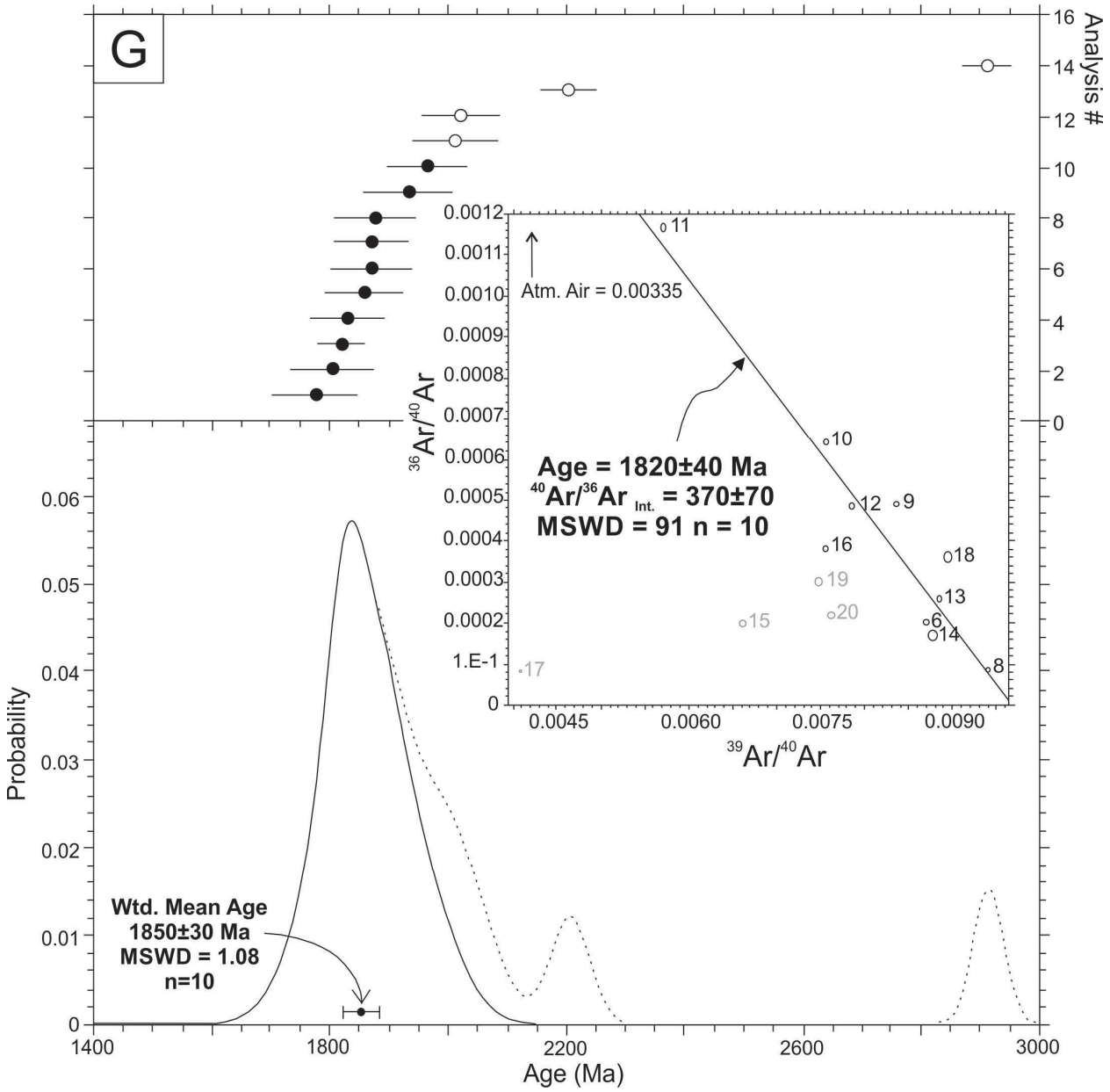

Fig. 17: Age probability distribution plot for 14 single-fusion analyses of actinolite from sample LM-P-060 of the Podolsky deposit. The error ellipses shown, and values represent the errors at 2σ. The most prominent peak, using 10 of the 14 analyses (rejected analyses are plotted as open circles), is at age 1850 ± 30 Ma. The dotted line shows the peaks of the rejected data. The inset plot shows the inverse isochron diagram of the 14 analyses in which all the analyses plotted blow the atmospheric line (not shown because it falls outside the scale of the diagram) that indicates all the analyses contained excess ^{40}Ar. The scatter of the data and the very high mean square weighted deviation (MSWD = 91) for the regression line through the 10 analyses that were used for the weighted mean age illustrates the highly variable composition of the excess argon in these grains. A best estimate of the actinolite age (corrected for excess) would be 1820 ± 40 Ma, with a ^{40}Ar/^{36}Ar intercept of ~370. The diagram is unmodified as presented in MacInnis et al. (2014).

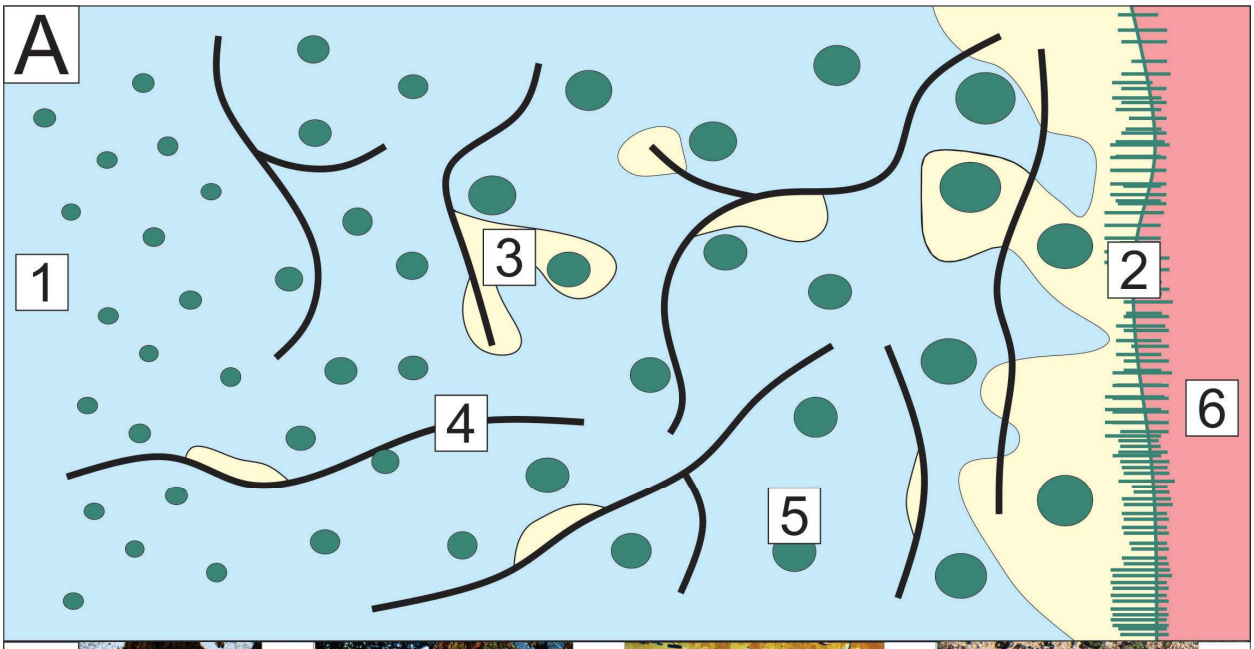

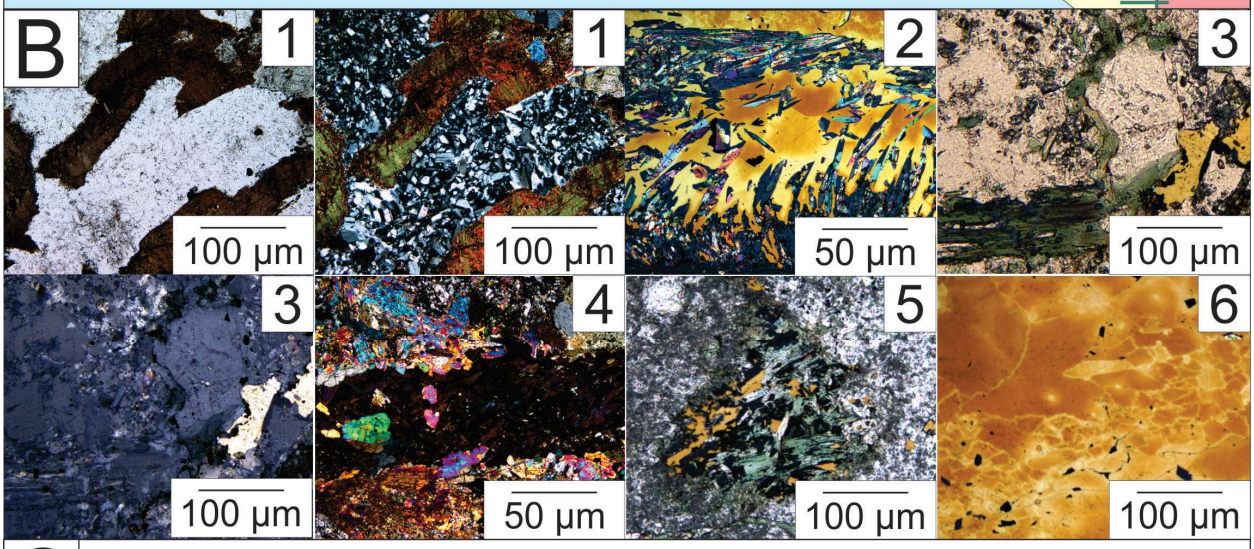

C

Grey gabbro (GG) syn- and post-bolide impact

Stages	Timing
Bolide impact	
Alkali-gabbro (GG) fragment dislodged	
Formation of Whistle offset	
GG entrapped in Whistle offset	(1)
Actinolite fibers grow along dilated fractures	(2)
SIC cools (contact metamorphism)	(3)
Hydrothermal Alteration (veins and clots)	(4,5)
Entrapment of Cu(-Ni)-PGEs in fractures	(6)

1850 Ma

Fig. 18: Diagram summarizing the paragenesis for the grey gabbro (GG) both schematically and with supporting photomicrographs. Note that numbers 1-6 in sections A, B, and C represent the same part of the paragenesis. A) A schematic summary of the observed alteration and veining in the GG (blue). The left side of the image is the least altered GG and transitions to the most altered towards the right of the image (beige). The sharp-walled sulfide vein is in red whereas green is for alteration clots, beige the most altered GG, and the black lines are micro-veins; B) Photomicrographs summarizing events that affected the GG as follows: 1) Plane-polarized (PPL) and cross polarized light (CPL) images of relict plagioclase with granoblastic (mosaic) texture surrounded by biotite and clinopyroxene; 2) Combined RL and CPL image of a sharp-walled sulfide vein at contact of GG showing chalcopyrite (yellow) intergrown with acicular actinolite oriented perpendicular to the wall rock; 3) PPL and combined reflected light (RL) and CPL images of sericite-rich plagioclase surrounded by chlorite, actinolite, and chalcopyrite; 4) CPL image of a chlorite-rich micro-vein (dark brown) surrounded by epidote, actinolite, and clinopyroxene; 5) Alteration clot in combined RL and CPL image that is dominated by actinolite with magnetite and chalcopyrite; 6) RL image of massive chalcopyrite with micro-inclusions of GG material; C) Paragenesis of events for the Podolsky area and the GG unit and associated sharp-walled veins.

Appendices:

Sample	Cu (ppm)	Co (ppm)	Ni (ppm)	Zn_{68} (ppm)	As (ppm)	Se_{82} (ppm)	Ag (ppm)	Pd108 (ppb)
CPY_A	34900000	<LOD	1	41	4	226	47.1	0
CPY_A	59200000	0.19	8.1	236	0.9	211	62	17
CPY_A	59300000	0.18	7.2	261	3	217	50.6	84
CPY_A	52100000	<LOD	8.5	188	<LOD	253	78	85
CPY_A	64200000	0.12	6.3	270	<LOD	203	53.5	46
CPY_A	51900000	0.08	9.2	288	1.6	223	60.5	62
CPY_A	57000000	0.11	11.4	250	1.3	216	69.2	67
CPY_A	55300000	0.1	6.7	162	<LOD	199	55.6	45
CPY_A	66800000	0.09	5.9	102	<LOD	190	52.8	15
CPY_A	46300000	0.24	10.1	96	2.8	207	57.8	39
CPY_A	69400000	<LOD	5.8	138	<LOD	184	57.5	<LOD
CPY_A	60200000	0.4	80	40	0.4	203	83.8	19
CPY_A	64300000	<LOD	3.3	<LOD	2.2	182	46.4	<LOD
CPY_A	54800000	0.39	9.4	47	4.8	197	48.1	37
CPY_A	63000000	0.24	11.5	7	0.6	176	57.3	10
CPY_A	13100000	9	820	160	15	138	74	<LOD
CPY_A	3900000	410	56000	5500	74	330	55	<LOD
CPY_A	68300000	0.07	10.3	8	0	156	40.8	<LOD
CPY_A	54600000	0.32	31.5	35	1	139	60.6	45
CPY_A	59400000	0.64	50	48	0.8	173	49.3	18
CPY_A	27800000	5.4	680	190	9.8	155	46.3	4
CPY_A	2400000	193	26000	2000	140	<LOD	136	<LOD
CPY_A	2510000	470	73000	10400	70	240	37.2	200
CPY_A	21900000	40	4900	400	<LOD	74	430	18
CPY_A	38300000	0.21	18.7	<LOD	0.8	15	43.6	13
CPY_A	19000000	0.6	4.5	210	2.9	27	7.9	70
CPY_A	9200000	82	200	340	45	9	97	<LOD
CPY_A	5300000	430	1040	3200	51	50	97	<LOD
CPY_A	1120000	20	<LOD	3300	220	120	55	<LOD
CPY_A	11600000	98	214	790	30	23	14.1	<LOD
CPY_E	19000000	0.72	5.4	147	10	9	3.64	<LOD
CPY_E	15700000	1.4	24	100	10	<LOD	26	60
CPY_E	19300000	29	140	320	15	<LOD	39	20
CPY_E	53300000	3.29	19.3	51	2.3	20.8	5.11	15
CPY_E	57800000	0.23	0.8	12	<LOD	13.9	6.6	52
CPY_E	34000000	49	193	350	1.5	8	6.42	30
CPY_E	50300000	<LOD	1.2	44	1.6	16.6	7.96	26
CPY_E	17400000	4.3	54	150	7	0	12.8	16
CPY_E	9700000	<LOD	<LOD	130	18	<LOD	124	<LOD
CPY_E	24500000	0	11.2	10	6.4	2.3	31.7	49
CPY_E	11740000	1.4	22	30	18	13	10.4	40
CPY_E	59900000	0.07	1.2	37	2.5	21.7	3.18	21
CPY_E	46400000	0.44	0.3	<LOD	0.9	17	5.56	<LOD
CPY_E	51700000	0.44	2.2	<LOD	1	19.6	5.14	42
CPY_E	16100000	0.6	38	250	9	95	4.1	120
CPY_E	18600000	4.4	31	70	1	4	163	<LOD
CPY_E	17600000	1.9	20	<LOD	19	24	1.72	<LOD
CPY_E	35200000	0.9	7.3	32	8.6	27	21.2	<LOD
CPY_E	28500000	0.49	2.8	101	4.2	11	19.4	2
CPY_E	10900000	5	40	180	17	33	3.7	<LOD
CPY_E	46500000	9.6	226	97	5.4	42.2	9	<LOD
CPY_E	4400000	2.3	46	4900	10	<LOD	65	520

Appendix 1: LA ICP-MS dataset of disseminated chalcopyrite located along transect 2225L, LM-P-043 (samples A, E, H, N, and P) that were in the host rock (grey gabbro). Pulse rate: 4 Hz; Fluence: 7 J/cm3; Pit size: LM-P-043 (A, E, H, N): 14µm; LM-P-043P: 10µm. Note that CPY_A, E, H, N, and P are short for LM-P-043A, E, H, N, and P.

Sample	Cu (ppm)	Co (ppm)	Ni (ppm)	Ag (ppm)	Zn_{68} (ppm)	As (ppm)	Se_{82} (ppm)
CPY_A	9800000	0.71	7.2	6.9	43	8.4	31
CPY_A	5900000	0.17	2.4	6.5	61	2.6	26
CPY_A	8300000	0.26	2.7	5.4	93	2.9	40
CPY_A	6400000	0.16	3.1	11	55	3.5	31
CPY_A	7900000	0.25	2.2	4.6	150	2.5	25
CPY_A	7600000	0.33	4	5.8	93	3.5	33
CPY_A	7300000	0.31	3	7.7	130	2.6	31
CPY_A	5000000	0.18	2.4	4.5	39	2.2	21
CPY_A	5900000	0.28	2.4	5.1	28	2.1	20
CPY_A	4400000	0.26	3.5	6.3	48	3	25
CPY_A	4300000	0.23	2	6.1	38	1.8	21
CPY_A	4100000	0.18	14	8.2	37	2.1	16
CPY_A	6000000	0.25	2.2	4.5	24	2.4	19
CPY_A	5700000	0.36	3.3	5.7	37	2.2	18
CPY_A	4000000	0.22	3.2	5.3	25	1.6	15
CPY_A	1900000	4.8	460	12	130	12	31
CPY_A	1200000	160	28000	40	3700	32	150
CPY_A	4300000	0.25	2.6	3.2	25	1.6	12
CPY_A	5800000	0.26	6.9	5.9	28	2.1	14
CPY_A	4500000	0.4	25	4	30	1.7	15
CPY_A	3100000	2.4	250	9	120	7.9	26
CPY_A	1000000	68	11000	54	1900	150	250
CPY_A	690000	110	19000	9.4	3400	99	140
CPY_A	3900000	10	1600	110	140	6.9	31
CPY_A	5800000	0.61	6.9	7.8	81	3.7	11
CPY_A	4900000	1.7	8.8	2.2	310	8	23
CPY_A	3300000	33	100	33	270	58	56
CPY_A	2900000	300	630	88	2300	53	180
CPY_A	270000	20	310	52	2800	170	430
CPY_A	1600000	19	42	2.2	210	11	20
CPY_E	3700000	0.68	9.1	0.83	76	12	21
CPY_E	6900000	1.9	27	20	240	30	28
CPY_E	6000000	23	120	38	460	22	21
CPY_E	4000000	0.48	3.9	0.97	27	2.6	5.1
CPY_E	8800000	0.37	1.7	1.6	28	2.1	4.3
CPY_E	8600000	23	85	0.93	210	6.5	12
CPY_E	3600000	0.25	1.6	0.77	24	2.2	5.7
CPY_E	4400000	1.9	18	3.6	200	10	27
CPY_E	2300000	1.9	35	35	220	21	35
CPY_E	4700000	1.1	8.9	5.5	110	5.5	8.8
CPY_E	700000	1.8	12	3.1	150	14	16
CPY_E	3200000	0.17	1.8	0.37	29	1.8	5
CPY_E	3400000	0.3	2.3	0.55	32	2.5	4.8
CPY_E	7900000	0.25	2.2	0.64	35	2.6	6.6
CPY_E	6500000	1.1	53	4	140	14	87
CPY_E	3400000	2	13	47	110	9.4	19
CPY_E	5000000	2.1	17	0.81	150	13	20
CPY_E	7900000	1.1	6.4	5.6	45	5.5	11
CPY_E	2800000	0.42	6.2	4.9	85	4	11
CPY_E	1100000	2.5	30	1.6	210	17	30
CPY_E	4600000	1.3	23	1.2	44	4.3	8.3
CPY_E	1300000	6.2	51	33	2600	110	100

Appendix 1 (cont.): LA ICP-MS dataset of disseminated chalcopyrite located along transect 2225L, LM-P-043 (samples A, E, H, N, and P) that were in the host rock (grey gabbro). Pulse rate: 4 Hz; Fluence: 7 J/cm3; Pit size: LM-P-043 (A, E, H, N): 14µm; LM-P-043P: 10 µm. Note that CPY_A, E, H, N, and P are short for LM-P-043A, E, H, N, and P

Sample	Cd (ppm)	In (ppm)	Sn (ppm)	Sb (ppm)	Pt (ppm)	Au (ppb)	Pb (ppm)
CPY_A	3.2	11.4	12.6	0.03	0	400	1.8
CPY_A	9.4	15	15.8	0.09	0	47	2.11
CPY_A	5.8	12.9	32.3	0.05	0	50	2.29
CPY_A	7.3	18.3	45.6	<LOD	0	320	2.74
CPY_A	17	12.4	25.5	0.08	0	159	2.09
CPY_A	15.2	14	37.5	<LOD	0	100	1.55
CPY_A	10.4	16.3	33.6	0.22	0	30	2.25
CPY_A	4.4	15	27.1	0.13	0	120	1.55
CPY_A	3.7	13.8	18.5	0.1	0	103	1.43
CPY_A	5.1	16.2	15.2	<LOD	0	340	2.47
CPY_A	5	13.7	19.9	0.044	0	610	2.46
CPY_A	2.6	9.24	0.39	0.06	0	260	22.4
CPY_A	2.04	11	5.62	0.002	0	42	0.89
CPY_A	2.5	15.9	19.2	0.03	0	38	16.6
CPY_A	2.4	12.5	15.1	0.024	0	143	1.27
CPY_A	3.5	39	1230	<LOD	0	380	104
CPY_A	5	29.6	38	<LOD	0	1900	10
CPY_A	1.24	11.1	8.9	0.12	0	<LOD	2.04
CPY_A	4	9.44	3.95	0.14	0	76	13.2
CPY_A	2.11	12.6	10.3	0.137	0	45	2.41
CPY_A	4.1	4.1	26.4	<LOD	0	160	37.5
CPY_A	<LOD	9.6	350	4.1	0	60000	210
CPY_A	0	8.7	463	3	0	1800	23
CPY_A	0	6.4	103	<LOD	0	70	66.2
CPY_A	1.3	5.4	118	0.05	0	270	6.8
CPY_A	0.6	3.6	2.6	0.18	0	20	6.4
CPY_A	<LOD	1	2.6	<LOD	0	<LOD	32
CPY_A	8	4.2	7.7	3.8	0	400	48
CPY_A	<LOD	15	44	<LOD	0	4000	280
CPY_A	3	6.8	192	0.19	0	<LOD	11.2
CPY_E	5.6	0.21	0.6	0.13	0	10	6.4
CPY_E	<LOD	0.63	1.2	0.71	0	460	19
CPY_E	3.5	0.9	3.8	0.8	0	310	10.4
CPY_E	1.28	1.23	0.06	0.1	0	<LOD	0.65
CPY_E	1.37	1.59	0.25	0.1	0	80	0.94
CPY_E	<LOD	0.18	<LOD	0.12	0	230	18
CPY_E	1.48	1.17	0.14	0.055	0	82	1.59
CPY_E	<LOD	0.95	0.3	0.43	0	480	19.5
CPY_E	3.7	0.7	<LOD	0.17	0	<LOD	30.7
CPY_E	<LOD	0.2	0.21	0.04	0	<LOD	8.1
CPY_E	1	0.34	<LOD	0.04	0	<LOD	370
CPY_E	2.16	1.39	0.19	0.105	0	6	0.19
CPY_E	1.47	1.95	0.06	0.08	0	120	1.61
CPY_E	2.8	1.72	0.21	0.025	0	<LOD	0.81
CPY_E	1.3	1.22	<LOD	<LOD	0	420	18.1
CPY_E	3.2	1.1	0.1	0.31	0	<LOD	47
CPY_E	<LOD	1.64	1.8	<LOD	0	<LOD	3.58
CPY_E	0.4	2.31	0.56	<LOD	0	<LOD	9.6
CPY_E	<LOD	1.32	0.34	0.13	0	80	12.9
CPY_E	2.9	1.05	0.3	0.04	0	<LOD	7.4
CPY_E	0.43	0.76	1.34	<LOD	0	<LOD	5.9
CPY_E	570	1.7	2	<LOD	0	<LOD	570

Appendix 1 (cont.): LA ICP-MS dataset of disseminated chalcopyrite located along transect 2225L, LM-P-043 (samples A, E, H, N, and P) that were in the host rock (grey gabbro). Pulse rate: 4 Hz; Fluence: 7 J/cm3; Pit size: LM-P-043 (A, E, H, N): 14µm; LM-P-043P: 10µm. Note that CPY_A, E, H, N, and P are short for LM-P-043A, E, H, N, and P.

Sample	*Pd108 (ppb)*	Bi (ppm)	*Cd (ppm)*	*In (ppm)*	*Sn (ppm)*	*Sb (ppm)*
CPY_A	*58*	0.51	*2.7*	*1.8*	*2.2*	*0.26*
CPY_A	*25*	0.79	*2.5*	*1.8*	*1.6*	*0.085*
CPY_A	*77*	0.87	*1.7*	*2.1*	*3.6*	*0.1*
CPY_A	*74*	0.92	*2.4*	*2.2*	*4.9*	*0.099*
CPY_A	*46*	0.58	*8.5*	*1.5*	*2.2*	*0.13*
CPY_A	*59*	0.31	*5.4*	*1.6*	*4*	*0.055*
CPY_A	*46*	0.74	*5.4*	*2.3*	*4*	*0.22*
CPY_A	*36*	0.69	*1.5*	*1.4*	*2.5*	*0.13*
CPY_A	*22*	0.73	*1.3*	*1.4*	*2*	*0.083*
CPY_A	*35*	1.75	*1.9*	*1.5*	*1.4*	*0.065*
CPY_A	*19*	2.06	*1.3*	*1.3*	*2.1*	*0.062*
CPY_A	*34*	18.1	*1.2*	*0.95*	*0.24*	*0.1*
CPY_A	*27*	0.58	*0.63*	*1.3*	*0.8*	*0.067*
CPY_A	*41*	4.26	*1.1*	*2*	*2.4*	*0.12*
CPY_A	*27*	1.12	*0.89*	*1.2*	*1.4*	*0.089*
CPY_A	*97*	23.7	*4.5*	*7.9*	*520*	*0.41*
CPY_A	*890*	101	*21*	*8.3*	*33*	*0.51*
CPY_A	*14*	2.33	*0.6*	*1.1*	*1.2*	*0.11*
CPY_A	*43*	5.57	*1.1*	*0.85*	*0.54*	*0.14*
CPY_A	*25*	2	*0.87*	*1.1*	*4*	*0.092*
CPY_A	*78*	12.3	*4.4*	*0.59*	*4.3*	*0.29*
CPY_A	*1500*	118	*22*	*5.2*	*140*	*7.2*
CPY_A	*1600*	32	*21*	*3.9*	*73*	*10*
CPY_A	*87*	14.9	*2.2*	*1.2*	*13*	*0.29*
CPY_A	*59*	15.5	*1.4*	*1.2*	*29*	*0.21*
CPY_A	*220*	12.6	*2.1*	*1.4*	*1.7*	*0.45*
CPY_A	*220*	23.2	*3.4*	*1.1*	*2.1*	*0.9*
CPY_A	*550*	40	*14*	*4.8*	*9.9*	*2.1*
CPY_A	*1900*	65	*6.1*	*15*	*48*	*4.4*
CPY_A	*88*	11.1	*2.4*	*1.1*	*42*	*0.38*
CPY_E	*71*	12.3	*3.3*	*0.28*	*1.1*	*0.4*
CPY_E	*200*	7.8	*2.4*	*0.76*	*2.5*	*0.94*
CPY_E	*140*	27.3	*7.3*	*1.3*	*3.1*	*1.7*
CPY_E	*22*	2	*0.72*	*0.2*	*0.28*	*0.16*
CPY_E	*49*	0.163	*0.83*	*0.31*	*0.44*	*0.13*
CPY_E	*72*	29.6	*1.2*	*0.18*	*0.55*	*0.19*
CPY_E	*19*	1.85	*0.59*	*0.15*	*0.16*	*0.081*
CPY_E	*84*	31	*1.7*	*0.58*	*1.7*	*0.85*
CPY_E	*77*	60.7	*4.1*	*0.45*	*1.5*	*0.7*
CPY_E	*89*	1.47	*1.2*	*0.17*	*0.89*	*0.31*
CPY_E	*130*	40.2	*3.1*	*0.39*	*1.3*	*0.53*
CPY_E	*24*	0.118	*0.88*	*0.14*	*0.13*	*0.097*
CPY_E	*17*	0.95	*0.7*	*0.22*	*0.21*	*0.09*
CPY_E	*44*	0.72	*1.3*	*0.26*	*0.25*	*0.09*
CPY_E	*280*	26.2	*4.8*	*0.71*	*1.2*	*0.77*
CPY_E	*55*	28.6	*3*	*0.26*	*1.1*	*0.56*
CPY_E	*96*	50	*3.1*	*0.46*	*1.1*	*0.42*
CPY_E	*30*	39	*1.7*	*0.39*	*0.77*	*0.27*
CPY_E	*43*	2.82	*0.47*	*0.31*	*0.52*	*0.26*
CPY_E	*100*	9.3	*4.9*	*0.38*	*1.2*	*0.51*
CPY_E	*22*	6.26	*0.64*	*0.14*	*0.54*	*0.1*
CPY_E	*690*	36.1	*300*	*1.1*	*4.5*	*1.9*

Appendix 1 (cont.): LA ICP-MS dataset of disseminated chalcopyrite located along transect 2225L, LM-P-043 (samples A, E, H, N, and P) that were in the host rock (grey gabbro). Pulse rate: 4 Hz; Fluence: 7 J/cm3; Pit size: LM-P-043 (A, E, H, N): 14µm; LM-P-043P: 10µm. Note that CPY_A, E, H, N, and P are short for LM-P-043A, E, H, N, and P.

Sample	Pt (ppm)	Au (ppb)	Pb (ppm)	Bi (ppm)
CPY_A	1	290	0.72	0.26
CPY_A	1	90	0.35	0.14
CPY_A	1	110	0.51	0.21
CPY_A	1	190	0.63	0.18
CPY_A	1	99	0.38	0.11
CPY_A	1	120	0.45	0.12
CPY_A	1	86	0.52	0.17
CPY_A	1	120	0.25	0.13
CPY_A	1	93	0.17	0.13
CPY_A	1	190	0.43	0.31
CPY_A	1	200	0.36	0.26
CPY_A	1	150	3.2	2
CPY_A	1	69	0.2	0.15
CPY_A	1	72	3.8	0.95
CPY_A	1	90	0.27	0.17
CPY_A	1	410	27	3.7
CPY_A	1	3600	11	22
CPY_A	1	63	0.27	0.23
CPY_A	1	97	3.4	0.76
CPY_A	1	93	0.72	0.82
CPY_A	1	400	7.2	1.8
CPY_A	1	120000	150	45
CPY_A	1	5200	12	12
CPY_A	1	300	9.7	3.1
CPY_A	1	250	4.9	9
CPY_A	1	450	1.7	3.7
CPY_A	1	1100	13	4
CPY_A	1	2100	30	23
CPY_A	1	10000	120	16
CPY_A	1	430	3.1	2.4
CPY_E	1	240	2.2	4.4
CPY_E	1	750	16	3.8
CPY_E	1	580	4.4	9.2
CPY_E	1	50	0.22	1.1
CPY_E	1	100	0.74	0.094
CPY_E	1	250	4.9	6.9
CPY_E	1	82	0.57	0.56
CPY_E	1	630	7	14
CPY_E	1	590	8.2	6.5
CPY_E	1	57	2	0.81
CPY_E	1	310	520	6.2
CPY_E	1	72	0.1	0.066
CPY_E	1	120	0.25	0.21
CPY_E	1	61	0.33	0.13
CPY_E	1	970	5.1	9.8
CPY_E	1	310	12	3.7
CPY_E	1	370	0.69	13
CPY_E	1	230	3.3	10
CPY_E	1	170	3.1	0.81
CPY_E	1	320	2.2	3.6
CPY_E	1	59	1	0.79
CPY_E	1	2100	340	9.5

Appendix 1 (cont.): LA ICP-MS dataset of disseminated chalcopyrite located along transect 2225L, LM-P-043 (samples A, E, H, N, and P) that were in the host rock (grey gabbro). Pulse rate: 4 Hz; Fluence: 7 J/cm3; Pit size: LM-P-043 (A, E, H, N): 14µm; LM-P-043P: 10µm. Note that CPY_A, E, H, N, and P are short for LM-P-043A, E, H, N, and P.

Sample	Cu (ppm)	Co (ppm)	Ni (ppm)	Zn_{68} (ppm)	As (ppm)	Se_{82} (ppm)	Ag (ppm)	Pd108 (ppb)
CPY_H	35000000	0.74	26.7	46	8.7	22	11.6	<LOD
CPY_H	32800000	11.4	212	146	10.7	13.5	19.6	<LOD
CPY_H	43300000	0.12	15.9	59	7.2	27.6	141	50
CPY_H	48700000	0.38	11.8	71	5.7	17.9	14.9	23
CPY_H	32900000	7.6	180	170	6.9	18	12.9	60
CPY_H	19800000	<LOD	11.3	20	17	26	8.7	240
CPY_H	15400000	<LOD	19	180	15	<LOD	5.6	10
CPY_H	37000000	0.79	56	50	4.3	27.3	33.4	<LOD
CPY_N	17500000	<LOD	34	170	<LOD	20	180	380
CPY_N	16000000	<LOD	1	460	19	13	277	<LOD
CPY_N	18900000	520	2000	4200	140	<LOD	13	<LOD
CPY_N	27800000	0	<LOD	90	4.1	19.5	39	<LOD
CPY_N	32000000	0.93	<LOD	38	5.2	8	42	106
CPY_N	11200000	410	1200	190	27	12	7	230
CPY_N	74600000	0.15	3.5	7	1.3	15.7	6.36	<LOD
CPY_N	70400000	0.26	2.7	28	0.9	18.2	6.42	13
CPY_N	73400000	0.46	6.5	13	2.1	19.3	17.7	21
CPY_N	53800000	4.52	33	14	5.4	24.1	8.79	19
CPY_N	34700000	33.4	146	330	10.9	21.4	10.6	76
CPY_N	33000000	15.3	332	88	6	29.5	14.2	<LOD
CPY_N	11700000	102	1390	510	35	30	16.3	20
CPY_N	38300000	16.7	88	310	7.8	18.5	10.4	64
CPY_N	33300000	1460	1750	180	10.9	18.9	32	31
CPY_N	51500000	12.7	71	99	5.7	17.2	15.8	1
CPY_N	56900000	0.98	9.4	4	4.4	12.9	7.8	30
CPY_N	42700000	3	20	<LOD	2.3	15.1	19.1	<LOD
CPY_N	58300000	0.32	24	231	2.2	30.9	31	10
CPY_N	60000000	0.28	9.7	277	1.2	34.8	9.7	42
CPY_N	4900000	28	96	560	56	<LOD	36.8	<LOD
CPY_N	600000	3960	17200	23700	610	<LOD	221	1000
CPY_N	5800000	4.7	25	140	<LOD	<LOD	20.3	70
CPY_N	12400000	36	98	<LOD	45	23	770	<LOD
CPY_N	14000000	183	940	980	42	36	67	<LOD
CPY_N	14400000	4.5	36	1230	6.7	6	173	<LOD
CPY_N	22200000	4.5	35	45	18.9	2	9.4	<LOD
CPY_N	16300000	199	770	500	40	35	199	340
CPY_P	11900000	7.4	n.d.	40	23	<LOD	128	270
CPY_P	17100000	2	n.d.	610	25	<LOD	380	<LOD
CPY_P	12000000	17	n.d.	30	57	48	1280	270
CPY_P	33000000	<LOD	n.d.	41	1.8	22	14.1	67
CPY_P	32800000	1.01	n.d.	12	2.7	22	12.4	<LOD
CPY_P	28300000	13.2	n.d.	82	2.5	21	29.4	83
CPY_P	16000000	35.3	n.d.	290	26	33	20.3	<LOD
CPY_P	38300000	0.14	n.d.	<LOD	8.7	18.4	2.21	<LOD
CPY_P	23400000	0.9	n.d.	10	13.5	22	2.01	<LOD
CPY_P	15700000	1.6	n.d.	40	23	17	510	190
CPY_P	6700000	206	n.d.	1900	62	<LOD	39	<LOD
CPY_P	12200000	1	n.d.	<LOD	14	<LOD	118	<LOD
CPY_P	4750000	3.2	n.d.	200	106	48	24.5	<LOD
CPY_P	23400000	<LOD	n.d.	<LOD	5.1	9	14.1	<LOD
CPY_P	21200000	36.2	n.d.	335	17.9	16	13.1	9
CPY_P	22200000	12.3	n.d.	60	16.1	13	20.5	47
CPY_P	20100000	30	n.d.	1120	10	25	18.1	50
CPY_P	25600000	18.6	n.d.	380	11.4	14	7.5	20
CPY_P	26600000	37	n.d.	1630	15.6	10	26	<LOD
CPY_P	24700000	13.9	n.d.	25	12.7	10	13.6	<LOD
CPY_P	23600000	8.7	n.d.	48	12.8	18.9	18.3	<LOD
CPY_P	28200000	11.6	n.d.	2510	7.6	33	22.6	<LOD
CPY_P	19400000	25	n.d.	150	26	33	16.6	<LOD
CPY_P	28100000	6.3	n.d.	700	3.3	18.7	25	<LOD
CPY_P	21300000	26.7	n.d.	1110	11.3	28	20.8	6
CPY_P	21600000	35.6	n.d.	1240	10.5	22	18.9	<LOD
CPY_P	27800000	10	n.d.	1100	4.9	35	25.6	<LOD
CPY_P	26100000	12.2	n.d.	2750	7	36	26.2	60
CPY_P	26600000	1.19	n.d.	80	12.5	16	19.5	38
CPY_P	9200000	105	n.d.	580	15	52	20.7	0

Appendix 1 (cont.): LA ICP-MS dataset of disseminated chalcopyrite located along transect 2225L, LM-P-043 (samples A, E, H, N, and P) that were in the host rock (grey gabbro). Pulse rate: 4 Hz; Fluence: 7 J/cm3; Pit size: LM-P-043 (A, E, H, N): 14µm; LM-P-043P: 10µm. Note that CPY_A, E, H, N, and P are short for LM-P-043A, E, H, N, and P.

Sample	Pd108 (ppb)	Bi (ppm)	Cd (ppm)	In (ppm)	Sn (ppm)	Sb (ppm)
CPY_H	51	6	2.3	0.25	0.66	0.29
CPY_H	33	10.5	1.9	0.16	1.2	0.16
CPY_H	33	1.27	1.2	0.22	0.37	0.16
CPY_H	29	1.3	1.8	0.21	0.26	0.077
CPY_H	130	8.1	2.2	0.5	0.96	0.25
CPY_H	400	3.2	5.1	0.51	1.1	0.77
CPY_H	200	3.7	4.7	0.78	2.6	0.73
CPY_H	40	7.5	2	0.18	0.99	0.19
CPY_N	510	0.25	7.7	1.5	2.1	1.3
CPY_N	180	5	3.8	0.45	2.8	0.67
CPY_N	600	29	17	0.9	12	7.1
CPY_N	46	14	1.5	0.29	0.74	0.35
CPY_N	66	0.11	1.5	0.32	0.96	0.2
CPY_N	260	22.8	3.2	1.3	1.4	0.66
CPY_N	14	0.65	0.47	0.24	0.18	0.078
CPY_N	21	0.357	0.56	0.33	0.17	0.081
CPY_N	22	2.6	0.55	0.23	0.18	0.091
CPY_N	32	15.7	0.74	0.19	1.5	0.19
CPY_N	70	30.3	11	0.33	0.63	0.25
CPY_N	31	32.7	0.95	0.2	0.68	0.14
CPY_N	130	38.2	2.7	0.66	4.4	1.2
CPY_N	56	14.9	4.5	0.2	0.48	0.15
CPY_N	40	34.1	1.2	0.22	0.4	0.19
CPY_N	17	9.9	0.68	0.15	0.25	0.11
CPY_N	27	3.4	0.97	0.18	0.32	0.17
CPY_N	30	5.9	0.78	0.32	0.48	0.15
CPY_N	32	0.86	2	0.55	0.24	0.082
CPY_N	26	0.53	1.5	0.49	0.18	0.093
CPY_N	350	53	9.2	1.1	3.9	1.4
CPY_N	4700	98	56	7.8	42	17
CPY_N	600	4.5	22	2.8	3.4	1.9
CPY_N	75	32	7	0.52	1.6	0.8
CPY_N	270	27.7	9	0.43	1.8	0.97
CPY_N	82	7.7	3.1	0.3	0.97	0.52
CPY_N	69	0.13	4.7	0.19	0.85	0.45
CPY_N	240	55	3.6	0.42	1.9	1.2
CPY_P	840	0.17	8.8	0.51	1.9	1.4
CPY_P	210	26	11	1.4	4.7	0.71
CPY_P	350	40	2.9	2.5	2.4	2.3
CPY_P	74	2.86	1.9	0.37	0.35	0.22
CPY_P	45	3.8	1.6	0.49	0.5	0.32
CPY_P	83	21.4	1.4	0.29	0.9	0.46
CPY_P	84	44.6	3	0.42	1.9	0.57
CPY_P	95	6.5	1.3	0.24	0.77	0.25
CPY_P	86	5.9	5.3	0.25	1.3	0.47
CPY_P	220	18.1	12	0.74	1.9	1.2
CPY_P	500	32	19	2.3	5.2	4.4
CPY_P	250	7.6	10	0.48	1.8	0.88
CPY_P	350	36	26	1	3	2.5
CPY_P	95	4.9	3.3	0.5	0.91	0.6
CPY_P	86	16.3	1.6	0.19	0.55	0.27
CPY_P	79	26.9	1.6	0.17	0.74	0.32
CPY_P	110	17.4	2.2	0.77	1.4	0.37
CPY_P	130	32	3.3	0.99	1	0.5
CPY_P	63	81	2.6	0.82	1	0.34
CPY_P	50	23.7	1.6	0.22	0.46	0.23
CPY_P	73	12.4	2.2	0.5	1.2	0.35
CPY_P	67	44.8	4.5	0.76	0.85	0.5
CPY_P	120	19.3	6.1	0.71	4	0.53
CPY_P	64	18.8	1.8	0.5	0.57	0.31
CPY_P	57	39.5	1.7	0.33	0.52	0.32
CPY_P	73	37.8	1.6	0.46	0.57	0.24
CPY_P	89	30.2	2.9	0.63	0.69	0.42
CPY_P	110	44.8	3.6	0.6	0.66	0.34
CPY_P	77	13.4	3.5	0.28	4.3	0.34
CPY_P	290	27	5.9	1.3	4	1.3

Appendix 1 (cont.): LA ICP-MS dataset of disseminated chalcopyrite located along transect 2225L, LM-P-043 (samples A, E, H, N, and P) that were in the host rock (grey gabbro). Pulse rate: 4 Hz; Fluence: 7 J/cm3; Pit size: LM-P-043 (A, E, H, N): 14µm; LM-P-043P: 10µm. Note that CPY_A, E, H, N, and P are short for LM-P-043A, E, H, N, and P.

Sample	Cd (ppm)	In (ppm)	Sn (ppm)	Sb (ppm)	Pt (ppm)	Au (ppb)	Pb (ppm)
CPY_H	3	1.2	<LOD	0.22	0	<LOD	54
CPY_H	3.2	0.72	5.1	0.16	0	<LOD	22.2
CPY_H	3.5	1.3	0.4	0.13	0	<LOD	3.18
CPY_H	4.6	1.42	0.53	<LOD	0	<LOD	6.1
CPY_H	2.3	1.4	1.01	<LOD	0	<LOD	10.2
CPY_H	3	1.19	1.8	0.03	0	110	11.1
CPY_H	<LOD	1.06	<LOD	<LOD	0	<LOD	21.2
CPY_H	2.2	0.86	2.75	0.08	0	200	11.3
CPY_N	3.3	2.7	<LOD	<LOD	0	0	850
CPY_N	<LOD	0.34	2.5	0.02	0	40	16
CPY_N	<LOD	1.39	3	4.1	0	200	13.4
CPY_N	0.5	0.82	0.58	0.28	0	70	16
CPY_N	<LOD	0.98	0.79	<LOD	0	20	7
CPY_N	<LOD	0.6	1.3	0.16	0	<LOD	15.9
CPY_N	1.02	2.28	0.14	0.108	0	<LOD	1.52
CPY_N	0.43	2.5	0	0.15	0	12	2.04
CPY_N	1.01	2.04	0.23	0.079	0	<LOD	4.7
CPY_N	0.7	1.43	6.9	0.16	0	<LOD	9.4
CPY_N	14	2.27	1.1	0.13	0	<LOD	9.2
CPY_N	3.39	1.79	3.67	0.18	0	<LOD	15.8
CPY_N	3.7	3.13	15.1	0.7	0	670	20.8
CPY_N	11.5	1.18	0.35	<LOD	0	<LOD	10.7
CPY_N	0.7	1.29	<LOD	0.37	0	80	37.2
CPY_N	0.94	0.84	0.29	0	0	22	3.56
CPY_N	1.12	1.04	0.23	0.16	0	<LOD	1.88
CPY_N	0.98	1.7	1.27	0.13	0	<LOD	4.2
CPY_N	8.1	5.07	0.19	<LOD	0	<LOD	0.53
CPY_N	8.7	5.12	0.33	0.142	0	<LOD	0.87
CPY_N	<LOD	1.4	1	0.1	0	<LOD	690
CPY_N	<LOD	9.5	12	0	0	<LOD	118
CPY_N	13	1.6	2.7	0.7	0	<LOD	340
CPY_N	5.4	0.61	1.3	0.07	0	800	82
CPY_N	28.7	0.06	1	0.17	0	<LOD	870
CPY_N	2.2	0.42	0.3	<LOD	0	280	12.6
CPY_N	4.5	0.15	0.45	0.03	0	<LOD	16
CPY_N	2.1	1.01	2.7	2.6	0	400	1650
CPY_P	<LOD	0.88	<LOD	0.6	0	<LOD	109
CPY_P	<LOD	3	<LOD	<LOD	0	400	8.7
CPY_P	<LOD	3.4	<LOD	0.4	0	<LOD	13.5
CPY_P	3.5	2.52	0.07	<LOD	0	160	9.9
CPY_P	1.1	2.35	0.46	0.07	0	90	28
CPY_P	<LOD	1.3	0.9	0.76	0	70	45
CPY_P	<LOD	2.17	7.1	<LOD	0	<LOD	29.4
CPY_P	1.6	0.81	0.45	0.13	0	<LOD	2.57
CPY_P	5.6	0.56	<LOD	0.19	0	<LOD	4.3
CPY_P	13	0.75	0.3	1.4	0	<LOD	9.5
CPY_P	5	2.6	1.9	0.9	0	<LOD	23
CPY_P	8	0.2	<LOD	0.87	0	<LOD	290
CPY_P	20	0.8	<LOD	<LOD	0	1000	4100
CPY_P	2.9	2.14	<LOD	0.11	0	<LOD	1.84
CPY_P	1	0.5	0.56	0.32	0	80	11.3
CPY_P	1.9	0.65	0.44	0.29	0	<LOD	15.4
CPY_P	<LOD	2.72	5.2	<LOD	0	<LOD	10.2
CPY_P	0.8	2.73	3.2	<LOD	0	<LOD	14.5
CPY_P	2.9	2.18	2.6	<LOD	0	100	76
CPY_P	1.1	0.89	0.23	<LOD	0	120	7.3
CPY_P	3.3	2.59	4	<LOD	0	80	5.4
CPY_P	7.1	2.67	<LOD	0.38	0	40	64
CPY_P	6	2.29	6.5	0.45	0	<LOD	7.3
CPY_P	1.5	2.72	0.9	0.25	0	300	28
CPY_P	1.6	2.49	<LOD	0.3	0	130	29.2
CPY_P	<LOD	2.47	0.15	<LOD	0	170	28.6
CPY_P	1.7	2.85	0.14	0.05	0	180	31.9
CPY_P	2.5	2.3	1.61	<LOD	0	560	33.5
CPY_P	2.8	1.12	7.7	<LOD	0	580	5.1
CPY_P	3.2	1.9	14.6	<LOD	0	900	14.8

Appendix 1 (cont.): LA ICP-MS dataset of disseminated chalcopyrite located along transect 2225L, LM-P-043 (samples A, E, H, N, and P) that were in the host rock (grey gabbro). Pulse rate: 4 Hz; Fluence: 7 J/cm3; Pit size: LM-P-043 (A, E, H, N): 14µm; LM-P-043P: 10µm. Note that CPY_A, E, H, N, and P are short for LM-P-043A, E, H, N, and P.

Sample	Cu (ppm)	Co (ppm)	Ni (ppm)	Ag (ppm)	Zn_{68} (ppm)	As (ppm)	Se_{82} (ppm)
CPY_H	4400000	0.78	5.2	1.6	50	6.5	11
CPY_H	3200000	2	33	2.7	39	3.7	9.1
CPY_H	2000000	0.39	2.6	36	25	3.6	7.5
CPY_H	3700000	0.31	2.8	2.3	33	2.7	6.5
CPY_H	5900000	4.8	110	4.7	130	9.1	19
CPY_H	6100000	2	9.9	3.9	230	15	48
CPY_H	4400000	2.6	14	2.3	320	24	35
CPY_H	4300000	0.6	13	5.1	44	3.6	9.3
CPY_N	6400000	2.5	33	110	570	38	50
CPY_N	3400000	2.3	12	60	140	17	29
CPY_N	7600000	390	1500	10	3600	130	230
CPY_N	6700000	1.3	8.1	14	130	7.4	9.8
CPY_N	8000000	0.98	7	27	89	5.8	13
CPY_N	4300000	530	2000	3.3	260	36	33
CPY_N	7700000	0.17	1.3	0.66	21	1.6	2.9
CPY_N	5900000	0.22	1.7	0.69	21	1.5	3.7
CPY_N	7500000	0.45	2.4	2	18	1.5	4.3
CPY_N	5900000	0.75	5.6	0.97	29	3.2	5.3
CPY_N	5800000	9.7	37	2.6	220	7	8.3
CPY_N	2400000	2.4	48	1.3	36	2.8	6.5
CPY_N	2000000	19	200	2.6	200	16	17
CPY_N	4700000	5.5	25	1.2	120	4.3	4
CPY_N	4700000	910	620	10	59	3.2	7.1
CPY_N	5600000	3.2	23	2	40	2	4.1
CPY_N	7200000	0.87	5.3	1.1	32	2.8	4.4
CPY_N	7300000	1.7	8.5	2.4	33	3	6.2
CPY_N	6100000	0.43	16	14	46	2.4	5.6
CPY_N	6700000	0.23	2.2	1.3	50	1.3	5.4
CPY_N	1400000	15	65	7.9	430	31	78
CPY_N	120000	940	4600	74	6200	370	970
CPY_N	1500000	5.4	54	6	900	35	170
CPY_N	2900000	23	73	340	270	30	36
CPY_N	3100000	45	240	15	320	18	16
CPY_N	2300000	6.4	36	30	310	8.4	17
CPY_N	4400000	1.5	15	1.3	78	7	14
CPY_N	2600000	46	210	90	260	13	25
CPY_P	4200000	6.5	n.d.	92	290	23	54
CPY_P	9000000	2.4	n.d.	390	720	15	69
CPY_P	6200000	14	n.d.	450	380	45	43
CPY_P	3200000	0.56	n.d.	2	57	4.5	10
CPY_P	4600000	0.59	n.d.	2.6	54	4.4	12
CPY_P	2900000	3.3	n.d.	4.8	71	4.9	11
CPY_P	1600000	9.1	n.d.	3.4	180	11	23
CPY_P	5400000	0.73	n.d.	0.77	64	4.5	9.6
CPY_P	4800000	0.95	n.d.	0.81	110	8.8	22
CPY_P	3200000	1.3	n.d.	390	380	18	22
CPY_P	3700000	98	n.d.	23	780	38	110
CPY_P	2600000	2.6	n.d.	58	240	41	52
CPY_P	720000	4.4	n.d.	8.9	340	56	65
CPY_P	3700000	1.2	n.d.	3	97	7.8	12
CPY_P	2300000	3.7	n.d.	1.6	76	6.2	12
CPY_P	2200000	1.1	n.d.	2.3	63	5.2	13
CPY_P	2800000	4.4	n.d.	3.2	310	14	21
CPY_P	4900000	9.2	n.d.	1.6	150	6.9	20
CPY_P	5800000	7.3	n.d.	5.2	270	8	20
CPY_P	2800000	2.3	n.d.	1.6	60	4.8	10
CPY_P	2800000	5	n.d.	3.1	83	4.4	9.8
CPY_P	4000000	4	n.d.	4.4	330	6.6	17
CPY_P	3900000	10	n.d.	4	120	12	26
CPY_P	2500000	1.9	n.d.	4.7	290	4	9.8
CPY_P	2600000	3.2	n.d.	3.1	420	4.7	18
CPY_P	2100000	4.6	n.d.	2.2	200	5.6	13
CPY_P	4500000	4.4	n.d.	5.7	310	8.5	21
CPY_P	4100000	2.9	n.d.	4.6	400	7.7	17
CPY_P	4200000	0.91	n.d.	3.6	88	8.5	17
CPY_P	2300000	43	n.d.	6.5	530	35	69

Appendix 1 (cont.): LA ICP-MS dataset of disseminated chalcopyrite located along transect 2225L, LM-P-043 (samples A, E, H, N, and P) that were in the host rock (grey gabbro). Pulse rate: 4 Hz; Fluence: 7 J/cm3; Pit size: LM-P-043 (A, E, H, N): 14µm; LM-P-043P: 10µm. Note that CPY_A, E, H, N, and P are short for LM-P-043A, E, H, N, and P.

Sample	Pt (ppm)	Au (ppb)	Pb (ppm)	Bi (ppm)
CPY_H	1	80	33	1.1
CPY_H	1	120	4.6	1.4
CPY_H	1	66	0.57	0.26
CPY_H	1	80	1.4	0.28
CPY_H	1	290	4.3	2.9
CPY_H	1	670	3.8	1.5
CPY_H	1	630	7.6	1.8
CPY_H	1	230	4	1.5
CPY_N	1	740	340	0.84
CPY_N	1	440	5.9	1.9
CPY_N	1	2700	8.3	17
CPY_N	1	390	10	6.3
CPY_N	1	210	3.7	0.15
CPY_N	1	800	6.6	7.8
CPY_N	1	47	0.3	0.35
CPY_N	1	62	0.44	0.078
CPY_N	1	60	2.1	1.1
CPY_N	1	95	1.2	2
CPY_N	1	140	3.4	7.9
CPY_N	1	96	1.9	2.6
CPY_N	1	660	3.4	6.3
CPY_N	1	93	1	1.7
CPY_N	1	140	7.3	4.1
CPY_N	1	85	0.52	2
CPY_N	1	87	0.8	1.7
CPY_N	1	82	1.1	1.4
CPY_N	1	62	0.23	0.51
CPY_N	1	60	0.18	0.15
CPY_N	1	830	300	11
CPY_N	1	6200	47	39
CPY_N	1	2700	340	1.3
CPY_N	1	1400	32	3.2
CPY_N	1	610	220	5.5
CPY_N	1	560	5.2	3.1
CPY_N	1	370	4.6	0.18
CPY_N	1	490	320	10
CPY_P	1	930	86	0.46
CPY_P	1	1100	6.7	17
CPY_P	1	430	5.2	12
CPY_P	1	200	2.1	0.7
CPY_P	1	220	12	1.5
CPY_P	1	250	11	2.8
CPY_P	1	280	3.2	3.5
CPY_P	1	160	0.93	2.1
CPY_P	1	240	1.8	1.9
CPY_P	1	440	3.6	4.8
CPY_P	1	2100	10	20
CPY_P	1	640	310	2.3
CPY_P	1	2200	2700	18
CPY_P	1	280	0.75	2.2
CPY_P	1	190	2.5	2.1
CPY_P	1	200	1.8	3.1
CPY_P	1	330	2.1	3.6
CPY_P	1	260	3.9	13
CPY_P	1	270	17	15
CPY_P	1	170	1.1	3.1
CPY_P	1	190	1.3	1.9
CPY_P	1	350	12	6.7
CPY_P	1	300	2.1	4.5
CPY_P	1	300	13	7.3
CPY_P	1	210	4.5	6.1
CPY_P	1	240	3.9	5.2
CPY_P	1	390	7.4	7.4
CPY_P	1	370	4	8.7
CPY_P	1	430	2.2	6.3
CPY_P	1	1600	7.3	9.4

Appendix 1 (cont.): LA ICP-MS dataset of disseminated chalcopyrite located along transect 2225L, LM-P-043 (samples A, E, H, N, and P) that were in the host rock (grey gabbro). Pulse rate: 4 Hz; Fluence: 7 J/cm3; Pit size: LM-P-043 (A, E, H, N): 14µm; LM-P-043P: 10µm. Note that CPY_A, E, H, N, and P are short for LM-P-043A, E, H, N, and P.

Sample Numbers	LM-P-043A	LM-P-043B	LM-P-043C	LM-P-043D	LM-P-043E	LM-P-043F	LM-P-043G
SiO2	-0.19	0.58	-4.11	3.88	1.04	-0.04	0.04
TiO2	0.00	-2.38	23.53	-16.05	-3.46	2.44	2.63
Al2O3	-1.77	0.96	-1.44	1.86	0.58	-1.77	0.83
FeOT	9.43	-0.01	8.23	-5.59	18.75	-0.87	2.91
FeO	9.41	-0.11	8.36	-5.61	19.73	-2.67	5.63
Fe2O3	10.10	3.13	4.35	-5.15	-3.96	74.14	-50.43
MgO	-2.78	-1.10	22.80	-17.89	1.84	3.81	3.81
MnO	6.67	0.00	-44.44	80.00	2.04	1.38	-2.03
CaO	-6.67	-2.91	7.07	-6.36	-5.63	-0.25	2.43
Na2O	-3.26	-0.59	21.51	-15.45	4.43	-1.25	0.95
K2O	-12.43	-7.33	87.25	-42.37	-4.32	-0.54	11.38
P2O5	-2.56	-2.50	110.53	-50.00	-5.00	0.00	8.11
LOI	8.38	4.37	-33.88	46.67	0.00	1.23	-7.39
Au	303.88	219.38	152.94	-65.54	640.00	b.d.	b.d.
Pd	743.75	b.d.	b.d.	b.d.	1150.00	100.00	-83.33
Pt	-16.06	398.18	b.d.	b.d.	b.d.	b.d.	b.d.
Cu	132.66	38.17	163.10	-83.41	780.21	-69.09	-64.97
Ni	65.12	-10.37	92.31	-89.56	572.40	11.11	-40.00
Co	5.54	-8.96	78.50	-37.69	-29.45	1.34	16.62
Cr	0.73	2.15	46.24	-26.16	-41.76	0.00	6.25
Ag	51.69	17.19	396.65	-79.00	-76.29	29.73	8.82
Sn	100.00	100.00	-50.00	0.00	b.d.	b.d.	b.d.
Mn	17.01	2.40	-43.65	59.30	-67.74	2.68	-0.88
Zn	-53.56	-63.40	936.51	-43.75	-54.29	-3.92	62.42
Cl						0.00	12.50
F						0.00	16.67
B						41.67	20.00
Li	-5.96	-7.23	99.15	-51.04	-7.31	0.00	4.00
Ga	4.79	-5.11	12.82	-11.36	-2.22	0.00	0.00
Ge	0.00	b.d.	b.d.	b.d.	b.d.	6.67	0.00
Cd	-82.85	-70.73	2113.68	-40.31	-56.44	-2.17	411.11
La	-2.44	-4.51	282.22	-72.31	4.84	-0.80	2.80
Ce	-3.20	-5.18	276.32	-72.17	0.78	0.00	4.92
Pr	-0.60	-3.93	246.88	-70.72	6.99	0.70	4.41
Nd	4.35	-4.99	215.76	-67.14	4.87	-0.74	5.49
Sm	3.33	-6.98	160.98	-61.64	2.38	-2.97	4.97
Eu	6.19	-1.87	116.16	-53.95	1.90	1.44	1.46
Gd	6.96	-9.80	104.06	-48.55	5.96	0.17	9.12
Tb	4.55	-5.71	75.00	-43.66	2.90	0.00	1.47
Dy	7.00	-9.50	54.07	-35.43	8.86	-1.41	4.41
Ho	5.26	-3.39	28.26	-26.98	0.00	-1.56	10.34
Er	6.92	-10.17	21.23	-17.05	3.53	-0.58	7.55
Tm	0.00	0.00	10.00	-13.04	-2.95	0.85	7.31
Yb	3.60	-4.79	10.61	-15.38	8.33	-2.70	2.78
Lu	16.67	-14.29	16.67	-18.18	0.92	-1.80	-2.20
Zr	-19.10	-13.25	209.56	-61.09	3.04	2.39	-1.88
Ba	0.21	-9.02	148.94	-52.84	-6.66	0.95	-4.99
Pb	-43.98	-25.18	628.13	-69.81	-70.56	-11.48	205.00
Th	0.00	0.00	45.45	-47.62	51.08	-1.77	-9.29
U	300.00	-66.67	-66.67	0.00	500.00	7.14	-72.00
Bi	-22.22	64.42	225.00	-43.86	-5.00	-40.00	66.67
Tl	48.48	-5.71	169.23	-66.67	-18.75	-12.73	-5.17
Rb	-13.97	-17.46	99.67	-45.81	0.18	-1.75	5.56
Sr	-5.00	-5.74	95.07	-47.55	-6.38	-1.98	-0.55
Nb	-4.41	-5.56	105.71	-56.25	19.40	1.52	-1.49
Cs	14.29	-12.50	-72.41	222.22	50.00	-14.29	-12.50
Be	0.00	0.00	0.00	0.00	-80.00	-50.00	0.00
Hf	-24.07	-8.47	126.92	-48.00	6.38	4.44	-6.25
Y	2.31	-7.98	41.35	-31.09	15.57	1.83	5.81
Ta	0.00	-33.33	50.00	-33.33	-48.28	-18.31	-16.47
Sc	14.29	-6.67	-65.91	131.58	-90.50	0.00	5.26
V	6.78	-9.23	-31.94	57.85	-9.02	0.00	3.10
As	50.00	b.d.	b.d.	266.67			
Mo	100.00	0.00	-75.00	60.00			

Appendix 2: Mass balance gain and loss values for transect 2225L, LM-P-043 sample set. Sample D was omitted due to carbonate-rich micro-vein present in sample. b.d. = below detection.

Sample Numbers	LM-P-043H-1	LM-P-043I	LM-P-043J	LM-P-043K	LM-P-043L-1	LM-P-043M	LM-P-043N
SiO2	-0.31	0.51	-0.82	0.55	0.87	-1.63	0.47
TiO2	-2.44	-0.85	-1.43	5.95	-3.78	3.53	-3.29
Al2O3	1.23	0.00	0.98	-1.22	-2.14	2.78	-2.22
FeOT	0.29	0.89	1.99	0.87	-2.83	-1.41	-3.35
FeO	0.00	1.43	2.94	0.00	-1.45	0.00	-9.21
Fe2O3	6.36	-9.09	-12.95	16.81	-22.73	-18.09	308.70
MgO	-3.52	-0.87	-2.55	3.98	1.04	-0.45	-1.46
MnO	1.37	2.10	0.00	0.70	-4.05	4.23	2.16
CaO	-1.14	-1.12	1.01	-0.50	2.84	-0.13	-0.39
Na2O	-2.46	1.56	0.31	-0.93	5.57	-1.93	-5.18
K2O	-11.64	-0.53	-1.04	6.08	0.00	7.10	-7.14
P2O5	-2.63	-2.56	-2.50	0.00	2.56	0.00	2.63
LOI	-2.22	7.14	-10.16	12.65	-12.63	-5.00	8.70
Au	b.d.	b.d.	b.d.	b.d.	-66.67	-66.67	800.00
Pd	b.d.	b.d.	b.d.	b.d.	b.d.	-94.89	b.d.
Pt	b.d.	b.d.	b.d.	b.d.	b.d.	-76.12	b.d.
Cu	207.84	410.00	-52.38	-82.93	-18.00	-24.24	127.59
Ni	66.67	-10.00	0.00	0.00	-60.00	-50.98	264.29
Co	-15.57	1.33	-4.26	9.05	-8.49	8.28	-2.25
Cr	-5.88	0.00	0.00	6.25	0.00	0.00	0.00
Ag	6.25	14.29	16.67	-25.00	18.52	0.00	3.85
Sn	b.d.	b.d.	b.d.	b.d.	b.d.	-50.00	b.d.
Mn	-5.04	11.21	2.88	-7.14	-3.45	2.65	-2.59
Zn	-53.41	66.01	-16.80	49.69	3.82	-10.80	-27.27
Cl	-11.11	-10.00	25.00	0.00	14.29	-12.50	-20.00
F	-14.29	16.67	-14.29	0.00	0.00	16.67	0.00
B	66.67	b.d.	b.d.	-40.00	-16.67	-14.29	-17.65
Li	-3.85	23.81	-8.70	0.00	-14.81	0.00	-12.90
Ga	0.00	0.00	0.00	0.00	0.00	0.00	0.00
Ge	0.00	0.00	7.14	-6.67	15.38	-13.33	0.00
Cd	-86.57	109.38	-36.00	284.62	160.00	-50.00	-74.36
La	-3.95	1.44	4.17	-2.60	0.99	-0.65	-1.61
Ce	-3.94	-0.78	3.23	-0.80	0.81	2.48	-3.20
Pr	-4.90	0.70	0.00	1.43	1.45	2.22	-3.57
Nd	-3.95	-0.75	2.10	0.38	0.19	1.36	-2.10
Sm	-2.70	3.01	-2.04	0.00	0.00	3.16	-2.95
Eu	-2.84	-0.47	1.92	-2.35	0.95	0.48	0.48
Gd	-4.96	-0.53	-1.56	3.78	-0.71	-1.93	1.60
Tb	-2.86	-2.78	-4.00	0.00	10.29	-11.69	14.93
Dy	-0.87	1.78	-12.24	1.59	7.39	-9.04	12.17
Ho	-6.45	5.08	-14.49	0.00	11.29	-8.82	9.68
Er	-4.22	5.73	-16.93	1.07	11.31	-10.64	8.67
Tm	-2.67	2.27	-17.29	2.70	7.92	-11.11	9.76
Yb	-3.36	3.47	-15.29	1.19	9.09	-8.33	11.26
Lu	-1.73	-0.43	-14.07	1.50	9.92	-5.47	12.28
Zr	0.00	-1.84	14.81	-6.90	3.57	-1.51	-7.44
Ba	0.80	0.00	0.91	5.91	-10.58	12.80	-2.33
Pb	-67.74	3.33	-3.23	181.82	22.22	-48.57	27.27
Th	9.47	0.35	-30.05	17.34	9.15	-14.56	33.94
U	233.33	0.00	-88.97	47.83	73.58	-53.91	666.67
Bi	-33.33	200.00	-25.00	0.00	-33.33	-40.00	66.67
Tl	9.43	1.92	-1.89	-7.02	-3.39	0.00	9.26
Rb	-10.00	0.00	-4.76	5.00	-3.23	5.08	1.72
Sr	2.69	-0.89	2.16	-4.56	2.79	1.47	-3.81
Nb	0.00	0.00	-15.19	5.33	5.63	-7.79	14.93
Cs	0.00	0.00	-27.27	0.00	0.00	10.00	42.86
Be	0.00	0.00	0.00	0.00	0.00	0.00	0.00
Hf	2.13	-2.08	14.29	-6.67	0.00	0.00	-2.17
Y	-4.32	0.62	-15.71	6.70	8.48	-9.84	13.66
Ta	30.77	-4.41	-31.31	19.28	-9.78	2.22	20.00
Sc	-5.00	0.00	0.00	0.00	5.26	-5.00	0.00
V	-3.73	1.52	-1.49	4.69	-0.78	0.78	0.00
As							
Mo							

Appendix 2 (cont.): Mass balance gain and loss values for transect 2225L, LM-P-043 sample set. Sample D was omitted due to carbonate-rich micro-vein present in sample. b.d. = below detection.

Sample Numbers	LM-P-043O-1	LM-P-043P	LM-P-055A	LM-P-055B	LM-P-055C	LM-P-055D	LM-P-060A
SiO2	-1.25	1.08	10.74	0.12	0.57	-0.11	2.33
TiO2	1.23	-17.81	-30.86	-1.64	0.83	22.67	-2.80
Al2O3	0.38	-1.15	-6.94	1.16	0.86	2.05	-7.73
FeOT	7.04	-15.78	-16.94	-0.33	-1.13	-13.01	10.65
FeO	13.43	-18.77	-19.70	1.54	-1.52	-19.98	8.64
Fe2O3	-73.26	56.60	6.91	-13.99	1.78	155.84	36.45
MgO	0.44	1.69	-34.22	0.19	-4.37	-18.02	7.44
MnO	-2.11	0.24	-35.38	-4.41	0.74	-4.71	4.08
CaO	0.65	-7.89	-39.22	-2.88	-3.78	-5.51	-17.32
Na2O	1.86	-9.38	-0.56	-1.65	3.42	-1.22	-6.05
K2O	-0.55	23.09	-10.15	1.55	-1.02	31.84	-26.03
P2O5	0.00	-31.33	-31.82	-9.59	7.35	22.89	-7.50
LOI	-10.24	b.d.	24.83	-9.15	10.07	56.84	5.78
Au	-96.23	b.d.	16250.00	b.d.	b.d.	b.d.	330.77
Pd	b.d.	b.d.	b.d.	-100.00	40800.00	b.d.	2575.00
Pt	b.d.	b.d.	b.d.	-100.00	b.d.	b.d.	1615.00
Cu	-28.69	b.d.	82.73	20.88	727.27	125.72	203.26
Ni	-61.11	326.54	316.67	-14.29	16.67	-28.91	111.38
Co	-12.92	10.21	21.84	8.04	-14.25	-6.18	-6.00
Cr	0.00	24.55	-33.33	0.00	-10.00	-22.16	-9.52
Ag	8.33	156.59	32.00	-7.41	0.00	188.67	-21.43
Sn	b.d.	50.00	250.00	100.00	0.00	50.00	150.00
Mn	-2.52	131.22	-33.98	-2.67	1.92	92.55	-3.54
Zn	-18.24	221.74	2.40	0.60	-2.92	85.87	2.55
Cl	0.00	650.00	57.14	0.00	-12.50	500.00	0.00
F	0.00	200.00	-28.57	0.00	-12.50	300.00	0.00
B	41.67	b.d.	b.d.	14.29	-58.82	b.d.	-12.50
Li	-3.13	57.64	4.17	9.09	0.00	8.37	-17.39
Ga	0.00	-3.91	-5.00	0.00	0.00	6.76	-11.76
Ge	7.14	133.33	0.00	-13.33	25.00	100.00	-33.33
Cd	-17.02	786.79	b.d.	-20.00	-16.67	13.21	-25.00
La	3.15	-13.47	2.31	-3.54	7.92	1.29	-21.08
Ce	2.46	-14.06	-3.85	-4.88	7.89	7.07	-15.56
Pr	4.48	-19.20	-10.56	-5.26	7.34	6.73	-18.57
Nd	4.79	-21.84	-13.97	-5.56	5.73	6.24	-11.18
Sm	6.41	-17.57	-17.88	-5.83	5.26	13.62	-5.72
Eu	3.98	-16.37	-18.77	-2.97	1.51	10.26	-21.18
Gd	3.69	-21.18	-16.04	-0.28	-2.31	7.03	-20.23
Tb	-5.63	-9.75	-15.91	-2.22	-3.23	18.22	-10.14
Dy	-4.96	-6.52	-15.01	-0.69	-6.24	19.74	-14.04
Ho	-1.59	-8.25	-13.51	-3.90	-7.23	20.87	-12.07
Er	1.76	-6.93	-13.07	-5.69	-5.80	22.63	-12.50
Tm	2.50	-2.83	-15.66	-3.10	-6.75	25.91	-14.04
Yb	0.67	-3.23	-14.77	-5.88	-2.09	23.23	-10.64
Lu	-4.20	7.85	-4.92	-9.59	0.00	32.33	-3.37
Zr	4.37	-4.69	3.38	-2.47	-0.41	12.89	-16.59
Ba	-0.94	-1.52	-24.14	-2.30	5.73	18.95	-34.87
Pb	12.24	56.38	253.85	25.81	14.81	-13.83	-19.05
Th	-12.62	60.37	381.88	53.33	20.81	-24.62	63.09
U	-70.00	194.12	904.44	246.15	8.33	-29.41	68.42
Bi	0.00	b.d.	433.33	0.00	50.00	566.67	-25.00
Tl	1.89	87.06	39.62	35.90	2.63	34.12	25.00
Rb	0.00	58.04	35.19	12.50	-5.88	38.96	-20.00
Sr	2.80	-6.55	-23.20	-3.75	0.60	5.16	-30.97
Nb	-2.90	-8.00	12.63	0.00	9.20	16.00	-11.27
Cs	-12.50	100.00	75.00	33.33	0.00	50.00	-20.00
Be	0.00	160.87	0.00	0.00	0.00	160.87	-50.00
Hf	-2.13	-5.37	7.55	-1.85	-3.57	12.75	-15.22
Y	0.00	-16.44	-15.94	-2.82	-0.47	11.07	-12.03
Ta	-27.18	33.77	90.91	1.15	19.18	-5.19	-29.33
Sc	5.26	113.48	-27.78	0.00	-5.26	113.48	0.00
V	-0.78	-18.35	-32.18	-2.25	1.71	10.76	-11.51
As							
Mo							

Appendix 2 (cont.): Mass balance gain and loss values for transect 2225L, LM-P-043 sample set. Sample D was omitted due to carbonate-rich micro-vein present in sample. b.d. = below detection.

Sample Numbers	LM-P-060B	LM-P-039A	LM-P-039B	LM-P-026	LM-P-027	LM-P-031
SiO2	-0.23	4.21	-7.35	-5.94	-2.82	-16.20
TiO2	-16.59	-2.74	48.14	14.46	7.35	48.45
Al2O3	-4.17	0.86	1.99	-10.26	-10.01	-5.11
FeOT	1.64	-7.79	25.28	15.91	-3.12	58.32
FeO	-1.80	-7.79	26.09	9.11	-11.50	40.63
Fe2O3	84.83	-7.76	5.61	180.42	199.54	486.34
MgO	-3.68	15.59	-23.39	-2.94	-4.28	-14.14
MnO	3.76	23.08	-8.24	-5.41	21.41	26.35
CaO	-23.72	-25.05	20.19	-39.90	-10.04	-54.78
Na2O	11.73	18.82	0.19	-33.02	-8.26	-40.62
K2O	-50.90	171.43	-81.17	-28.03	-60.31	-95.29
P2O5	-27.71	-3.57	51.81	-2.41	-4.22	26.51
LOI	191.58	-4.74	166.32	352.63	248.42	528.42
Au	11600.00	-67.74	1760.00	28100.00	47900.00	5129900.00
Pd	b.d.	b.d.	b.d.	b.d.	b.d.	b.d.
Pt	b.d.	b.d.	b.d.	b.d.	b.d.	b.d.
Cu	1787.82	-71.31	10813.41	14776.88	5132.56	10837.07
Ni	1878.67	11.16	-41.59	10871.56	2968.72	7482.94
Co	-2.95	23.91	-35.95	78.79	16.46	23.15
Cr	63.47	25.90	-63.34	32.33	1.19	-53.30
Ag	199.36	184.60	-59.05	295.58	488.03	1578.55
Sn	800.00	b.d.	200.00	2450.00	3050.00	2600.00
Mn	119.56	28.16	-19.95	90.80	170.08	158.42
Zn	155.43	24.44	-2.17	178.26	183.70	183.70
Cl	500.00	b.d.	-100.00	725.00	275.00	500.00
F	250.00	b.d.	-100.00	200.00	200.00	200.00
B	b.d.	b.d.	b.d.	b.d.	b.d.	b.d.
Li	13.30	6.72	-33.99	126.60	57.64	37.93
Ga	-9.25	-13.49	14.77	-19.93	-9.25	12.10
Ge	200.00	0.00	-83.33	116.67	183.33	116.67
Cd	50.94	33.33	-83.02	126.42	-62.26	-43.40
La	-17.77	-2.54	40.83	-10.46	-15.90	3.30
Ce	-17.59	-4.34	39.61	-3.50	-10.54	8.48
Pr	-15.58	-3.12	41.05	-7.74	-11.96	5.53
Nd	-23.24	-6.07	38.69	-10.30	-13.57	2.65
Sm	-19.87	-3.45	35.75	-11.50	-5.91	2.66
Eu	-29.26	-23.60	48.13	-33.01	-29.68	-23.02
Gd	-13.04	-6.70	41.06	-17.11	-11.59	-3.01
Tb	-12.29	-3.85	32.20	-16.10	-8.47	5.51
Dy	-10.13	-0.59	31.85	-14.25	-7.30	2.75
Ho	-15.53	-9.30	25.24	-15.53	-8.25	4.85
Er	-12.41	-8.68	32.48	-9.67	-5.29	8.94
Tm	-7.69	-15.15	33.60	-1.62	-1.62	12.96
Yb	-9.03	-7.00	29.03	-0.65	-0.65	14.84
Lu	-5.74	-7.41	22.36	7.40	6.95	26.89
Zr	-5.15	-5.74	52.36	36.95	0.40	19.37
Ba	-39.55	446.75	-84.09	-43.58	-56.29	-94.01
Pb	34.04	-60.98	-47.66	14.89	-58.51	-39.36
Th	17.88	14.29	77.07	289.54	-10.96	52.28
U	11.76	0.00	17.65	223.53	11.76	141.18
Bi	9233.33	b.d.	b.d.	53566.67	28233.33	10566.67
Tl	-43.53	40.00	-82.35	44.71	-47.06	-78.82
Rb	-45.50	135.80	-77.93	-4.63	-59.13	-94.55
Sr	-22.02	-38.18	40.26	-29.02	-8.85	-65.71
Nb	-5.33	-18.63	36.00	42.67	-2.67	24.00
Cs	25.00	33.33	-25.00	100.00	-25.00	b.d.
Be	160.87	-33.33	-60.87	b.d.	30.43	b.d.
Hf	-7.38	-2.82	42.95	28.86	-1.34	14.77
Y	-17.99	-5.36	35.47	-19.55	-13.32	3.29
Ta	-2.60	0.00	-61.04	51.95	31.17	53.25
Sc	147.19	-36.00	-71.91	79.78	113.48	91.01
V	-12.03	-9.22	37.34	-13.92	-6.96	30.38
As		-40.00	275.00	2150.00	b.d.	b.d.
Mo		-60.00	328.57	b.d.	b.d.	b.d.

Appendix 2 (cont.): Mass balance gain and loss values for transect 2225L, LM-P-043 sample set. Sample D was omitted due to carbonate-rich micro-vein present in sample. b.d. = below detection.